Multi-scale structuration and dynamic mechanical response of multi-phasic elastomer systems

Robins Kumar

N°d'ordre

NNT : 2022ISAL0111

THESE de DOCTORAT DE L'INSA LYON, membre de l'Université de Lyon

Ecole Doctorale N° EDA 034
(Matériaux de Lyon)

Spécialité/ discipline de doctorat : Matériaux

Soutenue publiquement le 12/12/2022, par :
(Robins KUMAR)

Multi-scale structuration and dynamic mechanical response of multi-phasic elastomer systems

---

Devant le jury composé de :

ROYAUD, Isabelle	Professeur	Université de Lorraine	Rapporteur
PLANES, Emilie	Maitre de conférences HDR	Université Savoie Mont Blanc	Rapporteur
GAUCHER, Valerie	Professeur	Université de Lille	Examinatrice
GAUTHIER, Catherine	Professeur	INSA Lyon	Examinatrice
CHAZEAU, Laurent	Professeur	INSA Lyon	Directeur de thèse
DALMAS, Florent	Maitre de conférences	INSA Lyon	Co-directeur de thèse
MALICKI, Nicolas	Ingénieur de recherche	Michelin	Invité

Département FEDORA – INSA Lyon - Ecoles Doctorales

SIGLE	ECOLE DOCTORALE	NOM ET COORDONNEES DU RESPONSABLE
CHIMIE	**CHIMIE DE LYON** **https://www.edchimie-lyon.fr** Sec. : Renée EL MELHEM Bât. Blaise PASCAL, 3e étage secretariat@edchimie-lyon.fr	**M. Stéphane DANIELE** C2P2-CPE LYON-UMR 5265 Bâtiment F308, BP 2077 43 Boulevard du 11 novembre 1918 69616 Villeurbanne **directeur@edchimie-lyon.fr**
E.E.A.	**ÉLECTRONIQUE, ÉLECTROTECHNIQUE, AUTOMATIQUE** **https://edeea.universite-lyon.fr** Sec. : Stéphanie CAUVIN Bâtiment Direction INSA Lyon Tél:04.72.43.71.70 secretariat.edeea@insa-lyon.fr	**M. Philippe DELACHARTRE** INSA LYON Laboratoire CREATIS Bâtiment Blaise Pascal, 7 avenue Jean Capelle 69621 Villeurbanne CEDEX Tél : 04.72.43.88.63 **philippe.delachartre@insa-lyon.fr**
E2M2	**ÉVOLUTION, ÉCOSYSTÈME, MICROBIOLOGIE, MODÉLISATION** **http://e2m2.universite-lyon.fr** Sec. : Bénédicte LANZA Bât. Atrium, UCB Lyon 1 Tél : 04.72.44.83.62 secretariat.e2m2@univ-lyon1.fr	**Mme Sandrine CHARLES** Université Claude Bernard Lyon 1 UFR Biosciences Bâtiment Mendel 43, boulevard du 11 Novembre 1918 69622 Villeurbanne CEDEX **sandrine.charles@univ-lyon1.fr**
EDISS	**INTERDISCIPLINAIRE SCIENCES-SANTÉ** **http://ediss.universite-lyon.fr** Sec. : Bénédicte LANZA Bât. Atrium, UCB Lyon 1 Tél : 04.72.44.83.62 secretariat.ediss@univ-lyon1.fr	**Mme Sylvie RICARD-BLUM** Institut de Chimie et Biochimie Moléculaires et Supramoléculaires (ICBMS) - UMR 5246 CNRS - Université Lyon 1 Bâtiment Raulin - 2ème étage Nord 43 Boulevard du 11 novembre 1918 69622 Villeurbanne Cedex Tél : +33(0)4 72 44 82 32 **sylvie.ricard-blum@univ-lyon1.fr**
INFOMATHS	**INFORMATIQUE ET MATHÉMATIQUES** **http://edinfomaths.universite-lyon.fr** Sec. : Renée EL MELHEM Bât. Blaise PASCAL, 3e étage Tél : 04.72.43.80.46 infomaths@univ-lyon1.fr	**M. Hamamache KHEDDOUCI** Université Claude Bernard Lyon 1 Bât. Nautibus 43, Boulevard du 11 novembre 1918 69 622 Villeurbanne Cedex France Tél : 04.72.44.83.69 **hamamache.kheddouci@univ-lyon1.fr**
Matériaux	**MATÉRIAUX DE LYON** **http://ed34.universite-lyon.fr** Sec. : Yann DE ORDENANA Tél : 04.72.18.62.44 yann.de-ordenana@ec-lyon.fr	**M. Stéphane BENAYOUN** Ecole Centrale de Lyon Laboratoire LTDS 36 avenue Guy de Collongue 69134 Ecully CEDEX Tél : 04.72.18.64.37 **stephane.benayoun@ec-lyon.fr**
MEGA	**MÉCANIQUE, ÉNERGÉTIQUE, GÉNIE CIVIL, ACOUSTIQUE** **http://edmega.universite-lyon.fr** Sec. : Stéphanie CAUVIN Tél : 04.72.43.71.70 Bâtiment Direction INSA Lyon mega@insa-lyon.fr	**M. Jocelyn ONJOUR** INSA Lyon Laboratoire CETHIL Bâtiment Sadi-Carnot 9, rue de la Physique 69621 Villeurbanne CEDEX **jocelyn.bonjour@insa-lyon.fr**
ScSo	**ScSo*** **https://edsciencessociales.universite-lyon.fr** Sec. : Mélina FAVETON INSA : J.Y. TOUSSAINT Tél : 04.78.69.77.79 melina.faveton@univ-lyon2.fr	**M. Bruno MILLY** Université Lumière Lyon 2 86 Rue Pasteur 69365 Lyon CEDEX 07 **bruno.milly@univ-lyon2.fr**

*ScSo : Histoire, Géographie, Aménagement, Urbanisme, Archéologie, Science politique, Sociologie, Anthropologie

Abstract

In this study, new types of elastomer systems - seen as an alternative for conventional nanocomposites widely used in tire industry - were prepared and investigated thoroughly. They are made of an SBR (Styrene-Butadiene Rubber) matrix, blended with one resin among three resins with low molecular weight resins, with a higher Tg than the polymer, and different miscibilities. Such materials raise different questions: How does the resin incorporation influence the elastomer network structure? Depending on the miscibility and the resin content, what is the resulting morphology? How does the morphology evolve with the temperature, the processing conditions and the crosslinking protocol? And of course, how this morphology impacts the macroscopic mechanical properties?

Two of the studied resins showed good miscibility, with the absence of phase separation, and no strong influence on the chemical crosslinking reactions of the polymer. Their impact on the viscoelastic behavior is the consequence (i) of a modification of the polymer glass transition, which is broadened due to the presence of resin concentration fluctuations, and shifted towards higher temperature, and (ii) of the dilution of the polymer during its crosslinking, which results in a decrease of the modulus above the glass transition temperature. The third resin has a lower miscibility. In addition to a modification of the glass transition and to a dilution effect, it leads to a phase separation, and therefore the existence of a resin rich phase. This phase is rigid at ambient temperature and reinforces the polymer rich phase, i.e the elastomer matrix. Interestingly, this phase separation slightly depends on the temperature, with a kinetics which may provide a new way to pilot the viscoelastic response of the material.

Key-words: Elastomer, Polymer/resin blends, phase separation, dynamic mechanical analysis.

Résumé

Dans cette étude, de nouveaux types de systèmes élastomères - considérés comme une alternative aux nanocomposites conventionnels largement utilisés dans l'industrie pneumatique - ont été préparés et étudiés de manière approfondie. Ils sont constitués d'une matrice SBR (Styrene-Butadiene Rubber), mélangée à une résine parmi trois résines à faible poids moléculaire, avec une Tg plus élevée que le polymère, et différentes miscibilités. De tels matériaux soulèvent différentes questions : Comment l'incorporation de la résine influence-t-elle la structure du réseau de l'élastomère ? En fonction de la miscibilité et de la teneur en résine, quelle est la morphologie résultante ? Comment la morphologie évolue-t-elle avec la température, les conditions de traitement et le protocole de réticulation ? Et bien sûr, quel est l'impact de cette morphologie sur les propriétés mécaniques macroscopiques ?

Deux des résines étudiées ont montré une bonne miscibilité, avec l'absence de séparation de phase, et aucune influence forte sur les réactions chimiques de réticulation du polymère. Leur impact sur le comportement viscoélastique est la conséquence (i) d'une modification de la transition vitreuse du polymère, qui est élargie en raison de la présence de fluctuations de concentration de la résine, et déplacée vers une température plus élevée, et (ii) de la dilution du polymère pendant sa réticulation, qui entraîne une diminution du module au-dessus de la température de transition vitreuse. La troisième résine présente une miscibilité plus faible. En plus d'une modification de la transition vitreuse et d'un effet de dilution, elle conduit à une séparation de phase, et donc à l'existence d'une phase riche en résine. Cette phase est rigide à température ambiante et renforce la phase riche en polymère, c'est-à-dire la matrice élastomère. Il est intéressant de noter que cette séparation de phase dépend légèrement de la température, avec une cinétique qui peut fournir une nouvelle façon de piloter la réponse viscoélastique du matériau.

Mots clés : élastomère, mélange résine/polymère, séparation de phase, analyse mécanique dynamique.

Contents

List of Figures

List of Tables

Introduction

This project is built in the frame of researches on the impact of the multiphasic character of elastomers on their performance, when they are used in tires parts. This multiphasic character may be one possibility to control the tires rolling resistance and grip properties, a central research theme of Michelin company. In particular, one wishes to decorrelate the temperature/frequency domain involved in the rolling resistance from the one involved in the grip.

In this study, new types of elastomer systems, seen as an alternative for conventional nanocomposites widely used in industrial applications such as tire industry, were prepared and investigated thoroughly. They are made of an SBR (Styrene-Butadiene Rubber) matrix, blended with three different low molecular weight and high T_g resins. Such materials raise different questions: How does the resin incorporation influence the elastomer network structure? Depending on the miscibility and the resin content, what is the resulting morphology? How does the morphology evolve with the temperature, the processing condition and the crosslinking protocol? And of course, how this morphology impacts the macroscopic mechanical properties? In order to answer these questions, the evolution of microstructure in such systems and its consequences on the macroscopic dynamic mechanical behavior were studied by closely combining the analysis with different techniques such as swelling, NMR, DSC, DMA, SAXS, and electron microscopy.

The chapter 1 of the manuscript is bibliographical. It first begins with basic knowledge on polymers. Then we recall what is an elastomer, how it is crosslinked and the impact of the cross-linking process on the glass transition temperature. We also recall basic concepts about the physics of rubber elasticity, the reinforcement of elastomers by fillers, and the impact of these fillers on the glass transition temperature and viscoelastic properties. Finally, we discuss about polymer blends with a focus on the thermodynamics of miscibility and phase separation, the impact of blending on the glass transition temperature, the mechanical reinforcement and the viscoelastic behavior.

In chapter 2, all the materials used in this study and their processing are presented. The concepts and principles behind using different methods and techniques to answer the question we raised are then introduced.

In chapter 3, we first evaluate the modification of the SBR matrix after crosslinking with peroxide and sulfur system; peculiar attention is paid to the glass transition temperature, the network

characteristics, the viscoelastic behavior and the morphology. Then the glass transition temperature of resins is evaluated by DSC analysis. Finally, the miscibility properties of raw materials are evaluated using Hansen solubility parameter approach.

In chapter 4, we first study the influence of the presence of R2 and R3 resins (resins described in Chapter 2) on the crosslinking reactions, with sulfur or peroxide curing systems. We then evaluate how the glass transition temperature is modified as well as the viscoelastic behavior. The discussion is then completed by a morphological analysis of the blends.

Finally, in chapter 5, the influence of resin R1 on curing reactions and on SBR network is investigated. Great importance is given to the evolution of viscoelastic behavior with temperature and resin concentration. The morphological details from nano to micro scale are investigated by AFM, TEM, and SEM in the PC and SC crosslinked systems. The stability of the microstructure with temperature change is also investigated by SAXS and DMA analysis.

The manuscript ends with the conclusions on the main results and on the research perspectives opened by this work.

1 Bibliography

In this chapter, we first present a brief overview of the important concepts about polymers and their properties. Then we recall what is an elastomer, how it is crosslinked and the impact of the cross-linking process on the glass transition temperature. We also recall basic concepts about the physics of rubber elasticity, the reinforcement of elastomers by fillers, and the impact of these fillers on the glass transition temperature and viscoelastic properties. Finally, we discuss about polymer blends with a focus on the thermodynamic of miscibility and phase separation, the impact of blending on the glass transition temperature, the mechanical reinforcement and the viscoelastic behavior.

Contents

1.1 Generalities about Polymers

1.1.1 Polymers

A polymer is a material made of macromolecules which are themselves composed of a large monomer units. The molecular weights of these polymer chains can be more or less distributed depending on the polymerization processes. It is therefore useful to define a number average molecular weight (M_n) and a weight average molecular weight (M_w) as:

$$M_n = \frac{\sum_i N_i M_i}{\sum_i N_i} \tag{1.1}$$

Where N_i is the number of chains and M_i the molecular weight of the i chain,

and

$$M_w = \frac{\sum_i N_i M_i^2}{\sum_i N_i M_i} \tag{1.2}$$

The polydispersity index (PDI) is defined as $(M_w/M_n) \geq 1$ and is an indication of the broadness of the molecular weight distribution.

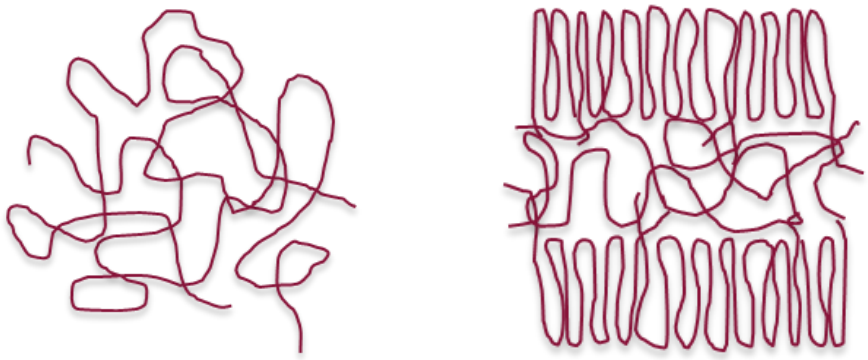

FIGURE 1. 1 MOLECULAR CHAINS ARRANGEMENT IN AMORPHOUS POLYMERS (LEFT) AND SEMI-CRYSTALLINE POLYMERS (RIGHT).

The cohesion between polymer chains is due to the weak Van der Walls interactive forces. [1] Polymers can be amorphous or semi-crystalline as shown in Figure 1. 1. In amorphous polymers, the chains are arranged in random or disordered fashion whereas in semi-crystalline polymers, chains are arranged in partially ordered fashion, with a degree of ordering "known as crystallinity", that can vary from a few % (for instance for Natural rubber) up to more than 95% (for instance in cellulose whiskers).

1.1.2 Glass transition phenomenon in amorphous polymers

When a polymer is cooled down from molten state, it can either undergo crystallization or reach the glassy state, depending on the cooling rate and polymer characteristics. The transition from

rubbery to glassy state is called glass transition, during which many physical parameters such as specific volume, heat capacity, and mechanical properties change significantly. The temperature dependence of these parameters is readily used to characterize this glass transition phenomenon as depicted in Figure 1. 2. Below the glass transition temperature T_g, the rearrangement of atoms and mobility of molecular chains are restricted (their characteristic relaxation time is much longer than the experimental time). The glass transition is a kinetic phenomenon: slower the cooling rate, lower the T_g as the molecules have more time to get closer to their equilibrium state.

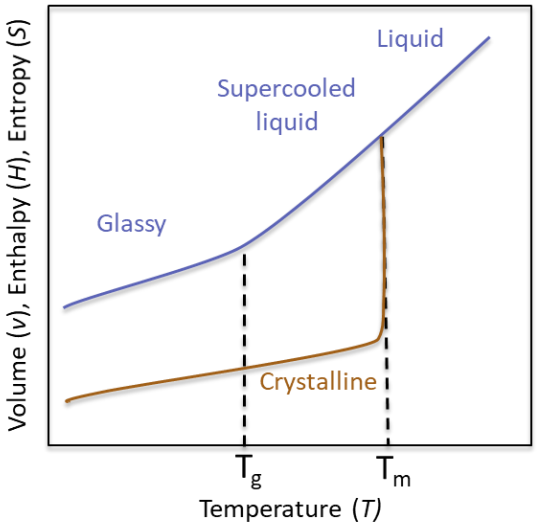

FIGURE 1. 2 SCHEME OF THE EVOLUTION OF THERMODYNAMIC STATE FUNCTIONS (V, H, S) AS A FUNCTION OF TEMPERATURE (T) FOR AN AMORPHOUS AND A CRYSTALLINE POLYMER.

During the glass transition, a strong change in the mechanical properties of amorphous polymers is observed. For instance, when measuring the mechanical response of a polymer to which a small deformation is applied (for instance 1% tensile strain), a strong decrease in the modulus can be measured, as illustrated in Figure 1. 3 for an amorphous polymer. Different temperature domains can be distinguished.

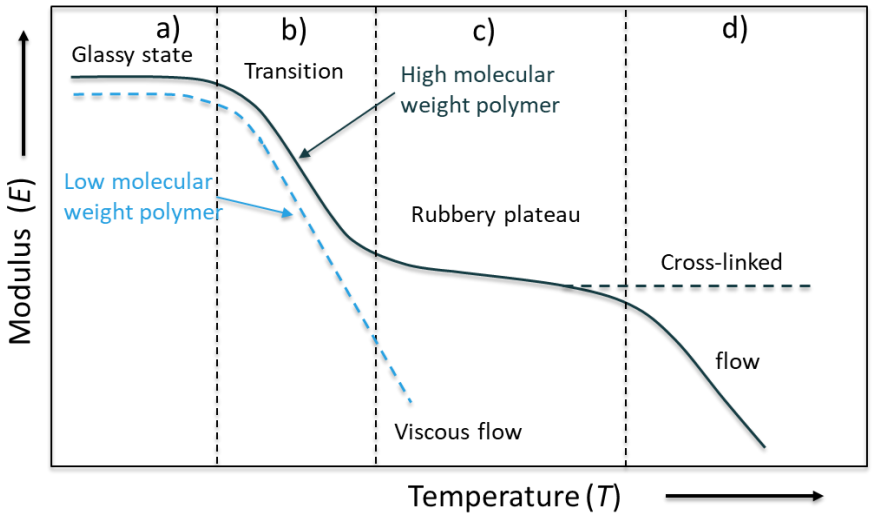

FIGURE 1. 3 SCHEMATIC EVOLUTION OF THE ELASTIC MODULUS (*E*) AS A FUNCTION OF TEMPERATURE (*T*) FOR AN AMORPHOUS POLYMER.

- at low temperatures, in the so-called glassy state, molecular chains motions are either completely restricted or localized, and the polymers are “rigid” materials with a very high value of modulus (few GPa).

- when increasing the temperature, in an intermediate temperature domain which corresponds to the glass transition, segmental molecular motions of chains can take place in the polymer, more easily with the temperature increase, which explain the drastic modulus decrease by several decades with this temperature increase.

- at temperatures above the temperature domain of the glass transition, the modulus can be stable over a temperature domain whose width depends on the polymer molecular weight. The polymer is said to be in the rubbery state. The higher the molecular weight of the polymer, the higher the possibility of entanglements between the macromolecules, and the higher the maximal temperature of the rubbery domain. The modulus is in the range of MPa.

- at last, at higher temperature, large molecular motions can occur in the polymers, which can therefore flow, if the polymer is not crosslinked, in other words if it is not an elastomer.

1.1.3 Relaxation phenomena and viscoelasticity

As said previously, the polymer modulus is related to the possibility of the polymer chains to move, and therefore to relax under an applied external load, possibility which depends on the temperature. Different kinds of internal motions occur in a polymer macromolecule, which can extend over a more or less large spatial scales, depending on the polymer itself, on the temperature, and on the time during which the load is applied. These different scale motions are the origin of different

relaxations, that can be for instance characterized by mechanical spectroscopy (also called Dynamic Mechanical Analysis, DMA). In this experiment, oscillatory (sine) strain of pulse ω ($rad\ s^{-1}$) is applied (cf. Figure 1. 4):

$$\varepsilon(t) = \varepsilon_0 \sin(\omega t) \tag{1.3}$$

A measured stress response is measured, which is also harmonic when the applied strain is small enough (we are then in the so-called linear domain):

$$\sigma(t) = \sigma_0 \sin(\omega t + \delta) \tag{1.4}$$

Where δ is the delay or phase difference between strain and stress.

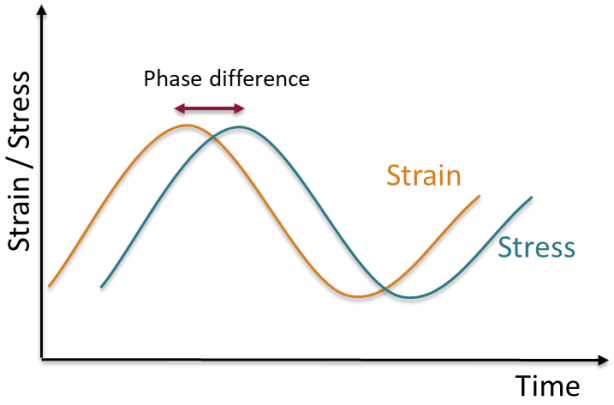

FIGURE 1. 4 ILLUSTRATION OF PHASE DELAY FOR AN APPLIED OSCILLATORY STRAIN.

The complex strain and stress can define as well a complex modulus;

$$E^*(\omega) = \frac{\sigma^*(t)}{\varepsilon^*(t)} = E'(\omega) + iE^{"}(\omega) \tag{1.5}$$

$$\tan\delta = \frac{E^{"}}{E'} \tag{1.6}$$

The real part is the storage modulus (E') and the imaginary part is the loss modulus (E''). Note that the notation E is used when the solicitation is in tension, whereas G is used for shear. E' is related to the stored elastic energy and E'' is proportional to the dissipated energy during the deformation cycle. In case of a purely elastic material, stress and strain are in phase and E'' is null whereas in case of a purely viscous materials, stress and strain are out of phase and E' is null[2] [3]. A typical curve measured with a polymer showing a relaxation phenomenon occurring in the explored frequency range is schematized in Figure 1. 5. The relaxation time is estimated from the frequency at the E'' peak. As said previously, different relaxations can be evidenced by this technique.

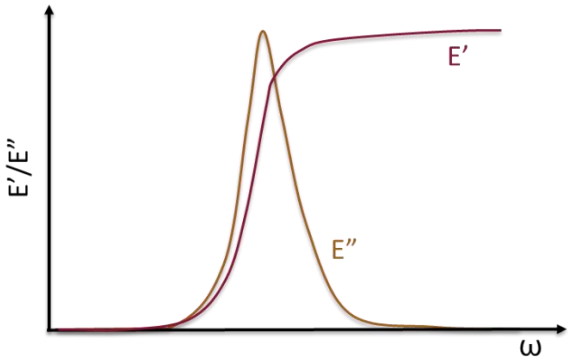

FIGURE 1. 5 TYPICAL VARIATION OF THE VISCOUS AND ELASTIC COMPONENTS OF THE COMPLEX MODULUS OF A POLYMER IN A FREQUENCY DOMAIN WHERE A RELAXATION OCCURS.

Secondary or Simple relaxations

Secondary relaxations are generally due to local mode relaxations in the main chain, side group motions, and alkyl group motion in side group, i.e. limited to a few bonds of the polymer chain only. H-bonding, crystallites, and tacticity can also give rise to secondary relaxation if the movement of parts of the chain is restricted by them. [4] [5] The characteristic relaxation times in secondary relaxations follows the Arrhenius law:

$$\tau = \tau_0 \, exp\left(\frac{E_a}{k_B T}\right) \tag{1.7}$$

Where the parameter τ_0 is the relaxation time at $T \to \infty$, E_a is the activation energy and k_B is the Boltzmann's constant. Due to their quite non-cooperative character, the position of the peak of secondary relaxations is mostly not affected if some plasticizers are added to the polymers. [6]

Primary (segmental α-relaxation) or Complex relaxation

The α-relaxation which occurs at lower pulsations (corresponding to larger time), and which is much more intense, involves cooperative molecular motions.[7] The large inter and intra molecular interactions involved in this relaxation gives rise to larger activation energies. Addition of small molecules like plasticizers by modifying these interactions, change the relaxation times. The spectrum of cooperative motions is reflected into the distribution of the relaxation times, which corresponds to the distribution of activation energies. [8] Williams, Landel, and Ferry [9] established a universal function for the temperature dependence of the relaxation times :

$$\log\left(\frac{\tau}{\tau_{T_g}}\right) = \frac{-C_1\left(T - T_g\right)}{\left(C_2 + T - T_g\right)} \tag{1.8}$$

Where C_1 and C_2 are constants. This law is applicable for the temperature between T_g and $T_g + 100$.

1.1.4 Conclusion

Amorphous polymers are viscoelastic material. The mobility of their chains enables to relax an external load over a time scale which depends on the chemical nature of the polymer. Different relaxation mechanisms can be activated depending on the time (or frequency) of the mechanical loading and the temperature at which this loading is performed. We will see in section 1.3 how blending the polymer with plasticizer, resin, or another polymer can influence these phenomena. Moreover, among the different relaxation mechanisms which can occur in a polymer, the one corresponding to its flow can be suppressed by the creation of crosslinks between the macromolecules, i.e the transformation of the polymer as an elastomer. This class of material is described in the next section.

1.2 Elastomers

1.2.1 Generalities

Amorphous polymers can be crosslinked, which, as said previously, change their properties mainly at temperature above the glass transition temperature. The crosslinking process of polymer chains enables to create a class of materials, which are called elastomers. These materials have unique characteristics above their T_g: [10] [11] [12] [13]

- they are made of initially high molecular weight polymers whose T_g is usually below the ambient temperature. This molecular weight is high enough for the macromolecules to form physical entanglements.
- because their crosslink density (the number of cross-links per unit volume in a polymer) is usually in the range of the entanglement density, the elastomers show a high degree of deformability under an applied stress, and because of the presence of these crosslinks, large deformation can be recovered once the stress is removed.

Among all the existing elastomers, one can distinguish natural rubber (NR). This one is mainly obtained from the Hevea Brasiliensis trees in the form of latex by a process called tapping. The latex of natural rubber is a colloidal suspension of rubber particle containing 30-40 wt % of solid content. The latex can be coagulated to form the dry rubber sheets used in various applications such as tires. The chemical composition of natural rubber is cis-1,4 polyisoprene. NR is classified into different grades based on the fraction of impurities present in the final product. The glass transition temperature of NR ranges between -50˚C to -75˚C depending on its grade and testing conditions.

NR can partially crystallize under two conditions: 1) if stored at low temperatures (0˚C or lower) for a long time and 2) if stretched, a phenomenon known as strain-induced crystallization of NR. The crystallites created in the network by deformation induce reinforcing effect. Due to this mechanism of self-reinforcing, NR displays higher tensile strength compared to the non-crystallizing rubbers. [14] [15] The expansion of automobile industry increased the demand of rubber in late 18th century. Production of NR became unsufficient to fulfill that demand and then came therefore the need for investigating the synthetic routes to produce rubber.

The first synthetic rubber based on the chemical structure of polyisoprene was produced in 1909. Later, different synthetic rubbers based from petroleum derivatives were developed using various routes of polymer synthesis. The most widely used synthetic rubber is a copolymer of styrene and butadiene monomers (see in Figure 1. 6 a styrene-butadiene rubber or SBR). This is the material that we will study in this Ph-D. Depending on the synthesis process, the arrangement of the comonomers can be random or by blocks. This synthesis is made via emulsion or solution polymerization techniques. The first emulsion polymerized SBR was produced in 1929 and the solution polymerization method to produce SBR was developed in the 1950s. SBRs can vary by their styrene content and the microstructure of its polybutadiene unit which can have a cis, trans, or vinyl conformation.

Increasing the vinyl and styrene content increases the T_g of SBR. In the tyre, this is a way to optimize the glass transition, and therefore the energy dissipation in relation with the traction/rolling resistance compromise.

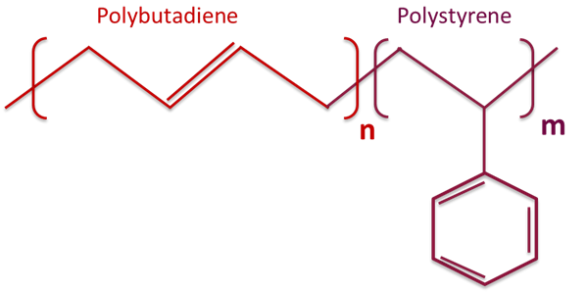

FIGURE 1. 6 CHEMICAL STRUCTURE OF SBR SHOWING THE POLYBUTADIENE AND STYRENE UNITS

1.2.2 Cross-linking of elastomers and its effect on T_g

The cross-linking of elastomers is necessary to prevent the flow of the polymer chains and provide dimensional stability in technical applications. A typical cross-linked network of polymer chains is shown in Figure 1. 7.

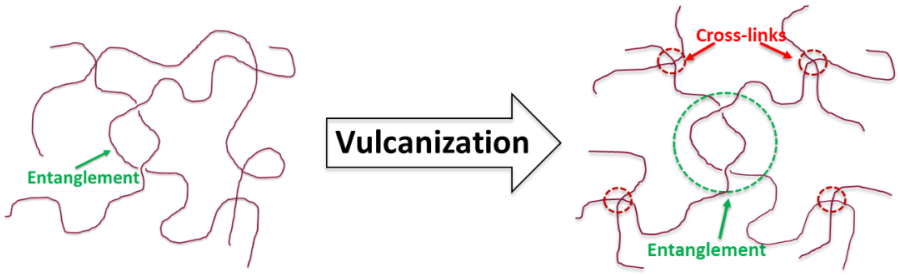

FIGURE 1. 7 DEPICTION OF ENTANGLEMENTS AND CROSS-LINKS IN A TYPICAL ELASTOMER NETWORK.

Several chemical additives are used to cross-link elastomers. Among them, sulfur-based systems are the most widely used to "vulcanize" the polymer by forming sulfur bridges between the chains at the level of the diene monomers. To optimize this process, accelerators and activators are added in the formulation. Depending on the sulfur accelerator ratio, sulfur vulcanization systems are classified as conventional (CV), semi-efficient (semi-EV), and efficient vulcanization (EV). Peroxide curing systems can also be used. They are generally employed where improved compression set and ageing properties are required for the cured compounds. They are more efficient curing systems for saturated polymers. [16]

The properties of elastomers are dictated by their cross-link density. [17] Higher cross-link density shifts the T_g of elastomer towards higher temperature. A 3˚C shift towards the higher temperature in the T_g of CB filled SBR composite due to the increased cross-link density of the SBR matrix was reported by Nuthathai et al. [18] when sulfur amount was adjusted from 1.4 phr to 2.2 phr (cf. Figure 1. 8). Most of the authors claim that this shift is due to the restricted mobility of the molecular chains by the increase of the topological constraints. [19] [20]

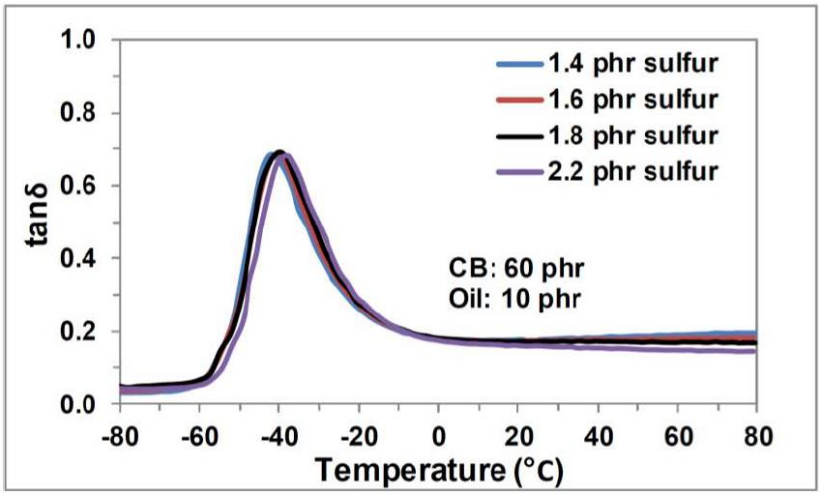

FIGURE 1. 8 EFFECT OF SULFUR CONCENTRATION IN FILLED SBR ON THE TEMPERATURE DEPENDENCE OF TANΔ (TA) AT THE 0.05% STRAIN AND FREQUENCY OF 10HZ. [18]

Recent studies have found that part of the curative does not necessarily connect the chains via intermolecular cross-links but instead participates to the creation of pendent groups of sulfur or accelerator, sulfur/accelerator complexes which can hinder the mobility of chains. This explains why the size of the curatives can also influence the T_g of the elastomer: the bulkier or higher the molecular weight additives, the more the molecular mobility of polymer chains is reduced. [21]

1.2.3 Rubber elasticity

Rubber elasticity pertains to the reversible extensibility of elastomer chains. This was first investigated in quasi-static conditions in unfilled elastomers. The effect of temperature on the elastic properties of elastomers was reported by Gough in 1805 and later confirmed by Joule in 1859 and is known as "Thermo-elastic effect". [13] According to this effect:

- rubber in stretched state under constant load contracts on heating
- when subjected to stretching, the material releases heat.

In the general case of a volume submitted to a quasi-constant force f at temperature T, thermodynamics for a reversible transformation, with no volume variation enables to write:

$$f = \left(\frac{\partial U}{\partial l}\right)_T - T\left(\frac{\partial S}{\partial T}\right)_l \quad (1.9)$$

Where f is the force applied to the extended rubber sample, l is the length of the sample, T is the temperature and U is the internal energy. Thus, f results from the variation of internal energy and entropy. In the case of an elastomer, the first term can be neglected and the force is directly related to the entropy variation. Thus, according to this relationship, force is therefore proportional to the temperature, which in other word means the modulus of unfilled rubber increases with the increase in temperature. Moreover, this means that a prediction of the force can be obtained from the calculation of the entropy variation, which explains the use of the term "entropic elasticity" for elastomer.

Single chain description

In the frame of the rubber elasticity theory, simplifications have been proposed for the calculation of the entropy variation, starting from the molecular scale. In the simplest case of a freely jointed chains, made of n segments of length l, linked by bonds, a free rotation of these segments can occur around the bonds. Thus, the root mean square distance between the two chain ends is written as: [13]

$$\langle R_0^2 \rangle^{1/2} = l\sqrt{n} \quad (1.10)$$

If the chain is represented in a $3D$ space (cf. Figure 1. 9) such that one end of the chain, A, is fixed at a position in a cartesian coordinate and another end, B, is freely moving, then the probability distribution, P, of finding the chain end B at the coordinate (x,y,z) is:

$$P(\mathrm{x},\mathrm{y},\mathrm{z}) = \left(\frac{3}{2\pi\langle \mathrm{R}_0^2\rangle}\right)^{3/2} \exp\left(-\frac{3\left(\mathrm{x}^2+\mathrm{y}^2+\mathrm{z}^2\right)}{2\langle \mathrm{R}_0^2\rangle}\right) \tag{1.11}$$

This formula uses the Gaussian approximation, which consider that B is at a distance R from A much lower than the distance of the completely stretched chain.

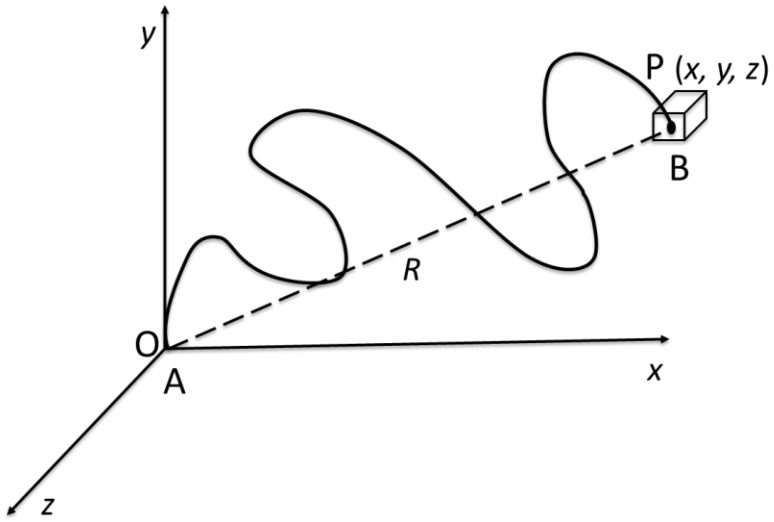

FIGURE 1. 9 FREELY JOINTED CHAIN IN 3D SPACE WITH ONE END OF CHAIN FIXED AT ORIGIN OF A CARTESIAN COORDINATE.

The density probability function, $\mathrm{P}(\mathrm{x},\mathrm{y},\mathrm{z})$, for a distance R between chain ends is the number of conformations associated to this distance divided by the whole number of possible conformations (for all R):

$$\mathrm{P}(\mathrm{x},\mathrm{y},\mathrm{z}) = \frac{\Omega(\mathrm{R})}{\int \Omega(\mathrm{R})\mathrm{dR}} \tag{1.12}$$

The Boltzmann relation then enables to deduce the entropy S:

$$\mathrm{S} = \mathrm{k}\ln\Omega(\mathrm{R}) \tag{1.13}$$

With k the Boltzmann constant ($\mathrm{k} = 1{,}380\ 10^{-23}\ \mathrm{JK}^{-1}$).

Simplifying this equation leads to:

$$\mathrm{S} = \mathrm{k}\ln\Omega_0^3\ -\frac{3}{2}\frac{\mathrm{kR}^2}{\langle \mathrm{R}_0^2\rangle} \tag{1.14}$$

Where $\mathrm{k}\ln\Omega_0^3$ and R_0^2 are the mean square distance between chain ends.

It is then possible to derive the expression for the force:

$$f = \left(\frac{\partial F}{\partial l}\right)_T = -T\left(\frac{\partial S}{\partial l}\right)_T \equiv -T\left(\frac{\partial S}{\partial R}\right)_T = \frac{3kT}{\langle R_0^2\rangle} R \quad (1.15)$$

Affine network

The previous reasoning for one active chain can be generalized at the scale of the macromolecular network, [22] [23] [24] [13] with the assumption that the strain state is the same for all the active chains of the network. Thus, assuming a homogeneous network with N_c active chains per volume unit:

$$S_r = N_c S \quad (1.16)$$

The free energy variation for a unit volume with N_c active chains between the undeformed and deformed states writes:

$$\Delta F_N = -N_c T[S - S_0] \quad (1.17)$$

Using expression of equation (1.14), one gets:

$$\Delta F_N = -N_c \frac{3kT}{2}\left(\frac{R^2}{\langle R_0^2\rangle} - 1\right) \quad (1.18)$$

Moreover:

$$\langle R^2\rangle = \lambda_x^2 x_0^2 + \lambda_y^2 y_0^2 + \lambda_z^2 z_0^2 = \left(\lambda_x^2 + \lambda_y^2 + \lambda_z^2\right)\frac{\langle R_0^2\rangle}{3} \quad (1.19)$$

where λ_i^2 is the relative variation of the length (extension ratio) in the 3 orthogonal directions x, y and z. Therefore, one can write:

$$\Delta F_N = \frac{N_c kT}{2}\left(\lambda_x^2 + \lambda_y^2 + \lambda_z^2 - 3\right) \quad (1.20)$$

In tensile test this expression leads to:

$$\Delta F_N = \frac{N_c kT}{2}(\lambda^2 + 2\lambda^{-1} - 3) \quad (1.21)$$

Considering unitary volume and sections, the nominal stress can be deduced as:

$$\sigma_n(t) = \left(\frac{d\Delta F_r}{d\lambda}\right)_T = N_c kT\,(\lambda - \lambda^{-2}) \quad (1.22)$$

From which one can deduce the elastic modulus:

$$E = 3N_c kT = 3\frac{\rho RT}{M_c} \quad (1.23)$$

Where ρ is the density of elastomer, R is the gas constant, M_c is the molecular weight between cross-link points and G represents the modulus of rubber in shear condition.

Phantom network

In the affine network, the end of each chain is assumed to be fixed to a non-fluctuating background where change in the displacement between chain ends remains the same as macroscopic displacement. This explains why this model usually overestimates the stress for a given stretching

of an elastomer. Phantom network [25] [13] considered instead that cross-links fluctuate around their average position in the bulk. The free energy expression becomes:

$$\Delta F_N = \frac{1}{2} NkT \left(1 - \frac{2}{\emptyset}\right) \quad (1.24)$$

Where $\emptyset$ is the crosslinks functionality [26] [27] . This leads to the expression for the nominal stress in tensile test:

$$\sigma_n(t) = N_c kT \left(1 - \frac{2}{\emptyset}\right)(\lambda - \lambda^{-2}) \quad (1.25)$$

Slip tube model

Actually, the phantom model appears to usually underestimate the stress level of a stretched elastomer. Thus, other models have been developed such as the Slip tube model. It is a molecular model, [28] [29] [30] which combine the features of slip-link [31] [32] and tube models [33]. In this model the entanglements can be trapped due to the permanent cross-links and chains can slide along these links. Thus, every monomer of the chain is subjected to the topological constraint formed collectively from neighboring chains in which the fluctuations of the chain are effectively restricted to a confining tube. Rubinstein and Panyukov [34] obtained the following expression in tensile test:

$$\sigma_R = \left(G_c + \frac{G_e}{.0.74\lambda + 0.61\lambda^{-1/2} - 0.35}\right)\left(\lambda - \frac{1}{\lambda}^2\right) \quad (1.26)$$

Where G_c and G_e are the parts of elastic modulus representing phantom network (cross-linked) and slip-links (entanglements), respectively. This model is often preferred to describe the mechanical behavior of unfilled elastomer. However, in most application, elastomers need to be reinforced by fillers.

1.2.4 Filled elastomers: means and behavior

As discussed earlier, elastomer are usually reinforced with fillers to increase their stiffness and strength. [35]. Carbon black is the most commonly used filler in rubber industry, particularly the tire industry. Silica based fillers is now often used as an alternative, even though their use needs surface treatments. [36] [37] We will describe here the classical mechanical behavior of elastomeric nanocomposites in the linear and non-linear domains.

Linear domain

In the rubbery state (temperature range where the ratio between Young's moduli of fillers and polymer matrix is the highest), the addition of rigid fillers into the elastomer matrix leads to a well-known reinforcement effect which may increase the modulus of matrix up to two order of magnitude. [38] [39] [40] [41] as evidenced by dynamic mechanical studies done on several nanocomposites

in the linear domain (strain usually below 1%). [42] [43] [44] [45] [46] This reinforcement greatly depends on the filler characteristics such as (1) geometrical factors such as shape, and aspect ratio, (2) the quality of their dispersion, (3) their intrinsic properties i.e. modulus, and (4) their size (in other words their specific surface area) and the nature of their surface. In the case of well dispersed particles, the surface exposed to the polymer implies more polymer-particle interactions and hence a possible better reinforcement. However, a poor dispersion often occurs because of some chemical incompatibility of the fillers with the elastomers. This problem is addressed by surface treatment of the fillers. [47] [48] [49] [50] [51] [52]

Different models have been developed to describe the reinforcement of composite as a function of the filler content. The classical models based on hydrodynamic approach such as Guth and Gold [53] is often used for nanofillers even though it usually fails at nanofiller volume fraction above 10%. [43] At low volume fraction this model is actually close to the three-phase composite sphere model, developed for micron size particles; in this one, the composite is simplified as a representative volume element in which one particle is surrounded by a matrix shell which is embedded in an "equivalent homogeneous matrix" whose properties are the one of the composites. The solution of this problem was given by Christensen and Lo and is recalled in chapter 2 [54] [55] [56] It has been proved to predict the modulus of composites with micron size fillers up to large volume fraction (up to around 40%) of well-dispersed micronic spherical fillers (> 0.4) [57] [58]. However, like the Guth-Gold equation, this model fails to predict the modulus of nanocomposite elastomers.

Non-linear domain

When an elastomer reinforced by nanofillers is submitted to a sinusoidal deformation, the storage moduli decreases when the amplitude of the deformation is increased above few %. This phenomenon known as "Payne effect" increases with the increase in filler concentration as shown in Figure 1. 10 for a solution SBR loaded with different amounts of carbon black. [59] [60] [61] [62]

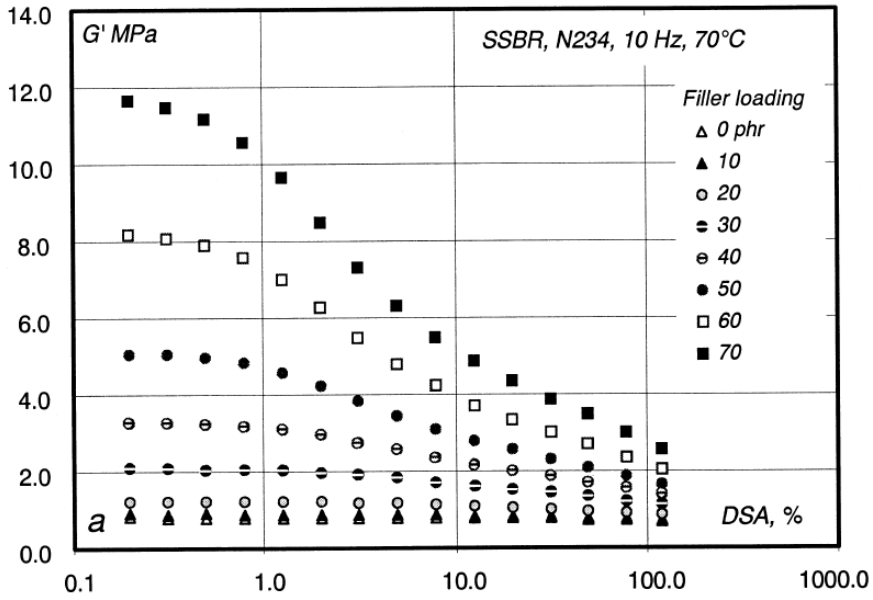

FIGURE 1. 10 STORAGE MODULUS VERSUS DOUBLE STRAIN AMPLITUDE AT 70˚C AND 10 HZ FOR SSBR COMPOUND WITH DIFFERENT LOADINGS OF CARBON BLACK. [43]

Apart from Payne effect, addition of nanofillers to the cross-linked matrix also results in other nonlinear mechanical behavior at higher strain such as stress softening (Mullins effect). [63] [64] Figure 1. 11 provides a microstructural description of the materials which could provide the origin of the Payne and Mullins effect: rupture of the chain bridging, increase in mobility of an initially glassy polymer layer around the particle, strain softening [65] [66] However, there is still ongoing discussion about the fact that these effects involve or not the polymer matrix as it may also originate from direct filler-filler interactions. [67] [68] [69] [70] [71] [72]

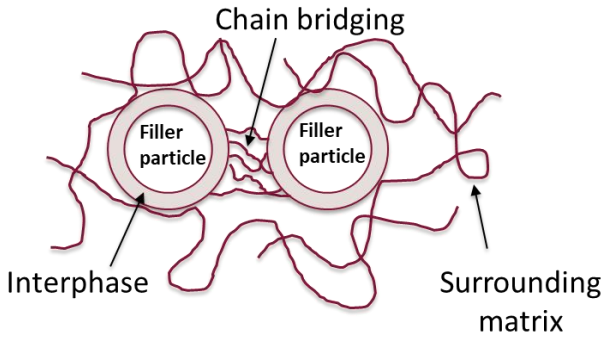

FIGURE 1. 11 TYPICAL REPRESENTATION OF THE NANOFILLERS SURROUNDED BY AN ELASTOMER MATRIX.

1.2.5 Conclusion

Cross-linking is needed in elastomers to make them dimensionally stable above their T_g. The increased degree in cross-linking restricts the chain mobility and therefore increases the T_g of elastomers. This one can also be influenced by the part of curatives which is not consumed during the cross-linking process and modify the network chains. The resulting cross-linked networks can be described by different existing models of rubber elasticity. Moreover, fillers are necessary to improve the mechanical properties of elastomers. Depending on their characteristics and their state of dispersion, they significantly change their viscoelastic properties in both linear and non-linear domains. Micromechanical model based on the three-phase composite sphere model can be used to model the reinforcement of highly filled elastomers (up to 40 vol.%) with micron size spherical particles assuming their very good dispersion.

1.3 Polymer blends

Blending of at least two polymers [73] is a widely used method to produce a novel polymer material combining properties of the two initial polymers. The polymer blends offer several advantages over co-polymers in terms of cost effectiveness, simplicity of the manufacturing, and flexibility for tuning the properties. The properties of polymer blends are firstly determined by the miscibility characteristics of the constituent polymers.

1.3.1 Thermodynamics aspect of miscibility and phase separation

In the thermodynamics terminology, the extent of miscibility depends on the specific interactions between two polymer constituents. The two polymers are said to be thermodynamically miscible if: [74] [75]

1. Free energy of mixing ΔG_M to be ≤ 0 and,

2. Second derivative of ΔG_M with respect to composition $\partial^2 \Delta G_M / \partial \emptyset^2 > 0$

ΔG_M is defined as:

$$\Delta G_M = \Delta H_M - T\Delta S_M \quad (1.27)$$

Where, ΔH_M is the enthalpy of mixing and ΔS_M is the entropy of mixing. For ΔG_M to become negative and higher in magnitude, the enthalpy of mixing, ΔH_M, is also required to be negative. This becomes possible only when there are specific interactions between two polymers. Therefore, the nature of these specific interactions e.g. dipole-dipole, hydrogen bonding, electron donor-

acceptor complexes, and ionic interactions are of great importance to influence the miscibility of polymer blends.

Flory-Huggins relationship

Flory-Huggins relationship [76] is the most commonly used method to predict the free energy of mixing of polymers which is given as:

$$\frac{\Delta G_m}{RT} = \frac{\varphi_1}{V_1} ln\, \varphi_1 + \frac{\varphi_2}{V_2} ln\, \varphi_2 + \chi'_{12}\varphi_1\varphi_2 \quad (1.28)$$

Where φ_i and V_i are the volume fraction and the molar volume of polymer i, respectively, and $\chi'_{12} = \frac{\chi_{12}}{V_{ref}}$ with χ_{12} being the Flory-Huggins (or polymer-polymer) interaction parameter and V_{ref} an arbitrary reference volume (taken to be 0.1 nm^3 in [76]). The solubility parameter formalism (see next section) may be used to predict the χ_{12} parameters:

$$\chi_{12} = \frac{V_{ref}}{RT}(\delta_1 - \delta_2)^2 \quad (1.29)$$

Where δ_1 and δ_2 are the solubility parameters of polymer 1 and polymer 2, respectively. In equation 1.28 the first two terms are related to the entropy of mixing while the third term is related to the enthalpy of mixing. In case of polymers, the molar volumes are quite large and the entropic terms becomes negligibly small, and, therefore, the third term dictates the miscible or immiscible behavior of blends. This thermodynamic miscibility or immiscibility in a typical binary system is represented by the schematic phase diagram as shown in Figure 1. 12. The x-axis represents the volume fraction of components and y-axis represents the temperature or $1/\chi N$ where χ is the Flory interaction parameter and N is the degree of polymerization. Depending on the degree of miscibility, three regions exist, namely single phase, metastable and two phases (phase 1 and phase 2), that are separated by the boundaries of spinodal and binodal decomposition. The binodal and spinodal lines are defined as $(\partial \Delta G_m/\partial \emptyset_1)_{P,T}^{phase\ 1} = (\partial \Delta G_m/\partial \emptyset_2)_{P,\ T}^{phase\ 2}$ and $(\partial^2 \Delta G_m/\partial \emptyset_i^2)_{P,T} = 0$, respectively. Apart from these three regions, there exist two critical solution temperatures i.e. the lower critical solution temperature (LCST) and the upper critical solution temperature (UCST). However, in case of polymers blends, due to their high molar masses, only one critical temperature, either LCST (most often) or UCST appears in the phase diagram. Some blends which show UCST are PS-SBS, BR-SBR, and SAN-NBR.

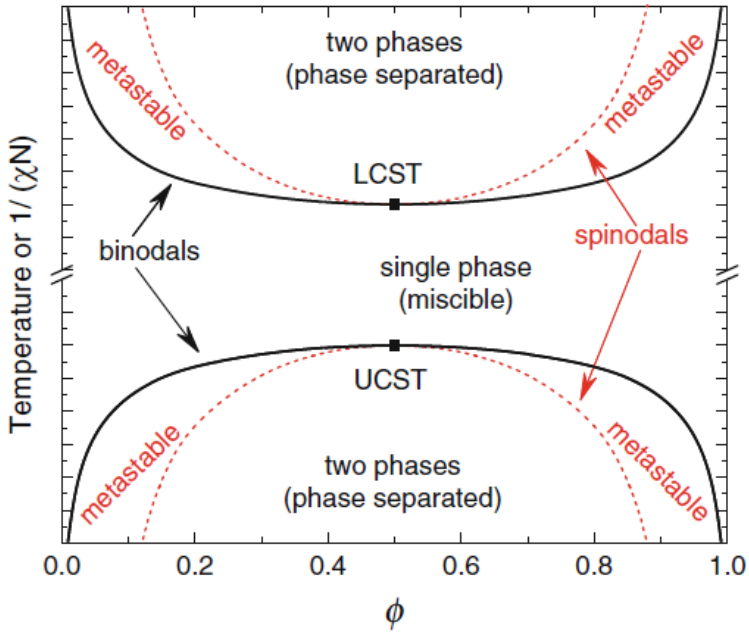

FIGURE 1. 12 THE SCHEMATIC OF A BINARY SYSTEM PHASE DIAGRAM. [74]

In a phase diagram, the metastable regions correspond to the one component rich phase in which another component of blend is dispersed. The point at which binodal and spinodal lines cross each other corresponds to the critical interaction parameter χ_c. The value of this parameter (χ_c) at which phase transformation occurs is defined as:

$$\chi_c = \frac{1}{2}\left(\frac{1}{N_1^{1/2}} + \frac{1}{N_2^{1/2}}\right)^2 \tag{1.30}$$

Where N_i is the number of monomers of volume V_{ref} in a chain of type i. The mechanism of phase separation is significantly different when the single phase transforms into metastable or two phases regions. In the former case, the phase separation follows the nucleation and growth process, whereas in the second case, when single phase is forced to jump into the spinodal or two phases region, the phases separate spontaneously, a phenomenon known as spinodal decomposition.

Solubility Parameter Approach

The solubility parameter concept was developed from regular solution theory of Hildebrand [77] for low molecular weight non-polar liquids at ambient temperature. According to this theory, the solubility parameter δ is givent by:

$$\delta = \sqrt{E/V}, \tag{1.31}$$

where E is the molar energy of vaporization and V the molar volume of the liquid. Later, Hansen took all the intermolecular forces such as non-polar, polar, hydrogen into account and wrote the total solubility parameter δ_i of a substance i as:

$$\delta_i^2 = \delta_{id}^2 + \delta_{ip}^2 + \delta_{ih}^2 \quad (1.32)$$

Where subscripts d, p, and h represent respectively the dispersive, polar, and hydrogen interaction. The two compounds are said to be miscible if the solubility parameter difference between them is less than 1.8 $(cal/cm^3)^{1/2}$.

In the Hansen solubility parameter theory, [78] the miscibility of two compounds requires their solubility parameters to be inside a critical radius of a sphere as:

$$R_{12\,crit}^2 = \Theta(\delta_{1d} - \delta_{2d})^2 + \left(\delta_{1p} - \delta_{2p}\right)^2 + (\delta_{1h} - \delta_{2h})^2 \quad (1.33)$$

Where Θ is the semiempirical fudge parameter and its value lies between 4-5 (cf. Figure 1. 13). The squared sum of solubility parameter differences is weighted (Θ:1:1) due to the dominant role played by the dispersion forces.

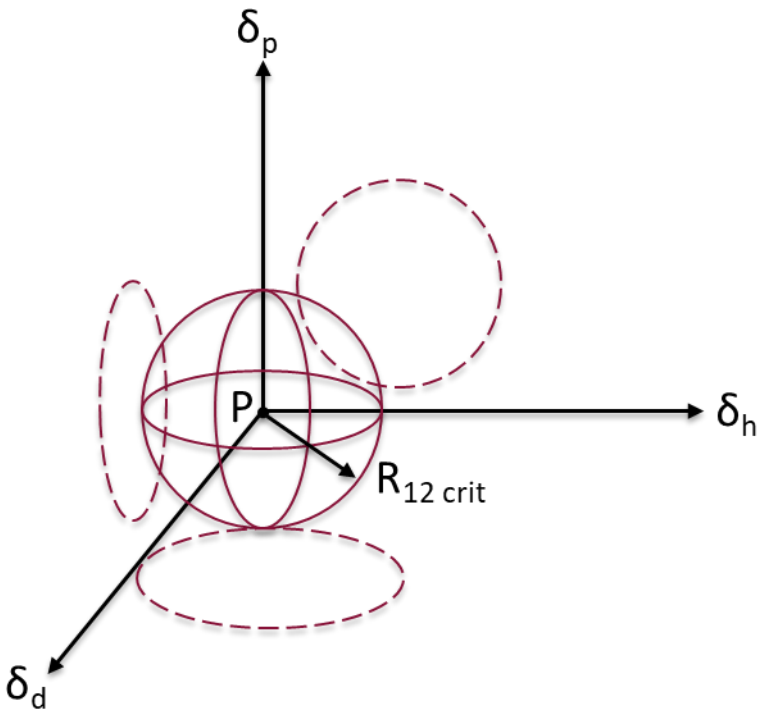

FIGURE 1. 13 DEPICTION OF THE CRITICAL RADIUS OF A TYPICAL COMPOUND SPHERE IN THREE HANSEN SOLUBILITY PARAMETERS COORDINATES.

The above-mentioned Hansen solubility parameter approach gives a qualitative analysis of miscibility whereas Flory-Huggins method can be used to give the quantitative estimate of phase

equilibria. The two methods can be related based on the van Laar type relationship between the Flory-Huggins interaction parameter and the solubility parameters as described by eq (1.29). [79] Therefore, it becomes possible to get a quantitative thermodynamic description of miscibility from the Flory-Huggins method using solubility parameter approach, and the relationship to determine the miscibility of two polymers given by Hansen:

$$\frac{\Delta G_m}{RT} = \frac{\varphi_1}{V_1} ln\, \varphi_1 + \frac{\varphi_2}{V_2} ln\, \varphi_2 + \frac{D^2}{RT} \varphi_1 \varphi_2 \quad (1.34)$$

where D is the distance between centers of two polymer solubility spheres.

Glass transition temperature approach

The miscibility of a polymer blends is commonly analyzed from the T_g measurement of the blend and of its components. The indication of single glass transition temperature in the blend is generally referred as miscible blend whereas multiple glass transition temperature in a blend are referred to a multiphase system.

Different theoretical equations have been proposed for the composition dependence of T_g of binary miscible blends. Among all, the most commonly used are Gordon and Taylor equation, [80] Fox law, [81] and Couchman equation. [82] However, these laws fail to predict the composition dependence of T_g in case of strong intermolecular interactions as they do not take them into account. Lu et. al. [83] proposed a relationship which not only takes into account the strong intermolecular forces but also relates the Flory-Huggins interaction parameters with the glass transition temperature of blends. The before-mentioned laws are therefore found to be the special case of this relationship. Another advantage of this theory is that when interaction parameter, χ, is known from other experimental methods, the glass transition temperature of blends can be predicted; and alternatively, if composition-T_g relationship is known, it can be used to estimate χ. The relationship between the T_g of binary polymer blend and χ is derived as:

$$T_{gB} = \frac{w_1 T_{g1} + k w_2 T_{g2}}{w_1 + k w_2} + \frac{A w_1 w_2}{(w_1 + k w_2)(w_1 + b w_2)(w_1 + c w_2)^2} \quad (1.35)$$

$$A = \frac{-\chi R (T_{g1} - T_{g2}) c}{M_1 \Delta c_{p1}} \quad (1.36)$$

$$k = \frac{\Delta c_{p2} - w_1 \delta c_p^l}{\Delta c_{p1} - w_2 \delta c_p^g} \quad (1.37)$$

Where, $c = \rho_1/\rho_2$ and $b = M_2/M_1$. ρ_1 and ρ_2 are the densities of two polymers. Here, polymer 1 is the lower T_g component. M_1 and M_2 are the molar mass per chain segment of both components and δc_p is the change in specific heat due to mixing in liquid (superscript l) and glassy state

(superscript g) respectively. Δc_{p1} and Δc_{p2} are the specific heat change, w_1 and w_2 are the weight fraction, of both polymers and R is the gas constant. Depending upon the strength of interactions the equation 1.35 is transformed into more simplified forms of miscibility prediction laws.

- for very weak or no specific interactions, δc_p and χ are very small and hence, can be neglected. The equation (1.35) reduces to the Couchman's equation:

$$T_{gB} = (w_1 T_{g1} + K_0 w_2 T_{g2})/(w_1 + K_0 w_2) \quad (1.38)$$

where $K_o = \Delta c_{p2}/\Delta c_{p1}$

- for the condition of $\Delta c_{pi} T_{gi} = const$, the equation (1.35) becomes the Fox equation:

$$\frac{1}{T_{gB}} = \frac{w_1}{T_{g1}} + \frac{w_2}{T_{g2}} \quad (1.39)$$

- for relatively weak specific interactions, the effect of k exceeds that of A, the equation (1.35) reduces to the Gordon- Taylor equation:

$$T_g = \left(w_1 T_{g1} + K' w_2 T_{g2}/w_1 + K' w_2\right) \quad (1.40)$$

where $K' = k + A/T_{g2} - 1$

- for very strong specific interactions in blends, the effect of A becomes more important and δc_pmay be neglected, the equations (1.35-1.37) then become:

$$T_{gB} = \frac{w_1 T_{g1} + k_0 w_2 T_{g2}}{w_1 + k_0 w_2} + \frac{A w_1 w_2}{(w_1 + k_0 w_2)(w_1 + b w_2)(w_1 + c w_2)^2} \quad (1.41)$$

$$A = \frac{-\chi R (T_{g1} - T_{g2}) c}{M_1 \Delta c_{p1}} \quad (1.42)$$

$$k_0 = \Delta c_{p2}/\Delta c_{p1} \quad (1.43)$$

1.3.2 Impact of blending on T_g/α-relaxation and viscoelasticity

Addition of miscible small molecules like plasticizers (whose glass transition is below that of the polymer) into a polymer can increase the free volume between chains. This eases the molecular motions of the chains and therefore decrease the glass transition. [84] [85] [86] [87] . One can also add small molecules with higher T_g than the polymer, which therefore will raise the T_g of the blend. [88] [89] Such molecules, called resin in this manuscript, will be used during this thesis.

Even though the single T_g is often used as an indication of the miscibility in a two components blend system, significant enlargement of T_g has also been reported in many studies [90] [91] [92] [93]. This phenomenon as depicted in Figure 1. 14 has been seen even in blends which have been proven to be thermodynamically miscible. However, this raises the question of scale at which two

components can be considered as miscible, [94] since the observed enlargement of the associated α-transition is related to local heterogeneities.

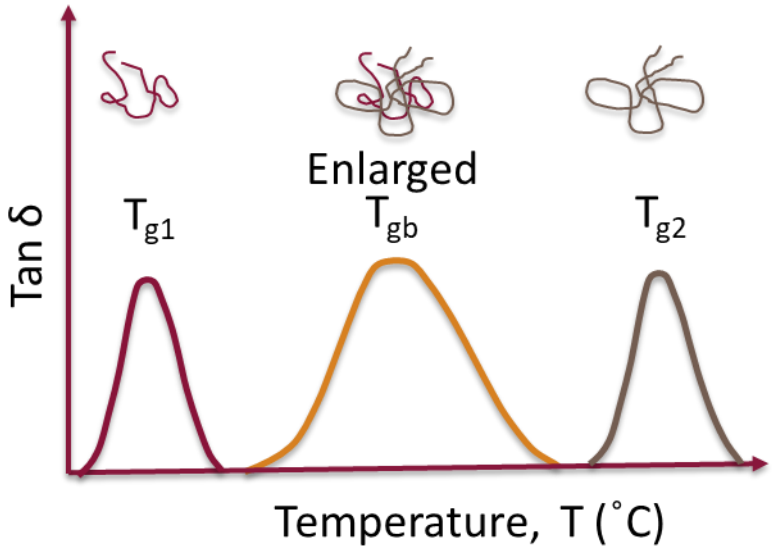

FIGURE 1. 14 ILLUSTRATION OF THE ENLARGEMENT OF THE α-RELAXATION IN A MISCIBLE BINARY POLYMER BLEND.

The reason for these local heterogeneities of concentration (also called concentrations fluctuations) is the local surrounding of each components 1 or 2. For polymers, because of the chains connectivity, it may be richer in the same type of monomer, leading to the concept of self-concentration. [95] as shown in Figure 1. 15.

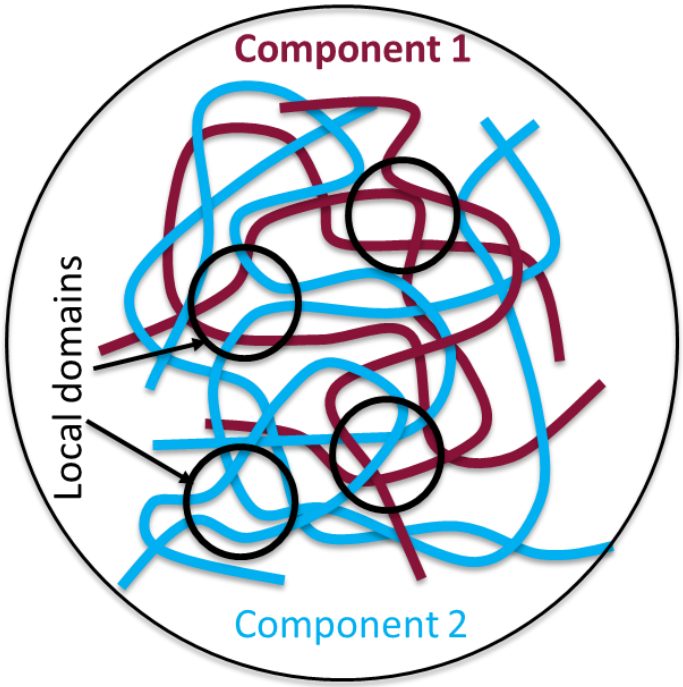

FIGURE 1. 15 DEPICTION OF LOCAL DOMAINS OF COMPONENT 1 AND 2 AS COMPARED TO THE BULK COMPOSITION IN A TYPICAL MISCIBLE BINARY POLYMER BLEND.

This concept needs the definition of the relevant length scale or volume of the local region, as the probability of a fluctuation of a given amplitude should decrease when the associated volume increases. In this one, the relaxation is affected by the monomer concentration. Lodge et al. [96] assumes that the relevant length scale is the Kuhn length, l_k, of the polymer chains, with a corresponding l_k^3. Moreover, the appearance of a monomer of a long chain at a particular site guarantees, because of these monomers connectivity, a certain number of other monomers of the same chains in the vicinity. Consequently, this monomer experiences *on average* an effective local concentration given by:

$$\emptyset_{eff} = \emptyset_s + (1 - \emptyset_s)\emptyset \tag{1.44}$$

Where $\emptyset_s$ is the "self-concentration" and is defined as the volume actually occupied by the repeat units equivalent to the Kuhn length divided by volume $V = l_k^3$:

$$\emptyset_s = \frac{C_\infty M_0}{k\rho N_{av} V} \tag{1.45}$$

Where M_0 represents the molar mass of repeat unit, k the number of backbone bonds per repeat unit, ρ the density, C_∞ the characteristic ratio, and N_{av} the Avogadro number. The component which is more flexible or has lower α-transition temperature is said to have larger self-concentration because of smaller associated volume. [95 97] These concepts can be particularly useful

in works devoted to the understanding and the tuning of the viscoelastic behavior of miscible blends. [98] [99] [100]

In addition to shifting and enlarging the T_g of the blend, low molecular weight polymers or plasticizers also act as diluent i.e. decrease the modulus of the main polymer matrix since they increase the distance between their topological constraints. [101] Thus, they enable to tune the properties of polymers in the rubbery plateau region as well. [102] [103]

1.3.3 Reinforcement effect when one phase is rigid

Depending on the polymerization degree, the temperature, the Flory interaction parameters and the composition, when not fully miscible, blends can show different types of phase separation with various microstructure and composition of the separated phases. Since most of the polymers are not compatible with each other, polymer blends are generally heterogeneous in nature except a few. However, this heterogeneity can be exploited for property enhancement where the main polymer matrix is reinforced by the separated domains of the other rigid phase as shown in Figure 1. 16.

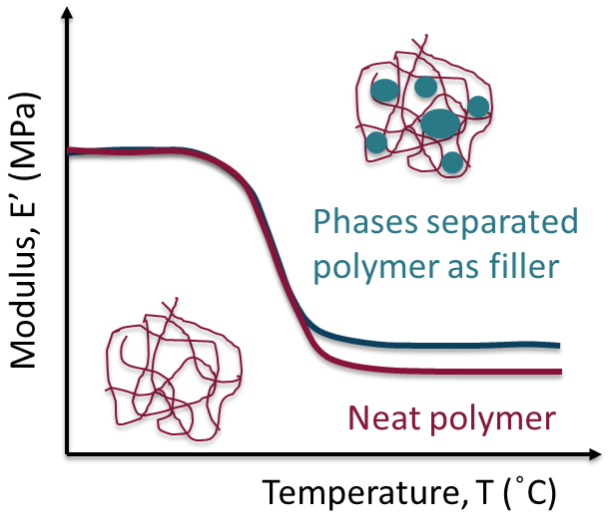

FIGURE 1. 16 DEPICTION OF PHASE SEPARATED DOMAINS OF A RIGID POLYMER REINFORCING THE MATRIX AND CORRESPONDING SCHEMATIC EVOLUTION OF THE STORAGE MODULUS WITH TEMPERATURE.

The phase separated domains can vary in size from nanometers to micrometers and their size distribution plays an important role in controlling the viscoelastic behavior. [104] The rigid polymers used as fillers in crosslinked soft rubber are generally thermoplastics whose T_g are relatively high which keeps them rigid at their intended working temperature. [105] [106] [107] This makes the reinforcement effect in such systems temperature dependent. [108] [109] Interestingly, on the other hand, phase separated polymer blends can also be used to decrease the stiffness of rigid polymers. In that

case elastomers which have very low T_g are added in the dispersed form to the rigid thermoplastic matrices in order to enhance the toughness properties of the compounds. [110]

1.3.4 Conclusion

The physical and viscoelastic properties of an elastomer can be easily modified over a wide temperature range by blending it with another polymer. The tuning of the properties primarily depends on the miscibility of the two blended polymers that drive the morphology. Therefore, understanding of this miscibility using appropriate methods as described in this section is very important in order to efficiently design new materials with desired properties.

1.4 References

(1) Gedde, U. W.; Hedenqvist, M. S. *Fundamental Polymer Science*; Graduate Texts in Physics; Springer International Publishing, 2019.
(2) Ward, I. M.; Sweeney, J. *An Introduction to the Mechanical Properties of Solid Polymers*; Wiley, 2005.
(3) Shaw, M. T.; MacKnight, W. J. *Introduction to Polymer Viscoelasticity*; Wiley, 2018.
(4) Starkweather, H. W. Aspects of Simple, Non-Cooperative Relaxations. *Polymer* **1991**, *32* (13), 2443–2448. https://doi.org/10.1016/0032-3861(91)90087-Y.
(5) Williams, J.; Eisenberg, A. Methyl Group Tunneling and Viscoelastic Relaxation in Poly (Methyl Methacrylate). *Macromolecules* **1978**, *11* (4), 700–707.
(6) Heijboer, J. Secondary Loss Peaks in Glassy Amorphous Polymers. *Int. J. Polym. Mater. Polym. Biomater.* **1977**, *6* (1–2), 11–37. https://doi.org/10.1080/00914037708075218.
(7) Halary, J. L.; Laupretre, F.; Monnerie, L. *Polymer Materials: Macroscopic Properties and Molecular Interpretations*; Wiley, 2011.
(8) Ngai, K. L. *Relaxation and Diffusion in Complex Systems*; Partially Ordered Systems; Springer New York, 2011.
(9) Williams, M. L.; Landel, R. F.; Ferry, J. D. The Temperature Dependence of Relaxation Mechanisms in Amorphous Polymers and Other Glass-Forming Liquids. *J. Am. Chem. Soc.* **1955**, *77* (14), 3701–3707. https://doi.org/10.1021/ja01619a008.
(10) Bhowmick, A. K.; Stephens, H. *Handbook of Elastomers*; Plastics Engineering; CRC Press, 2000.
(11) Cowie, J. M. G.; Arrighi, V. *Polymers: Chemistry and Physics of Modern Materials, Third Edition*; CRC Press, 2007.
(12) Mark, J. E.; Erman, B.; Roland, M. *The Science and Technology of Rubber*; Elsevier Science, 2013.
(13) Treloar, L. R. G. *The Physics of Rubber Elasticity*; Oxford Classic Texts in the Physical Sciences; OUP Oxford, 1975.
(14) Gent, A. N. Crystallization in Natural Rubber. II. The Influence of Impurities. *Rubber Chem. Technol.* **1955**, *28* (2), 457–469. https://doi.org/10.5254/1.3557517.
(15) Toki, S.; Fujimaki, T.; Okuyama, M. Strain-Induced Crystallization of Natural Rubber as Detected Real-Time by Wide-Angle X-Ray Diffraction Technique. *Polymer* **2000**, *41* (14), 5423–5429. https://doi.org/10.1016/S0032-3861(99)00724-7.

(16) Franta, I. *Elastomers and Rubber Compounding Materials*; Studies in Polymer Science; Elsevier Science, 2012.
(17) Nielsen, L. E. Cross-Linking–Effect on Physical Properties of Polymers. *J. Macromol. Sci. Part C* **1969**, *3* (1), 69–103. https://doi.org/10.1080/15583726908545897.
(18) Warasitthinon, N.; Robertson, C. G. INTERPRETATION OF THE TANδ PEAK HEIGHT FOR PARTICLE-FILLED RUBBER AND POLYMER NANOCOMPOSITES WITH RELEVANCE TO TIRE TREAD PERFORMANCE BALANCE. *Rubber Chem. Technol.* **2018**, *91* (3), 577–594. https://doi.org/10.5254/rct.18.82608.
(19) Diez, J.; Bellas, R.; López, J.; Santoro, G.; Marco, C.; Ellis, G. Study of the Crosslink Density, Dynamo-Mechanical Behaviour and Microstructure of Hot and Cold SBR Vulcanizates. *J. Polym. Res.* **2009**, *17* (1), 99. https://doi.org/10.1007/s10965-009-9295-6.
(20) Mansilla, M. A.; Rodríguez Garraza, A. L.; Silva, L.; Salgueiro, W.; Macchi, C.; Marzocca, A. J.; Somoza, A. Evolution of the Free Volume and Glass Transition Temperature with the Degree of Cure of Polybutadiene Rubbers. *Polym. Test.* **2013**, *32* (4), 686–690. https://doi.org/10.1016/j.polymertesting.2013.03.001.
(21) Bandzierz, K.; Reuvekamp, L.; Dryzek, J.; Dierkes, W.; Blume, A.; Bielinski, D. Influence of Network Structure on Glass Transition Temperature of Elastomers. *Materials* **2016**, *9* (7). https://doi.org/10.3390/ma9070607.
(22) Kuhn, W.; Grün, F. Statistical Behavior of the Single Chain Molecule and Its Relation to the Statistical Behavior of Assemblies Consisting of Many Chain Molecules. *J. Polym. Sci.* **1946**, *1* (3), 183–199. https://doi.org/10.1002/pol.1946.120010306.
(23) Wall, F. T.; Flory, P. J. Statistical Thermodynamics of Rubber Elasticity. *J. Chem. Phys.* **1951**, *19* (12), 1435–1439. https://doi.org/10.1063/1.1748098.
(24) Flory, P. J.; Gordon, M.; Flory, P. J.; McCrum, N. . G. Statistical Thermodynamics of Random Networks. *Proc. R. Soc. Lond. Math. Phys. Sci.* **1976**, *351* (1666), 351–380. https://doi.org/10.1098/rspa.1976.0146.
(25) James, H. M.; Guth, E. Simple Presentation of Network Theory of Rubber, with a Discussion of Other Theories. *J. Polym. Sci.* **1949**, *4* (2), 153–182. https://doi.org/10.1002/pol.1949.120040206.
(26) Staverman, A. J. Properties of Phantom Networks and Real Networks. In *Polymer Networks*; Dušek, K., Ed.; Springer Berlin Heidelberg: Berlin, Heidelberg, 1982; pp 73–101.
(27) Heinrich, G.; Straube, E.; Helmis, G. Rubber Elasticity of Polymer Networks: Theories. In *Polymer Physics*; Springer Berlin Heidelberg: Berlin, Heidelberg, 1988; pp 33–87.
(28) Rubinstein, M.; Panyukov, S. Elasticity of Polymer Networks. *Macromolecules* **2002**, *35* (17), 6670–6686. https://doi.org/10.1021/ma0203849.
(29) Horkay, F.; McKenna, G. B. Polymer Networks and Gels. In *Physical Properties of Polymers Handbook*; Mark, J. E., Ed.; Springer New York: New York, NY, 2007; pp 497–523. https://doi.org/10.1007/978-0-387-69002-5_29.
(30) Rubinstein, M.; Colby, R. H. *Polymer Physics*; Oxford University Press, 2003.
(31) Edwards, S. F.; Vilgis, T. A. The Tube Model Theory of Rubber Elasticity. *Rep. Prog. Phys.* **1988**, *51* (2), 243–297. https://doi.org/10.1088/0034-4885/51/2/003.
(32) Ball, R. C.; Doi, M.; Edwards, S. F.; Warner, M. Elasticity of Entangled Networks. *Polymer* **1981**, *22* (8), 1010–1018. https://doi.org/10.1016/0032-3861(81)90284-6.
(33) De Gennes, P.-G.; Gennes, P.-G. *Scaling Concepts in Polymer Physics*; Cornell university press, 1979.
(34) Rubinstein, M.; Panyukov, S. Elasticity of Polymer Networks. *Macromolecules* **2002**, *35* (17), 6670–6686. https://doi.org/10.1021/ma0203849.

(35) Johnsen, B. B.; Kinloch, A. J.; Mohammed, R. D.; Taylor, A. C.; Sprenger, S. Toughening Mechanisms of Nanoparticle-Modified Epoxy Polymers. *Polymer* **2007**, *48* (2), 530–541. https://doi.org/10.1016/j.polymer.2006.11.038.
(36) Zhang, P.; Morris, M.; Doshi, D. MATERIALS DEVELOPMENT FOR LOWERING ROLLING RESISTANCE OF TIRES. *Rubber Chem. Technol.* **2016**, *89* (1), 79–116. https://doi.org/10.5254/rct.16.83805.
(37) Wang, M.-J. Effect of Polymer-Filler and Filler-Filler Interactions on Dynamic Properties of Filled Vulcanizates. *Rubber Chem. Technol.* **1998**, *71* (3), 520–589. https://doi.org/10.5254/1.3538492.
(38) Kraus, G. Reinforcement of Elastomers by Carbon Black. In *Fortschritte der Hochpolymeren-Forschung*; Springer Berlin Heidelberg: Berlin, Heidelberg, 1971; pp 155–237.
(39) Chazeau, L.; Gauthier, C.; Chenal, J. M. Mechanical Properties of Rubber Nanocomposites: How, Why… and Then. *Rubber Nanocomposites* **2010**, 291–330.
(40) Ramier, J.; Gauthier, C.; Chazeau, L.; Stelandre, L.; Guy, L. Payne Effect in Silica-Filled Styrene–Butadiene Rubber: Influence of Surface Treatment. *J. Polym. Sci. Part B Polym. Phys.* **2007**, *45* (3), 286–298. https://doi.org/10.1002/polb.21033.
(41) El-Nashar, D. E.; Mansour, S. H.; Girgis, E. Nickel and Iron Nano-Particles in Natural Rubber Composites. *J. Mater. Sci.* **2006**, *41* (16), 5359–5364. https://doi.org/10.1007/s10853-006-0179-4.
(42) Medalia, A. I. Effect of Carbon Black on Dynamic Properties of Rubber Vulcanizates. *Rubber Chem. Technol.* **1978**, *51* (3), 437–523. https://doi.org/10.5254/1.3535748.
(43) Wang, M.-J. The Role of Filler Networking in Dynamic Properties of Filled Rubber. *Rubber Chem. Technol.* **1999**, *72* (2), 430–448. https://doi.org/10.5254/1.3538812.
(44) Bokobza, L.; Rahmani, M.; Belin, C.; Bruneel, J.-L.; El Bounia, N.-E. Blends of Carbon Blacks and Multiwall Carbon Nanotubes as Reinforcing Fillers for Hydrocarbon Rubbers. *J. Polym. Sci. Part B Polym. Phys.* **2008**, *46* (18), 1939–1951.
(45) Ramorino, G.; Bignotti, F.; Pandini, S.; Riccò, T. Mechanical Reinforcement in Natural Rubber/Organoclay Nanocomposites. *Compos. Sci. Technol.* **2009**, *69* (7), 1206–1211. https://doi.org/10.1016/j.compscitech.2009.02.023.
(46) Choi, S.-S.; Park, B.-H.; Song, H. Influence of Filler Type and Content on Properties of Styrene-Butadiene Rubber (SBR) Compound Reinforced with Carbon Black or Silica. *Polym. Adv. Technol.* **2004**, *15* (3), 122–127. https://doi.org/10.1002/pat.421.
(47) Stöckelhuber, K. W.; Svistkov, A. S.; Pelevin, A. G.; Heinrich, G. Impact of Filler Surface Modification on Large Scale Mechanics of Styrene Butadiene/Silica Rubber Composites. *Macromolecules* **2011**, *44* (11), 4366–4381. https://doi.org/10.1021/ma1026077.
(48) Tian, Q.; Zhang, C.; Tang, Y.; Liu, Y.; Niu, L.; Ding, T.; Li, X.; Zhang, Z. Preparation of Hexamethyl Disilazane-Surface Functionalized Nano-Silica by Controlling Surface Chemistry and Its "Agglomeration-Collapse" Behavior in Solution Polymerized Styrene Butadiene Rubber/Butadiene Rubber Composites. *Compos. Sci. Technol.* **2021**, *201*, 108482. https://doi.org/10.1016/j.compscitech.2020.108482.
(49) Lei, Y.; Tang, Z.; Zhu, L.; Guo, B.; Jia, D. Thiol-Containing Ionic Liquid for the Modification of Styrene–Butadiene Rubber/Silica Composites. *J. Appl. Polym. Sci.* **2012**, *123* (2), 1252–1260. https://doi.org/10.1002/app.34026.
(50) Zhang, X.; Xue, X.; Jia, H.; Wang, J.; Ji, Q.; Xu, Z. Influence of Ionic Liquid on the Polymer–Filler Coupling and Mechanical Properties of Nano-silica Filled Elastomer. *J. Appl. Polym. Sci.* **2017**, *134* (7).

(51) Zou, Y.; He, J.; Tang, Z.; Zhu, L.; Liu, F. Structural and Mechanical Properties of Styrene–Butadiene Rubber/Silica Composites with an Interface Modified in-Situ Using a Novel Hindered Phenol Antioxidant and Its Samarium Complex. *Compos. Sci. Technol.* **2020**, *188*, 107984. https://doi.org/10.1016/j.compscitech.2019.107984.
(52) Raman, V. S.; Das, A.; Stöckelhuber, K. W.; Eshwaran, S. B.; Chanda, J.; Malanin, M.; Reuter, U.; Leuteritz, A.; Boldt, R.; Wießner, S. Improvement of Mechanical Performance of Solution Styrene Butadiene Rubber by Controlling the Concentration and the Size of in Situ Derived Sol–Gel Silica Particles. *RSC Adv.* **2016**, *6* (40), 33643–33655.
(53) Guth, E. Theory of Filler Reinforcement. *Rubber Chem. Technol.* **1945**, *18* (3), 596–604. https://doi.org/10.5254/1.3546754.
(54) Christensen, R.; Mccoy, J. Mechanics of Composite Mateials. *J. Appl. Mech.* **1980**, *47*, 460. https://doi.org/10.1115/1.3153710.
(55) Christensen, R. M.; Lo, K. H. Solutions for Effective Shear Properties in Three Phase Sphere and Cylinder Models. *J. Mech. Phys. Solids* **1979**, *27* (4), 315–330. https://doi.org/10.1016/0022-5096(79)90032-2.
(56) Christensen, R. M. A Critical Evaluation for a Class of Micro-Mechanics Models. *J. Mech. Phys. Solids* **1990**, *38* (3), 379–404. https://doi.org/10.1016/0022-5096(90)90005-O.
(57) Gusev, A. A. Controlled Accuracy Finite Element Estimates for the Effective Stiffness of Composites with Spherical Inclusions. *Int. J. Solids Struct.* **2016**, *80*, 227–236. https://doi.org/10.1016/j.ijsolstr.2015.11.006.
(58) Raos, G. Application of the Christensen-Lo Model to the Reinforcement of Elastomers by Fractal Fillers. *Macromol. Theory Simul.* **2003**, *12* (1), 17–23. https://doi.org/10.1002/mats.200390002.
(59) Payne, A. R. The Dynamic Properties of Carbon Black-Loaded Natural Rubber Vulcanizates. Part I. *Rubber Chem. Technol.* **1963**, *36* (2), 432–443.
(60) Payne, A. R. The Dynamic Properties of Carbon Black Loaded Natural Rubber Vulcanizates. Part II. *Rubber Chem. Technol.* **1963**, *36* (2), 444–450.
(61) Chazeau, L.; Brown, J. D.; Yanyo, L. C.; Sternstein, S. S. Modulus Recovery Kinetics and Other Insights into the Payne Effect for Filled Elastomers. *Polym. Compos.* **2000**, *21* (2), 202–222.
(62) Sternstein, S. S.; Zhu, A.-J. Reinforcement Mechanism of Nanofilled Polymer Melts As Elucidated by Nonlinear Viscoelastic Behavior. *Macromolecules* **2002**, *35* (19), 7262–7273. https://doi.org/10.1021/ma020482u.
(63) Mullins, L.; Tobin, N. R. Stress Softening in Rubber Vulcanizates. Part I. Use of a Strain Amplification Factor to Describe the Elastic Behavior of Filler-reinforced Vulcanized Rubber. *J. Appl. Polym. Sci.* **1965**, *9* (9), 2993–3009.
(64) Harwood, J. A. C.; Mullins, L.; Payne, A. R. Stress Softening in Natural Rubber Vulcanizates. Part II. Stress Softening Effects in Pure Gum and Filler Loaded Rubbers. *J. Appl. Polym. Sci.* **1965**, *9* (9), 3011–3021.
(65) Scotti, R.; Conzatti, L.; D'Arienzo, M.; Credico, B. D.; Giannini, L.; Hanel, T.; Stagnaro, P.; Susanna, A.; Tadiello, L.; Morazzoni, F. Shape Controlled Spherical (0D) and Rod-like (1D) Silica Nanoparticles in Silica/Styrene Butadiene Rubber Nanocomposites: Role of the Particle Morphology on the Filler Reinforcing Effect. *Polymer* **2014**, *55* (6), 1497–1506. https://doi.org/10.1016/j.polymer.2014.01.025.
(66) Stöckelhuber, K. W.; Svistkov, A. S.; Pelevin, A. G.; Heinrich, G. Impact of Filler Surface Modification on Large Scale Mechanics of Styrene Butadiene/Silica Rubber Composites. *Macromolecules* **2011**, *44* (11), 4366–4381. https://doi.org/10.1021/ma1026077.

(67) Kaufman, S.; Slichter, W. P.; Davis, D. D. Nuclear Magnetic Resonance Study of Rubber–Carbon Black Interactions. *J. Polym. Sci. Part -2 Polym. Phys.* **1971**, *9* (5), 829–839. https://doi.org/10.1002/pol.1971.160090505.
(68) O'brien, J.; Cashell, E.; Wardell, G. E.; McBrierty, V. J. An NMR Investigation of the Interaction between Carbon Black and Cis-Polybutadiene. *Macromolecules* **1976**, *9* (4), 653–660.
(69) Tadiello, L.; D'Arienzo, M.; Di Credico, B.; Hanel, T.; Matejka, L.; Mauri, M.; Morazzoni, F.; Simonutti, R.; Spirkova, M.; Scotti, R. The Filler–Rubber Interface in Styrene Butadiene Nanocomposites with Anisotropic Silica Particles: Morphology and Dynamic Properties. *Soft Matter* **2015**, *11* (20), 4022–4033. https://doi.org/10.1039/C5SM00536A.
(70) Waldrop, M. A.; Kraus, G. Nuclear Magnetic Resonance Study of the Interaction of SBR with Carbon Black. *Rubber Chem. Technol.* **1969**, *42* (4), 1155–1166. https://doi.org/10.5254/1.3539286.
(71) Zhu, Z.; Thompson, T.; Wang, S.-Q.; von Meerwall, E. D.; Halasa, A. Investigating Linear and Nonlinear Viscoelastic Behavior Using Model Silica-Particle-Filled Polybutadiene. *Macromolecules* **2005**, *38* (21), 8816–8824. https://doi.org/10.1021/ma050922s.
(72) Jancar, J.; Douglas, J. F.; Starr, F. W.; Kumar, S. K.; Cassagnau, P.; Lesser, A. J.; Sternstein, S. S.; Buehler, M. J. Current Issues in Research on Structure–Property Relationships in Polymer Nanocomposites. *Polymer* **2010**, *51* (15), 3321–3343. https://doi.org/10.1016/j.polymer.2010.04.074.
(73) Utracki, L. A.; Wilkie, C. A. *Polymer Blends Handbook*; Kluwer academic publishers Dordrecht, 2002; Vol. 1.
(74) Manias, E.; Utracki, L. A. Thermodynamics of Polymer Blends. In *Polymer Blends Handbook*; Utracki, L. A., Wilkie, C. A., Eds.; Springer Netherlands: Dordrecht, 2014; pp 171–289. https://doi.org/10.1007/978-94-007-6064-6_4.
(75) Eitouni, H. B.; Balsara, N. P. Thermodynamics of Polymer Blends. In *Physical Properties of Polymers Handbook*; Mark, J. E., Ed.; Springer New York: New York, NY, 2007; pp 339–356. https://doi.org/10.1007/978-0-387-69002-5_19.
(76) Flory, P. J.; chemistry, P. *Principles of Polymer Chemistry*; Baker lectures 1948; Cornell University Press, 1953.
(77) Hildebrand, J. H. A History of Solution Theory. *Annu. Rev. Phys. Chem.* **1981**, *32* (1), 1–24.
(78) Hansen, S. A. C. M. *Hansen Solubility Parameters in Practice*; Hansen-Solubility.
(79) Lindvig, T.; Michelsen, M. L.; Kontogeorgis, G. M. A Flory–Huggins Model Based on the Hansen Solubility Parameters. *Fluid Phase Equilibria* **2002**, *203* (1), 247–260. https://doi.org/10.1016/S0378-3812(02)00184-X.
(80) Gordon, M.; Taylor, J. S. Ideal Copolymers and the Second-Order Transitions of Synthetic Rubbers. i. Non-Crystalline Copolymers. *J. Appl. Chem.* **1952**, *2* (9), 493–500. https://doi.org/10.1002/jctb.5010020901.
(81) Berry, G. C.; Fox, T. G. The Viscosity of Polymers and Their Concentrated Solutions. In *Fortschritte der Hochpolymeren-Forschung*; Springer Berlin Heidelberg: Berlin, Heidelberg, 1968; pp 261–357.
(82) Couchman, P. R. Compositional Variation of Glass-Transition Temperatures. 2. Application of the Thermodynamic Theory to Compatible Polymer Blends. *Macromolecules* **1978**, *11* (6), 1156–1161. https://doi.org/10.1021/ma60066a018.
(83) Lu, X.; Weiss, R. A. Relationship between the Glass Transition Temperature and the Interaction Parameter of Miscible Binary Polymer Blends. *Macromolecules* **1992**, *25* (12), 3242–3246. https://doi.org/10.1021/ma00038a033.

(84) Boyer, R. F.; Spencer, R. S. Effect of Plasticizers on Second-order Transition Points of High Polymers. *J. Polym. Sci.* **1947**, *2* (2), 157–177.
(85) Nielsen, L. E.; Pollard, R. E.; McIntyre, E. Transition Temperatures of Plasticized Material and Copolymer Systems. *J. Polym. Sci.* **1951**, *6* (5), 661–664.
(86) Hata, N.; Tobolsky, A. V.; Bondi, A. Effect of Plasticizers on the Viscoelastic Properties of Poly (Vinyl Chloride). *J. Appl. Polym. Sci.* **1968**, *12* (12), 2597–2613.
(87) Kopesky, E. T.; Haddad, T. S.; McKinley, G. H.; Cohen, R. E. Miscibility and Viscoelastic Properties of Acrylic Polyhedral Oligomeric Silsesquioxane–Poly (Methyl Methacrylate) Blends. *Polymer* **2005**, *46* (13), 4743–4752.
(88) Class, J. B.; Chu, S. G. The Viscoelastic Properties of Rubber–Resin Blends. III. The Effect of Resin Concentration. *J. Appl. Polym. Sci.* **1985**, *30* (2), 825–842.
(89) Aubrey, D. W. The Nature and Action of Tackifier Resins. *Rubber Chem. Technol.* **1988**, *61* (3), 448–469. https://doi.org/10.5254/1.3536196.
(90) Roland, C. M.; Ngai, K. L. Dynamical Heterogeneity in a Miscible Polymer Blend. *Macromolecules* **1991**, *24* (9), 2261–2265.
(91) Alegria A; Colmenero J; Ngai KL; Roland CM. Observation of the Component Dynamics in a Miscible Polymer Blend by Dielectric and Mechanical Spectroscopies. *Macromolecules* **1994**, *27* (16), 4486–4492. https://doi.org/10.1021/ma00094a009.
(92) Lodge, T. P.; Wood, E. R.; Haley, J. C. Two Calorimetric Glass Transitions Do Not Necessarily Indicate Immiscibility: The Case of PEO/PMMA. *J. Polym. Sci. Part B Polym. Phys.* **2006**, *44* (4), 756–763. https://doi.org/10.1002/polb.20735.
(93) Rathi, A.; Hernández, M.; Garcia, S. J.; Dierkes, W. K.; Noordermeer, J. W.; Bergmann, C.; Trimbach, J.; Blume, A. Identifying the Effect of Aromatic Oil on the Individual Component Dynamics of S-SBR/BR Blends by Broadband Dielectric Spectroscopy. *J. Polym. Sci. Part B Polym. Phys.* **2018**, *56* (11), 842–854.
(94) Kant, R.; Kumar, S. K.; Colby, R. H. What Length Scales Control the Dynamics of Miscible Polymer Blends? *Macromolecules* **2003**, *36* (26), 10087–10094. https://doi.org/10.1021/ma0347215.
(95) Shenogin, S.; Kant, R.; Colby, R. H.; Kumar, S. K. Dynamics of Miscible Polymer Blends: Predicting the Dielectric Response. *Macromolecules* **2007**, *40* (16), 5767–5775. https://doi.org/10.1021/ma070503q.
(96) Lodge, T. P.; McLeish, T. C. B. Self-Concentrations and Effective Glass Transition Temperatures in Polymer Blends. *Macromolecules* **2000**, *33* (14), 5278–5284. https://doi.org/10.1021/ma9921706.
(97) Kumar, S. K.; Shenogin, S.; Colby, R. H. Dynamics of Miscible Polymer Blends: Role of Concentration Fluctuations on Characteristic Segmental Relaxation Times. *Macromolecules* **2007**, *40* (16), 5759–5766. https://doi.org/10.1021/ma070502y.
(98) Roland, C. M.; Casalini, R. The Role of Density and Temperature in the Dynamics of Polymer Blends. *Macromolecules* **2005**, *38* (21), 8729–8733. https://doi.org/10.1021/ma051481f.
(99) Haley, J. C.; Lodge, T. P.; He, Y.; Ediger, M. D.; von Meerwall, E. D.; Mijovic, J. Composition and Temperature Dependence of Terminal and Segmental Dynamics in Polyisoprene/Poly(Vinylethylene) Blends. *Macromolecules* **2003**, *36* (16), 6142–6151. https://doi.org/10.1021/ma034414z.
(100) Gambino, T.; Shafqat, N.; Alegría, A.; Malicki, N.; Dronet, S.; Radulescu, A.; Nemkovski, K.; Arbe, A.; Colmenero, J. Concentration Fluctuations and Nanosegregation in a Simplified

Industrial Blend with Large Dynamic Asymmetry. *Macromolecules* **2020**, *53* (16), 7150–7160. https://doi.org/10.1021/acs.macromol.0c01376.

(101) Compatibility and Viscoelastic Properties of Brominated Isobutylene-Co-p-Methylstyrene Rubber/Tackifier Blends. *Journal of Applied Polymer Science*, 2008, *110*, 1485–1497.

(102) Oberth, A. E.; Bruenner, R. S. Tensile Properties and Equilibrium Swelling of Plasticized Amorphous Polyurethane Rubbers. *J. Polym. Sci. Part -2 Polym. Phys.* **1970**, *8* (4), 605–624. https://doi.org/10.1002/pol.1970.160080411.

(103) Roos, A.; Creton, C. Effect of the Presence of Diblock Copolymer on the Nonlinear Elastic and Viscoelastic Properties of Elastomeric Triblock Copolymers. *Macromolecules* **2005**, *38* (18), 7807–7818. https://doi.org/10.1021/ma050322t.

(104) Roland, C. M. Immiscible Rubber Blends. In *Advances in Elastomers I: Blends and Interpenetrating Networks*; Visakh, P. M., Thomas, S., Chandra, A. K., Mathew, Aji. P., Eds.; Springer Berlin Heidelberg: Berlin, Heidelberg, 2013; pp 167–181. https://doi.org/10.1007/978-3-642-20925-3_6.

(105) Kraus, G.; Rollmann, K. W.; Gruver, J. T. Dynamic Properties of a Model Reinforced Elastomer. Styrene-Butadiene Reinforced with Polystyrene. *Rubber Chem. Technol.* **1971**, *44* (3), 598–606. https://doi.org/10.5254/1.3544778.

(106) Diamant, J.; Soong, D.; Williams, M. C. The Mechanical Properties of Styrene-Butadiene-Styrene (SBS) Triblock Copolymer Blends with Polystyrene (PS) and Styrene-Butadiene Copolymer (SBR). *Polym. Eng. Sci.* **1982**, *22* (11), 673–683. https://doi.org/10.1002/pen.760221104.

(107) Morton, M. Mechanisms of Reinforcement of Elastomers by Polymeric Fillers. *J. Elastoplast.* **1971**, *3* (2), 112–125. https://doi.org/10.1177/009524437100300203.

(108) Chabert, E.; Bornert, M.; Bourgeat-Lami, E.; Cavaillé, J.-Y.; Dendievel, R.; Gauthier, C.; Putaux, J. L.; Zaoui, A. Filler–Filler Interactions and Viscoelastic Behavior of Polymer Nanocomposites. *Mater. Sci. Eng. A* **2004**, *381* (1), 320–330. https://doi.org/10.1016/j.msea.2004.04.064.

(109) Kraus, G.; Rollmann, K. W.; Gruver, J. T. Dynamic Properties of a Model Reinforced Elastomer. Styrene-Butadiene Reinforced with Polystyrene. *Macromolecules* **1970**, *3* (1), 92–96. https://doi.org/10.1021/ma60013a019.

(110) Ishida, H.; Lee, Y.-H. Dynamic Mechanical and Thermal Analysis of Reactive Poly (Butadiene-Co-Acrylonitrile) Rubber-Modified Polybenzoxazine Resin. *Polym. Polym. Compos.* **2001**, *9* (2), 121–134. https://doi.org/10.1177/096739110100900204.

2 Materials and methods

In this chapter, the characteristics of the raw materials and the preparation of the blends are first presented. Then different techniques and procedures involved in the characterization of the materials are detailed.

Contents

2.1 Materials

SBR polymer matrix

A random copolymer of styrene and butadiene (SBR) provided by Michelin is used a matrix. The butadiene co-monomer contains 1,4 (cis and trans) and 1,2 (vinyl) configurations as illustrated in Figure 2. 1. The microstructural composition, average molecular weights ($\overline{M_n}$ and $\overline{M_w}$), density, and polydispersity value ($\overline{M_w}/\overline{M_n}$) are given in Table 2. 1.

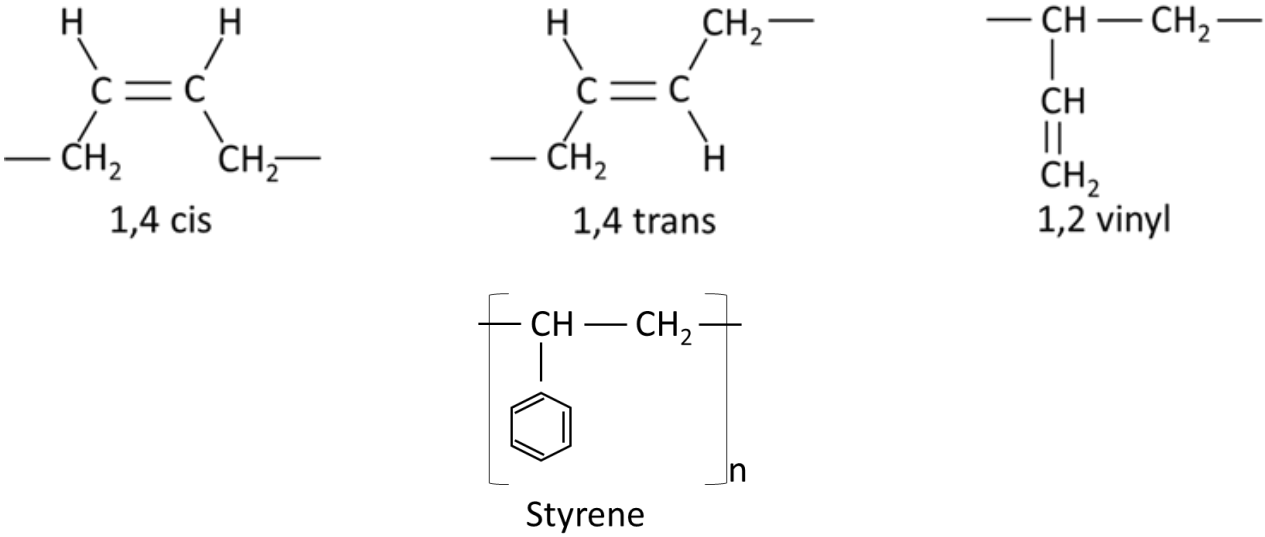

FIGURE 2. 1 BUTADIENE CONFIGURATIONS (1,4 CIS, 1,4 TRANS AND 1,2 VINYL) AND STYRENE CO-MONOMER

TABLE 2. 1 CHARACTERISTICS OF SBR COPOLYMER

	Styrene	**Butadiene microstructure (molar distribution)**			**Density**	**M_n**	**M_w**	**IP**
	(wt%)	**% cis**	**% trans**	**% vinyl**	**(g/cm^3)**	**(g/mol)**	**(g/mol)**	
SBR	15.5	30	46	24	0.92	158000	306000	1.9

Resins

Three commercial grades of resins (R1 = IMPERA R1508 from Eastman, R2 = Oppera PR 373 from Exxon Mobil Chemical, and R3 = ESCOREZ 5615 from Exxon Mobil Chemical) as shown

in Figure 2. 2 with varying composition of aromatic, aliphatic and ethylene contents are also provided by Michelin. All three resin have their T_g above room temperature. The three different resins have different molecular weights and Table 2. 2 lists their main characteristics.

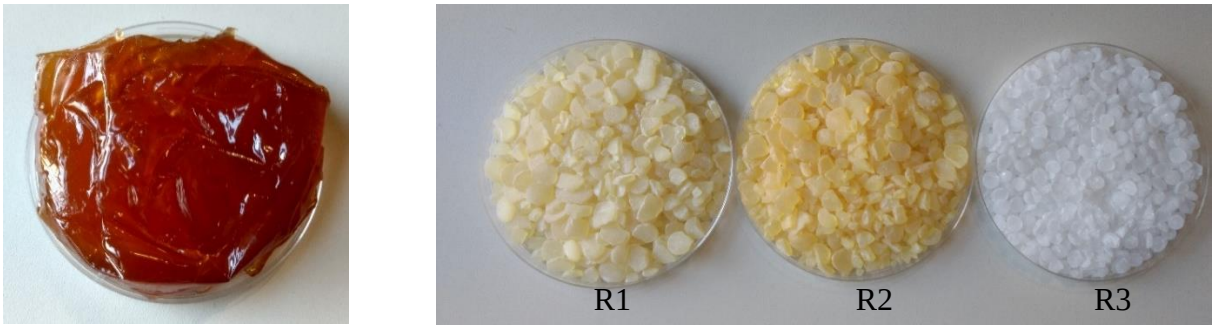

A) B)

FIGURE 2. 2 A) RAW SBR AND B) RESINS R1, R2 AND R3

TABLE 2. 2 CHARACTERISTICS OF RESINS

Resins	% Aromatic	% Ethylene	% Aliphatic	M_n (g/mol)	M_w (g/mol)	IP
R1	1	4	95	1000	2000	2
R2	11	3	86	800	1500	1.8
R3	11	0	89	500	800	1.6

2.2 Sample preparation

Blends were prepared at Michelin. Each resin is added in two proportions (25 and 45 wt % of blends) in the SBR matrix along with the other compounding ingredients. Three different types of compound formulations are prepared depending on the types of curing systems used. The first one is based on the sulfur curing system for which details are given in Table 2. 3. Second type of compound formulations are based on the peroxide curing system as shown in Table 2. 4. Table 2. 5 shows the third type of compound formulations which are prepared without any curing system (uncured). A total of seven formulations for each type of curing system are prepared.

TABLE 2. 3 COMPOUND FORMULATIONS FOR SULFUR CURED MATERIALS

Sample name	**Ingredients (phr)**								
	SBR	**R1**	**R2**	**R3**	**6PPD[1]**	**Stearic acid**	**ZnO**	**S**	**CBS[2]**
SBR_SC	100	-	-	-	1.5	3	1.45	1.4	1.6
SBR_R1_25_SC	100	33	-	-	1.5	3	1.45	1.4	1.6
SBR_R1_45_SC	100	83	-	-	1.5	3	1.45	1.4	1.6
SBR_R2_25_SC	100	-	33	-	1.5	3	1.45	1.4	1.6
SBR_R2_45_SC	100	-	83	-	1.5	3	1.45	1.4	1.6
SBR_R3_25_SC	100	-	-	33	1.5	3	1.45	1.4	1.6
SBR_R3_45_SC	100	-	-	83	1.5	3	1.45	1.4	1.6

*The phr amounts, 33 and 83, of resins are taken such that the resin constitutes the 25 and 45 wt % of the blends respectively.

[1] N-(1,3-dimethylbutyl)-N'-phenyl-1,4-benzenediamine

[2] N-cyclohexyl1-2-benzothiazolesulfenamide

TABLE 2. 4 COMPOUND FORMULATIONS FOR PEROXIDE CURED MATERIALS

Sample name	**Ingredients (phr)**						
	SBR	**R1**	**R2**	**R3**	**6PPD**	**Stearic acid**	**DCP[3]**
SBR_PC	100	-	-	-	1.5	3	0.74
SBR_R1_25_PC	100	33	-	-	1.5	3	0.74
SBR_R1_45_PC	100	83	-	-	1.5	3	0.74
SBR_R2_25_PC	100	-	33	-	1.5	3	0.74
SBR_R2_45_PC	100	-	83	-	1.5	3	0.74
SBR_R3_25_PC	100	-	-	33	1.5	3	0.74
SBR_R3_45_PC	100	-	-	83	1.5	3	0.74

[3] Dicumylperoxide

TABLE 2. 5 COMPOUND FORMULATIONS FOR UNCURED SYSTEM

Sample name	**Ingredients (phr)**					
	SBR	**R1**	**R2**	**R3**	**6PPD**	**Stearic acid**
SBR_UC	100	-	-	-	1.5	3
SBR_R1_25_UC	100	33	-	-	1.5	3
SBR_R1_45_UC	100	83	-	-	1.5	3
SBR_R2_25_UC	100	-	33	-	1.5	3
SBR_R2_45_UC	100	-	83	-	1.5	3
SBR_R3_25_UC	100	-	-	33	1.5	3
SBR_R3_45_UC	100	-	-	83	1.5	3

For each formulation mixing is done in two steps: 1) a mixing in an internal mixer followed by 2) an external mixing in a two roll mill (see Figure 2. 3).

Internal (melt) mixing

In a first step, all the ingredients, except curing agents, are mixed in a stepwise manner in an Haake PolyLab internal mixer that has a mixing chamber volume of 85cm^3. Cam type rotors are used to mix the compounds. To obtain a similar thermo-mechanical history of all samples, the mixing chamber of the internal mixer is preheated at 80˚C. The SBR is introduced first with the rotor speed set at 30 rpm and after 1 min resin is introduced. The resin-SBR mixing takes place for 2.5 min and after that, other ingredients such as stearic acid, *N*-(1,3-dimethylbutyl)-*N*'-phenyl-1,4-benzenediamine (6PPD), and zinc oxide (ZnO) are introduced and mixed for another 3 min. The rotor speed is increased from 30 rpm up to 100 rpm after 30s. In case of peroxide cured and uncured compounds, ZnO is not added in the formulations. The final temperature of all the mix is 100-110°C. This is followed by the incorporation of curing agents in an external mixer (two roll mill) in a second step.

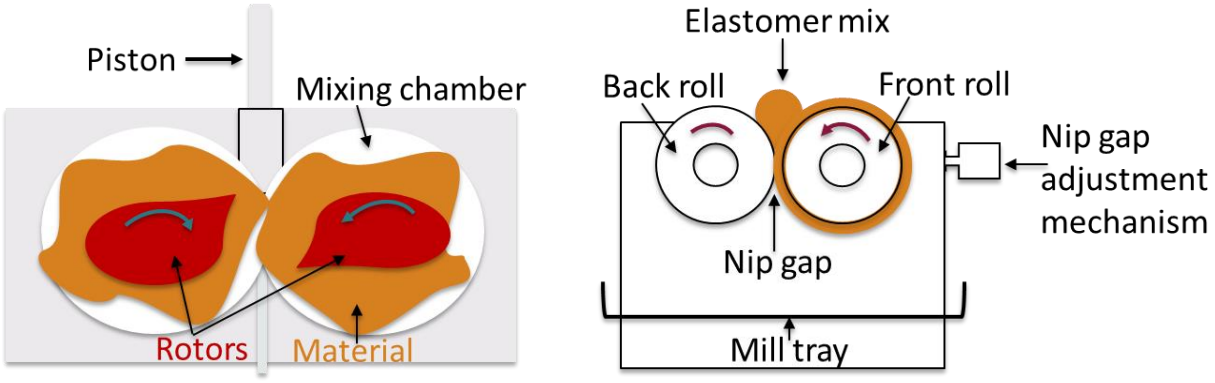

A) B)

FIGURE 2. 3 SCHEMATIC REPRESENTATION OF A) MIXING INSIDE THE INTERNAL MIXER, B) MIXING IN A TWO-ROLL MILL.

External mixing

In a two-roll mill, Sulfur and N-cyclohexyl1-2-benzothiazolesulfenamide (CBS) as curing agents are added to the melt mixed compound prepared for sulfur curing. Similarly, dicumylperoxide (DCP) is added for the peroxide curing formulations. After adding the curing agents in the compound, each compound is passed 12 times between nip gap of 1mm to homogenize them. In case of uncured compound formulations, the step of external mixing is suppressed.

Curing

The mixed compounds are cured/molded at 150˚C for 40 min in a CARVER INC. USA compression molding machine under 3000 psi in the form of 1 mm thick sheets. The curing time of 40 min at 150˚C for sulfur and peroxide cured compounds gives optimum curing for both type of curing systems. It was chosen based on the curing curves of similar previously mixed compounds at Michelin. The compounds without any crosslinking recipe (uncured compounds) are also molded at the same temperature and time to have the same thermal history as the sulfur and peroxide cured compounds.

2.3 Characterisation techniques

2.3.1 Swelling

The elastomer network is characterized by swelling 1 mm thick samples of 1 cm^2 in cyclohexane until the equilibrium swelling is achieved (see Figure 2. 4).

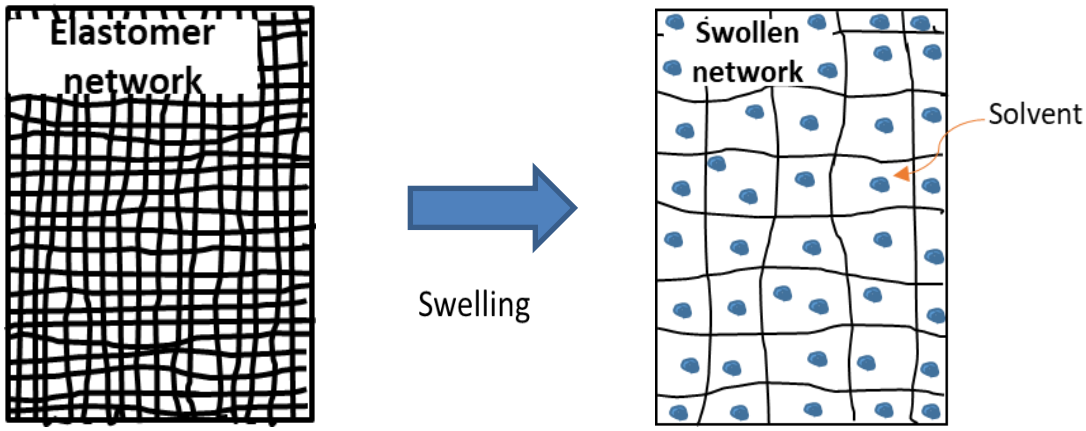

FIGURE 2. 4 EQUILIBRIUM SWELLING PHENOMENON IN A CROSS-LINKED ELASTOMER NETWORK

The weight of swollen samples is measured at regular intervals. After 15 days, the equilibrium swelling is reached and the samples are dried for 24 hours at room temperature under hood conditions followed by 12 hours of drying at 60˚C inside a vacuum oven. Then the weight of dried samples w_d is measured. The soluble fraction F_s, which mainly gives the weight fraction of soluble additives and uncross-linked chains, is estimated as

$$F_s = \frac{w_i - w_d}{w_i} \tag{2.1}$$

Where w_i is the initial weight of the sample.

Then the swelling volume ratio is calculated as:

$$Q_{swell} = 1 + \left(\frac{\rho_{polymer}}{\rho_{solvent}}\right)\left(\frac{w_s - w_d}{w_d}\right) \tag{2.2}$$

Where $\rho_{polymer}$ (= 0.92) is the density of SBR, and $\rho_{solvent}$ (= 0.779) is the density of cyclohexane. The cross-link density of the SBR network is calculated using Flory-Rehner equation under the affine assumption as:

$$\ln(1 - \emptyset_r) + \emptyset_r + \chi\emptyset_r^2 = -\frac{\rho_p}{M_c} V_s \left(\emptyset_r^{1/3} - \frac{\emptyset_r}{2}\right) \tag{2.3}$$

Where $\emptyset_r$ is the volume fraction of the polymer network at swelling equilibrium, i.e. $1/Q_{swell}$, χ is the polymer-solvent interaction parameter, ρ_p is the polymer density, M_c is the molecular weight between cross-links, and V_s is the molar volume of solvent. [1] The network functionality is assumed to be 4. The polymer-solvent interaction parameter is taken as 0.48 from literature [2] : our 12.5 % styrene containing SBR copolymer is close from the 15.5% styrene containing SBR copolymer used in this study. The small difference of 3% styrene between the two SBRs can be neglected as

the χ value changes only to its third decimal place of 0.489 for 12.5 % styrene to 0.482 for 28.5 % styrene in literature.

2.3.2 DSC

Differential scanning calorimetry (DSC) measures the heat flow into or out of the sample as a function of temperature. DSC measurements are performed with a Perkin Elmer DSC instrument (Pyris 8500). While the upper temperature limit of the instrument is 550˚C, the lowest operational temperature that can be achieved is -180˚C using a liquid nitrogen cooling system. A small sample of 10-16 mg is placed into the aluminum pan for the measurement. To keep the sample environment inert, a nitrogen gas flow rate of 20 mL/min is maintained throughout the experiment. Typically, three cycles, heating – cooling – heating, for each sample in the temperature range of -90˚C to 150˚C are performed at the heating/cooling rate of 10˚C/min. Each cycle starts with an isothermal step of 5 min in order to have comparable thermal history. The T_g is measured at the half ΔC_p by extending the tangents from the heat flow curve around the glass transition domain using Pyris software as shown in Figure 2. 5. The onset and end values are taken as T_{g1} and T_{g2} respectively. The uncertainty in the T_g measurement is $\pm 1°C$. The specific heat C_p is calculated as the heat flow divided by mass of sample and heating rate. The difference between the onset and end point gives the ΔC_p.

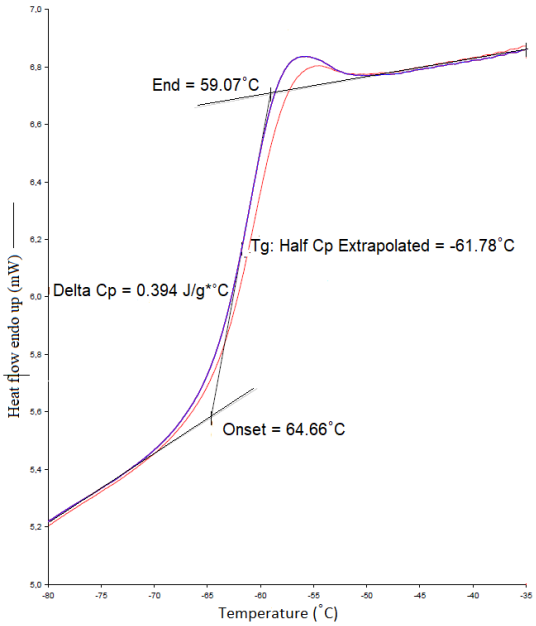

FIGURE 2. 5 DEPICTION OF THE T_g CALCULATION USING PYRIS SOFTWARE FROM THE DSC HEAT FLOW CURVE (2ND HEATING) OF A RAW SBR SAMPLE.

2.3.3 Solubility parameter analysis

The solubility characteristics of a compound in a solvent in terms of thermodynamic parameters can be analyzed from the regular solution theory of Hildebrand [3] at ambient temperature, where the solubility parameter, $\delta = \sqrt{E/V}$, is defined as the square root of cohesive energy density. This solubility parameter is based only on the dispersive forces between solvent and compound and does not consider the polar and hydrogen forces contributions towards the solubility. For that, a thermodynamic approach based on the three components of solubility parameters viz. dispersive, polar, and hydrogen given by Hansen [4] is used and is given as:

$$\delta_{TOT}^2 = \delta_D^2 + \delta_P^2 + \delta_H^2 \quad (2.4)$$

The three components of solubility parameters of SBR and resins are measured by putting approx. 70 mg of each sample in 10 mL of each 27 different solvents. At least two solvents are good solvents for each material. The solvents dissolving the samples are marked as 1 and the solvents that do not dissolve or just swell the samples are marked as 0 (see Table 2. 6). The values 0 and 1 are estimated after a period of 15 days.

TABLE 2. 6 DISSOLUTION VALUES (0 OR 1) OF SBR AND RESIN IN DIFFERENT SOLVENTS

Solvent	**SBR**	**R1**	**R2**	**R3**
Acetone	0	0	0	0
Ethanol	0	0	0	0
Toluene	1	1	1	1
Tetrahydrofuran	1	1	1	1
Pyridine	1	0	1	1
Dimethyl formamide	0	0	0	0
Ethyl acetate	0	0	1	0
Morpholine	0	0	0	0
m-Cresol	0	0	0	0
Isoamyl alcohol	0	0	0	0
1-Butanol	0	0	0	0
Benzyl amine	1	0	1	1
Butyl lactate	0	0	0	0
Chloroform	1	1	1	1
y-Butyrolactone	0	0	0	0
1,4-Dioxane	1	0	1	1
Acetonitrile	0	0	0	0
Hexane	1	1	1	1
2-Propanol	0	0	0	0
Dichloromethane	1	1	1	1
Ethylene glycol monoethyl ether acetate	0	0	0	0
Diethyl ether	1	1	1	1
Methanol	0	0	0	0
Methyl ethyl ketone	0	0	0	0
Cyclohexane	1	1	1	1
Mesitylene	1	1	1	1
Xylenes	1	1	1	1

The three components of solubility parameter of SBR and resins are then calculated by HSPiP software. [5] Afterwards, the miscibility characteristics of SBR and resins are analyzed based on these parameters.

2.3.4 Mechanical characterization

2.3.4.1 Dynamic Mechanical Analysis

Dynamic mechanical analysis (DMA) is a key technique to characterize the viscoelastic behavior of materials as a function of time, temperature, frequency, and strain amplitude under dynamic loading conditions. An oscillatory (sinusoidal) stress $\sigma(t)$ or strain $\varepsilon(t)$ is applied to a sample and the complementary response (strain or stress) is measured. Depending on the viscoelastic behavior of the sample the phase shift between deformation and stress, δ, varies between 0˚ and 90˚. For purely elastic materials phase shift is 0˚ and for purely viscous materials phase shift is 90˚ as shown in Figure 2. 6. For polymeric materials phase shift lies between these two extremes ($0^\circ < \delta < 90^\circ$). In dynamic experiments the stress is expressed as a complex, σ^* which contains a real part, the elastic stress, $\sigma' = \sigma_0 \cos\delta$ which is in phase with the strain and the viscous stress, and an imaginary part, $\sigma'' = \sigma_0 \sin\delta$ which is in phase with strain rate:

$$\sigma^* = \sigma' + i\sigma'' \tag{2.5}$$

Similarly, complex strain (ε^*) in real and imaginary parts is defined as:

$$\varepsilon^* = \varepsilon' + i\varepsilon'' \tag{2.6}$$

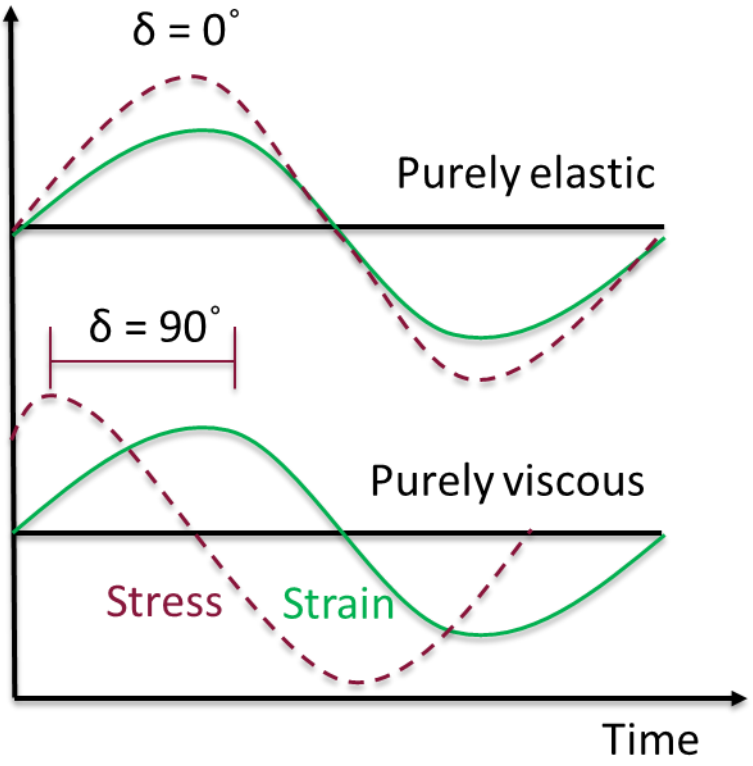

FIGURE 2. 6 APPLIED OSCILLATORY STRAIN (IN GREEN) WITH STRESS RESPONSE (IN RED) FOR PERFECTLY ELASTIC AND VISCOUS SYSTEM

The complex modulus is defined as:

$$E^* = \frac{\sigma^*}{\varepsilon^*} \tag{2.7}$$

The materials ability to store energy, which is the measure of elasticity of the material is defined by the storage modulus:

$$E' = \left(\frac{\sigma_0}{\varepsilon_0}\right) cos\ \delta \tag{2.8}$$

The materials ability to dissipate energy is defined by the loss modulus:

$$E'' = \left(\frac{\sigma_0}{\varepsilon_0}\right) sin\ \delta \tag{2.9}$$

The loss modulus/storage modulus ratio is the loss factor (tan δ) :

$$tan\ \delta = \frac{E''}{E'} \tag{2.10}$$

DMA is effectively used to locate the main relaxation temperature (α-transition) and other relaxations corresponding to different molecular motions in the sample. [6]

The instrument consists of a temperature controller system using a thermocouple close to the sample monitors the temperature inside the furnace. The low temperature is maintained by a gas cooling device using liquid nitrogen. A drive motor is used to apply the force to the sample and a displacement sensor measures the linear displacement. Sample clamp is used to hold the samples. Figure 2. 7 shows the schematic of the working principle and primary components of the DMA Q800 from TA instrument used in this study in the tension mode.

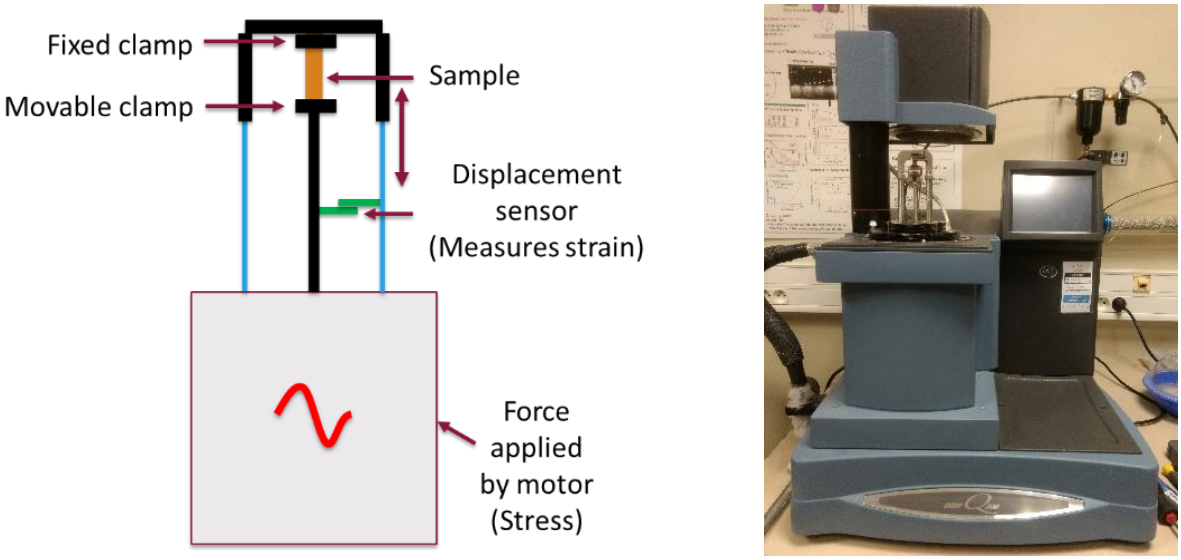

A) B)

FIGURE 2. 7 A) WORKING PRINCIPLE OF DMA UNDER CONTROLLED STRESS; B) DMA Q800 INSTRUMENT

DMA experiments in the linear domain

The samples of rectangular shape of 5 mm width and 12 mm length are cut using a die/punch. Calibrations are performed for instrument force, position, clamp mass, gauge length, and clamp compliance before starting the experiment. A torque of approximately 3 Nm is applied using a torque wrench to tighten the samples in the tension clamps. The isothermal time before the starting of experiment is 10 min in order to have same thermal history for all the samples. The dynamic analysis is typically done with a controlled strain amplitude of $\varepsilon_0 = 0.05$, over a temperature range from -120˚C to 120˚C. For sulfur cured sample, the strain amplitude of $\varepsilon_0 = 0.1$ is used above ambient temperature. This strain amplitude is still low, in order to avoid any influence of the deformation on the modulus, as shown in Figure S2. 1 of supporting information section of this chapter. The temperature ramp is performed with a heating rate of 1˚C/min. The frequency is maintained at 1 Hz.

- *Note that the letter S in figure caption is used to refer the supporting information data*

In our DMA experiments, we trust more the modulus at high temperature i.e at or above glass transition than at low temperature i.e. measured below the glass transition of materials. The reproducibility of elastic modulus at or above T_g has been checked, but different modulus was found below T_g for the same sample as shown in Figure S2. 2 in the supporting information section of this chapter. This may be due to contraction of the sample during cooling, dimensional variation of the clamp, additional friction at the clamp etc…. Because of the large uncertainty in the measurement at low temperature, the moduli at these temperatures will be considered with caution and a grey box is added on the curve to avoid irrelevant discussion on the found moduli variations.

DMA experiments in the non-linear domain

Non-linear DMA experiments are performed in two modes: tensile and shear sandwich mode. For the tensile test, rectangular samples are used and three loading-unloading cycles are measured. The sample is maintained 30 minutes at 0N force between two consecutive loading-unloading cycles. The measurement is done at the strain rate of 0.6/min (0.01 s^{-1}) at ambient temperature.

In shear sandwich mode, strain sweep measurements are performed using two circular specimens of 8 mm diameter which are glued in shear sandwich clamps (cf. Figure 2. 8). At least 30 min time is ensured after mounting the specimens to be sure of the correct gluing (with a cyanoacrylate glue). The shear strain amplitude, γ, is varied from 0.1 % to 50 % under isothermal conditions. The measurements are performed at two isothermal temperatures of 30˚C and 90˚C. The frequency of 1 Hz is maintained throughout. Three strain sweeps are performed for each sample with the 30 min isothermal time between two consecutive sweeps. Second sweep for all the blends is taken for the comparative analysis of the Payne effect.

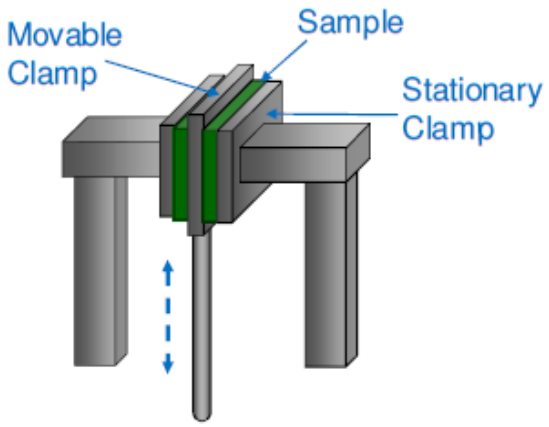

FIGURE 2. 8 DEPICTION OF SAMPLES FIXED IN A SHEAR SANDWICH CLAMP.

2.3.4.2 Rheometer

Rheological analysis is used to characterize the flow behavior and viscoelasticity of the materials. A shear strain is applied to the sample in the plane/plane geometry and torque generated is measured using the transducers. The rheological experiments are performed using parallel plate geometry of 8 mm diameter on an Ares rheometer from TA Instruments (Figure 2. 9). Dynamic shear modulus is measured from frequency sweep experiments performed at 0.5% strain in the frequency range of 100 rad/s to 0.05 rad/s from 130˚C to 30˚C, with an interval of 10˚C. In temperature sweep experiments, dynamic shear modulus is measured at the strain of 0.5% and frequency of 1Hz, from room temperature up to 130˚C, with an heating rate of 1˚C/min.

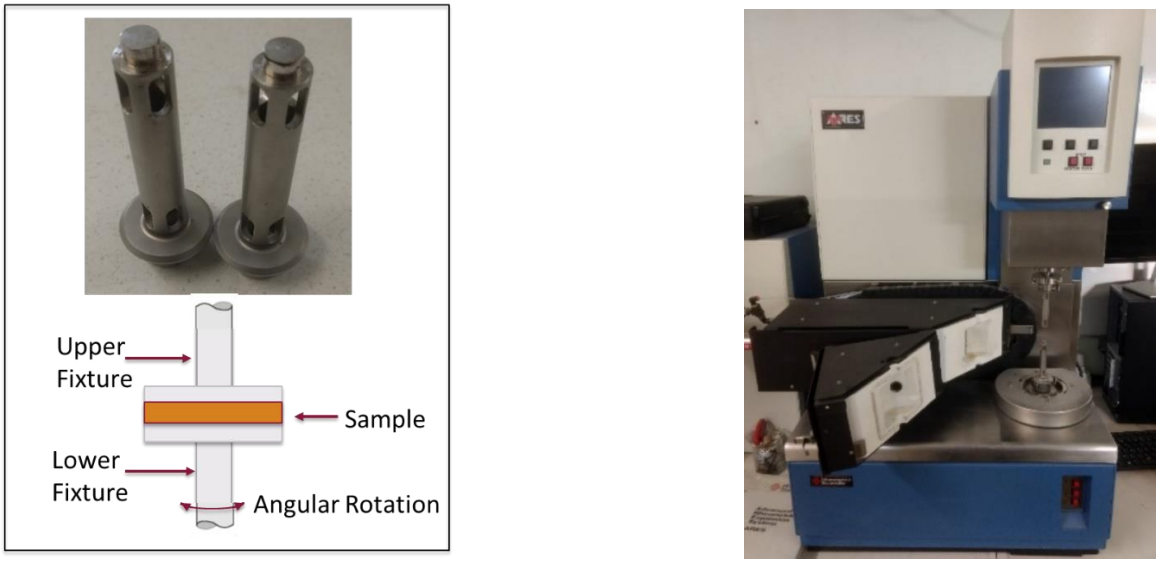

A) B)

FIGURE 2. 9 A) PARALLEL PLATE GEOMETRY AND SCHEMATIC DIAGRAM OF SAMPLE BETWEEN THE PARALLEL PLATES; B) ARES RHEOMETER INSTRUMENT

2.3.5 Morphological characterization

2.3.5.1 Atomic Force Microscope (AFM)

AFM is an observation technique involving forces of interaction between a sharp tip and the surface of a sample (Figure 2. 10). A tip mounted on the cantilever spring scans the sample surface and the cantilever deflects due to the force between tip and sample. This deflection is measured through the use of a laser reflecting on the cantilever surface and a photodetector. Using so-called "on-resonance" observation modes, such as tapping mode, contrast of topological origin (height image) along with the contrast of energy dissipation (phase image, highlighting the local differences of

elastic/inelastic interaction forces) is obtained.[7] AFM is performed with a Dimension 3100 AFM device connected to a Nanoscope V scanning probe controller (VEECO Instruments, Plainview, NY). All images are obtained at ambient temperature in tapping mode using a pointprobe-plus® silicon (PPP-NCH-50) from Nanosensors with a high resonance frequency (ca. 300 kHz). A lateral resolution of 3-5 nm can be achieved by this configuration with a vertical resolution of 0.5 nm. Very flat surfaces of the samples, necessary for AFM measurements, are obtained by cryo-ultramicrotomy (experimental details are given in the next section).

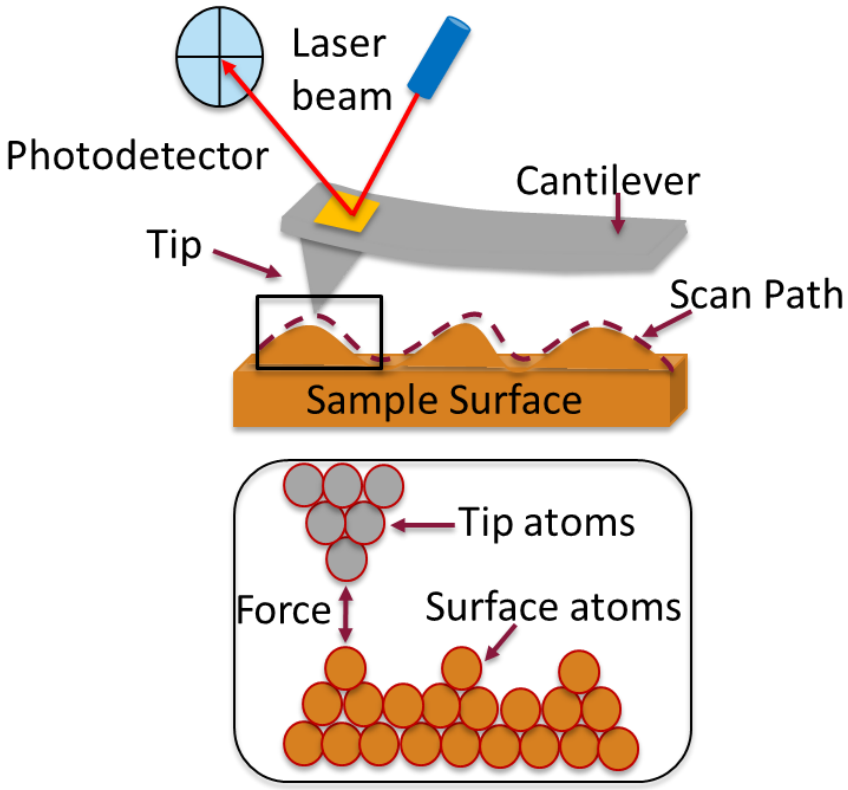

FIGURE 2. 10 SCHEMATIC ILLUSTRATION OF THE WORKING PRINCIPLE OF AFM

2.3.5.2 Electron Microscope: Transmission & Scanning (TEM & SEM)

Electron microscopes allow the analysis of morphological details ranging from micrometer length scales to tens of nanometer scale. These tools are readily used to understand the phase separation in polymer blends.

TEM observations are done on a Philips CM120 instrument available at the CTμ (Microstructure Technology Centre). The samples are prepared by cryo-ultramicrotomy at -80°C on a Leica UC7 microtome using two diamond knives, the first being a pre-cut knife to cut a pyramid in the sample and the second one for cutting the samples to be analyzed. Thin slices of approximately 100 nm

thickness are cut at a cutting speed of 0.1 mm/s and placed on copper grids. TEM observations are done under an accelerating voltage of 120 kV at room temperature.

Scanning electron microscopy (SEM) analyses are made using a Zeiss SUPRA55VP microscope with an acceleration voltage of 0.8 kV in secondary electron mode. Samples are first cryo-fractured in liquid nitrogen, and their surface is observed in the SEM.

2.3.6 Small Angle X-ray Scattering (SAXS)

Scattering

Scattering is a phenomenon in which a radiation beam is redirected from its initial trajectory due to the inhomogeneities present in the medium through which it propagates. The experiments involving scattering thus only require a beam source, a sample to be examined, and a detector. A typical scattering set up is schematically illustrated in Figure 2. 11 where an incident beam of monochromatic radiation with wavelength λ and intensity $I(0)$ hits the sample and the scattered radiation $I(q)$ is measured by a detector (D) placed at a scattering angle 2θ from the initial radiation direction. Depending on the wavelength of radiation and distance between sample and detector, the scattered spectra is measured as intensity versus the wave vector q.

The directions of incident and scattered waves are given by the unit vectors $\overrightarrow{S_\iota}$ and $\overrightarrow{S_s}$ respectively, and the corresponding momentum transfer or wave vector q is expressed as;

$$\vec{q} = \overrightarrow{k_s} - \overrightarrow{k_\iota} \tag{2.11}$$

Where $\overrightarrow{k_\iota}\left(= \frac{2\pi}{\lambda}\overrightarrow{S_\iota}\right)$ and $\overrightarrow{k_s}\left(= \frac{2\pi}{\lambda}\overrightarrow{S_s}\right)$ are the incident and scattered wave vectors respectively and $\overrightarrow{|k_s|} = \overrightarrow{|k_\iota|} = \frac{2\pi}{\lambda}$.

The magnitude of q is then given by:

$$|q| = q = \left(\frac{4\pi}{\lambda}\right) sin\,\theta \tag{2.12}$$

The scattering angle $2\theta < 0.3^\circ$ is generally referred as small angle scattering. For the structural analysis of polymers by scattering, the selection of radiation source depends on the difference between electron density of polymer components. The higher the electron density difference between the material components, the better is the contrast as X-rays interact with the electrons. SAXS enables to estimate characteristic distances of the material microstructure and is therefore a useful tool to investigate structures at the scale of 1 nm up to ca. hundreds of nm depending on the

setup (laboratory or synchrotron). This technique is therefore adapted to investigate the nano-structuration arising out in our polymer blends. [8]

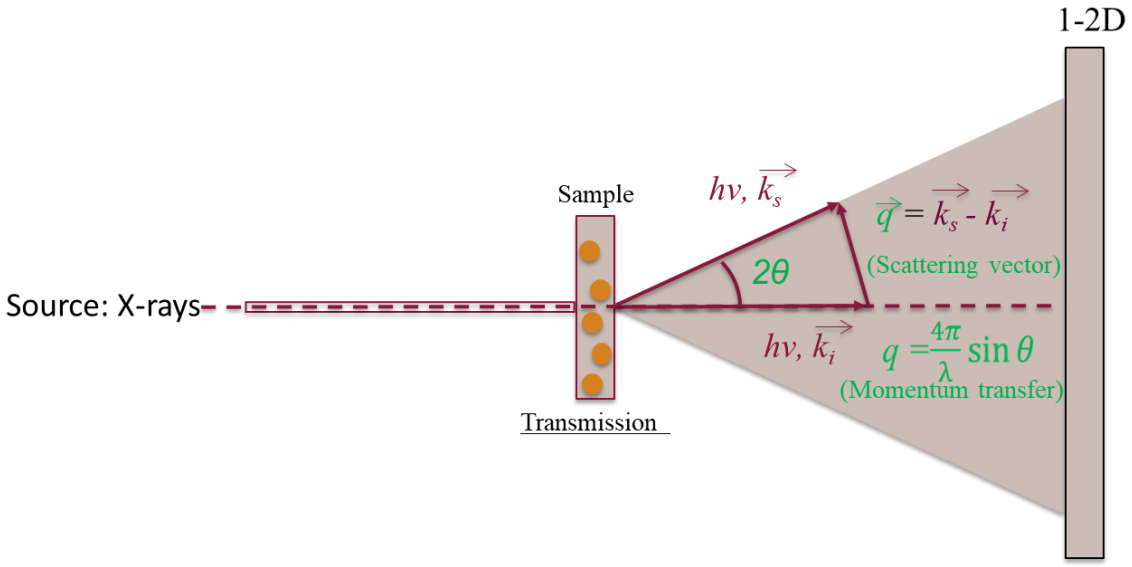

FIGURE 2. 11 SCHEMATIC REPRESENTATION OF THE WORKING PRINCIPLE OF SAXS

SAXS experimental conditions

In this study SAXS experiments are performed on samples which do not contain ZnO (i.e. peroxide cured samples) as the scattering of this metallic oxide is too intense and would hide the scattering related to phase separation in the resin/polymer blend. The tests are performed at two synchrotron facilities: ESRF and SOLEIL. At ESRF, the experiments are performed at ambient temperature at three different sample to detector distances of 0.8m, 8m and 30m corresponding to a 0.002 nm^{-1} to 10 nm^{-1} q-range. In-situ heat treatment experiments are performed at Soleil (SWING beamline), where samples are cooled down below T_g of polymer (-60˚C) and heated up to 110˚C. At Soleil, the experiments are performed at a sample to detector distance of 6m with a beam exposure time of 1 sec.

2.3.7 Modelling of composite modulus

The three-phase composite model, for which analytical solution was given by Christensen and Lo, [9] [10] [11] predicts the modulus of composite materials up to large volume fractions of spherical particles perfectly distributed in a matrix. Its accuracy up to relatively large volume fraction (up to 40%) has been confirmed by simulations. [12] In Figure 2. 12, representing the assumptions, the particles randomly distributed are replaced by a single spherical inclusion whose modulus (G) and Poisson ratio (υ) are the one of the particles. This inclusion is surrounded by a shell with a thickness of b-a whose mechanical properties (G_m and υ_m) are identical to that of the matrix phase. The outer

region of this sphere + shell is an homogeneous material whose properties are those of the composite. The ratio a^3/b^3 is equal to the volume fraction of inclusions.

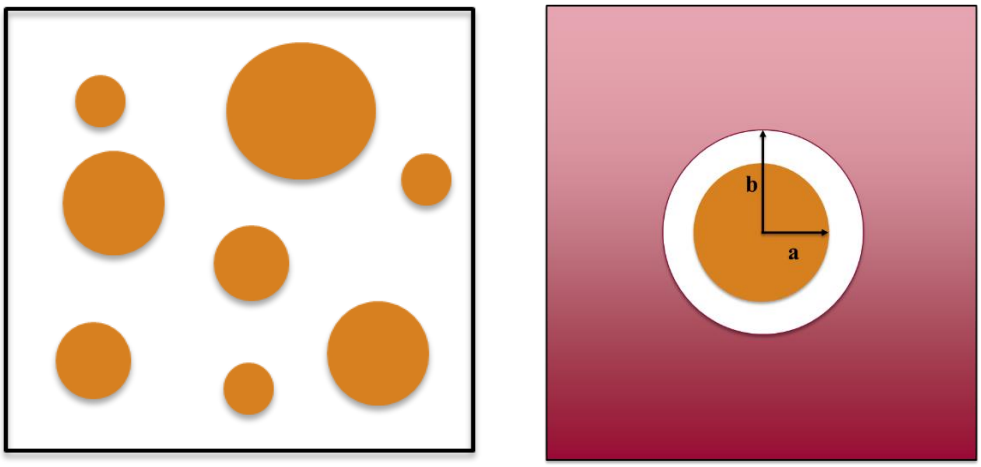

FIGURE 2. 12 ILLUSTRATION OF CHRISTENSEN-LO THREE PHASE COMPOSITE MODEL. YELLOW SPHERES: PARTICLES/INCLUSIONS, WHITE: MATRIX, WINE: EQUIVALENT HOMOGENEOUS MEDIUM

The individual phases are assumed isotropic and homogeneous. The condition of uniform shear strain at the infinite distance from the origin of sphere is assumed. [10] [13] The resulting modulus expression is programmed in MATLAB, which gives the composite modulus at different inclusion volume fractions.

The solution for the shear modulus of the composite is given by:

$$A\left(\frac{G}{G_m}\right)^2 + B\left(\frac{G}{G_m}\right) + C = 0 \tag{2.13}$$

Where, G = shear modulus of the composite, G_m = shear modulus of the matrix, and

$$A = 8(r-1)(4-5v_m)e - 2[63(r-1)\eta_2 + 2a]c^{7/3} + 252(r-1)f - 50(r-1)(7-12v_m+8v_m^2)d + 4(7-10v_m)b$$

$$B = -4(r-1)(1-5v_m)e + 4[63(r-1)\eta_2 + 2a]c^{7/3} - 504(r-1)f + 150(r-1)(3-v_m)v_m d + 3(15v_m-7)b$$

$$C = 4(r-1)(5v_m-7)e - 2[63(r-1)\eta_2 + 2a]c^{7/3} + 252(r-1)f + 25(r-1)(v_m^2-7)d - (7+5v_m)b$$

With,

$$\eta_1 = (r-1)(7-10v_m)(7+5v_f) + 105(v_f - v_m)$$

$$\eta_2 = (r-1)(7+5v_f) + 35(1-v_f)$$

$$\eta_3 = (r-1)(8-10v_m) + 15(1-v_m)$$

and,

$r = G_f/G_m$

$a = \eta_1 * \eta_3$

$b = \eta_2 * \eta_3$

$d = \eta_2 * c$

$e = \eta_1 * c^{10/3}$

$f = \eta_2 * c^{5/3}$

c = Volume fraction of filler,

G_f = Shear modulus of filler,

G_m = Shear modulus of matrix,

v_f = Poisson ratio of filler,

v_m = Poisson ratio of matrix

2.3.8 Nuclear Magnetic Resonance (NMR)

NMR experiments are performed on a Bruker minispec mq20 spectrometer operating at 0.5T with 90˚ pulse length of 2.8 µs and recycle dead time of 10 µs. The temperature of experiments is kept at 30˚C. In Multiple-Quantum NMR experiments (MQ-NMR) [14] [15] [16] two sets of data are measured as a function of double quantum evolution time (τ_{DQ}): 1) double quantum buildup (I_{DQ}) representing the contributions of dipolar coupled network and 2) reference decay (I_{ref}) curves representing the contributions of noncoupled segments. The relaxation of the coupled segments is faster whereas the relaxation of noncoupled segments is slower and shows an exponential decay. This difference can be amplified by plotting (I_{ref} -I_{DQ}). In order to get the information about elastically active elastomer chains in the network it is important to subtract the contribution of network defects, in the form of exponential decay, to the sum of the two signal :

$$I_{\sum MQ} = I_{DQ} + I_{ref} - Be^{\frac{-2\tau_{DQ}}{T_{B2}}} \quad (2.14)$$

Where B is the fraction of noncoupled polymer chains and T_{B2} is the exponential decay factor of these network defects, deduced from the fit at long time of (I_{ref} -I_{DQ}). The normalization of I_{DQ} signal of dipolar coupled network segments provides the structural information about the elastomer network that is independent of any temperature-dependent relaxation effect.

$$\mathrm{I_{nDQ}} = \frac{\mathrm{I_{DQ}}}{\mathrm{I_{\sum MQ}}} \quad (2.15)$$

The ultimate results from the MQ-NMR is the residual dipolar couplings, D_{res} which arises due to the non-isotropic segmental fluctuations between the topological constraints such as entanglements and cross-links in the network. This can be obtained from the analysis of I_{nDQ} plotted against the τ_{DQ} which can be expressed as:

$$I_{nDQ}(\tau_{DQ}) = \int P\left(\ln\left(\frac{D_{res}}{2\pi}\right)\right) \times I_{nDQ}\left(\tau_{DQ}, \frac{D_{res}}{2\pi}\right) d\ln\left(\frac{D_{res}}{2\pi}\right) \quad (2.16)$$

The "Tikhonov regularization" [17] is used to fit the $I_{nDQ}\left(\tau_{DQ}, \frac{D_{res}}{2\pi}\right)$ data as:

$$I_{nDQ}\left(\tau_{DQ}, \frac{D_{res}}{2\pi}\right) = 0.5\left(1 - e^{-\left(0.378\frac{D_{res}}{2\pi}2\pi\,\tau_{DQ}\right)^{1.5}} \times \cos\left(0.538\,\frac{D_{res}}{2\pi}2\pi\,\tau_{DQ}\right)\right) \quad (2.17)$$

A satisfactory fit of $I_{nDQ}(\tau_{DQ})$ is obtained by using the following distribution function:

$$P\left(\ln\left(\frac{D_{res}}{2\pi}\right)\right) = \frac{1}{\sigma_{ln}\sqrt{2\pi}} \times e^{-\frac{\left(\ln\left(\frac{D_{res}}{2\pi}\right) - \ln(D_{med})\right)^2}{2\sigma_{ln}^2}} \quad (2.18)$$

The molecular weight between cross-links/constraints (M_c) can be estimated by:

$$\mathrm{M_C} = \frac{656\ \mathrm{Hz}}{\mathrm{D_{res}}/2\pi}\ \mathrm{kg/mol} \quad (2.19)$$

Where ($\frac{D_{res}}{2\pi}$) is related to D_{med} as:

$$\langle\frac{D_{res}}{2\pi}\rangle = D_{med} * e^{\frac{\sigma_{ln}^2}{2}} \quad (2.20)$$

And then, the cross-link density (υ_{NMR}) can be estimated as:

$$\upsilon_{NMR} = \frac{\rho}{M_C} \quad (2.21)$$

Where ρ is the density of elastomer.

2.4 Supporting information

Reproducibility of elastic modulus in DMA

Figure S2. 1 show the reproducibility of elastic modulus with the small difference in low strain amplitude used in this study.

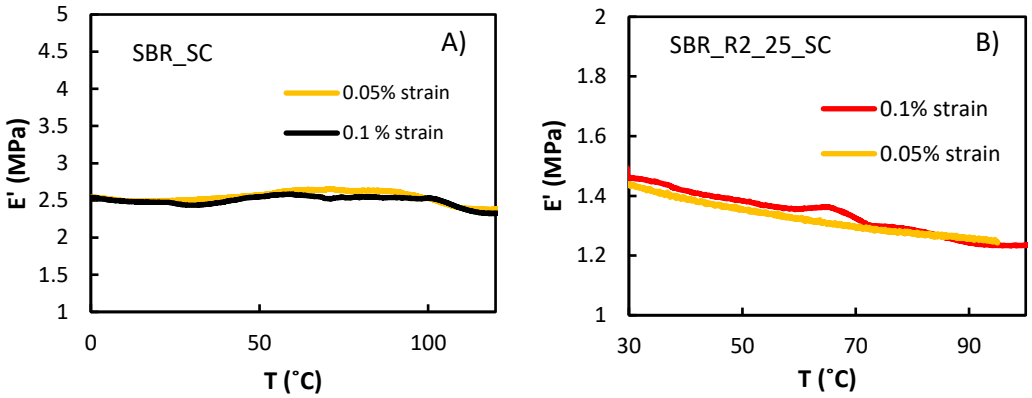

FIGURE S2. 1 ELASTIC MODULUS (E') OF: A) SBR_SC AND B) SBR_R2_25_SC AT TWO DIFFERENT LOW STRAIN AMPLITUDES.

The elastic modulus above glass transition temperature is reproducible irrespective of moduli difference observed at low temperature i.e. below the T_g of materials. The low temperature difference in different samples is highlighted by a grey transparent box as shown in Figure S2. 2.

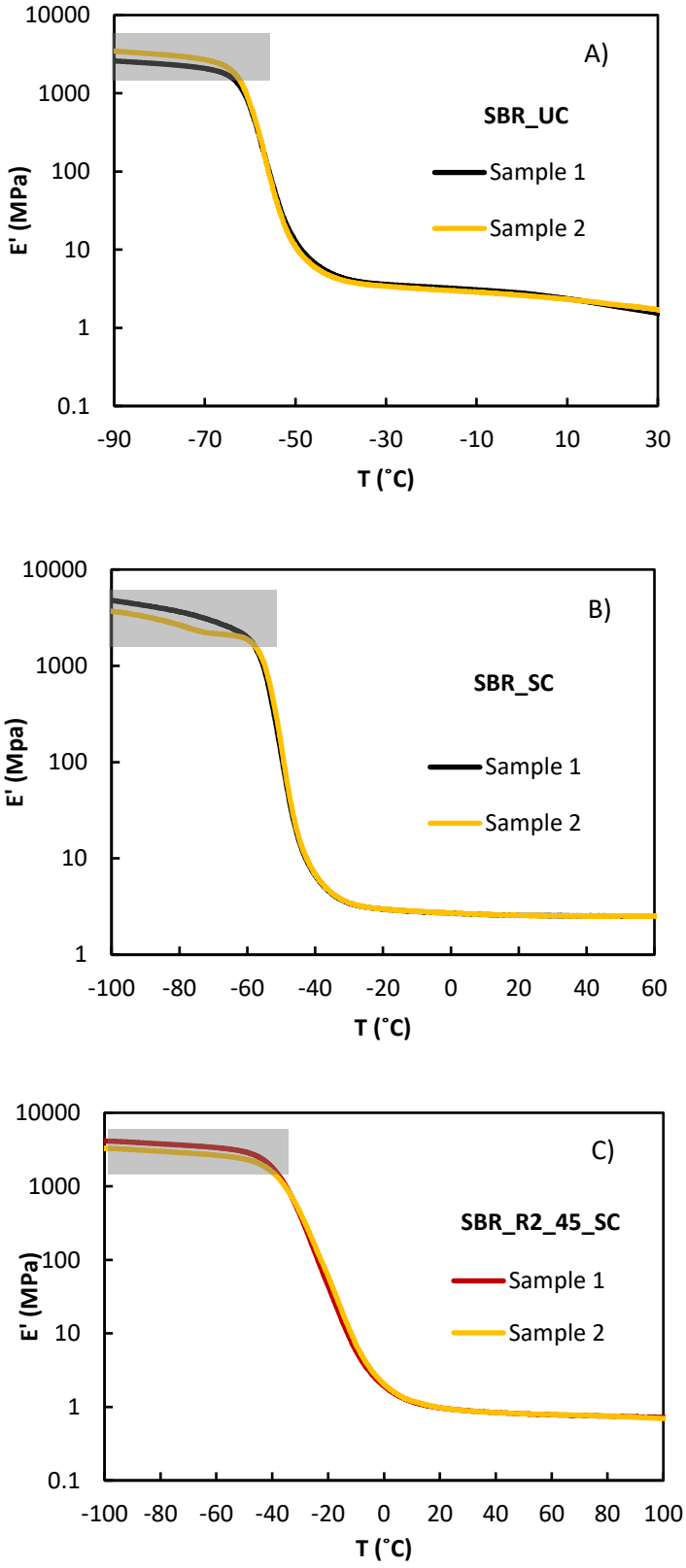

FIGURE S2. 2 ELASTIC MODULUS (*E′*) OF: A) SBR_UC, B) SBR_SC, AND C) SBR_R2_45_SC BLENDS ABOVE AND BELOW T_g.

2.5 References

(1) Rubinstein, M.; Colby, R. H. *Polymer Physics*; Oxford University Press, 2003.

(2) Bristow, G. M.; Watson, W. F. Cohesive Energy Densities of Polymers. Part 1.—Cohesive Energy Densities of Rubbers by Swelling Measurements. *Trans. Faraday Soc.* **1958**, *54* (0), 1731–1741. https://doi.org/10.1039/TF9585401731.

(3) Hildebrand, J. H. A History of Solution Theory. *Annual Review of Physical Chemistry* **1981**, *32* (1), 1–24.

(4) Hansen, C. M. *Hansen Solubility Parameters: A User's Handbook, Second Edition*; CRC Press, 2007.

(5) Hansen, S. A. C. M. *Hansen Solubility Parameters in Practice*; Hansen-Solubility.

(6) Ward, I. M.; Sweeney, J. *An Introduction to the Mechanical Properties of Solid Polymers*; Wiley, 2004.

(7) Schönherr, H.; Vancso, G. J. *Scanning Force Microscopy of Polymers*; 2010. https://doi.org/10.1007/978-3-642-01231-0.

(8) Cebe, P.; Science, A. C. S. D. of P. M.; and Hsiao, B. S.; Lohse, D. J.; Science, A. C. S. D. of P. M.; Engineering; Meeting, A. C. S. *Scattering from Polymers: Characterization by X-Rays, Neutrons, and Light*; ACS symposium series; American Chemical Society, 2000.

(9) Christensen, R. M.; Lo, K. H. Solutions for Effective Shear Properties in Three Phase Sphere and Cylinder Models. *Journal of the Mechanics and Physics of Solids* **1979**, *27* (4), 315–330. https://doi.org/10.1016/0022-5096(79)90032-2.

(10) Christensen, R.; Mccoy, J. Mechanics of Composite Mateials. *Journal of Applied Mechanics* **1980**, *47*, 460. https://doi.org/10.1115/1.3153710.

(11) Christensen, R. M. A Critical Evaluation for a Class of Micro-Mechanics Models. *Journal of the Mechanics and Physics of Solids* **1990**, *38* (3), 379–404. https://doi.org/10.1016/0022-5096(90)90005-O.

(12) Gusev, A. A. Controlled Accuracy Finite Element Estimates for the Effective Stiffness of Composites with Spherical Inclusions. *International Journal of Solids and Structures* **2016**, *80*, 227–236. https://doi.org/10.1016/j.ijsolstr.2015.11.006.

(13) Raos, G. Application of the Christensen-Lo Model to the Reinforcement of Elastomers by Fractal Fillers. *Macromolecular Theory and Simulations* **2003**, *12* (1), 17–23. https://doi.org/10.1002/mats.200390002.

(14) Vaca Chávez, F.; Saalwächter, K. Time-Domain NMR Observation of Entangled Polymer Dynamics: Analytical Theory of Signal Functions. *Macromolecules* **2011**, *44* (6), 1560–1569. https://doi.org/10.1021/ma102571u.

(15) Saalwächter, K. Proton Multiple-Quantum NMR for the Study of Chain Dynamics and Structural Constraints in Polymeric Soft Materials. *Progress in Nuclear Magnetic Resonance Spectroscopy - PROG NUCL MAGN RESON SPECTROS* **2007**, *51*, 1–35. https://doi.org/10.1016/j.pnmrs.2007.01.001.

(16) Saalwächter, K.; Herrero, B.; López-Manchado, M. A. Chain Order and Cross-Link Density of Elastomers As Investigated by Proton Multiple-Quantum NMR. *Macromolecules* **2005**, *38* (23), 9650–9660. https://doi.org/10.1021/ma051238g.

(17) Chassé, W.; Valentín, J. L.; Genesky, G. D.; Cohen, C.; Saalwächter, K. Precise Dipolar Coupling Constant Distribution Analysis in Proton Multiple-Quantum NMR of Elastomers. *J. Chem. Phys.* **2011**, *134* (4), 044907. https://doi.org/10.1063/1.3534856.

3 Characterization of SBR and resins

In this chapter, we first evaluate the modification of the SBR matrix after crosslinking with peroxide and sulfur system; peculiar attention is paid to the glass transition temperature, the network characteristics, the viscoelastic behavior and the morphology. Then the glass transition temperature of resins is evaluated by DSC analysis. Finally, the miscibility properties of raw materials are evaluated using Hansen solubility parameter approach.

Contents

3.1 SBR characterization

3.1.1 Curing of SBR with different Curing systems

The characteristics of the SBR (used as the main component of the blend materials) such as its microstructure and molecular weight distribution were presented in the chapter 2. This SBR was crosslinked using two types of curing systems: peroxide and sulfur (SBR_PC and SBR_SC). The

former is introduced in order to avoid the use of ZnO, necessary for sulfur curing of samples that introduces an intense signal in X-ray scattering experiments, which can mask the signal emanating from the presence of domains and phase separation in the blends. These two crosslinked materials are compared to raw SBR and to an uncured SBR (SBR_UC) which only contains processing additives such as stearic acid and 6PPD. Unlike crosslinked SBRs, both mixing steps (internal and external) are completely absent in case of raw SBR; whereas SBR_UC involves only internal mixing. All the materials are hot pressed under similar conditions. The formulations are recalled in Table 3. 1.

TABLE 3. 1 COMPOUND FORMULATIONS OF THE DIFFERENT STUDIED SBR.

Sample name	**Ingredients (phr)**						
	SBR	**6PPD**	**Stearic acid**	**DCP**	**ZnO**	**S**	**CBS**
SBR_raw	100	-	-	-	-	-	-
SBR_UC	100	1.5	3	-	-	-	-
SBR_PC	100	1.5	3	0.74	-	-	-
SBR_SC	100	1.5	3	-	1.45	1.4	1.6

3.1.2 DSC analysis of uncured and cured SBR

The T_g of uncured SBR copolymer, where chemical cross-links are absent and the interaction between chains is mainly due to the weak van der Waals forces, mainly depends on the styrene content, isomeric composition of butadiene, and molecular weight. The higher amount of styrene increases the steric hindrance of the polymer chains, which in turn shifts the T_g of SBR towards the higher temperature. [1] The increasing vinyl content in butadiene unit also increases the T_g of SBR by making chain structure stiffer. When the chemical crosslinks are introduced in SBR, they increase the T_g of SBR. [2] [3] The heat flow curves from the 2nd heating ramp of the materials are presented in Figure 3. 1.

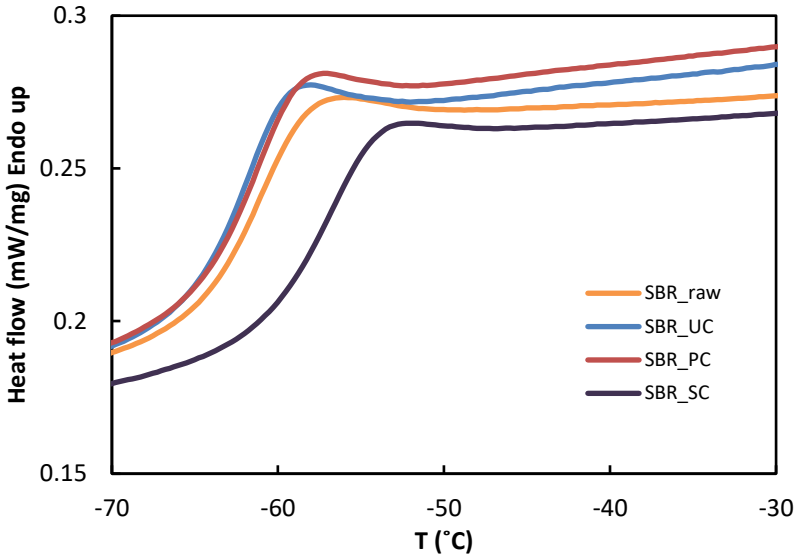

FIGURE 3. 1 DSC 2ND HEATING CURVES OF SBR_RAW, SBR_UC, SBR_PC, AND SBR_SC SAMPLES.

As shown on the curves, SBR-raw, SBR_UC, and SBR_PC have the same glass transition temperature, with a mid-point T_g around -62˚C. Conversely, the T_g of the SBR_SC is shifted by +5˚C. This is consistent with the literature. As already mentioned in chapter1, this shift in T_g is often attributed to the restricted chains mobility created by the formation of cross-links. [4] There is however another explanation: sulfur curatives also lead to a chemical modification of the polymer chains as shown in Figure 3. 2. These intramolecular modifications in the form of pendent groups (such as remaining fragments of sulfur, accelerator, and sulfur/accelerator complexes) and cyclic structures can also result in hindering the chain mobility. [5 6]

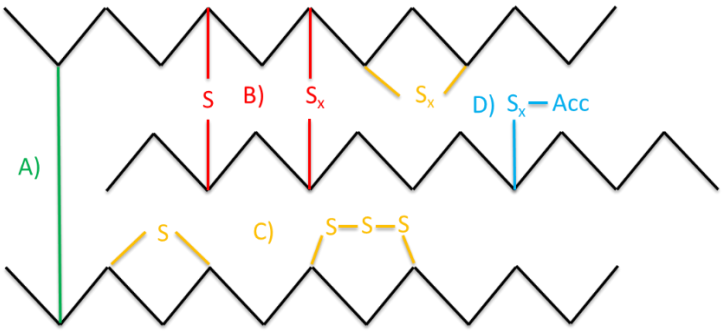

FIGURE 3. 2 TYPICAL REPRESENTATION OF DIFFERENT STRUCTURES FORMED AS A RESULTS OF SULFUR CURING: A) C-C CROSSLINKS, B) SULFIDIC CROSSLINKS, INTERMOLECULAR MODIFICATIONS AND C) CYCLIC STRUCTURES, D) PENDENT GROUPS, INTRAMOLECULAR MODIFICATIONS.

A reversible peak around 40˚C is observed on the DSC curves of the SBR_UC and SBR_PC (Figure 3. 3). The reversibility of this peak is shown in the heating-cooling-heating cycles of these samples in the supporting information section of this chapter (Figure S3. 1 and Figure S3. 2).

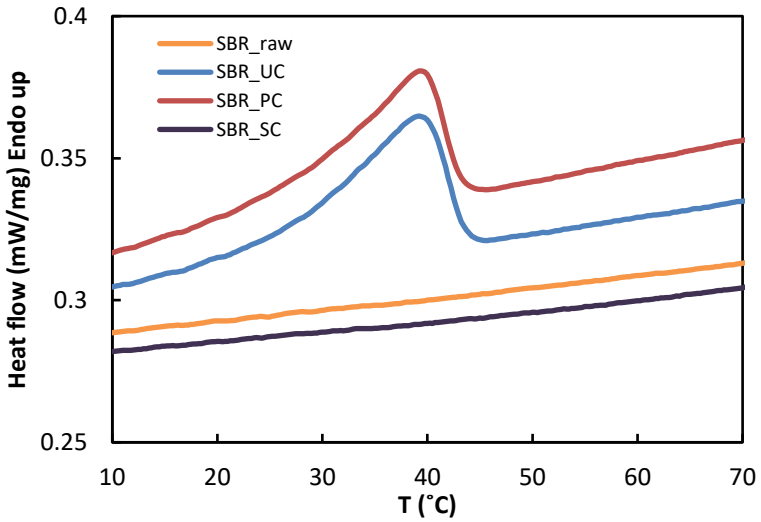

FIGURE 3. 3 DSC 2ND HEATING CURVES OF THE DIFFERENT SBRS AT HIGHER TEMPERATURES.

It is ascribed to the melting of the stearic acid, present in these two materials. However, such a peak is absent on the SBR_SC curve since all the stearic acid has reacted with ZnO to form zinc stearate complex.[7] This complex is known to form crystallites, as evidenced by the presence of a melting peak at 110°C. This melting seems reversible as shown on Figure 3. 4 (the difference between the two heating ramps, being likely due to the difference in the thermal history).

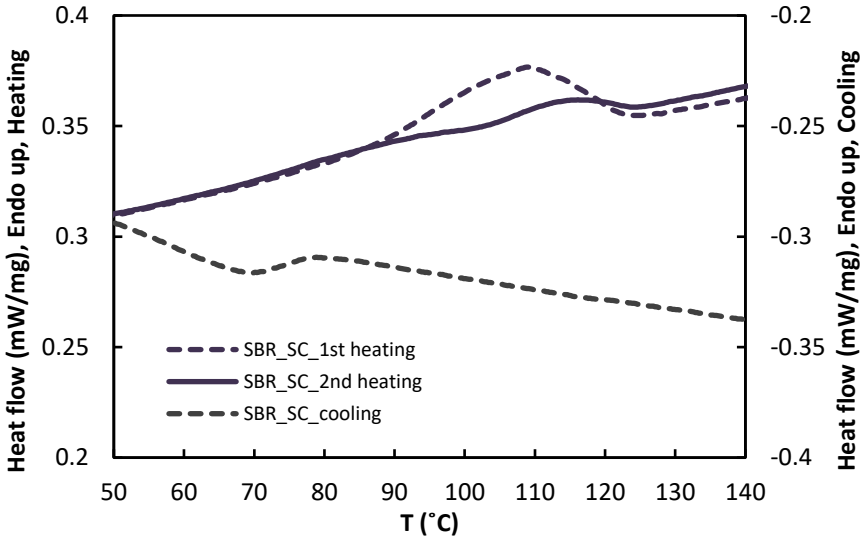

FIGURE 3. 4 DSC HEATING AND COOLING CURVES OF THE SBR_SC AT HIGH TEMPERATURES.

The presence of crystallites of zinc stearate complex have been confirmed by TEM observations which indeed show crystallites whose size varies from 1 μm to 2.5 μm in Figure 3. 5.

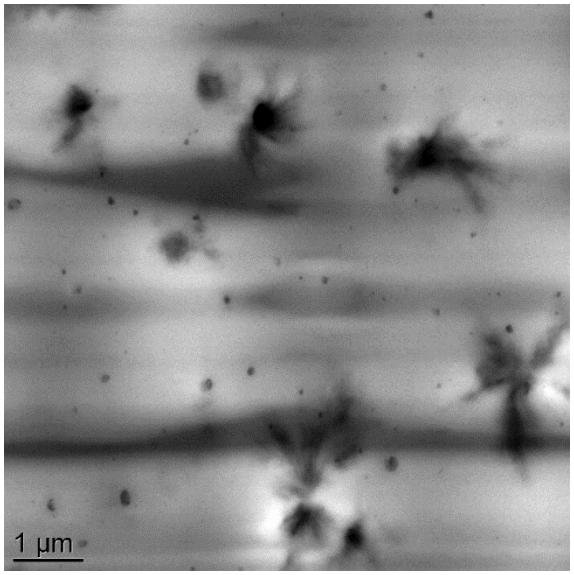

FIGURE 3. 5 TEM IMAGE OF SBR_SC THIN SECTION.

3.1.3 Viscoelastic behavior of uncured and cured SBR

The viscoelastic behavior of different SBRs was investigated by dynamic mechanical analysis over a large temperature range from -90˚C to 120˚C at the heating rate of 1˚C.min^{-1} and a frequency of 1Hz. The storage modulus, loss modulus, and loss factor as a function of temperature of the three differently cured SBRs are shown in Figure 3. 6.

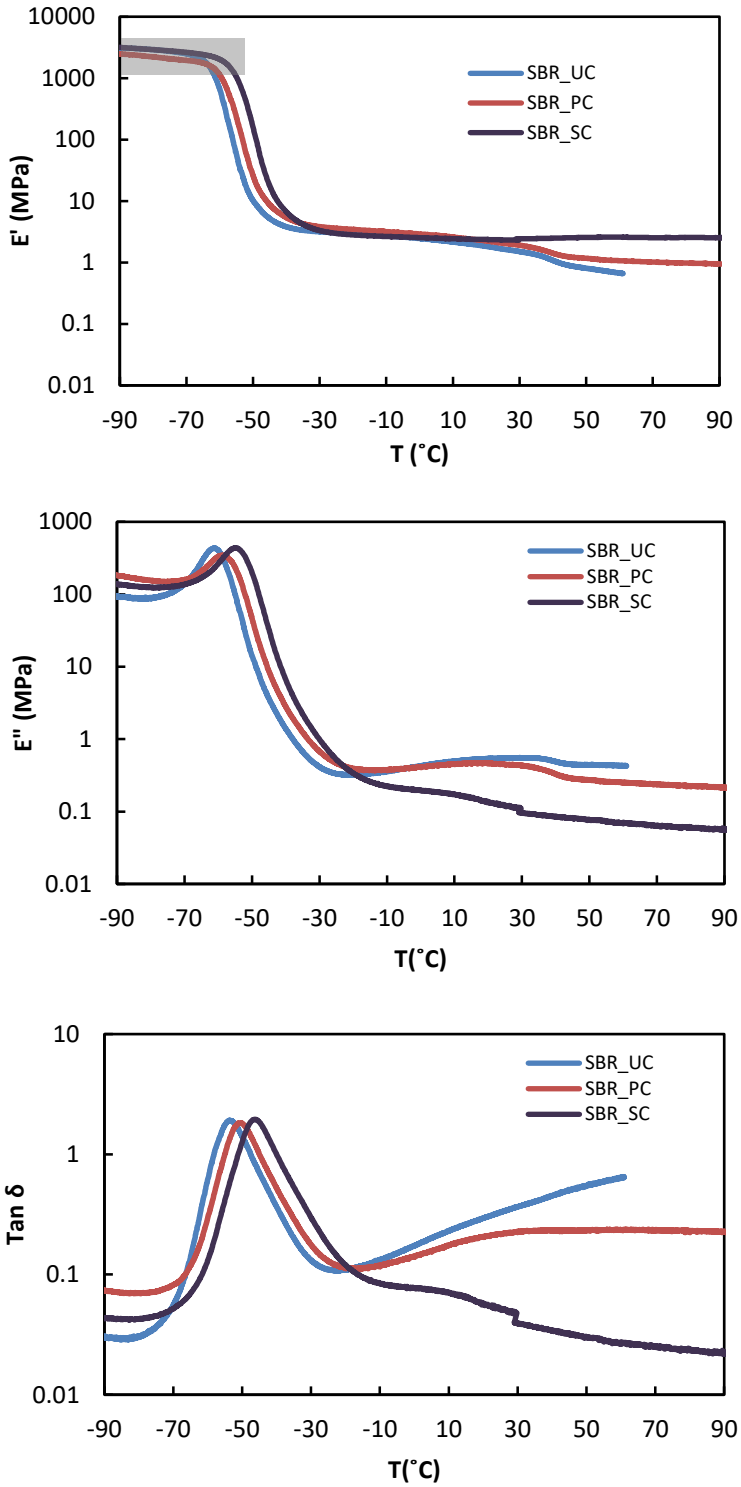

FIGURE 3. 6 TEMPERATURE DEPENDENCE OFE', E'', AND Tan δ OF THE DIFFERENT SBRS.

The α-relaxation temperature T_α is normally related to glass transition temperature T_g measured by DSC and is measured at the maximum of $Tan\ \delta$ peak or at the maximum of E'' peak. T_α, in our study, is estimated from the maximum of $Tan\ \delta$ peaks. Given the uncertainty in the temperature

(likely around $\pm 1°C$), the T_α differences observed between the different materials are consistent with the T_g differences observed in DSC. Indeed, T_α of SBR_UC is the lowest, and is 6°C lower than the T_α of SBR_SC. The T_α value of SBR_PC is in between those of the two other materials, slightly above the one of SBR_UC. Thus, these results are consistent with the fact that the crosslinking step increases the glass transition.

In the rubbery state, a continuous decrease of the storage modulus of SBR_UC is observed with the increase of temperature. It becomes more pronounced for temperature above 30°C, before the flowing of the material. This drop of E' in SBR_UC at 30°C is also confirmed by rheometry (cf. Figure S3. 3). This might be due to the presence of branched chains and/or a peculiar distribution of the molar weight. Such a decrease is also observed with SBR_PC but a plateau is reached above 30°C. Our assumption is that the crosslinks first link the longest chains, suppressing their flow at high temperature, but are not numerous enough to inhibit the relaxation of the branched chains. In the SBR_SC the crosslinking level is higher (this was expected given the chosen amount of peroxide and sulfur in the materials formulations) and enables to completely suppress the modulus decrease at 30°C, leading to a classical rubbery plateau beginning at the end of the main relaxation. The cross-link density can be estimated from the modulus (assimilated here to the storage modulus) at 30˚C using the classical formula:

$$E = 3\nu RT \tag{3.1}$$

Where ν is the elastically active chains density (EAC), R is the gas constant, and T is the temperature (with affine assumption, for an homogeneous network). The results are reported in Table 3. 2.

The EAC of SBR_UC and SBR_SC was also estimated using NMR technique. The experimental details and the data treatment of NMR analysis are described in chapter 2, and the data are reported in the supporting information section of this chapter (cf. Figure S3. 4 - Figure S3. 6).

TABLE 3. 2 CROSS-LINK DENSITY ESTIMATED FROM DMA AND NMR ANALYSIS AT 30˚C.

EAC density	SBR_UC	SBR_PC	SBR_SC	Ratio (SC/UC)
DMA, $\boldsymbol{v}$ $\boldsymbol{(10^{-4}\, mol/cm^3)}$	1.99	2.52	3.22	1.6
NMR, $\boldsymbol{v}$ $\boldsymbol{(10^{-4}\, mol/cm^3)}$	2.95	-	4.72	1.6

Like in the literature, [8] [9] [10] [11] [12] an affine relationship can be deduced from both techniques: $v_{NMR} = 1.41.\, v_{DMA} + 0.08$. The difference between EAC densities from both techniques may come from the fact that NMR probes the chain dynamics at much smaller time scales (10^{-4} s) than DMA and therefore involves topological constraints which are released in DMA experiment. Both techniques indicate that, at 30°C the cross-link density of SBR_SC is only 1.6 times the cross-link density of SBR_UC. This means that a large part of the modulus of the SBR_SC in the rubbery domain is related to the entanglements. To go further, T_g and T_α were plotted in Figure 3. 7 as a function of the EAC density calculated from DMA for all three SBRs.

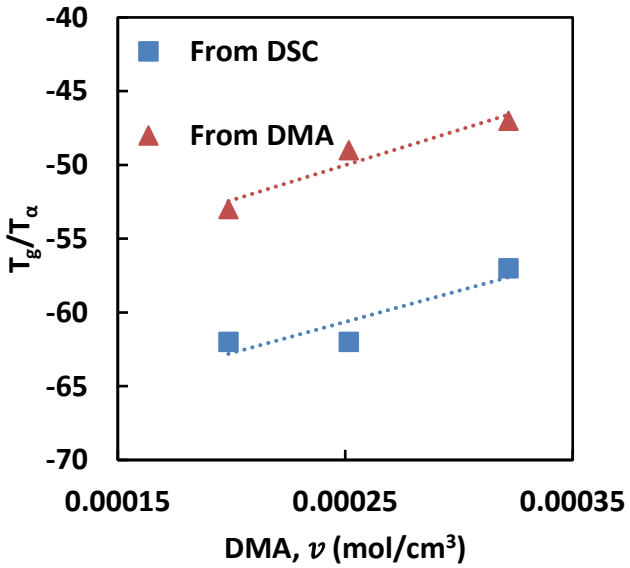

FIGURE 3. 7 T_g AND T_α VERSUS EAC DENSITY OF SBR_UC, SBR_PC AND SBR_SC FROM DMA.

Note that we also performed NMR measurement at 110°C with the SBR_SC material. The deduced EAC density was found equal to the one at 30°C, confirming the existence of the modulus plateau seen in DMA. Moreover, in Figure 3. 6, for SBR_PC, the *E'* drop still exist at 30°C, which is

correlated with a very wide E'' peak. It is related to the low cross-link density of this material, which leads to the creation of a weak elastomer network with numerous tethered chains and eventually uncrosslinked chains . [13] [14] These chains can relax at long time, as studied by Souillard et al. [15]

To estimate the number of free chains, swelling experiments were performed on the SBR_PC and SBR_SC samples in cyclohexane. The soluble fraction, F_s, is estimated as:

$$F_s = \frac{w_i - w_d}{w_i} \quad (3.2)$$

Where w_i is the initial weight and w_d is the dried weight of the SBRs. In case of SBR_SC, the estimated soluble fraction is found 3.2 wt% which can be attributed to the unreacted curing additives. Furthermore, we confirm that swelling experiment does not modify the viscoelastic behavior of SBR_SC as shown in Figure S3. 7 in supporting information section of this chapter. On the other hand, in case of SBR_PC, the amount of soluble fraction is estimated to be 28 wt% which confirms the significant amount of uncrosslinked chains in this material

An AFM phase image of SBR_PC and the extracted profiles along the yellow lines are shown in Figure 3. 8. In such an image, the brighter phase should correspond to the relatively stiffer phase, and therefore could be related to cross-linking heterogeneities, with high crosslinked densities surrounded by much less crosslinked polymer containing the uncrosslinked, or at least less crosslinked, polymer chains. This phase shows ramified domains of hundreds of nm in overall size with the average inter and intra correlation distance around 60 nm (the inter correlation distance being in the 2nd order range).

In order to confirm these heterogeneities, the SAXS patterns obtained on the SBR_PC and SBR_UC are presented in Figure 3. 9. For both SBR, at very low q values, a q^{-3} decrease of the intensity is observed and confirms the presence of large scattering objects with a ramified overall shape. The $Iq^3 = f(q)$ highlights then a correlation peak arising around $q^* = 0.028\, nm^{-1}$ and $q^* = 0.012\, nm^{-1}$ for SBR_PC and SBR_UC, respectively. According to the Bragg law, these peaks are associated to a correlation distance $d = \frac{2\pi}{q^*} = 224\, nm$ and $532\, nm$ for SBR_PC and SBR_UC, respectively. This gives the range of order of the average distance between such ramified objects, in the same range of what was observed by AFM. More interestingly, one can also observe that the crosslinking step leads to a halving of the size of these heterogeneities. At high q values, a

small sharp peak around $q = 2\,nm^{-1}$ is also visible which is likely due to the stearic acid crystallites.

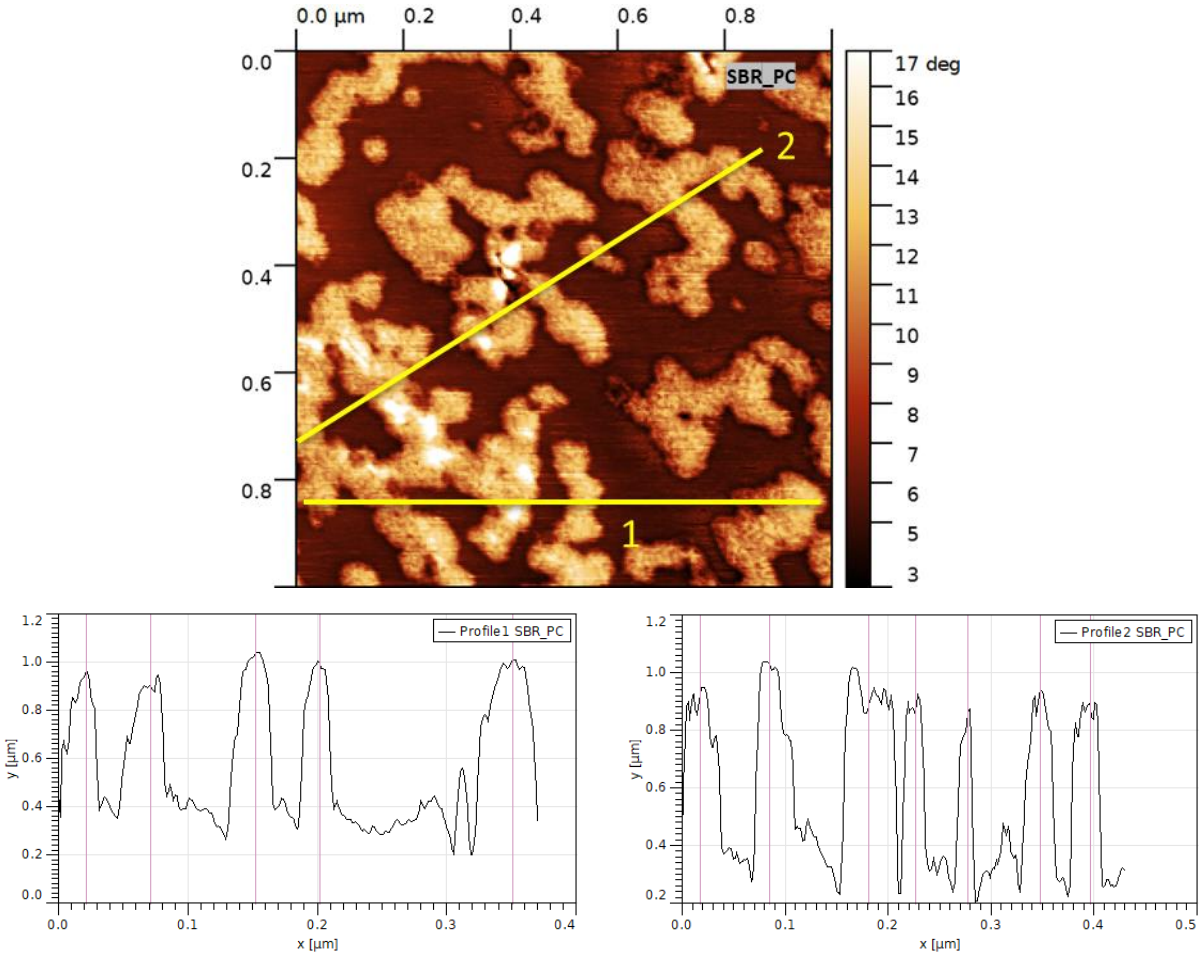

FIGURE 3. 8 AFM PHASE IMAGE OF SBR_PC AND THE EXTRATED PROFILES OF HETEROGENETIES ALONG THE YELLOW LINES.

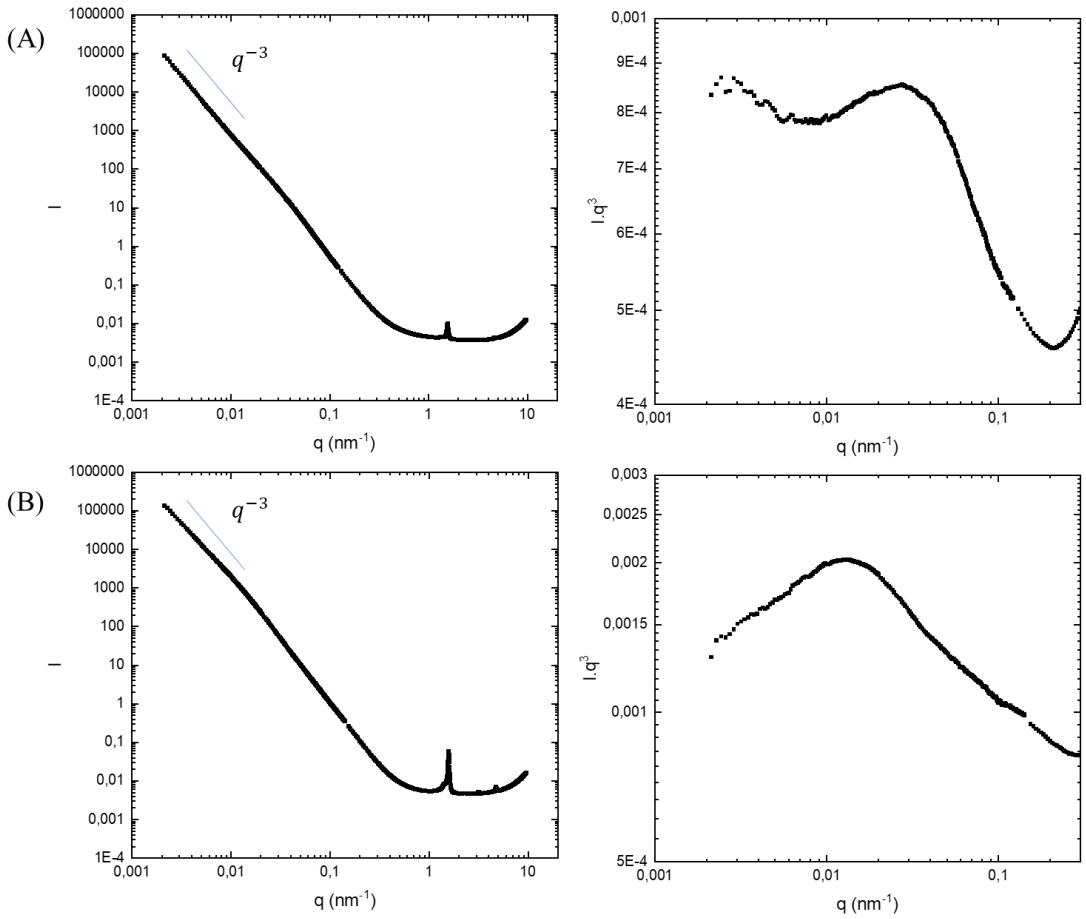

FIGURE 3. 9 SAXS PATTERN (LEFT) AND CORRESPONDING $Iq^3 = f(q)$ PLOT (RIGHT) OBTAINED ON (A) THE SBR_PC AND (B) SBR_UC.

Finally, a slight decrease in the storage modulus of SBR_SC, associated to a peak of $Tan\ \delta$, is found at around 100˚C, and is reproducible during the heating-cooling-heating cycles in DMA analysis as shown in Figure 3. 10. This slight decrease is confirmed with several samples of SBR_SC taken from the different part of the compression molded sheet.

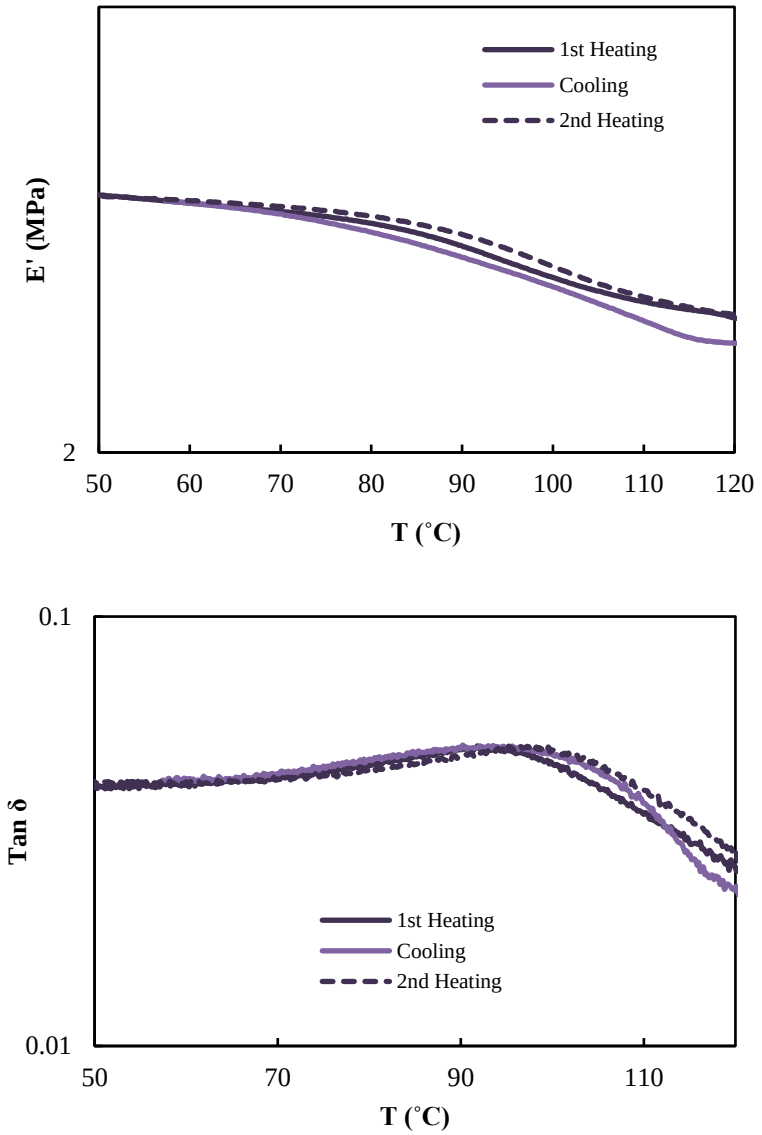

FIGURE 3. 10 DMA STORAGE MODULUS (*E′*) AND LOSS FACTOR (Tan δ) VERSUS TEMPERATURE (T) FOR SBR_SC DURING THREE HEATING-COOLING-HEATING CYCLES.

This may be first related to the peak found at around 110˚C in DSC and due to the zinc stearate complex (cf. Figure 3. 4). The decrease factor of the modulus is around 1.24. Assuming that this decrease would be due to the melting of a volume fraction ∅ of stiff reinforcing crystallites, the Guth and Gold [16] [17]equation can be used to estimate the Young's modulus E_c of such a composite:

$$E_c = E_{matrix}(1 + 2.5\emptyset + 14.1\emptyset^2) \quad (3.3)$$

with E_{matrix}, the modulus of the SBR matrix, taken here to be the modulus of the SBR_SC at high temperature. Following this equation, the minimum crystallite volume fraction should be 7 vol%. However, the complete crystallization of all the ZnO (which is impossible) can only lead to a

volume crystallite fraction below 4.5 vol%. Thus, it is difficult to ascribe this modulus decrease to the melting of zinc stearate complex. Actually, the superposition of the heating and cooling curve suggests better a relaxation phenomenon, which could originate from the relaxation of styrene domains. Indeed, the SBR is a random copolymer, in which the length of the styrene sequence is distributed. This can promote the formation of a styrene phase whose glass transition should be around 100˚C. Such assumption is supported by the literature: the presence of segregated phenyl rings forming the nanodomains in butadiene matrix has been reported in the SAXS/SANS study of SBR containing 20 wt % styrene by Gambino et al. [18] These domains can act like supplementary crosslinks in the material, whose influence vanishes above their glass transition temperature. Note that no relaxation is observed in this temperature range for SBR_UC and SBR_PC, but only a continuous decrease of the storage modulus that becomes lower than the SBR_SC one above 10°C. This is explained by the absence of crosslinks, or the very low crosslink density and this may lead to difficulty for identifying supplementary small modulus variations. AFM analysis of SBR_SC does not help to definitely conclude on the origin of this relaxation: in Figure 3. 11 one can see a nanostructuration of the SBR_SC sample. As for SBR_PC, this nanostructuration in SBR_SC is attributed to cross-link heterogeneities. The mean correlation distance between these nanoscale heterogeneities is about 30 nm which is slightly lower than the one found in SBR_PC. This can be expected since SBR_SC has a higher crosslinking density (higher number of crosslinks per unit volume) compared to the SBR_PC.

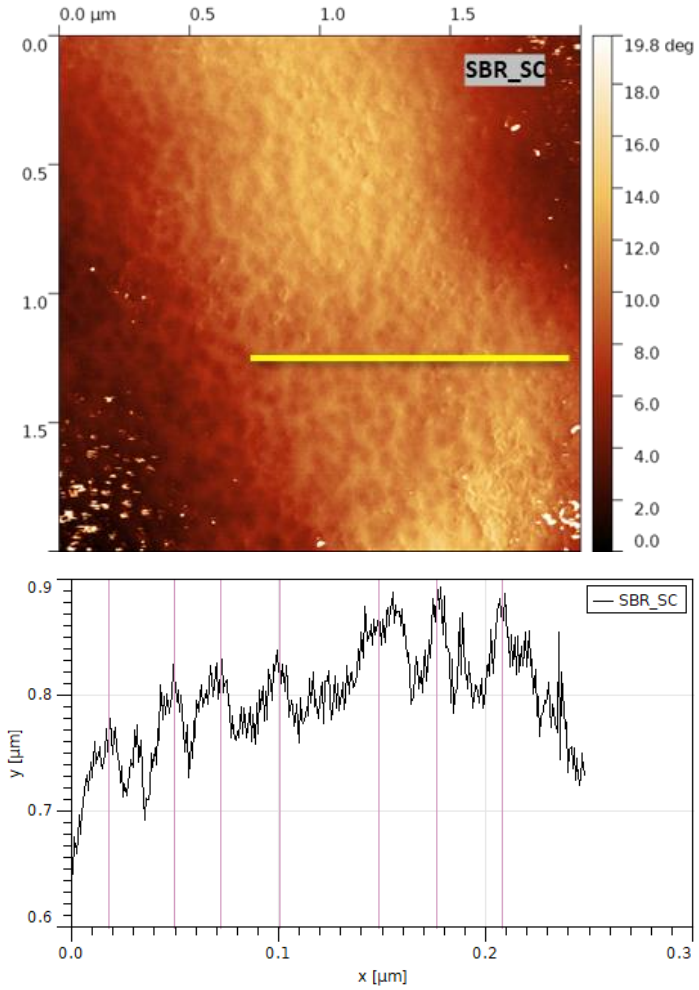

FIGURE 3. 11 AFM PHASE IMAGE OF SBR_SC AND THE EXTRACTED PROFILE ALONG THE YELLOW LINE.

3.1.4 Conclusions of SBR characterization

As expected, the cross-link density of SBR_SC is highest among all the SBRs. In SBR_SC most of the chains are part of elastomer network whereas SBR_PC has large number of dangling chains which relax above its T_g. The cross-link heterogeneities as seen in AFM images and SAXS are present in both SBR_SC and SBR_PC. In addition to that, micro-crystallites are present in SBR_SC due to the zinc stearate complex. A relaxation around 100˚C in SBR_SC may be attributed to the glass transition of styrene domains as reported in the literature.

3.2 Resins characterization

3.2.1 DSC Characterisation

The characteristics of all three resins, such as their compositions and molecular weight distributions were presented in the chapter 2. The heat flow curves of 1st and 2nd heating of all the three resins are shown in Figure 3. 12 and Figure 3. 13 respectively.

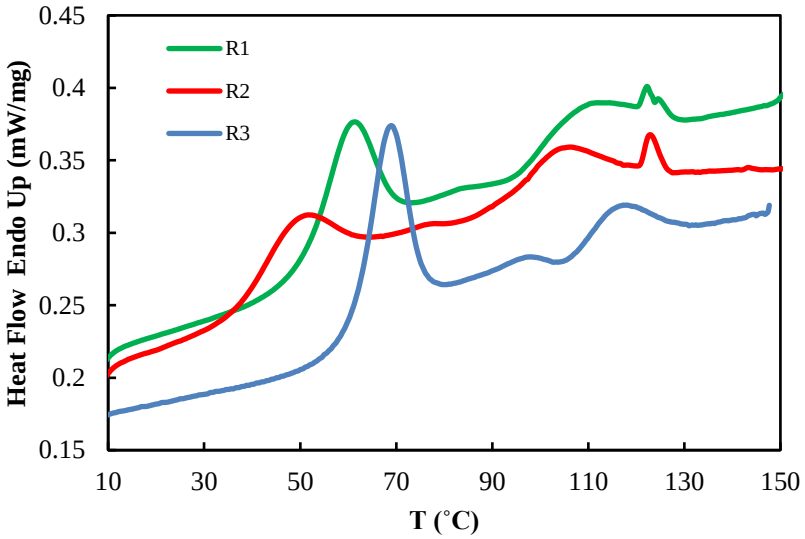

FIGURE 3. 12 DSC 1ST HEATING CURVES OF RESIN R1, R2, AND R3.

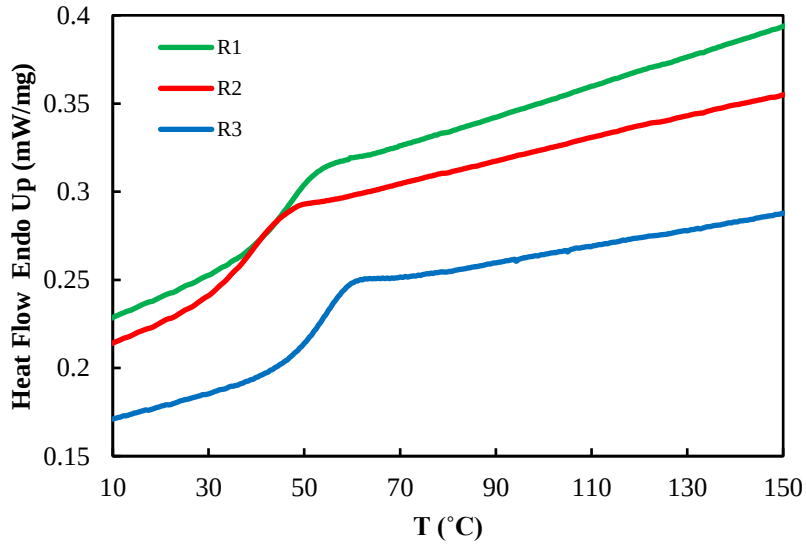

FIGURE 3. 13 DSC 2ND HEATING CURVES OF RESIN R1, R2, AND R3.

Sharp peaks at the end of glass transition are observed in 1st heating for all three resins. They are due to the ageing of the resins. At higher temperatures, other peaks are also observed for all three resins. These peaks are interestingly similar but occur at slightly different temperatures. Since these peaks are vanished in the 2nd heating cycle, they can be attributed to the presence of some volatile

fraction in the resins. The mid-point T_g measured for resins R1, R2, and R3 from the 2nd heating curves are 46˚C, 37˚C, and 52˚C respectively.

3.2.2 Miscibility of resins with SBR

We tried to evaluate the miscible characteristics of the raw materials prior to any processing. Hansen solubility parameter approach, [19] as described in chapter 2, is used to estimate the solubility parameters of the resins and SBR. Figure 3. 14 shows the solubility spheres of SBR in a 3-D plot where the three components of solubility parameter such as dispersive (D), polar (P), and hydrogen (H) corresponds to the three axes of the plot in $MPa^{1/2}$. The blue dots inside the sphere represent the solvents that dissolve the SBR. The red dots outside the sphere represent the solvents that do not dissolve the SBR.

The radius of the sphere is known as interaction radius, R_0. Higher radius indicates more solvents inside the sphere and thus more solubility.

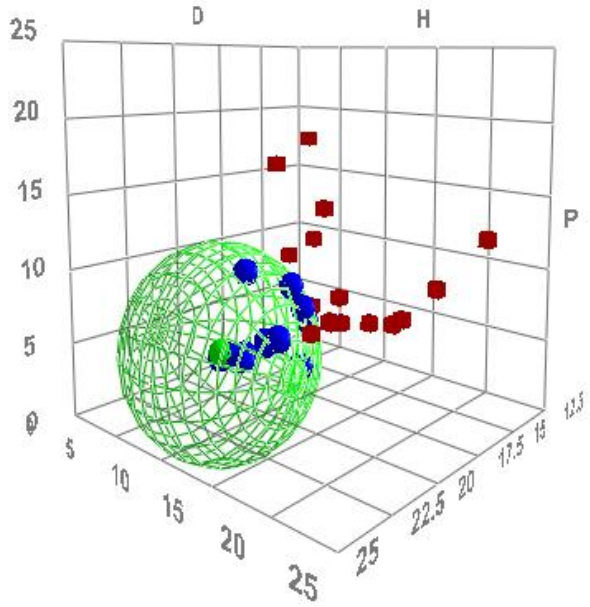

FIGURE 3. 14 HANSEN SOLUBILITY SPHERE OF SBR WITH 27 DIFFERENT SOLVENTS.

The three components of solubility parameters for SBR and all three resins estimated from 27 different solvents using HSPiP software [20] are listed in Table 3. 3.

TABLE 3. 3 HANSEN SOLUBILITY PARAMETERS OF SBR AND RESIN R1, R2, AND R3.

Materials	$\delta_D(MPa^{1/2})$	$\delta_P(MPa^{1/2})$	$\delta_H(MPa^{1/2})$	$\delta_{TOT}(MPa^{1/2})$
SBR	18.4 ± 0.2	1.6 ± 1.1	1.6 ± 0.8	18.6
Resin R1	17.8 ± 0.3	2.8 ± 0.9	1.7 ± 0.6	18.1
Resin R2	17.5 ± 0.2	2.9 ± 0.4	3.3 ± 0.7	18.0
Resin R3	18.4 ± 0.2	1.6 ± 1.1	1.6 ±0.8	18.6

TABLE 3. 4 SOLUBILITY SPHERE RADIUS (R_0), MISCIBILITY DISTANCE (D), AND RELATIVE ENERGY DIFFERENCE (RED) OF ALL THREE RESINS WITH RESPECT TO SBR.

Materials	Sphere radius, $R_0(MPa^{1/2})$	Distance, $D(MPa^{1/2})$	RED
SBR	8.5	-	-
Resin R1	7.2	1.7 ± 1.2	0.23
Resin R2	7.0	2.8 ± 1.0	0.40
Resin R3	8.5	0	0

The total solubility parameters for all the materials, SBR and resins, are close to each other. The SBR and resin R3 even have same solubility parameter values. The resins R1 and R2 have similar dispersive and polar solubility parameters however their hydrogen component is different by 1.6 $MPa^{1/2}$. Once the solubility parameters are estimated, the distance between both spheres for each compound in the Hansen solubility space is determined as:

$$D^2 = 4(\delta_{D1} - \delta_{D2})^2 + (\delta_{P1} - \delta_{P2})^2 + (\delta_{H1} - \delta_{H2})^2 \quad (3.4)$$

D is reported in Table 3. 4 and the Figure 3. 15 and Figure 3. 16 shows the respective solubility spheres of SBR with Resin R1 and R2. The bigger sphere corresponds to the SBR and the smaller ones to the resins R1 and R2.

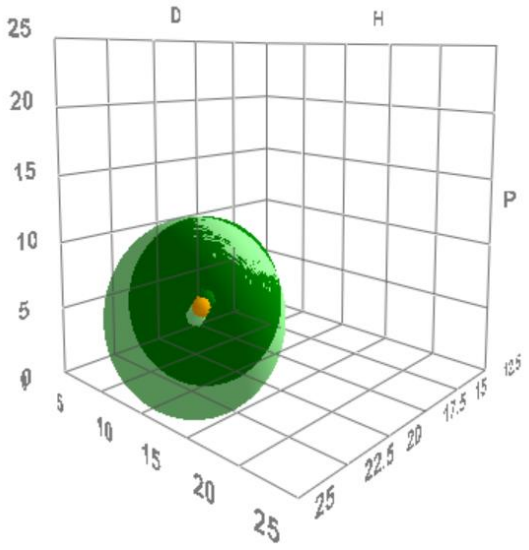

FIGURE 3. 15 HANSEN MISCIBILITY SPHERES OF SBR AND RESIN R1.

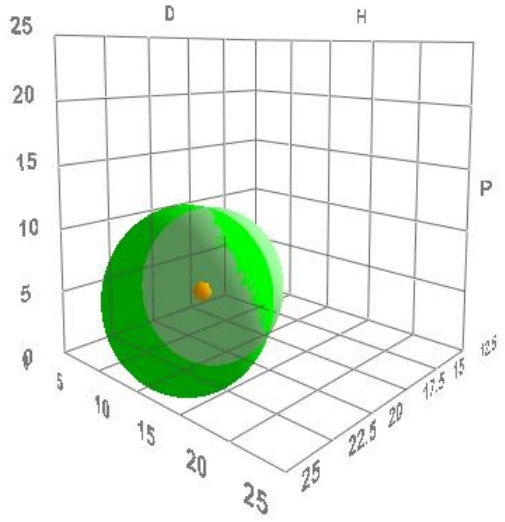

FIGURE 3. 16 HANSEN MISCIBILITY SPHERES OF SBR AND RESIN R2.

In order to determine the miscibility of two compounds, the distance between the centers of their two solubility spheres is divided by the minimum of the sphere radius among two (smaller of the two compounds). This gives the relative energy difference (RED) which effectively determines how compatible are two compounds mutually. If RED is 0, then there is no energy difference and two compounds have same solubility parameters and are fully compatible. The RED value higher than 1 indicates the incompatibility between two compounds and the value less than 1 indicates a partial compatibility between two compounds. The RED values estimated for R1 and R2 with respect to SBR are given in Table 3. 4. Resin R3 is completely compatible with SBR and higher RED value of resin R2 compared to R1 shows its lower compatibility with SBR. However, we must

be cautious about the interpretation of this data as the contribution of hydrogen component to the total solubility parameter in case of R2 is 50% higher than the R1. This means hydrogen bonding has larger contribution to the total solubility parameter of resin R2 and hydrogen bonding plays the significant role in the miscibility behavior of the compounds. [21] In any case, the Hansen solubility suggests the compatibility of all the resins with SBR in which R3 is the most compatible resin followed by R1 and R2. It should be clear that these predictions are completely based on solubility of compounds and do not take into the account the thermal history and processing conditions of the blends. Thus, they may predict the miscibility of the blends more accurately which are prepared by solvent casting than blends prepared by thermal and mechanical mixing methods.

3.3 Conclusions

In order to properly study the resin SBR blend, it was mandatory to perform a detailed analysis of the SBR matrix without resin. As expected, it has been shown that the sulfur crosslinking results in a higher crosslinking density (as observed by NMR and DMA) and a T_g value 5°C higher than the one of SBR either uncrosslinked or crosslinked with peroxide. This shift can be ascribed to restricted chain mobility in presence of crosslinks and the possibility of chemical modification of polymer chains (intramolecular modifications) with sulfur. More interestingly, a mechanical relaxation is observed by DMA around 40˚C in SBR_UC and SBR_PC, certainly due to a molecular weight distribution of chains or a large number of branched or dangling chains. This relaxation is not observed for SBR_SC, indicating that almost all the chains in SBR_SC become part of crosslinked network. The close values of modulus in case of SBR_UC and SBR_SC at the beginning of rubbery plateau signifies the dominating nature of entanglements in the SBR network. Another relaxation around 100˚C appears in SBR_SC and may be attributed to the glass transition of styrene domains reported in the literature but requires further investigation.

The introduction of crosslinks in SBR_PC and SBR_SC creates crosslinks heterogeneities which are seen in AFM images. The average correlation distance of these heterogeneities is larger for SBR_PC than for SBR_SC, this may be due to the more densely crosslinked network in case of SBR_SC. In order to confirm this, it would be interesting to see if crosslinked SBR with less sulfur (in order to get comparable crosslinked density than in SBR_PC) would show an increase of this correlation distance. In any case, even the systems without resin are nanostructured, which will make difficult the interpretation of the nanostructaration in the resins blends.

The three resin that have been chosen for this PhD are not model resins and petroleum industry by products. They have different T_g and small but different molecular weight; the highest T_g is that of resin R3 followed by R1 and R2. The total solubility parameters of these three resins are very close and therefore do not enable to precisely differentiate their miscibility behavior, even though the data seems to suggest that the resin R3 should be more fully compatible with SBR than the R1 and R2 resins. Actually, the characterization of the different blends, presented in the next chapters, showed that the R2 and R3 resin, leads to very similar blends, conversely to the R1 resin, which justifies that the next chapter is devoted to the R2 and R3 resin blends, while the last chapter is dedicated to the R1 blend.

3.4 Supporting information

DSC curves of SBR_UC and SBR_PC

The reversibility of the melting peak corresponding to the stearic acid in 1st heating-cooling-2nd heating cycles of SBR_UC and SBR_PC samples is shown in Figure S3. 1 and Figure S3. 2, respectively. The differennce in the two heating cycles is likely due to the difference in the thermal history.

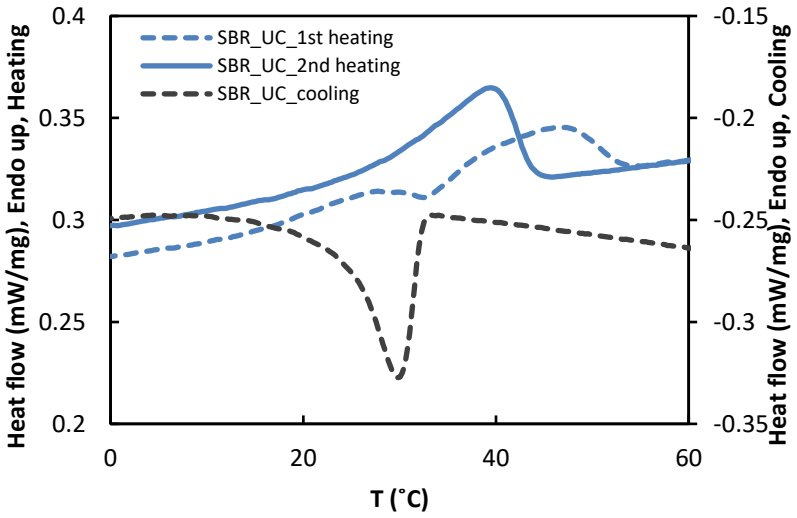

FIGURE S3. 1 DSC HEATING - COOLING CURVES OF SBR_UC.

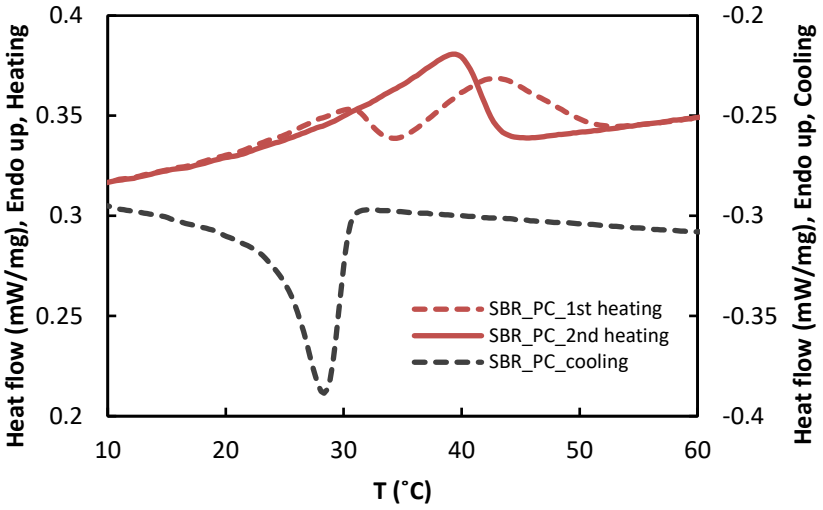

FIGURE S3. 2 DSC HEATING - COOLING CURVES OF SBR_PC.

Storage moduli of SBR_UC samples from rheometer

The decrease of modulus around 35˚C due to the branching or peculiar distribution of molar weight of chains is seen in two different samples of SBR_UC in Figure S3. 3.

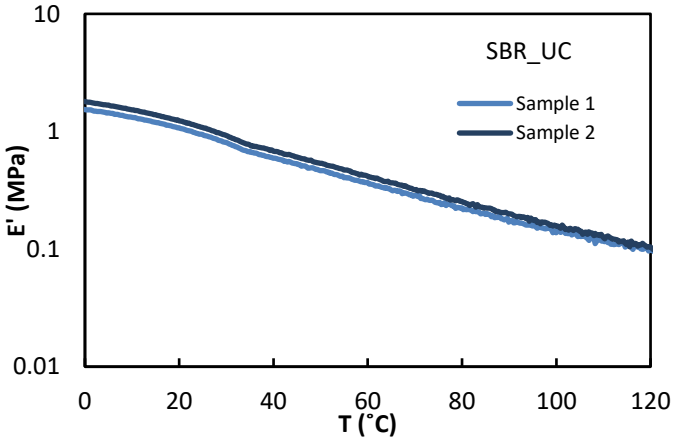

FIGURE S3. 3 STORAGE MODULUS (E') VERSUS TEMPERATURE (T) OF SBR_UC FROM RHEOMETER

Treated NMR data of SBR_UC and SBR_SC

Figure S3. 4 - Figure S3. 6 correspond to the NMR data treatment of SBR_UC and SBR_SC samples as described in chapter 2 and the EAC is estimated from these treated data.

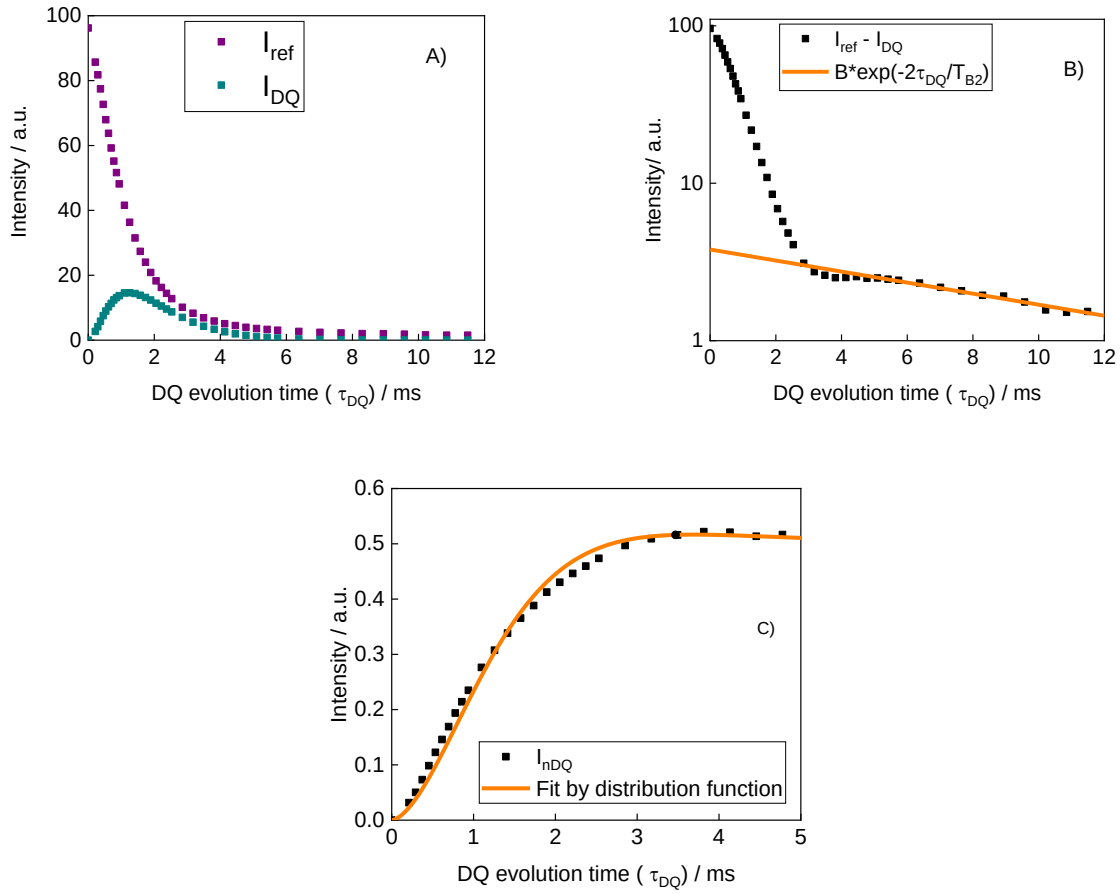

FIGURE S3. 4 A) RAW BUILD-UP (I_{DQ}) AND REFERENCE DECAY (I_{ref}) CURVES, B) THE DIFFERENCE OF I_{ref} - I_{DQ}, AND C) THE SUBTRACTED AND NORMALIZED BUILD-UP (I_{nDQ}) AS A FUNCTION OF DOUBLE QUANTUM EVOLUTION TIME (τ_{DQ}) OF SBR_UC.

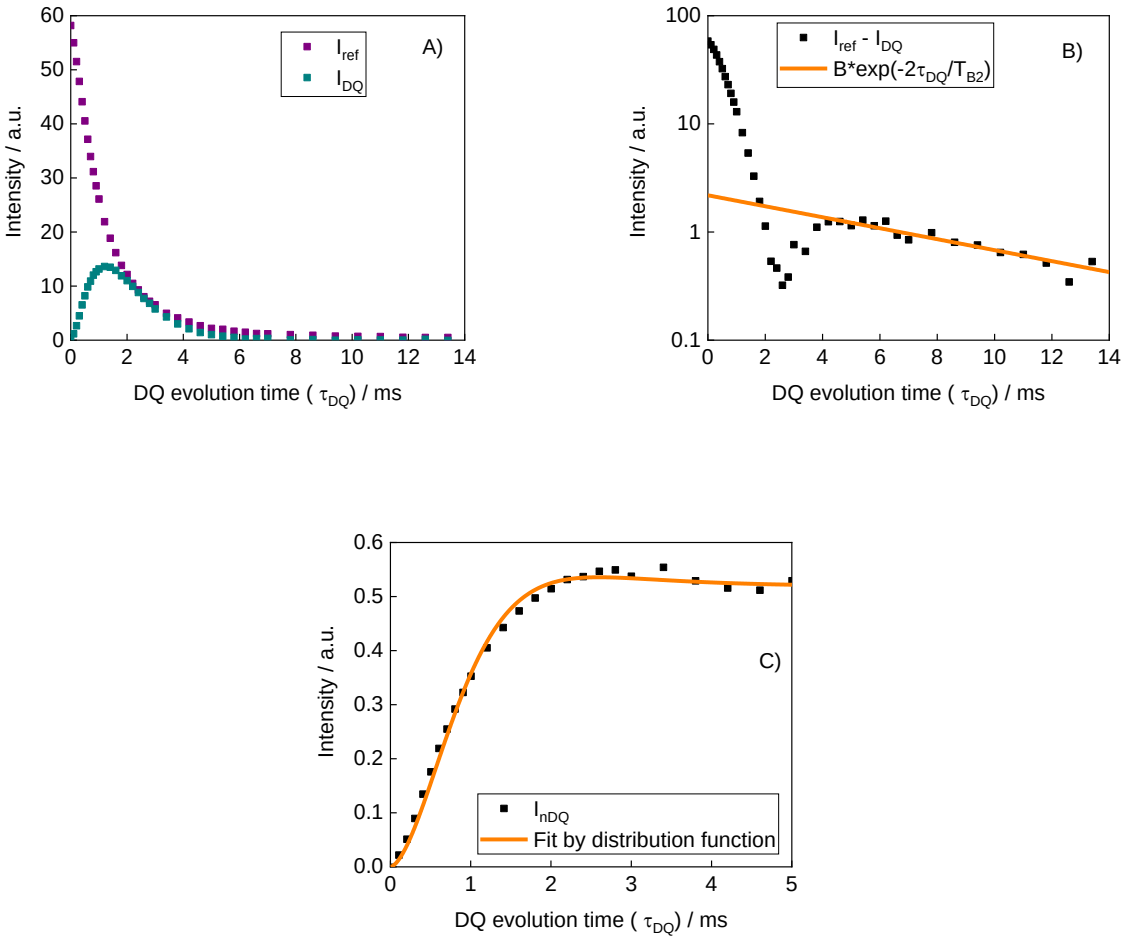

FIGURE S3. 5 A) RAW BUILD-UP (I_{DQ}) AND REFERENCE DECAY (I_{ref}) CURVES, B) THE DIFFERENCE OF I_{ref} - I_{DQ}, AND C) THE SUBSTRACTED AND NORMALIZED BUILD-UP (I_{nDQ}) AS A FUNCTION OF DOUBLE QUANTUM EVOLUTION TIME (τ_{DQ}) OF SBR_SC.

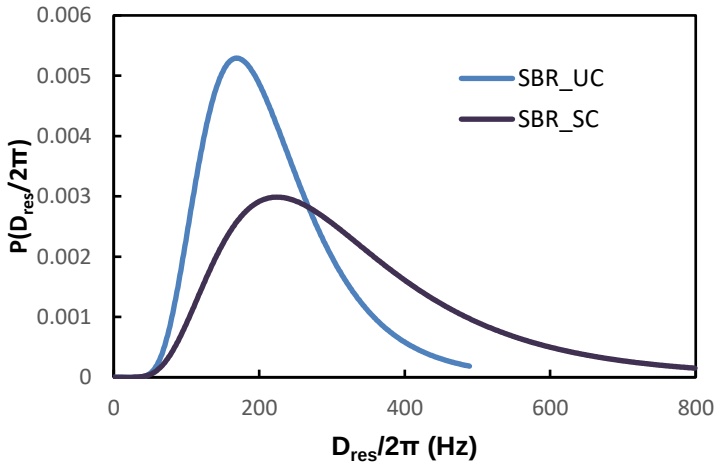

FIGURE S3. 6 THE CORRESPONDING DISTRIBUTIONS OF SBR_UC AND SBR_SC.

Influence of swelling experiment on viscolesatic behavior of SBR_SC

As shown in Figure S3. 7 the viscoelastic behavior of SBR_SC after performing swelling experiment remains same as prior to its swelling.

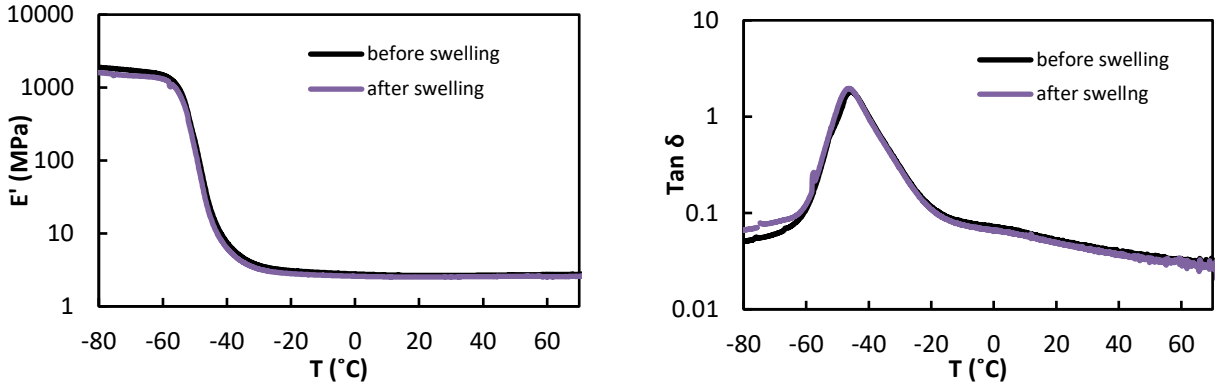

FIGURE S3. 7 STORAGE MODULUS E' (LEFT) AND LOSS FACTOR Tan δ (RIGHT) VERSUS TEMPERATURE OF SBR_SC BEFORE AND AFTER PERFORMING SWELLING EXPERIMENT.

3.5 References

(1) Cerveny, S.; Bergman, R.; Schwartz, G. A.; Jacobsson, P. Dielectric α- and β-Relaxations in Uncured Styrene Butadiene Rubber. *Macromolecules* **2002**, *35* (11), 4337–4342. https://doi.org/10.1021/ma010990o.

(2) Hofmann, A.; Alegría, A.; Colmenero, J.; Willner, L.; Buscaglia, E.; Hadjichristidis, N. Secondary and Segmental Relaxation in Polybutadienes of Varying Microstructure: Dielectric Relaxation Results. *Macromolecules* **1996**, *29* (1), 129–134. https://doi.org/10.1021/ma946419p.

(3) Jurkowski, B.; Olkhov, Y. A.; Jurkowska, B.; Menge, H. Comparative TMA and NMR Investigation of a Structure of Carbon-Black-Free Cured Butadiene Rubber. *Polymer Testing* **2002**, *21* (5), 597–606. https://doi.org/10.1016/S0142-9418(01)00130-1.

(4) Mansilla, M. A.; Garraza, A. L. R.; Silva, L.; Salgueiro, W.; Macchi, C.; Marzocca, A. J.; Somoza, A. Evolution of the Free Volume and Glass Transition Temperature with the Degree of Cure of Polybutadiene Rubbers. *Polymer Testing* **2013**, *32* (4), 686–690. https://doi.org/10.1016/j.polymertesting.2013.03.001.

(5) Bandzierz, K.; Reuvekamp, L.; Dryzek, J.; Dierkes, W.; Blume, A.; Bielinski, D. Influence of Network Structure on Glass Transition Temperature of Elastomers. *Materials* **2016**, *9* (7). https://doi.org/10.3390/ma9070607.

(6) Wang, Y.-Q.; Wang, Y.; Zhang, H.-F.; Zhang, L.-Q. A Novel Approach to Prepare a Gradient Polymer with a Wide Damping Temperature Range by In-Situ Chemical Modification of Rubber During Vulcanization. *Macromolecular Rapid Communications* **2006**, *27* (14), 1162–1167. https://doi.org/10.1002/marc.200600106.

(7) Kruger, F. W. H.; McGill, W. J. A DSC Study of Curative Interactions. I. The Interaction of ZnO, Sulfur, and Stearic Acid. *Journal of Applied Polymer Science* **1991**, *42* (10), 2643–2649. https://doi.org/10.1002/app.1991.070421002.

(8) Jurkowski, B.; Olkhov, Y. A.; Jurkowska, B.; Menge, H. Comparative TMA and NMR Investigation of a Structure of Carbon-Black-Free Cured Butadiene Rubber. *Polymer Testing* **2002**, *21* (5), 597–606. https://doi.org/10.1016/S0142-9418(01)00130-1.

(9) Litvinov, V. M.; Dias, A. A. Analysis of Network Structure of UV-Cured Acrylates by 1H NMR Relaxation, 13C NMR Spectroscopy, and Dynamic Mechanical Experiments. *Macromolecules* **2001**, *34* (12), 4051–4060. https://doi.org/10.1021/ma010066u.

(10) Wu, B.; Chassé, W.; Peters, R.; Brooijmans, T.; Dias, A. A.; Heise, A.; Duxbury, C. J.; Kentgens, A. P. M.; Brougham, D. F.; Litvinov, V. M. Network Structure in Acrylate Systems: Effect of Junction Topology on Cross-Link Density and Macroscopic Gel Properties. *Macromolecules* **2016**, *49* (17), 6531–6540. https://doi.org/10.1021/acs.macromol.6b01070.

(11) Saleesung, T.; Reichert, D.; Saalwächter, K.; Sirisinha, C. Correlation of Crosslink Densities Using Solid State NMR and Conventional Techniques in Peroxide-Crosslinked EPDM Rubber. *Polymer* **2015**, *56*, 309–317. https://doi.org/10.1016/j.polymer.2014.10.057.

(12) Dibbanti, M. K.; Mauri, M.; Mauri, L.; Medaglia, G.; Simonutti, R. Probing Small Network Differences in Sulfur-Cured Rubber Compounds by Combining Nuclear Magnetic Resonance and Swelling Methods. *Journal of Applied Polymer Science* **2015**, *132* (43). https://doi.org/10.1002/app.42700.

(13) Curro, J. G.; Pincus, P. A Theoretical Basis for Viscoelastic Relaxation of Elastomers in the Long-Time Limit. *Macromolecules* **1983**, *16* (4), 559–562.

(14) Curro, J. G.; Pearson, D. S.; Helfand, E. Viscoelasticity of Randomly Crosslinked Polymer Networks. Relaxation of Dangling Chains. *Macromolecules* **1985**, *18* (6), 1157–1162.

(15) Souillard, C.; Cavaillé, J.-Y.; Chazeau, L.; Schach, R. Dynamic Mechanical Relaxation of Cross-Linked Styrene-Butadiene Polymers Containing Free Chains: Possibility of Reptation. *Polymer* **2014**, *55* (20), 5218–5225. https://doi.org/10.1016/j.polymer.2014.08.016.

(16) Guth, E. Theory of Filler Reinforcement. *Rubber Chemistry and Technology* **1945**, *18* (3), 596–604. https://doi.org/10.5254/1.3546754.

(17) Wolff, S.; Donnet, J.-B. Characterization of Fillers in Vulcanizates According to the Einstein-Guth-Gold Equation. *Rubber Chemistry and Technology* **1990**, *63* (1), 32–45. https://doi.org/10.5254/1.3538240.

(18) Gambino, T.; Shafqat, N.; Alegría, A.; Malicki, N.; Dronet, S.; Radulescu, A.; Nemkovski, K.; Arbe, A.; Colmenero, J. Concentration Fluctuations and Nanosegregation in a Simplified Industrial Blend with Large Dynamic Asymmetry. *Macromolecules* **2020**, *53* (16), 7150–7160. https://doi.org/10.1021/acs.macromol.0c01376.

(19) Hansen, C. M. *Hansen Solubility Parameters: A User's Handbook, Second Edition*; CRC Press, 2007.

(20) Hansen, S. A. C. M. *Hansen Solubility Parameters in Practice*; Hansen-Solubility.

(21) Milliman, H. W.; Boris, D.; Schiraldi, D. A. Experimental Determination of Hansen Solubility Parameters for Select POSS and Polymer Compounds as a Guide to POSS–Polymer Interaction Potentials. *Macromolecules* **2012**, *45* (4), 1931–1936. https://doi.org/10.1021/ma202685j.

4 Study of the SBR/R2 or R3 resin blends

In this chapter, we first study the influence of the presence of R2 and R3 resins (resins described in Chapter 2) on the crosslinking reactions, with sulfur or peroxide curing systems. We then evaluate how the glass transition temperature is modified as well as the viscoelastic behavior. The discussion is then completed by a morphological analysis of the blends.

Contents

4.1 Formulation of the blends

The compound formulations of SBR_R2 and SBR_R3 blends with different curing systems used in this study have been presented in chapter 2. Both resin blends have similar resin content in their uncured (UC), peroxide cured (PC), and sulfur cured (SC) state. Therefore, only formulations of SBR_R2 blends with different curing systems are recalled in Table 4. 1. The processing of these resin blends was described in chapter 2.

TABLE 4. 1 COMPOUND FORMULATION OF SBR AND RESIN R2 WITH DIFFERENT CURING SYSTEMS.

Sample name	**Ingredients (phr)**							
	SBR	**Resin (R2)**	**6PPD**	**Stearic acid**	**DCP**	**ZnO**	**S**	**CBS**
SBR_UC	100	-	1.5	3	-	-	-	-
SBR_R2_25_UC	100	33	1.5	3	-	-	-	-
SBR_R2_45_UC	100	83	1.5	3	-	-	-	-
SBR_PC	100	-	1.5	3	0.74	-	-	-
SBR_R2_25_PC	100	33	1.5	3	0.74	-	-	-
SBR_R2_45_PC	100	83	1.5	3	0.74	-	-	-
SBR_SC	100	-	1.5	3	-	1.45	1.4	1.6
SBR_R2_25_SC	100	33	1.5	3	-	1.45	1.4	1.6
SBR_R2_45_SC	100	83	1.5	3	-	1.45	1.4	1.6

* Note that 33 and 83 phr of resin corresponds to the 25 and 45 wt% of the blends.

4.2 Influence of the resins on the curing reaction

4.2.1 Chemical aspects

The DSC analysis presented in chapter 3 enabled to show the presence of crystallized stearic acid in SBR_UC and SBR_PC and the presence of zinc stearate complex in SBR_SC material. As shown on FIGURE 4. 1 a reversible peak around 30-40˚C is also observed on the DSC curve for the UC and PC resin R2 and R3 blends. The reversibility of this peak is shown for all samples in the supporting information section of this chapter (Figure S4. 1). One can however observe that the temperature domain of the peak is shifted toward lower temperature in the blends compared to the SBR, which indicates that the presence of the resin R2 or R3 perturbs the nucleation and growth of these crystallites: the stearic acid may be more dispersed, and the resin may promote more

cristallites nucleation. The decrease of the peak area is also related to the decrease of stearic acid content per gram of SBR in the blend formulations.

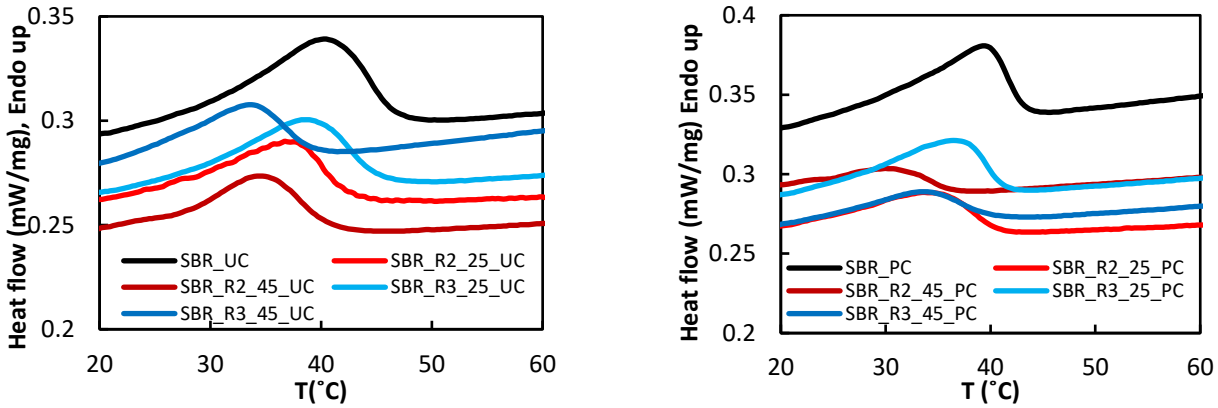

FIGURE 4. 1 DSC HEAT FLOW CURVES (2ND HEATING) VERSUS TEMPERATURE (T) OF SBR_UC AND ITS BLENDS WITH R2 & R3 (LEFT), AND SBR_PC AND ITS BLENDS WITH R2 & R3 (RIGHT).

Moreover, in the SC cured blend, like in SBR_SC, there is no such peak at 40°C: all the stearic acid reacted with ZnO to form a zinc stearate complex, and a peak related to this complex is also found at around 100-110˚C (cf. Figure 4. 2). Like for SBR_SC material, we observed difference between the DSC curves obtained during a 1st and 2nd heating cycle, that we ascribed to the different thermal history of samples (additional experiments would be necessary to confirm it).

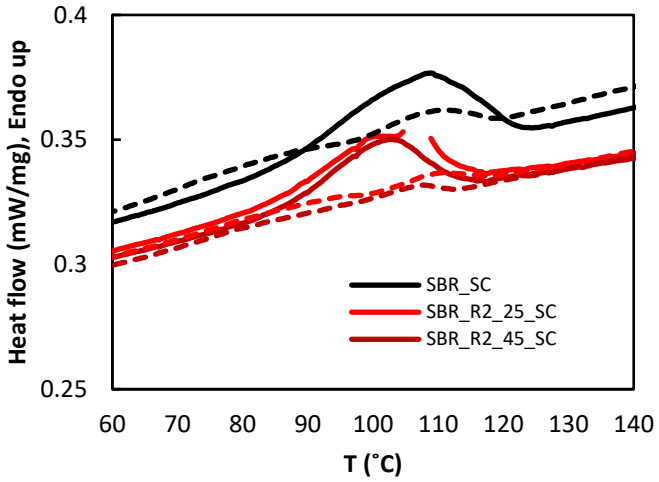

FIGURE 4. 2 DSC HEAT FLOW CURVES OF SBR_R2_SC BLENDS AT HIGHER TEMPERATURES (SOLID LINES 1ST HEATING AND DASHED LINES 2ND HEATING).

The presence of zinc stearate complex in the crystallites form, like previously seen in the SBR_SC, is also confirmed by TEM observations in SBR_R2_SC and SBR_R3_SC samples as shown in Figure 4. 3.

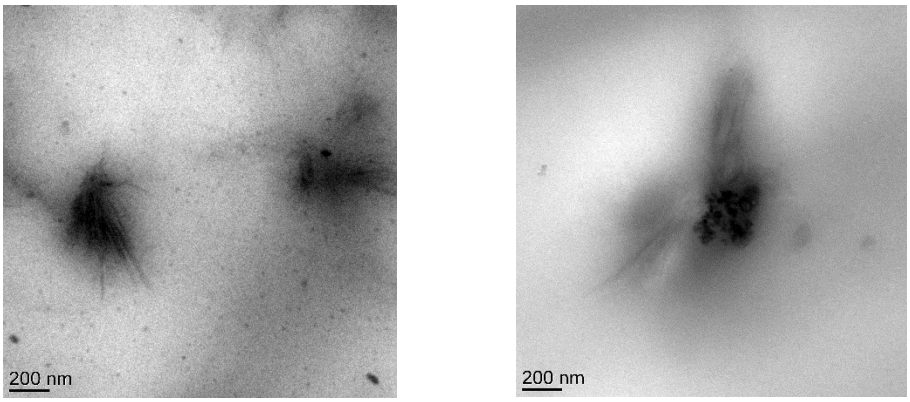

FIGURE 4. 3 TEM IMAGE OF MICROTOMED SBR_R2_25_SC (LEFT) AND SBR_R3_25_SC (RIGHT).

The amount of soluble fraction, deduced from swelling experiment in cyclohexane (cf. chapter 2), is reported in Figure 4. 4 and compared to the resin fraction for the SC materials. The soluble fraction of SBR_SC alone is around 3.5% and should correspond to the curing by- and unreacted products. The soluble fraction of the resin blends is very slightly above - around 2%, which corresponds to the soluble fraction without resin - the amount of resins initially added in the SBR. This indicates that most of the resin can be extracted from the material, and suggests, like the previous experiments, that the chemical crosslinking reactions involves very little the resins.

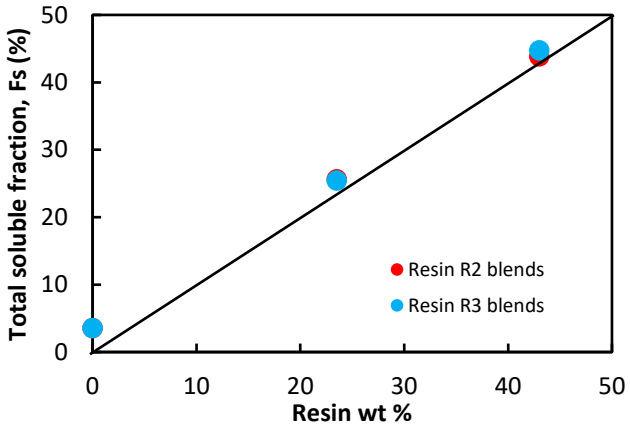

FIGURE 4. 4 TOTAL SOLUBLE FRACTION (IN CYCLOHEXANE) VERSUS THE RESIN WEIGHT FRACTION IN SBR_R2_SC AND SBR_R3_SC BLENDS.

Like in absence of resin (cf. chapter 3), the crosslinking reaction leads to a shift of the blends T_α towards higher temperatures as shown in Figure 4. 5 . The shift is significant with R2 and comparable to the one found without resin (around +5°C). It is lower with resin R3, around 3˚C for 25% resin content and in the uncertainty domain, 1°C, for 45% resin content. DSC and DMA curves with sulfur crosslinked blends from which the resin have been extracted confirm the existence of a shift (cf. Figure S4. 2). On Figure 4. 5, this one is very comparable for Peroxide curing and Sulfur curing for R2 blends, when the shift by the peroxide curing was lower in absence

of resin. In any case, same explanations can be given for a slight shift toward larger temperature: the most common one, usual in literature, is a reduction of the polymer chains mobility; nevertheless, given the low number of crosslinks, this may also be caused by additional significant modifications of the polymer chains backbone.

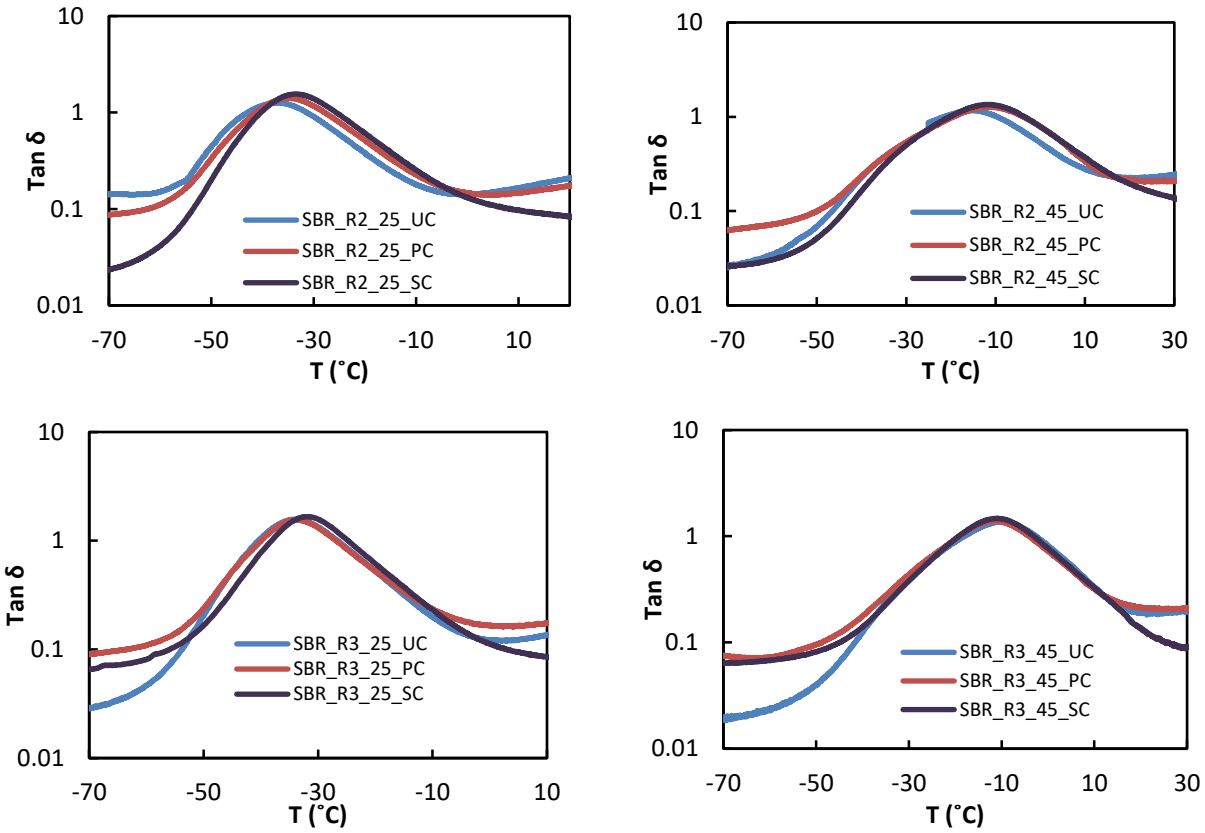

FIGURE 4. 5 DMA LOSS FACTOR (*Tan δ*) VERSUS TEMPERATURE (T) OF UC, PC, AND SC SBR_R2 BLENDS (TOP) AND SBR_R3 BLENDS (BELOW).

4.2.2 Influence on the swelling behavior

The previous paragraph suggests that the chemical reactions involved during the crosslinking process are not significantly influenced by the resin presence. They however create crosslinks on a polymer which is swollen by the resin (or at least by a fraction of the resin), i.e. on a polymer whose conformations are perturbed and therefore influences the way chemical junction between them are formed. The swelling experiments, from which was previously estimated the sol fraction, have been used to estimate the apparent crosslinks density of the crosslinked blends, from which the resin has been extracted (since it is solubilized in the cyclohexane). The estimated swollen volume ratio and the elastically active chain (EAC) density deduced from the Flory-Rhener equation are shown in Figure 4. 6.

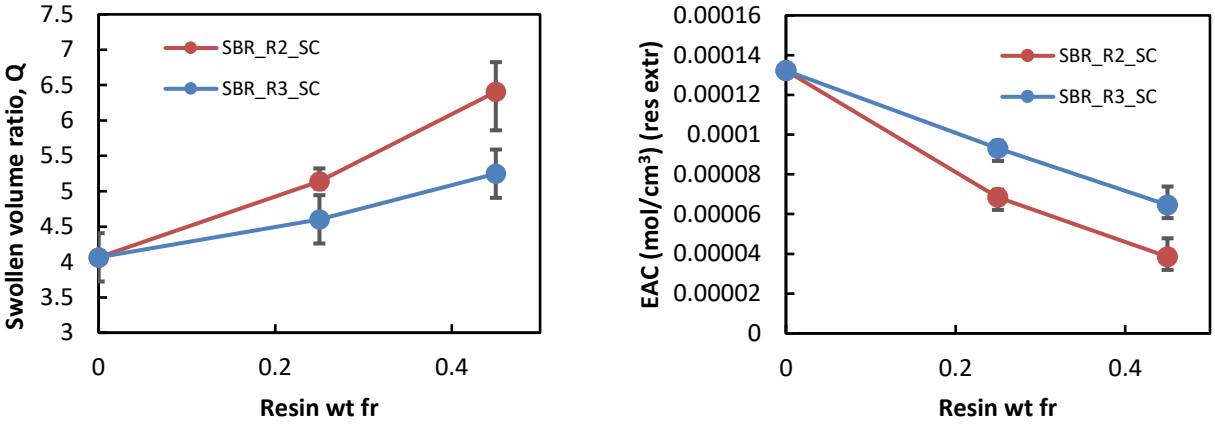

FIGURE 4. 6 SWELLING VOLUME RATIO VERSUS RESIN AMOUNT (LEFT) AND EAC DENSITY VERSUS RESIN AMOUNT (RIGHT) IN SBR_R2_SC AND SBR_R3_SC BLENDS.

The swollen volume ratio strongly increases with the resin amount, this is expected since the crosslinking reactions occur in a swollen sample. This leads to a lower number of entanglements trapped by the crosslinks, and therefore to an easier swelling of the material in cyclohexane. As can be seen in Figure 4. 7, tensile experiments performed on the resin extracted samples also confirm the results: the increase in the resin content leads to a decrease of the stress level for a given strain.

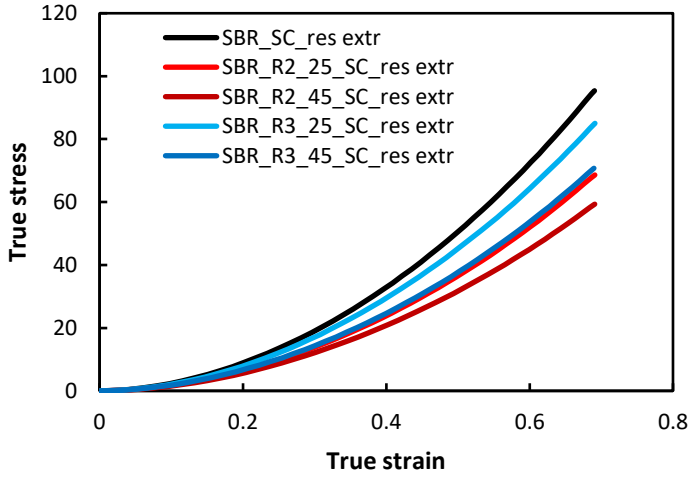

FIGURE 4. 7 TRUE STRESS AND TRUE STRAIN OF SBR_R2_SC_RES EXTR AND SBR_R3_SC_RES EXTR SAMPLES.

More interestingly, one can also notice a larger swelling ratio for the R2 resin. Two explanation can be proposed for this result:

- this result seems to contradict the previous comment on the absence of influence of the resin on the crosslinking reactions; due to their very low molecular weight, even though some resin molecules are involved in these reactions, it can hardly be detected by measurement of the still

soluble resin. Indeed, considering that half of the crosslinks in the SBR_SC ($1.3*10^{-4}$ mol/cm^3) are chemical crosslinks, given the molecular weight of the resin ca. 1500g/mol, considering that all the chemical crosslinks link one polymer chain and one resin molecule, this would involve 0.098 g of resin in a blend of 1g of SBR with 0.88g of resin (corresponding to a 45 wt% resin blend): this represents only 1/9 of all the resins introduced in the sample. These assumptions being largely exaggerated, the participation of few resin molecules to the crosslinking reaction is therefore possible. Within this assumption, R2 molecules react more easily during the crosslinking reactions than R3 molecules.

- or the conformation of the polymer chains before crosslinking is different in presence of R2 and R3. Therefore, because they are introduced in the same quantity, this would mean that the R3 resin is slightly less miscible with the SBR chains, leading to few resin-rich domains in the uncrosslinked blend, and therefore a decrease in the swelling ratio of the main fraction of the polymer chain in this blend. This would increase the number of entanglements which can be trapped by the crosslinking. This explanation actually assumes a better interaction parameter between the SBR chains and the R2 resin at the temperature at which the materials are crosslinked (150°C for 40 minutes) which was actually the opposite of what was previously observed in chapter 3 with solubility parameters estimation.

4.3 Influence of resins on the glass transition

The DSC heat flow curves for SBR_R2 and SBR_R3 blends with different curing systems are shown in Figure 4. 8 and Figure 4. 9 respectively.

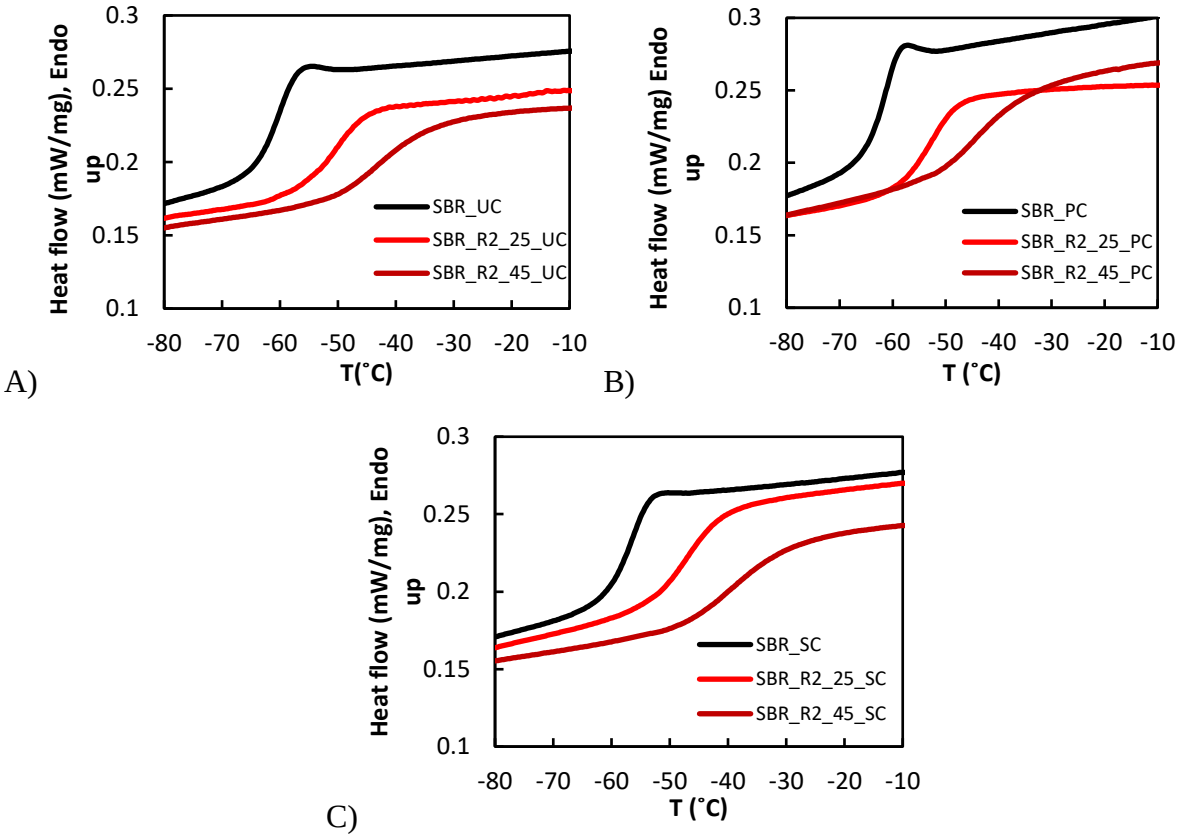

FIGURE 4. 8 DSC HEAT FLOW CURVES (2ND HEATING) VERSUS TEMPERATURE (T) OF: A) SBR_R2_UC, B) SBR_R2_PC AND C) SBR_R2_SC BLENDS.

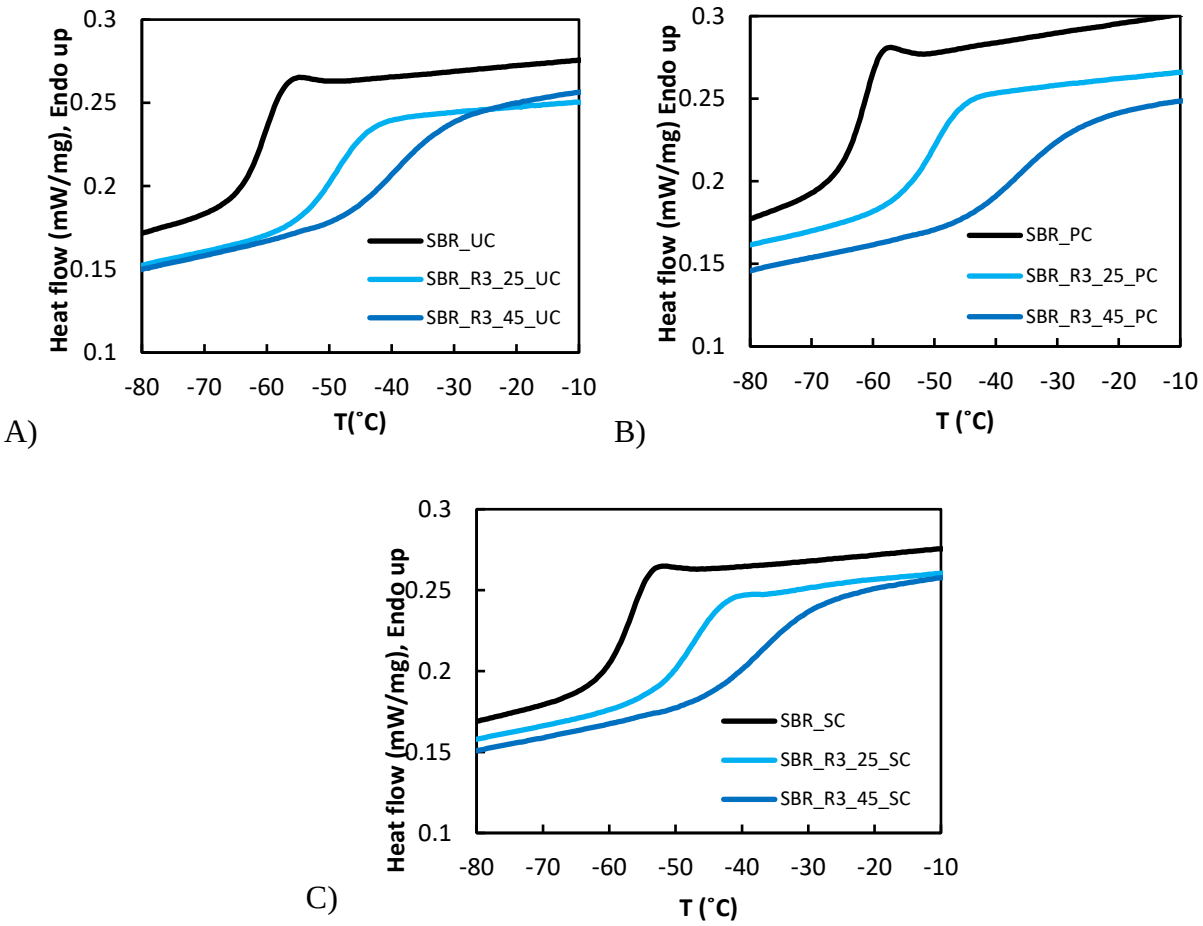

FIGURE 4. 9 DSC HEAT FLOW CURVES (2ND HEATING) VERSUS TEMPERATURE (T) OF: A) SBR_R3_UC, B) SBR_R3_PC AND C) SBR_R3_SC BLENDS.

A single glass transition is observed in all the blends, which suggests a good miscibility of the resin. One also observes a broadening of this transition and a shift toward higher temperature with the increase of the resin amount. Different T_g can be defined at the onset (T_{g1}), midpoint (T_g), and endpoint (T_{g2}) as previously described in chapter 2. These T_g can be compared to the classical fox law:

$$\frac{1}{T_g} = \frac{w_{SBR}}{T_{g\,SBR}} + \frac{w_{Resin}}{T_{g\,Resin}} \tag{4.1}$$

Where w_{SBR} and w_{Resin} are the weight fractions of SBR and resin, respectively and T_g, $T_{g\,SBR}$ and $T_{g\,Resin}$ are the glass transition temperatures of the blend, of SBR and of the resin, respectively.

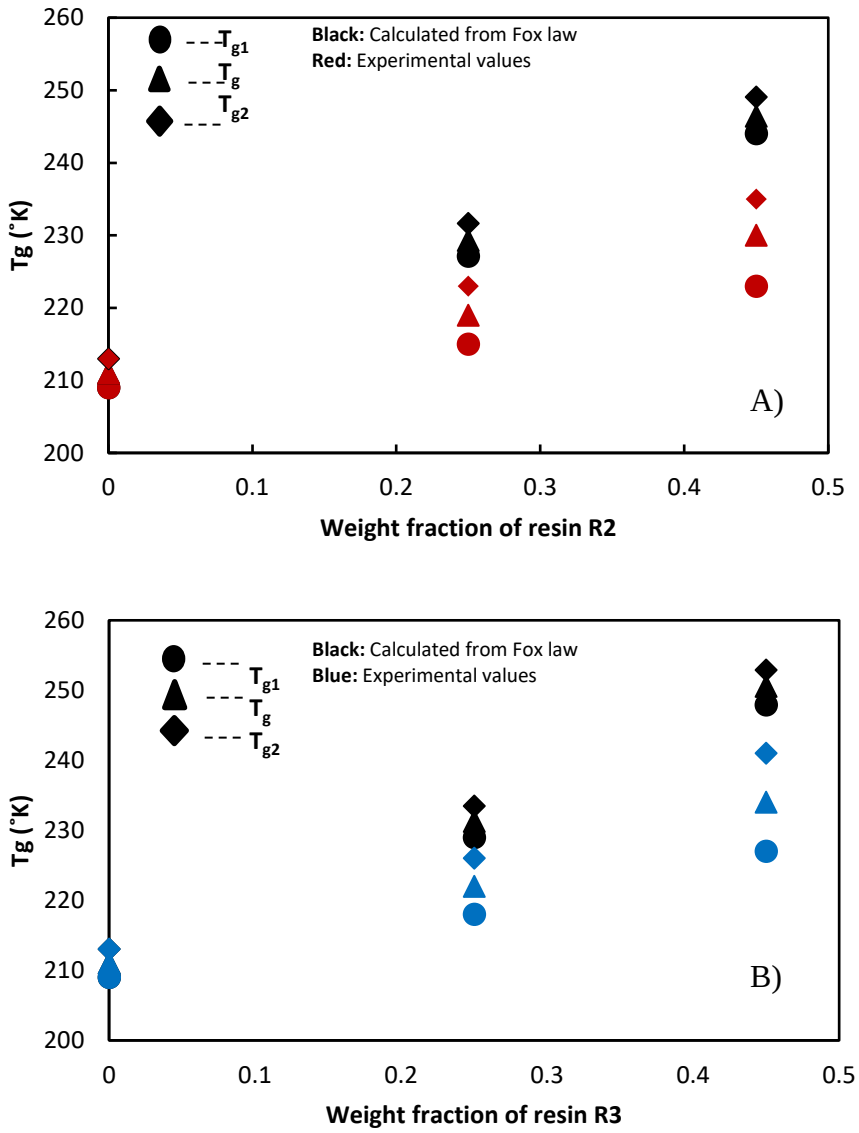

FIGURE 4. 10 EXPERIMENTAL T_g FROM DSC AND CALCULATED FROM FOX LAW VERSUS TOTAL RESIN AMOUNT IN A) SBR_R2_UC AND B) SBR_R3_UC BLENDS.

As shown in Figure 4. 10, the Fox law predicts higher T_g in both R2 and R3 resin blends compared to the experimental one, whether the T_g is taken at the onset, the midpoint or the end temperature of the transition. A same disagreement is found when comparing the Fox law prediction and the experimental T_g of the PC and SC blends (as shown in Figure S4. 3 and Figure S4. 4, respectively, in supporting information section of this chapter). These results and the large broadening of the glass transition is ascribed to the presence of concentration fluctuations in the miscible blends. [1] [2] [3] [4] [5] . The broadening of the T_g is slightly more important for the R3 resin than for the R2 one. Nevertheless, the gap between the predicted and experimental T_g at midpoint is the same for both

resins (16°C for 45 wt% resin blend) and the uncertainty in the measurement of the T_g is around $\pm 1^{\circ}C$. Thus, it is difficult to conclude from these results on the hypothetical weaker miscibility of the R3 resin evoked in the previous section (note in addition that this assumption is made for the curing temperature, much higher than the temperature range of the glass transitions).

Other models have also been proposed to predict the T_g of mixtures based on the properties of the mixture components. The equation proposed by Couchman and Karasz [6] is based on the assumption that the glass transition is the thermodynamic phenomenon and therefore this model weights on the change in the heat capacity (ΔC_p) instead change in volume at the glass transition:

$$ln\ T_{g\ CK} = \frac{\Delta C_{p\ SBR} w_{SBR}\ ln\ T_{g\ SBR} + \Delta C_{p\ Resin} w_{Resin}\ ln\ T_{g\ Resin}}{\Delta C_{p\ SBR} w_{SBR} + \Delta C_{p\ Resin} W_{Resin}} \quad (4.2)$$

The T_g predicted from different models and the experimental values of R2 and R3 blends are presented in Figure 4. 11 The error bar in T_g predicted from Couchman eq. are due to the uncertainty in the ΔC_p measurement (ΔC_p measurement using Pyris software are described in chapter2).

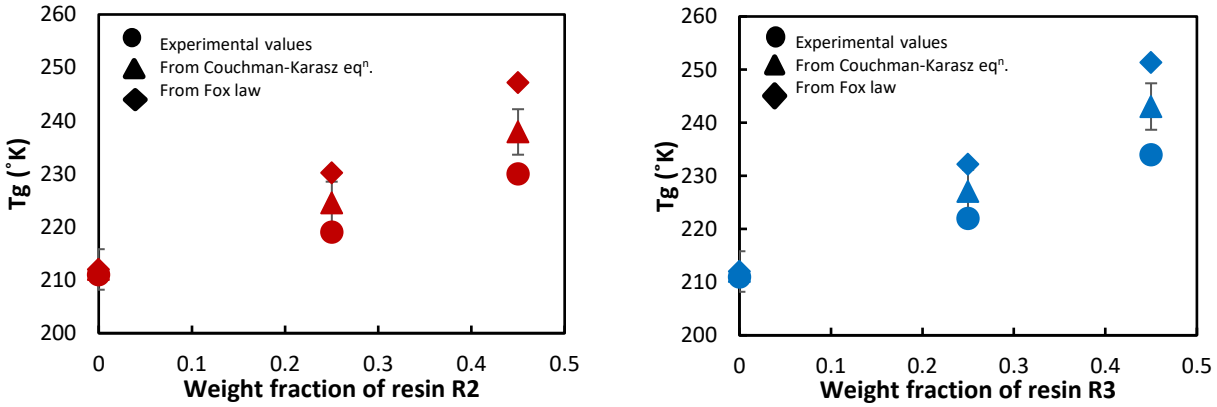

FIGURE 4. 11 EXPERIMENTAL MID POINT T_g FROM DSC AND CALCULATED FROM DIFFERENT MODELS VERSUS TOTAL RESIN AMOUNT IN SBR_R2_SC (LEFT) AND SBR_R3_SC BLENDS (RIGHT).

The Couchman and Karasz equation predicts the T_g of blends better than the Fox law, however still fails. Actually, this better prediction from C-K is because it takes into account that $\Delta C_{pSBR} \neq \Delta C_{pResin}$, conversely to the Fox law where ΔC_p at the glass transition are assumed equal. Also Fox law is generally applicable when interactions are negligible and the T_{g2}/T_{g1} is not far from unity. In our case the ratio of T_{gResin}/T_{gSBR} (~1.5) is more than unit. [7 8 9]

4.4 Influence of the resins on the viscoelastic behavior

4.4.1 Uncrosslinked blend

The viscoelastic behavior of all the cured and uncured SBR, SBR_R2, and SBR_R3 blends was characterized by DMA. In case of the UC samples, due to their very low modulus at temperature above 30°C - modulus which are out of the measurable range for this apparatus - rheology measurements have been performed for this temperature domain. On Figure 4. 12, the broadening and shift toward higher temperature of the α-relaxation by the addition of resin R2 and R3 confirm the previous DSC results.

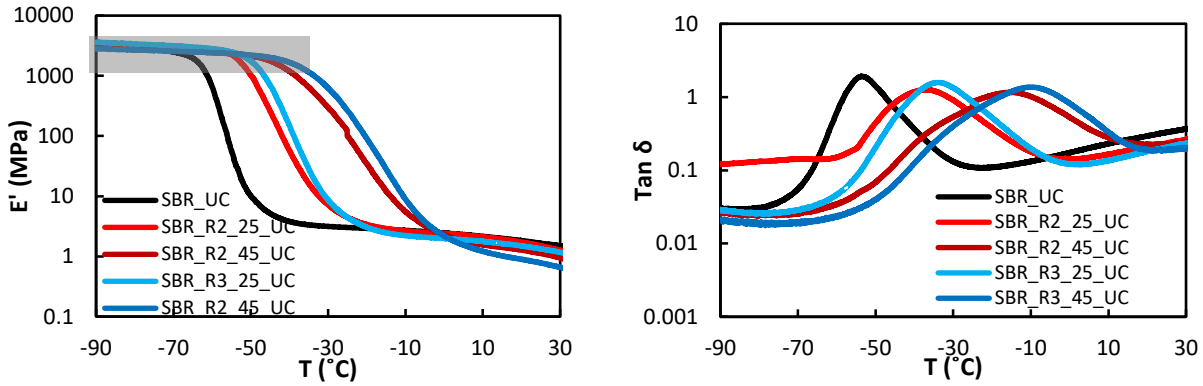

FIGURE 4. 12 DMA STORAGE MODULUS (E') AND LOSS FACTOR ($Tan\ \delta$) VERSUS TEMPERATURE (T) OF SBR_UC, SBR_R2_UC, AND SBR_R3_UC BLENDS.

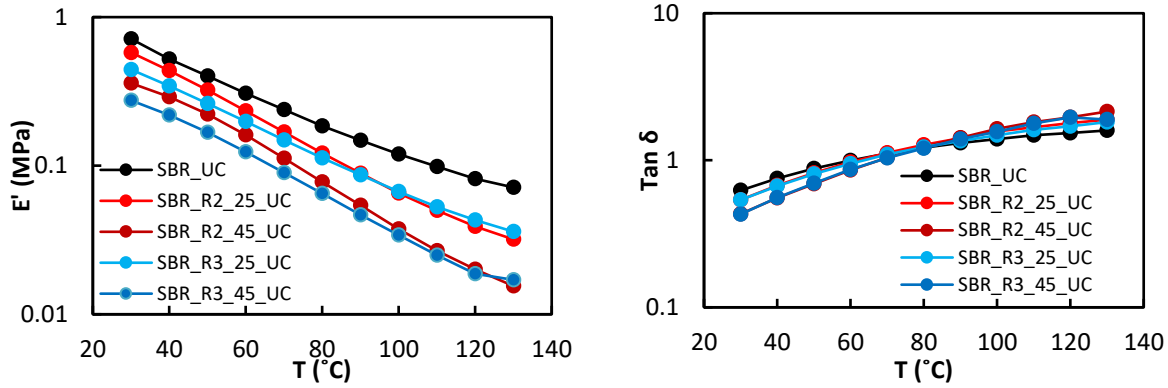

FIGURE 4. 13 STORAGE MODULUS (E') AND LOSS FACTOR ($Tan\ \delta$) FROM RHEOMETER VERSUS TEMPERATURE (T) OF SBR_UC, SBR_R2_UC, AND SBR_R3_UC BLENDS.

In the previous section, we applied the Fox law to try to predict the T_g of the blends measured by DSC. Like Class et al. did in reference [10] we can also use it to estimate their T_α : to do so, their T_g in the Fox law equation are replaced by their T_α and given the relatively narrow temperature domain of the glass transition of the resin (compared to that of the blends), we assume that the resins T_g and T_α are roughly equal. With these assumptions, Figure 4. 14 show that the Fox law gives much

better prediction (for DMA than DSC) for both resin blends, suggesting that this equation should actually rather be used with T_α (when the resin volume fraction is not too large, since a disagreement between the experimental and calculated values increase with the resin content and reaches few °C for 45 wt.% of resin).

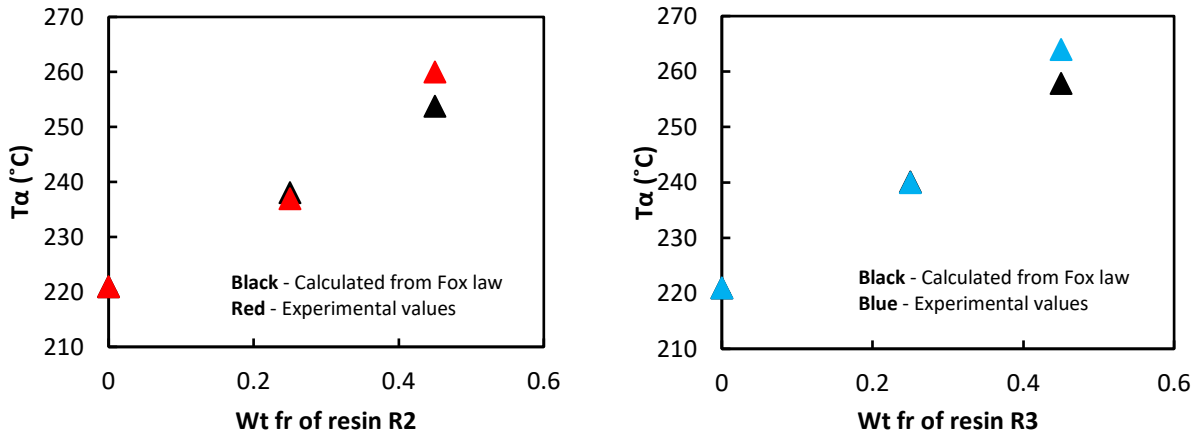

FIGURE 4. 14 EXPERIMENTAL T_α FROM DMA AND CALCULATED FROM FOX LAW VERSUS TOTAL RESIN AMOUNT IN SBR_R2_UC (LEFT) AND SBR_R3_UC (RIGHT) BLENDS.

As shown by the rheology curves (cf. Figure 4. 13), at high temperature, above 100°C, the elastic modulus is not influenced by the nature of the resin. Differences appear when the temperature decreases: the modulus of the SBR_R2_UC blends becomes higher than the one of the SBR_R3_UC blend. This is confirmed by DMA measurements, which show after the main relaxation, moduli higher for the resin R2.

To go further, we can compare the modulus of the uncrosslinked blends with the scaling model developed by de Gennes [11] for estimating the modulus of diluted entangled polymers:

$$E'_{dilute} = \varphi^{\alpha} E'_{undilute} \tag{4.3}$$

Where E'_{dilute} is the modulus of the resin diluted polymer and $E'_{undiluted}$ is the modulus without resin, φ represents the volume fraction of SBR in the blends. As proposed in references [12] [13] the different moduli of this expression are measured either at the minimum of $Tan\ \delta$, after the main relaxation, or at the onset of the modulus plateau (which is roughly equivalent). The exponent value α from experiments in literature often lies between 2 and 2.3, whereas the theory proposed by De Gennes [14] predicts an exponent of 2.25 for a theta-solvent or athermal solvent. Figure 4. 15 and Figure 4. 16 present a log-log plot of E'_{dilute} of the UC blends as a function of φ, when the modulus is taken at the loss factor minimum $Tan\ \delta_{min}$, and when the modulus is measured at 120°C, respectively. The theoretical prediction with an exponent 2.25 is plotted on the same graphs.

The dilution law actually works quite well at 120°C for both resins, even though the experimental modulus is slightly lower than the predicted values (Figure 4. 16). The prediction is also quite correct for the R3 resin when using the modulus value at $Tan\ \delta_{min}$ (Figure 4. 15). This resin can therefore be considered as an athermal or theta solvent. Conversely, the exponent for the R2 resin is much lower than 2.3; the resin does not behave like a solvent in the plateau modulus region. This actually may be the consequence of its larger average molecular weight, around 1500g/mol (compared to 800g/mol for R3): its longest chains might indeed contribute to the entanglement density of the blend.

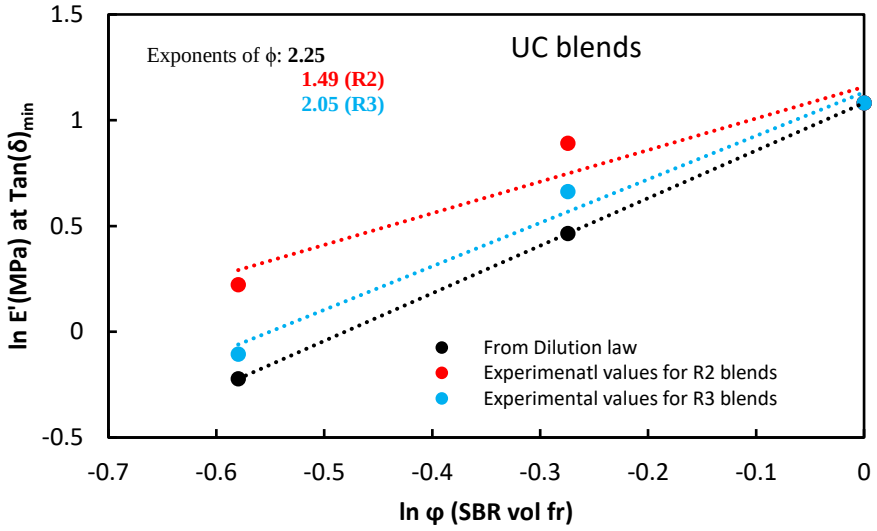

FIGURE 4. 15 LOGARITHM OF THE STORAGE MODULUS IN MPa MEASURED FROM DMA AT $Tan(\delta)_{min}$ AS A FUNCTION OF THE LOGARITHM OF THE SBR VOLUME FRACTION FOR UC R2 AND R3 BLENDS. COMPARISON WITH THE ESTIMATED VALUES FROM DILUTION LAW. DASHED LINES REPRESENT LINEAR FITS.

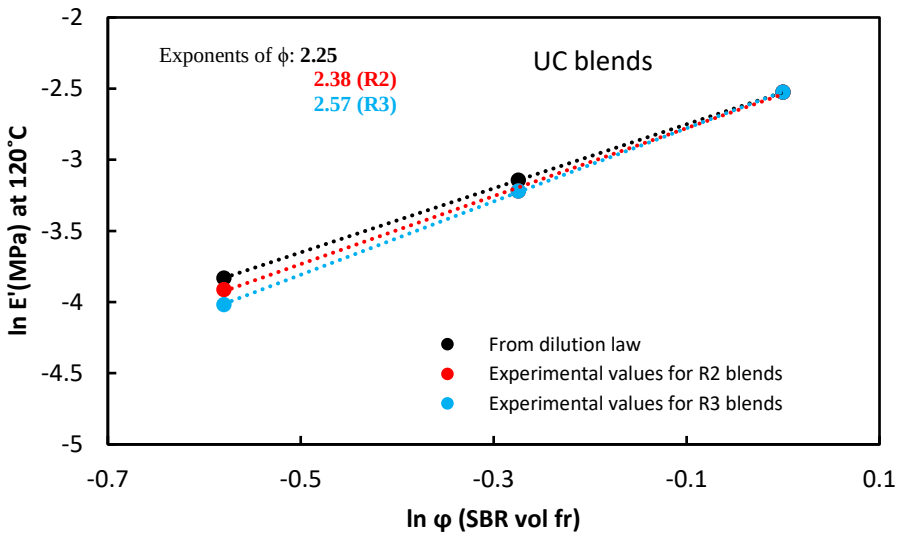

FIGURE 4. 16 LOGARITHM OF THE STORAGE MODULUS IN MPa MEASURED FROM RHEOMETER AT 120˚C AS A FUNCTION OF THE LOGARITHM OF THE SBR VOLUME FRACTION FOR UC R2 AND R3 BLENDS. COMPARISON WITH THE ESTIMATED VALUES FROM DILUTION LAW. DASHED LINES REPRESENT LINEAR FITS.

4.4.2 Crosslinked blends

Figure 4. 17 presents the DMA curves of the SBR_R2_PC blends. On Figure 4. 17 B) the DMA curves of the uncrosslinked samples have been reported for comparison. As already discussed above, the PC crosslinking is very limited which explains that it does not inhibit the relaxation observed at around 40°C. Its consequence should only be a decrease of the modulus drop, or even its stabilization above this temperature. Surprisingly the crosslinking process also decreases the modulus in this temperature domain. This result is also found for SC crosslinking, as shown on Figure 4. 18: the SC crosslinked blends have a lower modulus above T_α than the uncrosslinked ones, even though the crosslinking process increases the terminal modulus and creates sufficiently numerous crosslinks to observe a “nice” plateau on the E’ curves after the α relaxation.

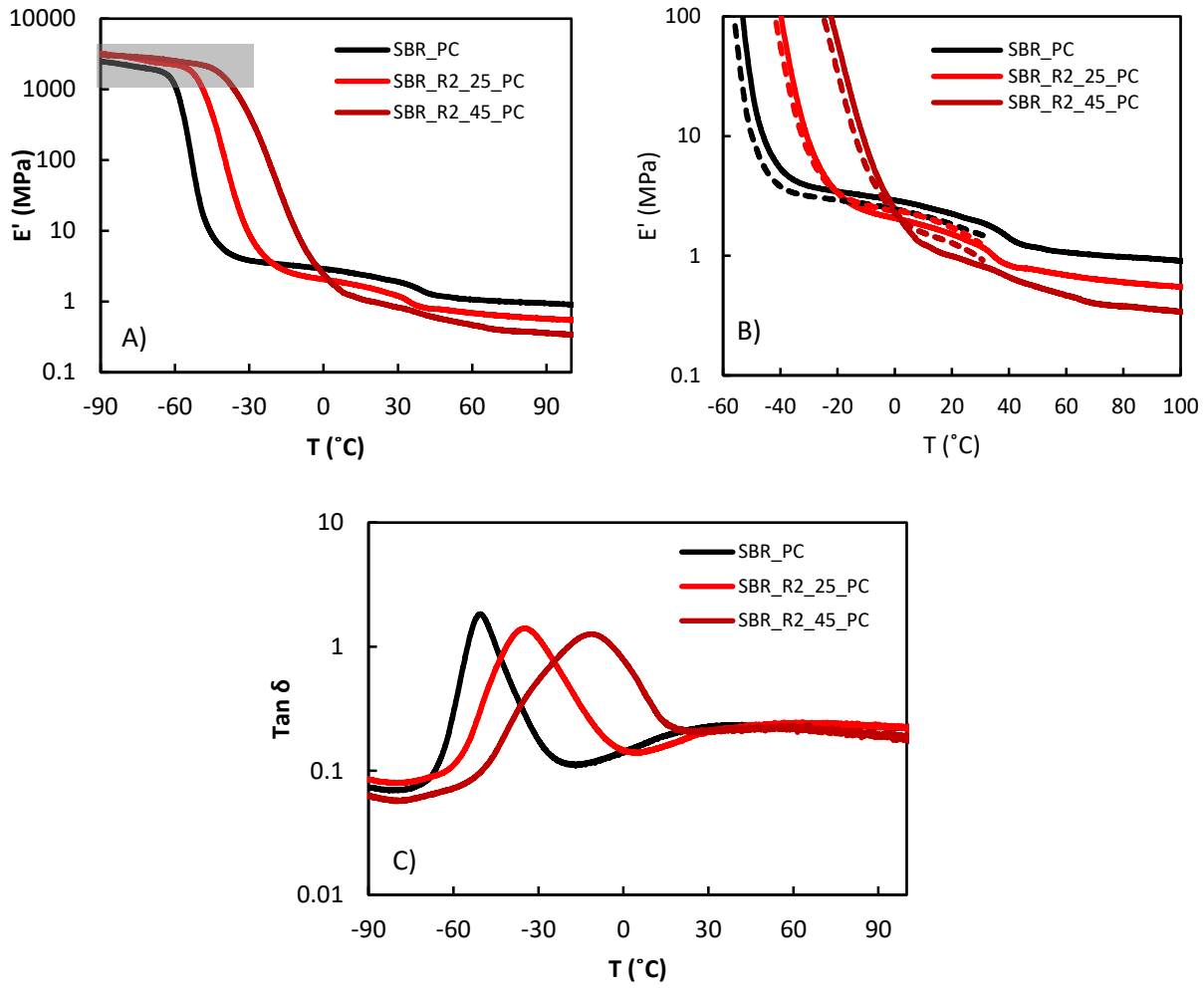

FIGURE 4. 17 A) DMA STORAGE MODULUS (E'), B) LOSS MODULUS (E'') AND C) LOSS FACTOR ($Tan\ \delta$) VERSUS TEMPERATURE (T) FOR THE SBR_R2_PC BLENDS. THE DOTTED CURVES ON FIGURE 4.17B ARE FOR THE SBR_R2_UC BLENDS

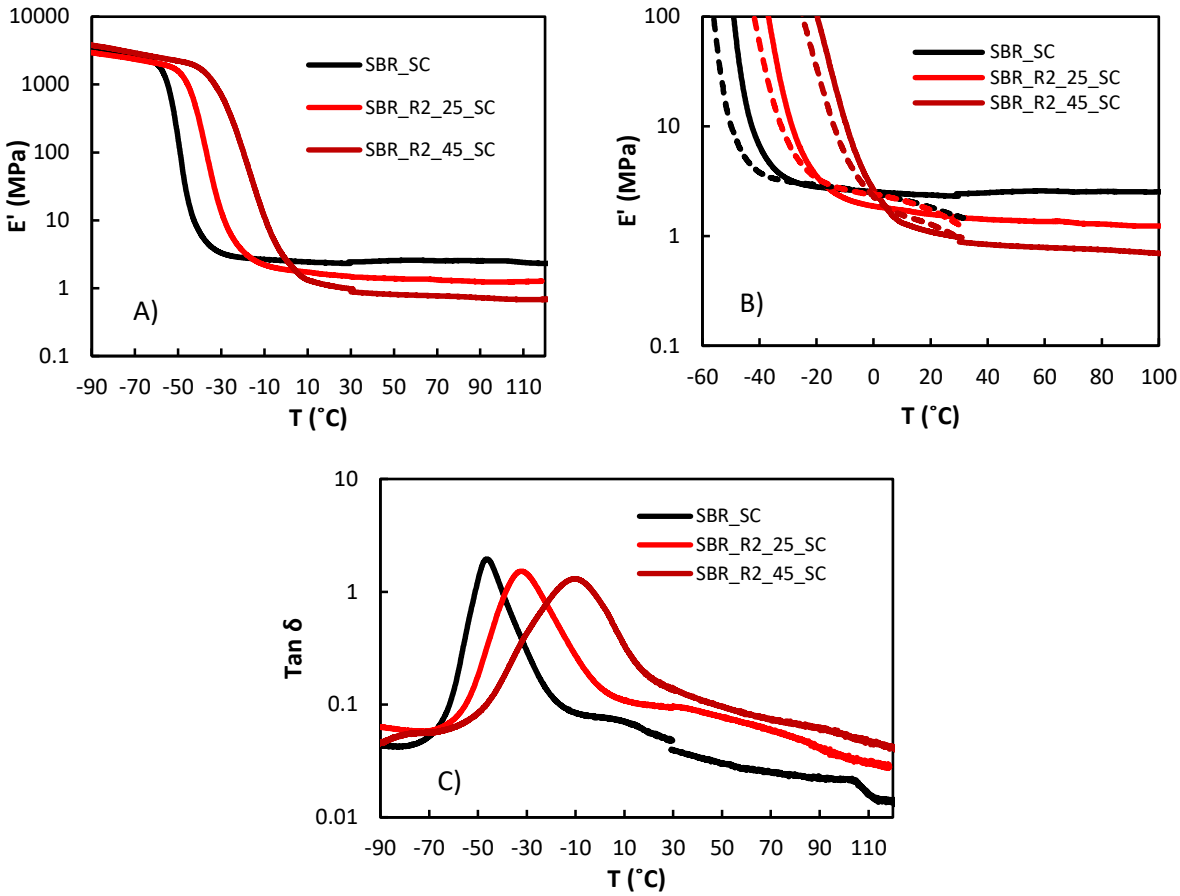

FIGURE 4. 18 A) DMA STORAGE MODULUS (E'), B) LOSS MODULUS (E'') AND C) LOSS FACTOR ($Tan\ \delta$) VERSUS TEMPERATURE (T) FOR THE SBR_R2_SC BLENDS. THE DOTTED CURVES ON FIGURE 4.18B ARE FOR THE SBR_R2_UC BLENDS

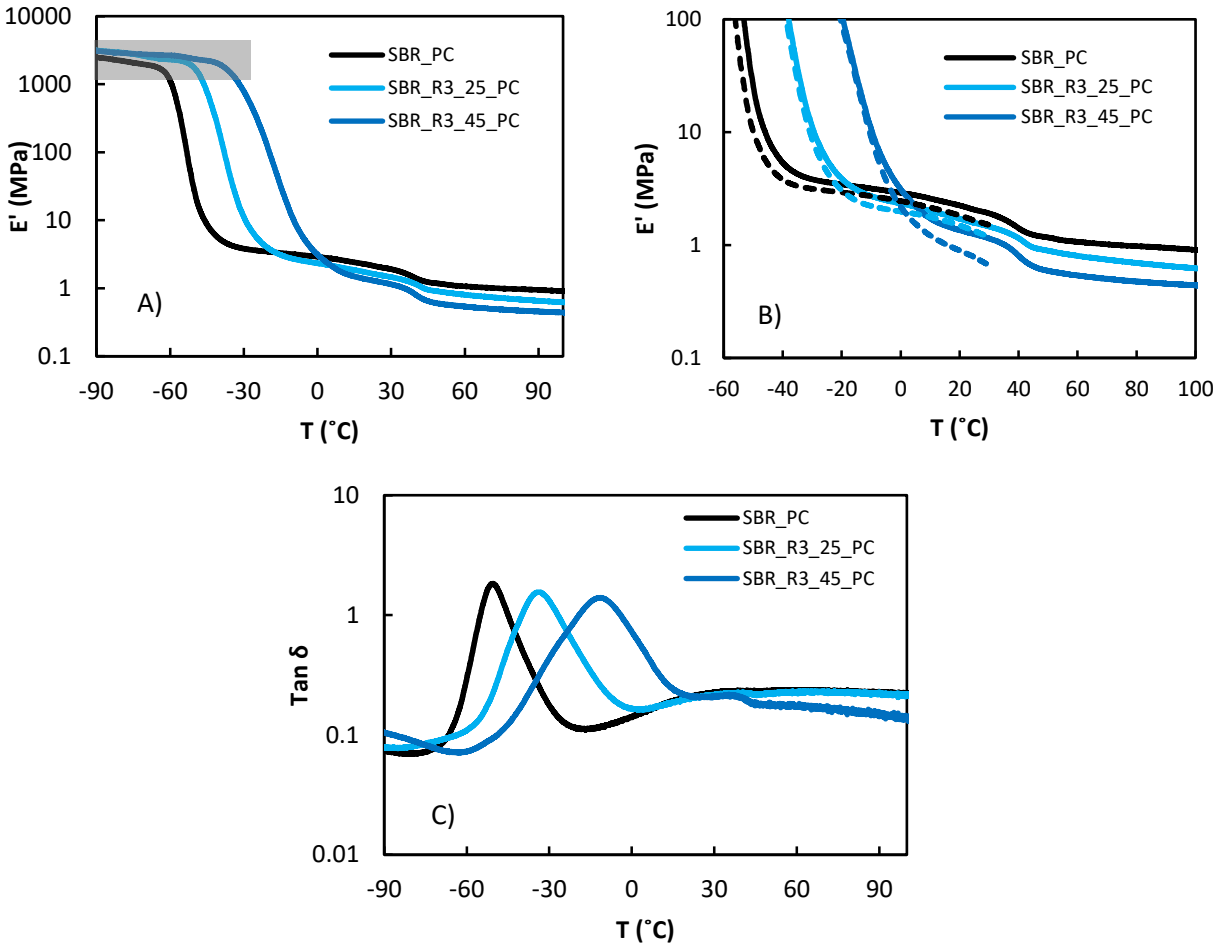

FIGURE 4. 19 A) DMA STORAGE MODULUS (E'), B) LOSS MODULUS (E'') AND C) LOSS FACTOR ($Tan\ \delta$) VERSUS TEMPERATURE (T) FOR THE SBR_R3_PC BLENDS. THE DOTTED CURVES ON FIGURE 4. 19B ARE FOR THE SBR_R3_UC BLENDS

The consequences of the crosslinking on the SBR_R3 blends is less surprising as the modulus increases with both crosslinking process (SC and PC), as shown on Figure 4. 19 and Figure 4. 20. The only difference between both processes is, as expected, that conversely to the PC crosslinking, the SC crosslinking creates sufficiently crosslinks to enable the observation of a plateau on the E' curves at temperature above T_α.

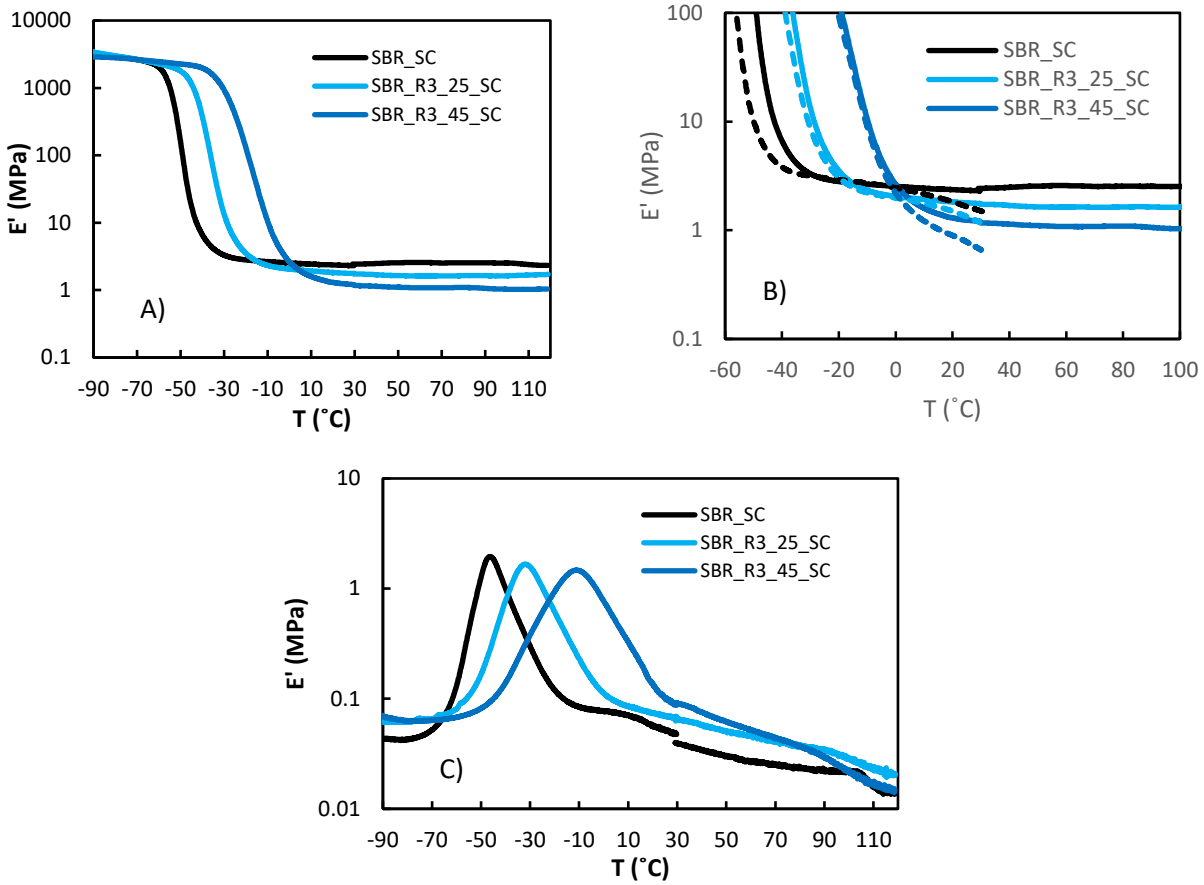

FIGURE 4. 20 A) DMA STORAGE MODULUS (E'), B) LOSS MODULUS (E'') AND C) LOSS FACTOR ($Tan\ \delta$) VERSUS TEMPERATURE (T) FOR THE SBR_R3_SC BLENDS. THE DOTTED CURVES ON FIGURE 4. 20B ARE FOR THE SBR_R3_UC BLENDS

Swelling experiments (section 4.2.2) have shown that the crosslinks density (including both chemical crosslinks and trapped entanglements) in SC R2 blend is low and significantly lower than in the SC SBR_R3 blends. This is sufficient to understand the difference between their modulus at high temperature or their tensile behavior at room temperature (cf. Figure 4. 21 and Figure 4. 22). The different effect of the crosslinking process on the modulus, as a function of the resin nature, is however difficult to understand (especially the fact that the crosslinking process decreases the modulus in R2 blend). The evolution of T_α with the resin content is roughly consistent with the Fox law prediction, for both resin type (see Figure S4. 5 and Figure S4. 6, respectively, in the supporting information section of this chapter). There is maybe a larger overestimation of the T_α with resin R2 blend, suggesting a lower miscibility of this resin, but this need to be confirmed.

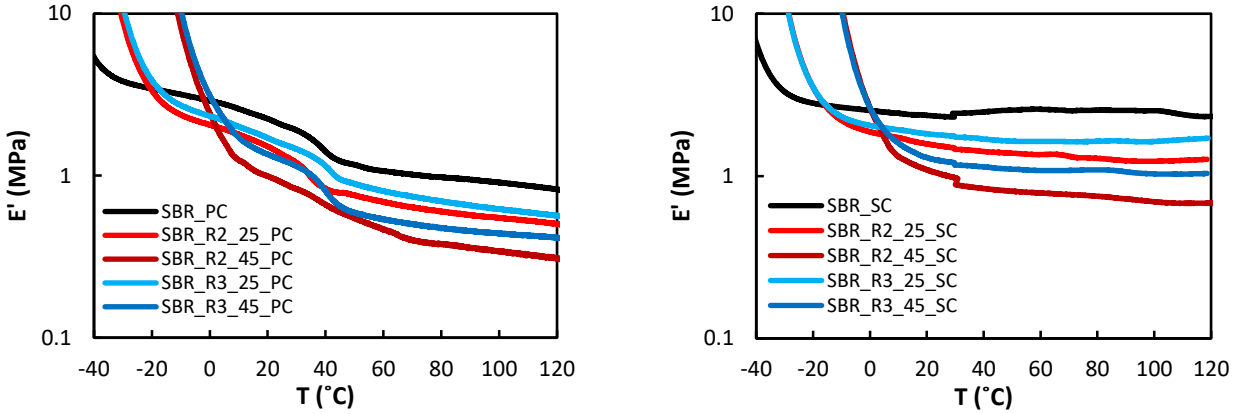

FIGURE 4. 21 DMA STORAGE MODULUS (*E′*) VERSUS TEMPERATURE (T) OF R2 AND R3 PC (LEFT) AND SC (RIGHT) BLENDS.

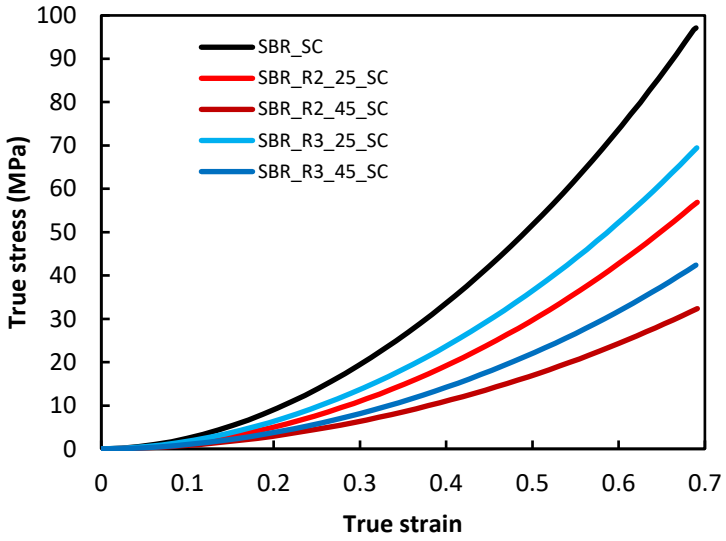

FIGURE 4. 22 TRUE STRESS VERSUS TRUE STRAIN CURVES OF SBR_R2_SC AND SBR_R3_SC BLENDS.

To go further, we used the slip-tube model prediction proposed by Rubinstein and Panyukov [15] for the nonlinear elasticity of polymer networks to quantitatively estimate the contributions of entanglements and chemical crosslinks in the mechanical response of the SC blends. This model is described in section 1.2.3 of chapter 1 (equation 1.26) and the elastic moduli, due to the entanglements ($E'_e = G'_e * 3$), and due to the cross-links ($E'_c = G'_c * 3$), calculated from the fitting of the uniaxial tensile experiments, are presented in Figure 4. 23.

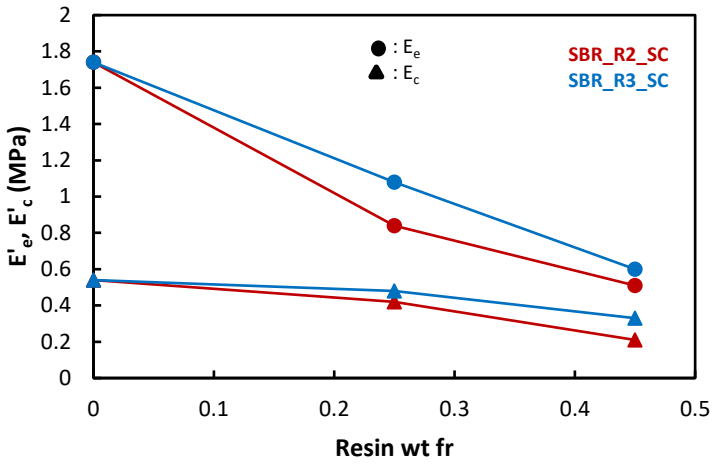

FIGURE 4. 23 E'_e AND E'_c ESTIMATED FROM RUBINSTEIN PANYUKOV MODEL FOR SBR_R2_SC AND SBR_R3_SC BLENDS.

As expected, the entanglement modulus is significantly larger than the crosslink modulus for both R2 and R3 blends. In addition, both E'_e and E'_c decrease with the increase of resin concentration, faster for the resin R2. We compared the evolution of E'_e with the dilution law for both R2 and R3 SC blends (cf. Figure 4. 24).

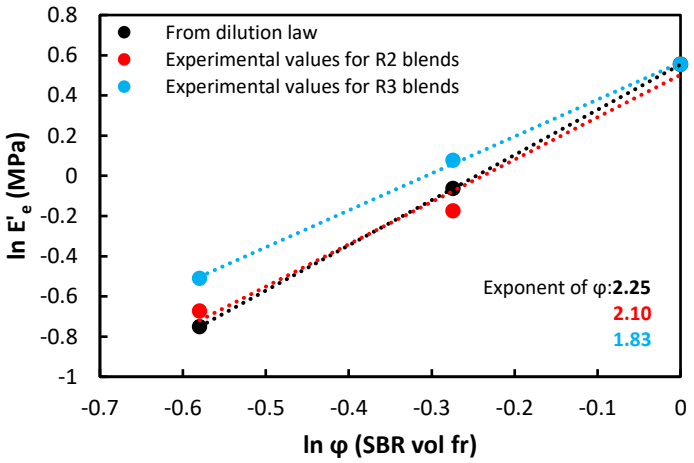

FIGURE 4. 24 LOGARITHM OF THE ENTANGLEMENT MODULUS E'_e IN MPA OF R2 AND R3 SC BLENDS ESTIMATED FROM RUBINSTEIN AND PANYKOV MODEL AND THE ONE PREDICTED FROM DILUTION LAW VERSUS THE LOGARITHM OF THE SBR VOLUME FRACTION (φ).

Unexpectedly, the dilution law works quite well for the R2 blends, whereas the prediction overestimates the decrease of the entanglement density for R3, with a smaller exponent. We recall that for the UC blends, on the contrary, the exponent was found larger for the resin R3 than the resin R2. A comparison with the dilution law may be therefore not pertinent, especially because the chemical crosslinks cannot be dissociated from the trapped entanglements. Thus, up to now, we do not have clear explanation for the more rapid decrease of the entanglement density with the

resin R2, when the material is crosslinked. A possible other explanation, which would need to be explored, may be the occurrence of few scissions of the polymer chains during crosslinking promoted by the presence of the resin R2.

4.5 Morphological analysis of blends

4.5.1 Uncrosslinked blends

We have tried to perform AFM imaging of the surface of uncrosslinked materials, but the quality of the images was not satisfactory enough to enable any analysis.

Figure 4. 25 shows the SAXS patterns obtained for uncrosslinked blends and SBR. SAXS profile of the SBR_UC was previously discussed in chapter 3 section 3: the q^{-3} slope indicates the scattering of objects with a ramified overall shape, and a peak can be revealed by a $Iq^3(q)$ plot, associated to a correlation distance of $532\,nm$, corresponding to the average distance between these large objects. As shown on the same figure, the addition of the resin R2 leads to the disappearance of the weak shoulder and in the q range of 0.2 to 1 nm^{-1} to a slight increase in the intensity. This is highlighted in this q range by subtracting the pure SBR scattering signal to the blend ones ($I_{Blend} - I_{SBR}) = f(q)$ plot on

Figure 4. 25b) [16] [17]. This q range corresponds to a correlation length $d = \frac{2\pi}{q}$ from 6 to 31 nm. This may originate from resin concentration fluctuations.

The addition of resin R3 also leads to an increase of intensity in this q domain, but this increase is more important, suggesting the presence of more heterogeneities/fluctuations. It is however difficult to relate this result to the fact that the modulus of the R3 UC blends is lower than the one of the R2 UC blends, at the temperature at which SAXS measurements have been performed.

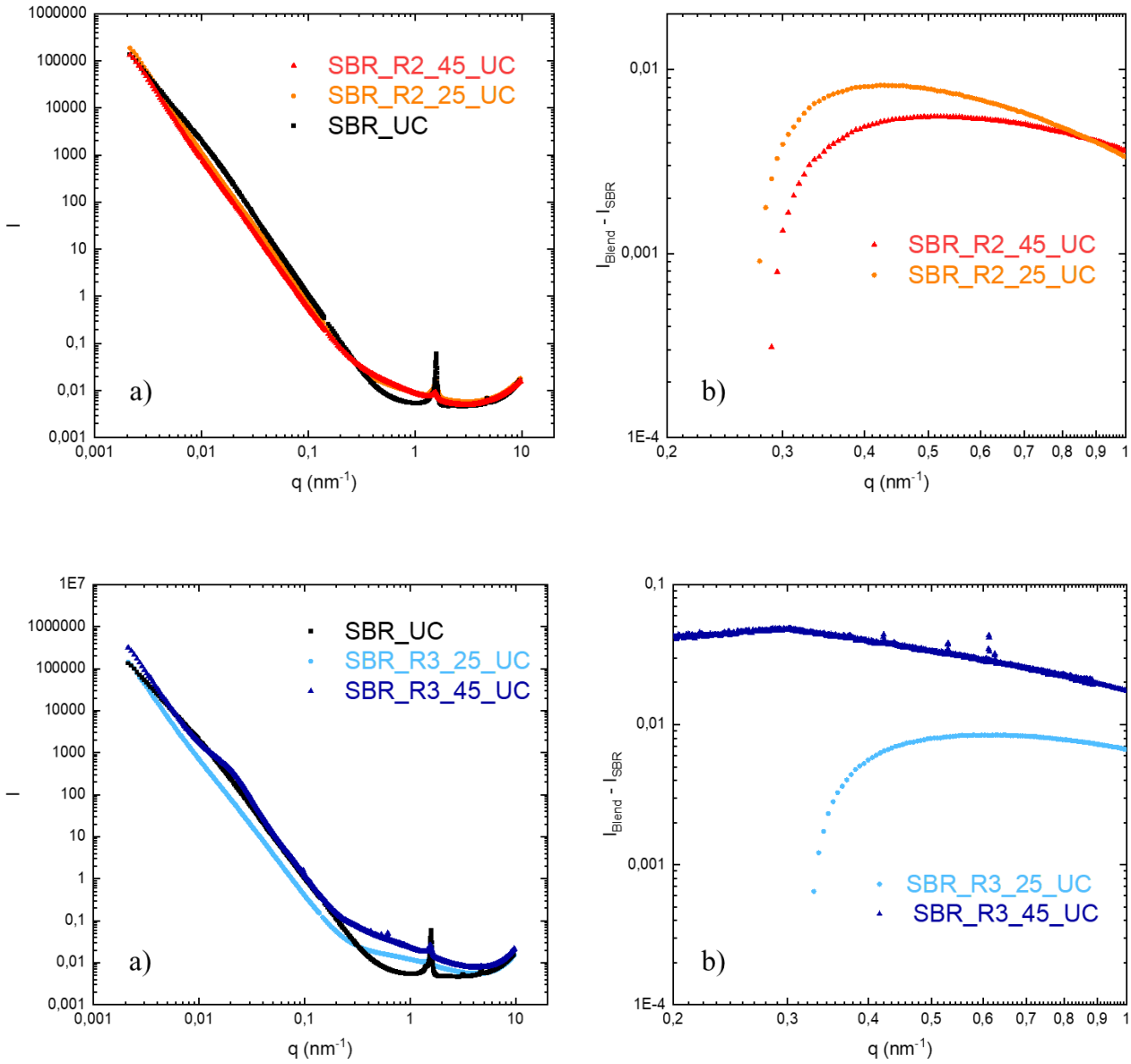

FIGURE 4. 25 SAXS PATTERNS OBTAINED ON THE UNCROSSLINKED SBR_R2 (TOP) AND SBR_R3 (BOTTOM) BLENDS: (A) $I = f(q)$ AND (B) CORRESPONDING INTENSITY PATTERN AFTER SUBSTRACTION OF THE SBR_UC SIGNAL, $I_{Blend} - I_{SBR} = f(q)$.

4.5.2 Crosslinked blends

PC crosslinked blend have also been studied by SAXS (conversely to the SC crosslinked blend, in which the ZnO particles leads to a too strong scattering intensity). The SAXS profiles are presented in Figure 4. 26, for the PC R2 blends and for the PC R3 blends.

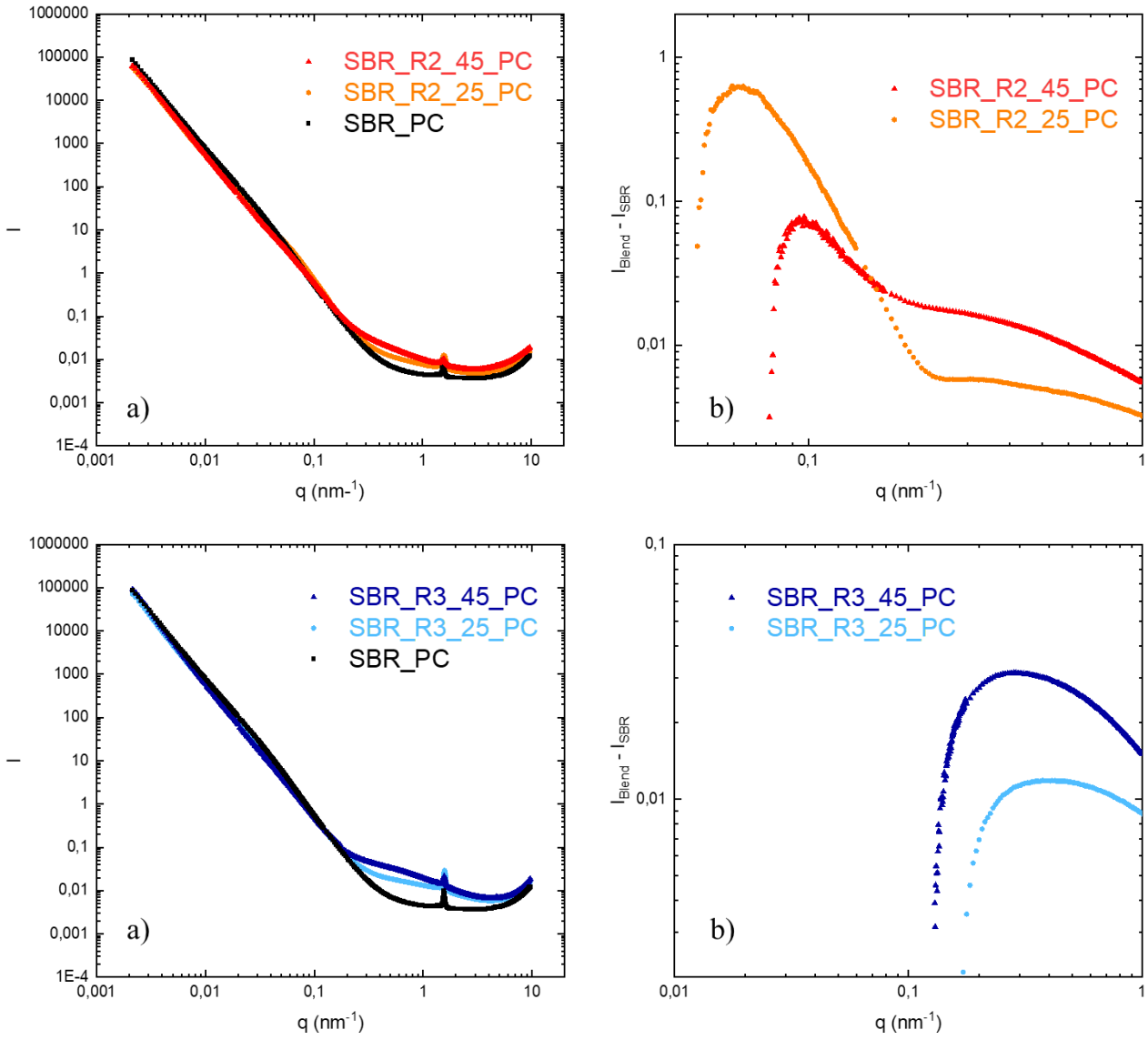

FIGURE 4. 26 SAXS PATTERNS OBTAINED ON THE PC CROSSLINKED SBR_R2 (TOP) AND SBR_R3 (BOTTOM) BLENDS: (A) $I = f(q)$ AND (B) CORRESPONDING INTENSITY PATTERN AFTER SUBSTRACTION OF THE SBR_UC SIGNAL, $I_{Blend} - I_{SBR} = f(q)$.

In chapter 3, we have already shown that crosslinking the matrix reduces the deduced correlation distance of the large ramified "domains" already present in the SBR matrix (the distance is halved by the crosslinking). The addition of resin R2 seems to decrease even more this distance, as shown by a correlation peaks in the $I_{Blend} - I_{SBR} = f(q)$ curve in the 0.01-1 nm^{-1} q range: the deduced distance is around 100 nm for 25 wt.% resin and 65nm for 45 wt. % resin. This plot also reveals, like for the UC materials, that the addition of resin leads to the formation of heterogeneities with correlation length around 30 nm. SAXS of the R3 PC samples suggest a slightly different nanostructure. The addition of resin R3 leads to the disappearance of the shoulder on the I(q) curve

in the [0.01 nm^{-1}, 0.1 nm^{-1}] q domain. However, a correlation peak can be again evidenced in the [0.1 nm^{-1}, 1 nm^{-1}] q domain whose position is about the same whatever the resin content ($q^* \approx 0.3\ nm^{-1}$). It corresponds to a correlation distance around 21 nm. Only the intensity appears to increase with the resin content.

AFM images of SBR_R2_SC and SBR_R3_SC blends are shown in Figure 4. 27. Both R2 and R3 SC blends clearly show the presence of nanoscale heterogeneities. The plot of an intensity profile over a line drawn on the figure enables to show the existence of a characteristic length. This one is roughly equal to 30 nm, 45 nm, 40 nm and 90 nm for respectively SBR_R2_25_SC, SBR_R2_45_SC, SBR_R3_25_SC and SBR_R3_45_SC. These distances are in the same range of order from the previous distance deduced from the SAXS experiment.

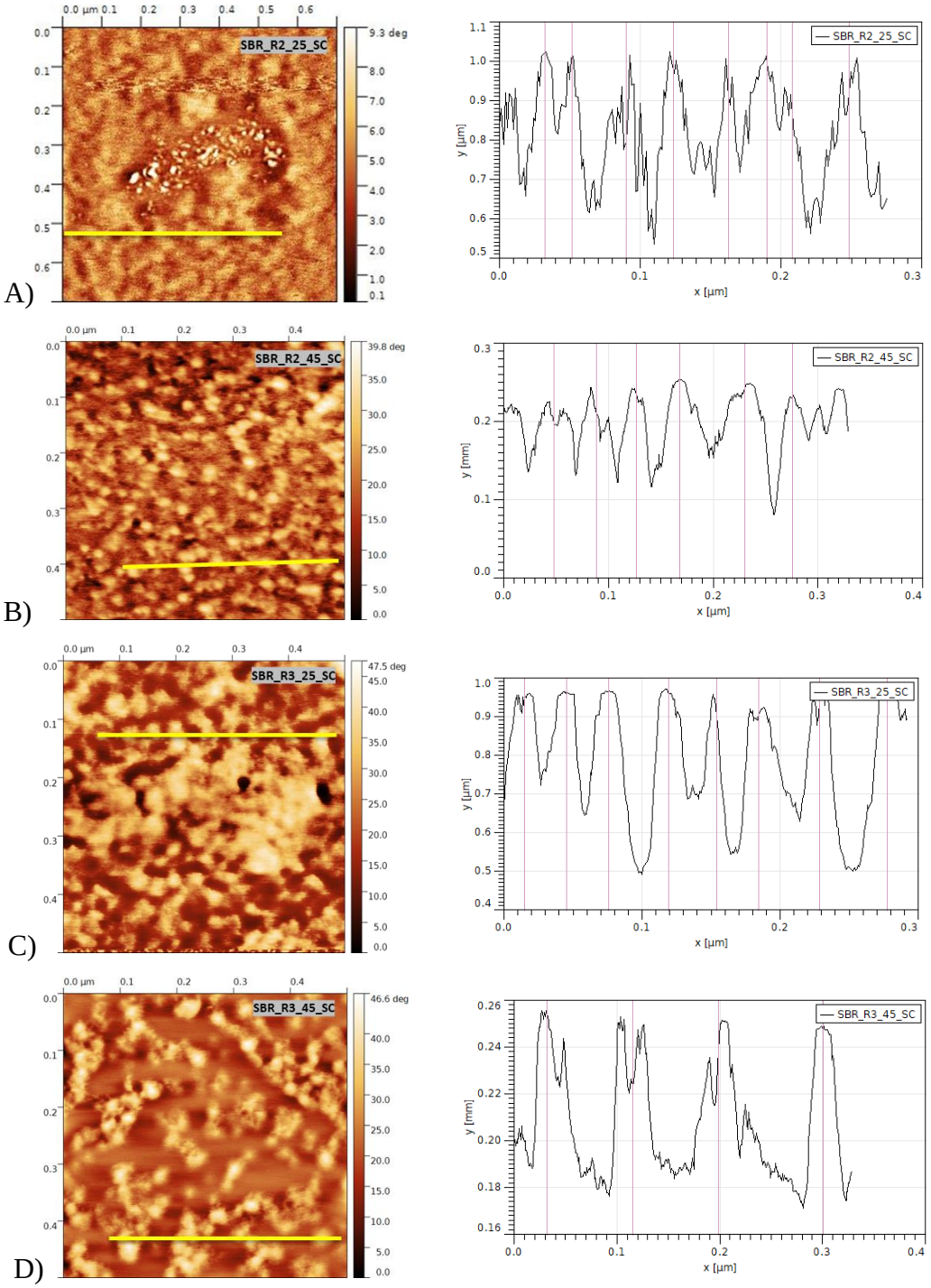

FIGURE 4. 27 AFM PHASE IMAGES AND INTENSITY PROFILE OVER THE YELLOW LINE FOR A) SBR_R2_25_SC, B) SBR_R2_45_SC, C) SBR_R3_25_SC, D) SBR_R3_45_SC

AFM images were also obtained on SC crosslinked blends after resin extraction. They are presented in Figure 4. 28 with an intensity profile along a line drawn on the image. The deduced characteristic lengths are 80 nm, 40 nm, 40 nm and 25 nm for the SBR_R2_25_SC, SBR_R2_45_SC, SBR_R2_25_SC, SBR_R3_45_SC respectively. It is difficult to comment these distances and their differences with the ones previously found for the same materials without extraction of the resin. One can however clearly see on the images for the resin extracted SBR_R2_45_SC and SBR_R3_45_SC the presence of little black disk which may be due to less crosslinked domains.

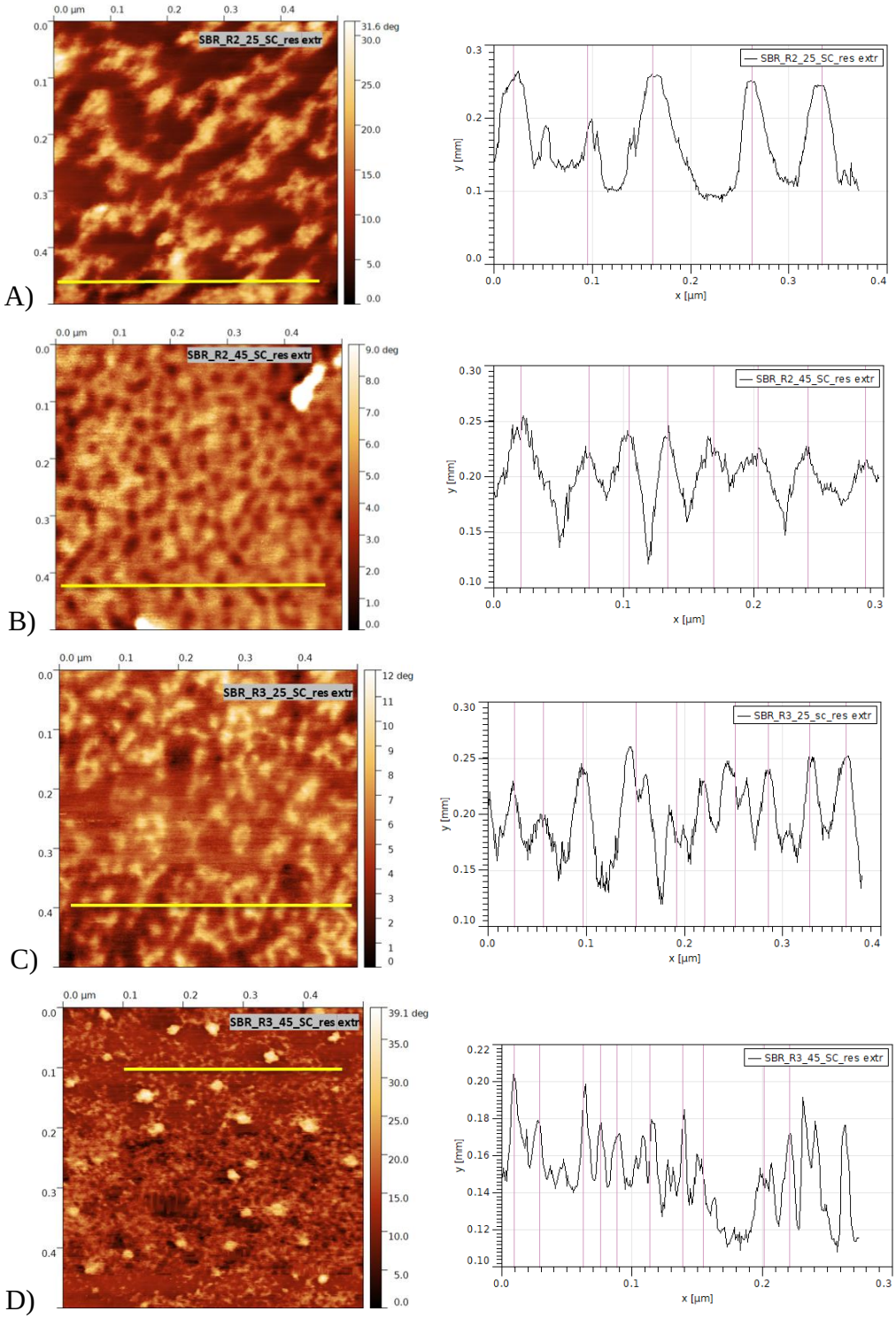

FIGURE 4. 28 AFM PHASE IMAGES AND INTENSITY PROFILE OVER THE YELLOW LINE FOR RESIN EXTRACTED A) SBR_R2_25_SC, B) SBR_R2_45_SC, C) SBR_R3_25_SC, D) SBR_R3_45_SC

4.6 Conclusions

As expected, the introduction of resin R2 and R3 in the Styrene Butadiene (uncrosslinked), shifts the glass transition temperature (and the associated main relaxation temperature) towards higher temperature. This shift is better predicted by the Couchman Karasz law (or the Fox law when this one is applied to T_α). These predictions are however not completely satisfactory, and in the same way for both resins. Indeed, the resin presence also enlarges the glass transition domain due to the presence of concentration fluctuation. It has also a dilution effect, visible above the main relaxation temperature. This effect corresponds to the prediction at high temperature (120°C). It is however weaker than the prediction, in the temperature domain corresponding to the plateau modulus domain of the SBR, that we previously ascribed to relaxation of dangling chains. In particular, in this domain, the resin R2 reduces the modulus less than expected (and less than the resin R3). This may be due to a weak phase separation at the scale of the heterogeneities already present in the SBR polymer. Another explanation, maybe complementary, is the length of some of the R2 molecules, which may introduce additional entanglements. SAXS data also reveals that the resin addition makes disappear a correlation distance in the range of few hundreds of nm, and make appear a correlation distance in the range of few tens of nm, suggesting the existence of heterogeneities at this scale.

These blends have been either crosslinked with peroxide, or with sulfur. All the resins can be extracted after crosslinking, indicating that most of the resin does not take part to the elastomer network. The peroxide crosslinking was performed only for SAXS study. The PC samples are weakly crosslinked and their behaviors/morphologies are intermediate between those of the uncrosslinked blends and those of the sulfur crosslinked blends. Like in SBR, the sulfur crosslinking in R2 blends also results in a T_α shift of around 5°C, compared to the uncross-linked ones. However, this shift due to the crosslinking is slightly less notable in resin R3 blends (for unexplained reason). The sulfur crosslinking suppresses the mechanical relaxation previously observed by DMA at around 40˚C in UC blends, since the crosslink density is high enough to also include the dangling chains in the elastomer network. The resins still have a dilution effect in the crosslinked sample. This is evidenced by the increase of the swelling ratio of the crosslinked blends with the resin content. However, these experiments also suggest that one of the resin or both interfere with the crosslinking reactions, and the presence of R2 leads to a lower global crosslink

density in the final product than the resin R3. Moreover, the crosslinking process of the R2 blends leads to a decrease of the modulus at ambient temperature. This may be due to a modification of the material morphology after crosslinking: the crosslinking may inhibit some phase separation which could increase local crosslink densities; or the R2 resin may induce some degradation of the polymer during the crosslinking reactions. The morphological characterizations of the crosslinked materials do not enable to choose among these explanations. They reveal complex morphologies, in which the correlation distances are in the range of tens of nanometer and seems to increase with the resin content. There is no doubt that these morphologies are also an indication of crosslinks/entanglement/resin heterogeneities.

4.7 Supporting information

DSC curves of UC and PC R2 and R3 blends

The reversibility of the melting peak corresponding to the stearic acid is seen (Figure S4. 1) in 1st heating and 2nd heating cycles of UC and PC cured R2 and R3 blends. The difference between the curves obtained from the 1st and the 2nd heating ramp is likely due to the difference in the thermal history of the sample (the stearic acid has less time to cristallise with the 2nd heating cycle).

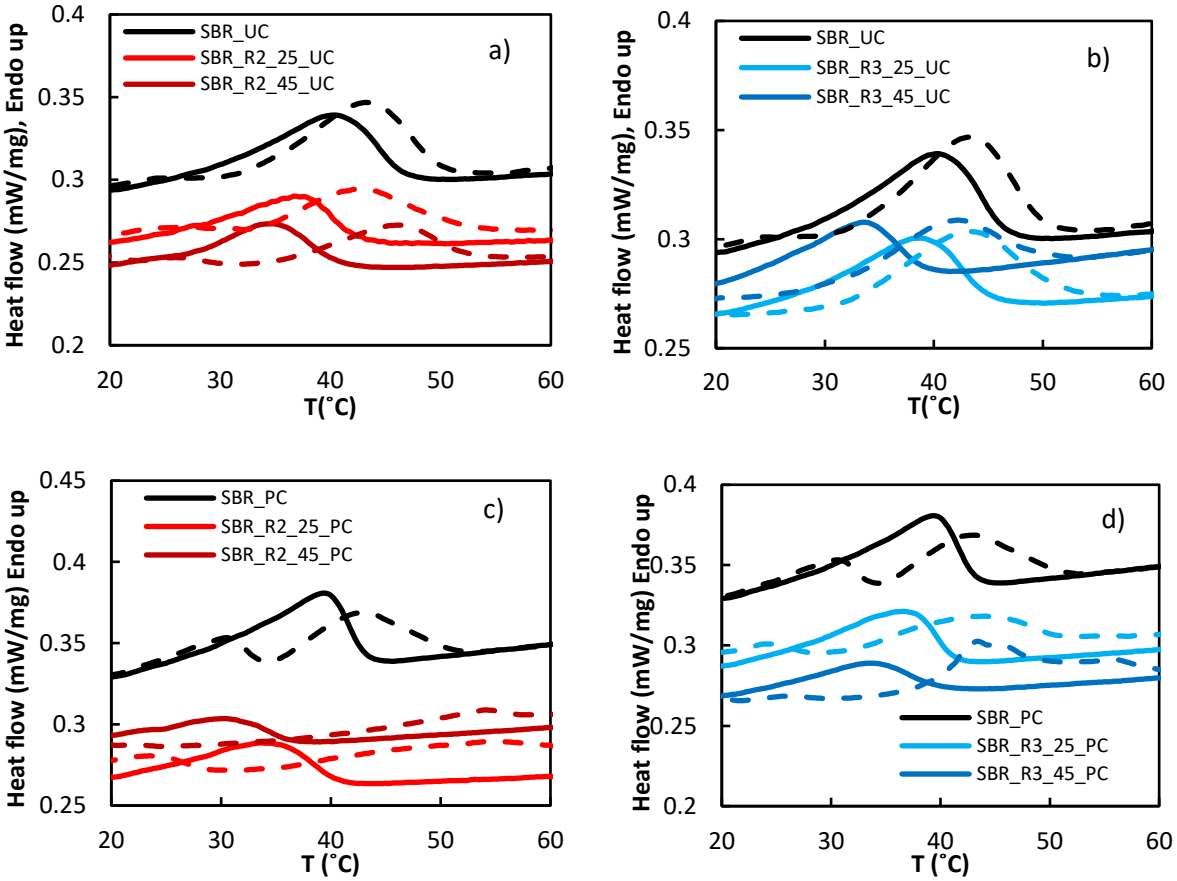

FIGURE S4. 1 DSC HEAT FLOW CURVES (SOLID LINE - 1ST HEATING AND DASHED LINE - 2ND HEATING) VERSUS TEMPERATURE (T) OF: A) SBR_R2_UC SAMPLES, B) SBR_R3_UC SAMPLES, C) SBR_R2_PC SAMPLES, AND D) SBR_R3_PC SAMPLES.

DSC curves of resin extracted samples

The derivatives of heat flow curves of resin extracted samples are shown in Figure S4. 2. The DMA curves show the absence of influence of the resin presence during curing on the final glass transition of the polymer. In spite of some small variation, the first derivative of the DSC heat flow curves confirms these results.

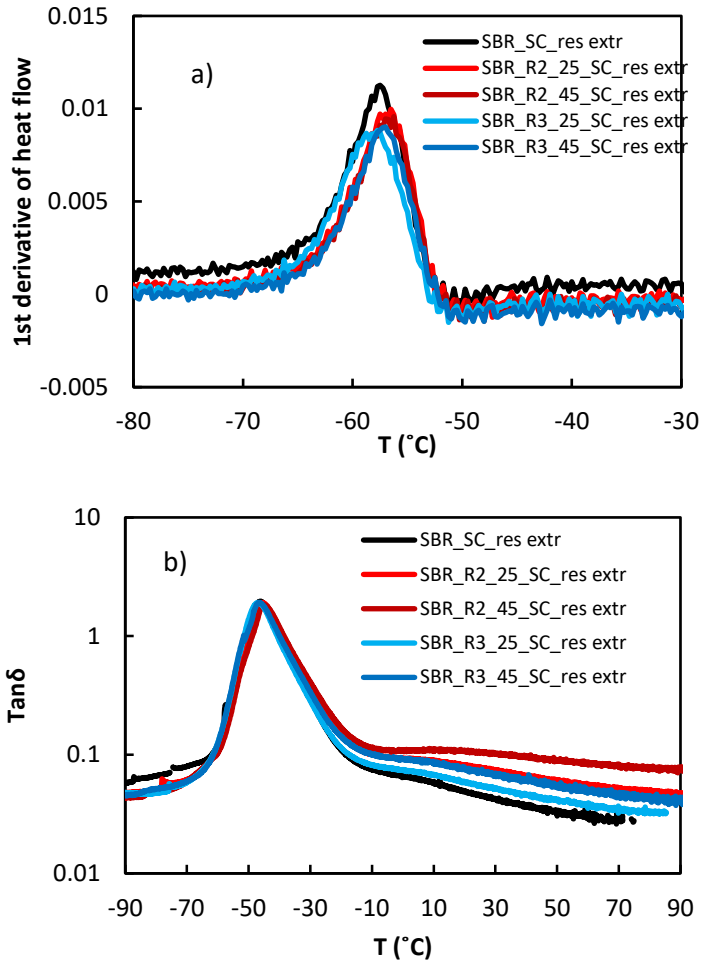

FIGURE S4. 2 A) DSC 1ST DERIVATIVE OF HEAT FLOW AND B) DMA LOSS FACTOR VERSUS TEMPERATURE OF RESIN EXTRACTED SAMPLES.

Theoretically calculated and experimental values of T_g/T_α of PC and SC R2 and R3 blends

The T_g of SBR_R2_PC and SBR_R3_PC blends calculated from Fox law and measured from DSC are plotted in Figure S4. 3. Similarly, Figure S4. 4 shows the calculated and measured T_g in SC R2 and R3 blends. In all cases, a large discrepancy is observed between the calculated T_g and the experimental one.

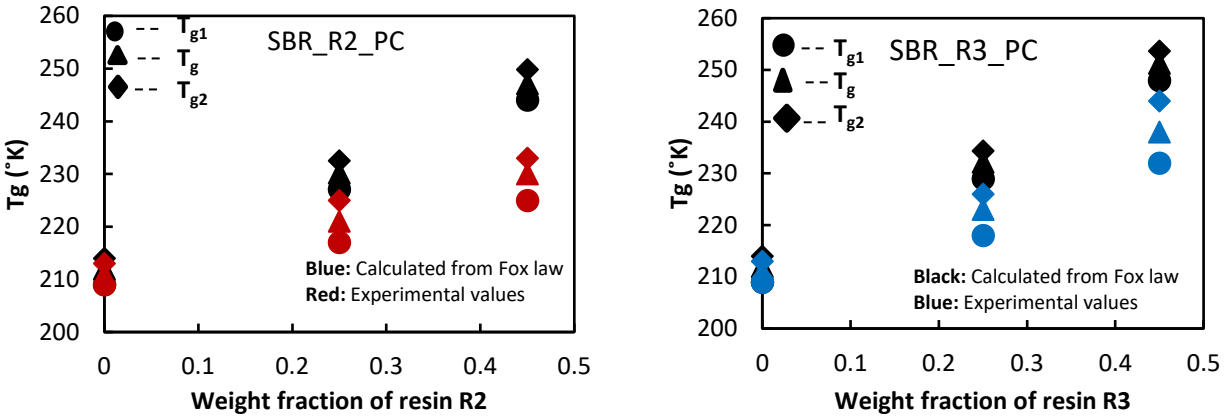

FIGURE S4. 3 EXPERIMENTAL T_g FROM DSC AND CALCULATED FROM FOX LAW VERSUS THE WEIGHT FRACTION OF THE RESIN IN SBR_R2_PC (LEFT) AND SBR_R3_PC (RIGHT) BLENDS.

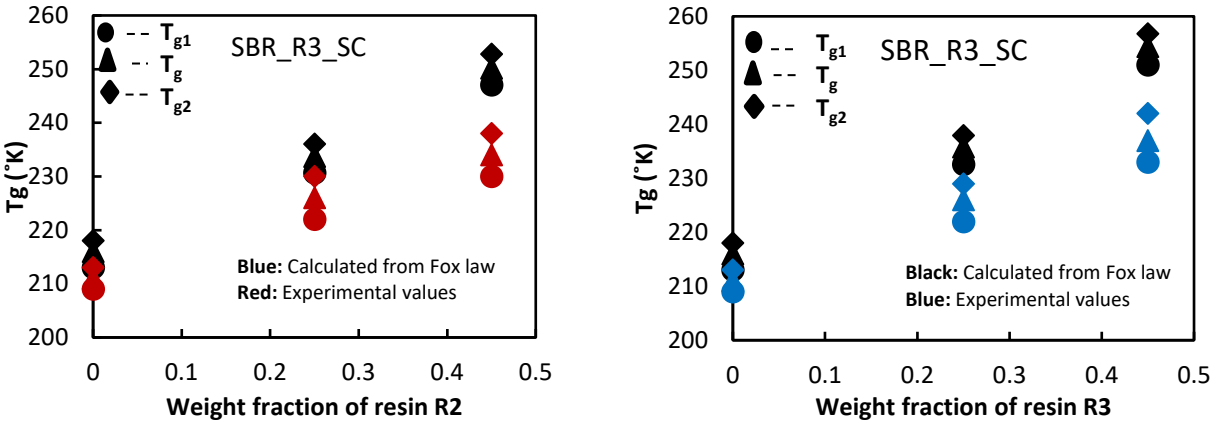

FIGURE S4. 4 EXPERIMENTAL T_g FROM DSC AND CALCULATED FROM FOX LAW VERSUS THE WEIGH FRACTION OF THE RESIN IN SBR_R2_SC (LEFT) AND SBR_R3_SC (RIGHT) BLENDS.

The Tα of PC and SC R2 and R3 blends calculated from Fox law and the ones measured with DMA are plotted in Figure S4. 5 and Figure S4. 6 respectively. They show the better predictable character of the Fox law when it is applied to Tα.

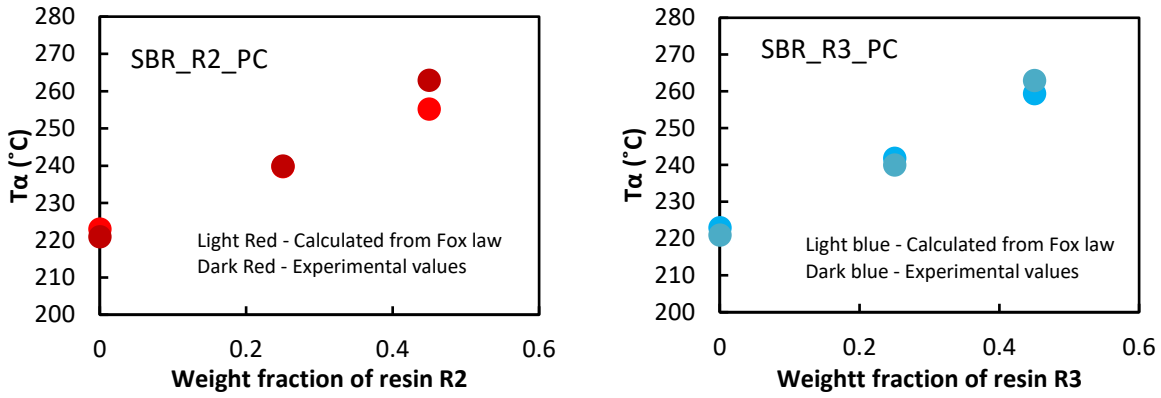

FIGURE S4. 5 EXPERIMENTAL T_α FROM DMA AND CALCULATED FROM FOX LAW VERSUS TOTAL RESIN AMOUNT IN SBR_R2_PC (LEFT) AND SBR_R3_PC (RIGHT) BLENDS.

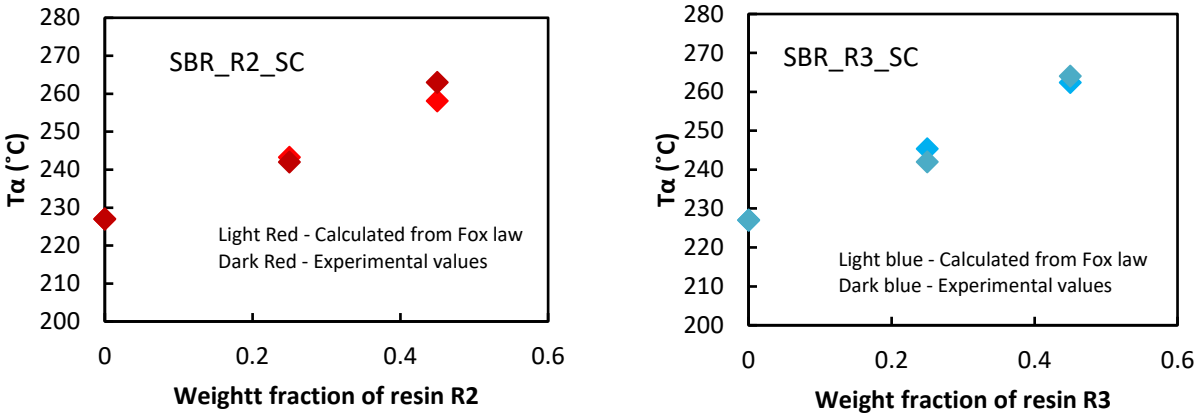

FIGURE S4. 6 EXPERIMENTAL T_α FROM DMA AND CALCULATED FROM FOX LAW VERSUS TOTAL RESIN AMOUNT IN SBR_R2_SC (LEFT) AND SBR_R3_SC (RIGHT) BLENDS.

4.8 References

(1) Shenogin, S.; Kant, R.; Colby, R. H.; Kumar, S. K. Dynamics of Miscible Polymer Blends: Predicting the Dielectric Response. *Macromolecules* **2007**, *40* (16), 5767–5775. https://doi.org/10.1021/ma070503q.

(2) Lodge, T. P.; McLeish, T. C. B. Self-Concentrations and Effective Glass Transition Temperatures in Polymer Blends. *Macromolecules* **2000**, *33* (14), 5278–5284. https://doi.org/10.1021/ma9921706.

(3) Roland, C. M.; Ngai, K. L. Dynamical Heterogeneity in a Miscible Polymer Blend. *Macromolecules* **1991**, *24* (9), 2261–2265.

(4) Roland, C. M.; Ngai, K. L. Segmental Relaxation in Miscible Polymer Blends. *J. Rheol.* **1992**, *36* (8), 1691–1706. https://doi.org/10.1122/1.550280.

(5) Kant, R.; Kumar, S. K.; Colby, R. H. What Length Scales Control the Dynamics of Miscible Polymer Blends? *Macromolecules* **2003**, *36* (26), 10087–10094. https://doi.org/10.1021/ma0347215.

(6) Couchman, P. R.; Karasz, F. E. A Classical Thermodynamic Discussion of the Effect of Composition on Glass-Transition Temperatures. *Macromolecules* **1978**, *11* (1), 117–119. https://doi.org/10.1021/ma60061a021.

(7) Aubin, M.; Prud'Homme, R. E. Analysis of the Glass Transition Temperature of Miscible Polymer Blends. *Macromolecules* **1988**, *21* (10), 2945–2949.
(8) Bhagabati, P.; Chaki, T. K. Compatibility Study of Chlorinated Polyethylene/Ethylene Methacrylate Copolymer Blends Using Thermal, Mechanical, and Chemical Analysis. *J. Appl. Polym. Sci.* **2014**, *131* (11).
(9) Fried, J. R.; Lai, S.-Y.; Kleiner, L. W.; Wheeler, M. E. Experimental Assessment of the Thermodynamic Theory of the Compositional Variation of Tg: PVC Systems. *J. Appl. Polym. Sci.* **1982**, *27* (8), 2869–2883.
(10) Class, J. B.; Chu, S. G. The Viscoelastic Properties of Rubber–Resin Blends. III. The Effect of Resin Concentration. *J. Appl. Polym. Sci.* **1985**, *30* (2), 825–842.
(11) De Gennes, P.-G.; Gennes, P.-G. *Scaling Concepts in Polymer Physics*; Cornell university press, 1979.
(12) Kumar, K. D.; Gupta, S.; Tsou, A. H.; Bhowmick, A. K. Compatibility and Viscoelastic Properties of Brominated Isobutylene-Co-p-Methylstyrene Rubber/Tackifier Blends. *J. Appl. Polym. Sci.* **2008**, *110* (3), 1485–1497. https://doi.org/10.1002/app.28649.
(13) Kraus, G.; Rollmann, K. W. The Entanglement Plateau in the Dynamic Modulus of Rubbery Styrene–Diene Block Copolymers. Significance to Pressure-Sensitive Adhesive Formulations. *J. Appl. Polym. Sci.* **1977**, *21* (12), 3311–3318. https://doi.org/10.1002/app.1977.070211210.
(14) De Gennes, P. G. Dynamics of Entangled Polymer Solutions. I. The Rouse Model. *Macromolecules* **1976**, *9* (4), 587–593.
(15) Rubinstein, M.; Panyukov, S. Elasticity of Polymer Networks. *Macromolecules* **2002**, *35* (17), 6670–6686. https://doi.org/10.1021/ma0203849.
(16) Jouault, N.; Dalmas, F.; Said, S.; Di Cola, E.; Schweins, R.; Jestin, J.; Boué, F. Direct Measurement of Polymer Chain Conformation in Well-Controlled Model Nanocomposites by Combining SANS and SAXS. *Macromolecules* **2010**, *43* (23), 9881–9891. https://doi.org/10.1021/ma101682t.
(17) Bandyopadhyay, J.; Sinha Ray, S. Structural Characterization of Polymer Nanocomposites. In *Processing of polymer-based nanocomposites*; Springer, 2018; pp 87–126.

5 Semi-compatible resin/elastomer blend system: Nano-structuration and properties.

The influence of resin R1 on curing reactions and on SBR network is investigated separately from the two resins because all the characterization of the blend we performed indicated a specific behavior for this resin. Great importance is given to the evolution of viscoelastic behavior with temperature and resin concentration. The morphological details from nano to micro scale are investigated by AFM, SAXS, TEM, and SEM in the PC and SC crosslinked systems. The stability of the microstructure with temperature change is also investigated by SAXS and DMA analysis.

Contents

5.1 Formulation of blends

The different formulations of the studied SBR_R1 blends are recalled in Table 5.1. Their processing was already described in chapter 2.

TABLE 5.1: COMPOUND FORMULATION OF THE DIFFERENT R1 BLENDS STUDIED IN THIS CHAPTER.

Sample name	**Ingredients (phr)**							
	SBR	**Resin (R1)**	**6PPD**	**Stearic acid**	**DCP**	**ZnO**	**S**	**CBS**
SBR_UC	100	-	1.5	3	-	-	-	-
SBR_R1_25_UC	100	33	1.5	3	-	-	-	-
SBR_R1_45_UC	100	83	1.5	3	-	-	-	-
SBR_PC	100	-	1.5	3	0.74	-	-	-
SBR_R1_25_PC	100	33	1.5	3	0.74	-	-	-
SBR_R1_45_PC	100	83	1.5	3	0.74	-	-	-
SBR_SC	100	-	1.5	3	-	1.45	1.4	1.6
SBR_R1_25_SC	100	33	1.5	3	-	1.45	1.4	1.6
SBR_R1_45_SC	100	83	1.5	3	-	1.45	1.4	1.6

* Resin amount of 33 and 83 phr corresponds to the 25 and 45 wt% of blends (SBR+resin), respectively.

5.2 Uncrosslinked R1/SBR blends

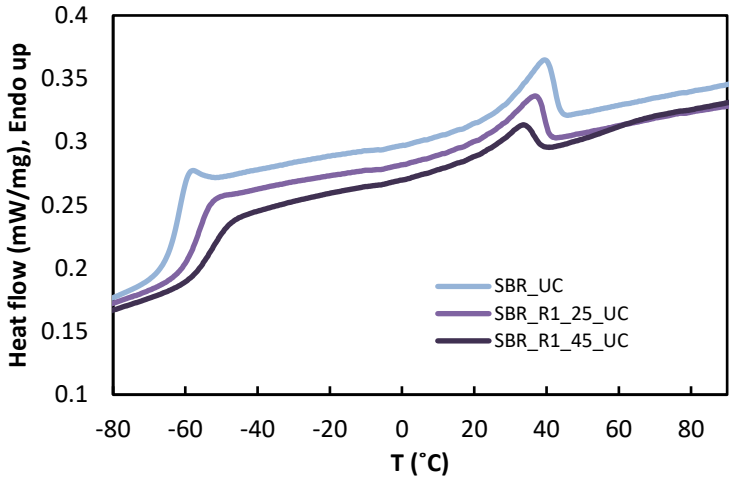

FIGURE 5. 1 DSC HEAT FLOW CURVES (2ND HEATING) OF SBR_R1_UC BLENDS.

Figure 5. 1 present the DSC curves of the R1_SBR_UC blends. As expected, the increase of the resin content broadens the glass transition temperature domain and leads to a higher glass transition temperature. The peak around 40°C related to the stearic acid crystallites is still present. The T_g at the onset (T_{g1}), midpoint (T_g), and endpoint (T_{g2}) can again be compared to the prediction of the Fox law. As shown on Figure 5. 2, the disagreement between the calculated and experimental value is much larger with this resin (27°C compared to ca. 15°C with resin R2 and R3, for 45% content), which suggests that some phase separation occurs. This is supported by the presence of a T_g type transition at ca. 50°C on the DSC curve of the SBR_R1_45_UC, which is likely related to the glass transition of the separated phase with the highest glass transition temperature (i.e. the resin rich phase).

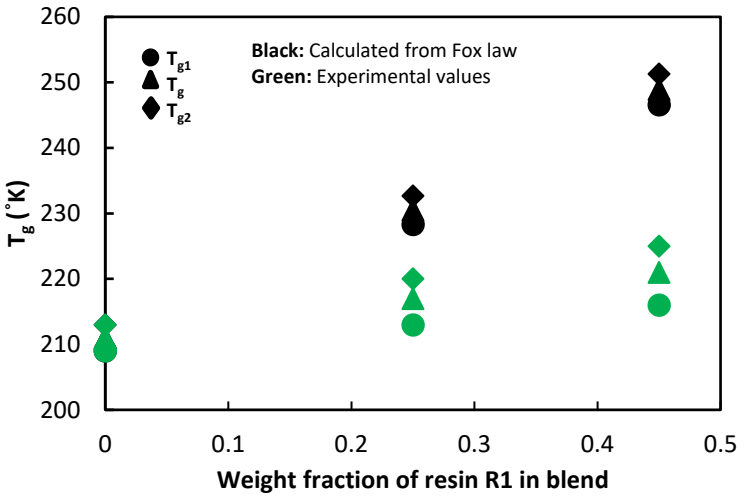

FIGURE 5. 2 EXPERIMENTAL T_g FROM DSC AND CALCULATED FROM FOX LAW VERSUS TOTAL RESIN AMOUNT IN THE SBR_R1_UC BLENDS.

The viscoelastic behavior of SBR_R1_UC blends have also been characterized by DMA in tension mode, and, for temperature above 30°C, by rheometer as shown in Figure 5. 3 and Figure 5. 4 respectively. The elastic modulus E' in Figure 5. 4 is obtained from the shear modulus measured from rheometer with the assumption of a perfectly incompressible material i.e. $E' = 3 * G'$.

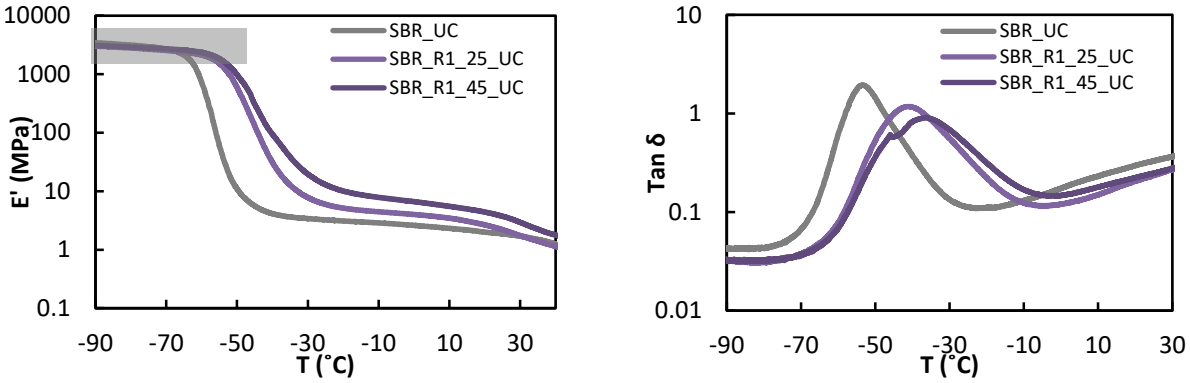

FIGURE 5. 3 STORAGE MODULUS (E') AND LOSS FACTOR (Tan δ) VERSUS TEMPERATURE (T) OF SBR_R1_UC BLENDS FROM DMA.

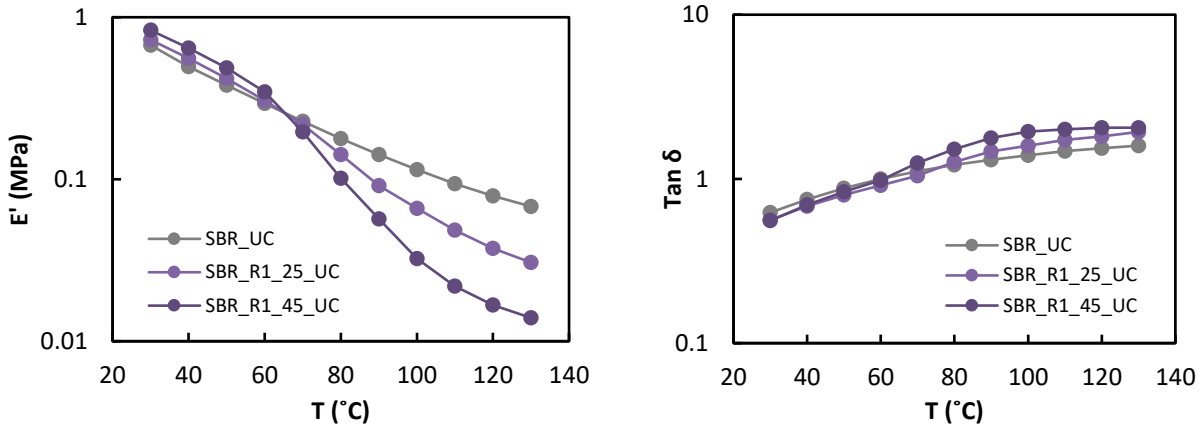

FIGURE 5. 4 STORAGE MODULUS (*E′*) AND LOSS FACTOR (Tan δ) VERSUS TEMPERATURE (T) OF SBR_R1_UC BLENDS FROM RHEOMETER.

As expected, a broadening of the T_α and its shift toward higher temperature is observed, in agreement with the DSC results. The shift increase is however small when the resin content increases from 25 to 45 wt.%, confirming our assumption of a phase separation, at least for the highest resin content. This can be further confirmed by the Figure 5. 5 where there is a disagreement of 5˚C for 25% and 17˚C for 45 wt.% resin content between the calculated (from Fox law) and experimental T_α values (whereas the experimental and theoretical T_α were roughly in agreement with resin R2 and R3).

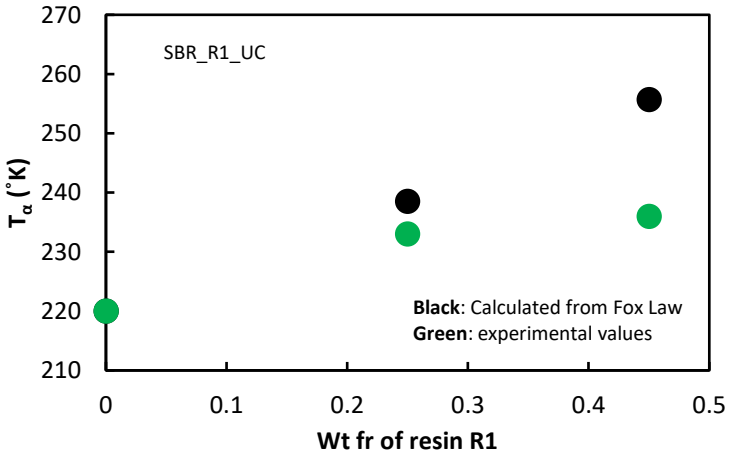

FIGURE 5. 5 EXPERIMENTAL T_α FROM DMA AND CALCULATED FROM FOX LAW VERSUS TOTAL RESIN AMOUNT IN THE SBR_R1_UC_BLENDS.

Another relaxation is observed at around 60˚C in SBR_R1_25 and SBR_R1_45 blends. With the fact that the modulus below 30°C increases with the resin content, this supports the idea of the presence of a separated phase which reinforces the modulus of the blend when it is in the glassy state. [1] By comparing the experimental T_α values with the ones predicted by the Fox law, we can estimate the weight fraction of the separated phase, assuming that this one is made of pure resin R1

(see the 1st heading of supporting information section). The results are reported in Table 5. 2. It suggests that a non-negligible content of separated phase exists in the 25wt% blend. It also says that more resin is phase separated in the 45wt% blend.

One can compare the modulus at high temperature, when all phases are above their glass transition temperature, with prediction of the dilution law (used in the previous chapter, section 4.4.1, eq 4.2), even though the dilution law was developed to predict the plateau modulus. As shown on Figure 5. 6 the found exponent is ca. 2.73, i.e. significantly higher than exponent of 2.25 proposed by de Gennes, and larger than the exponent found for the resin R2 and R3 (respectively 2.34 and 2.57). This cannot be correlated to the molar weight, M_w, of resins [2] since they follow the order $M_w(R1) > M_w(R2) > M_w(R3)$. Therefore, this is necessarily related to the different values of the interaction parameters at this temperature between the polymer and the resins.

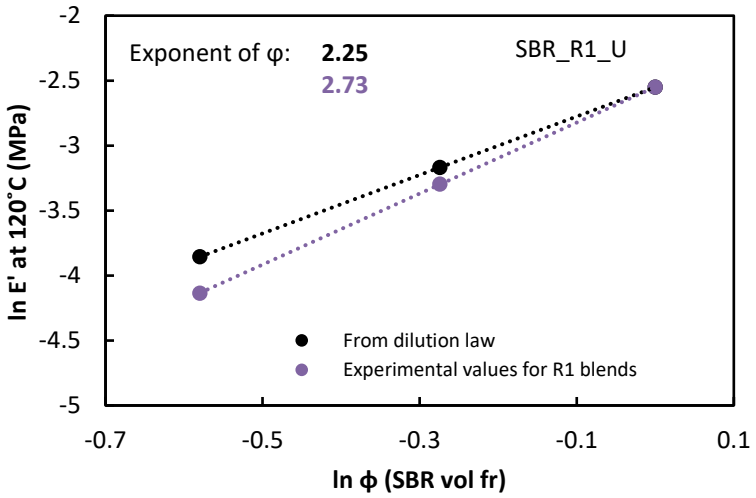

FIGURE 5. 6 LOGARITHM OF THE STORAGE MODULUS IN MPa MEASURED FROM RHEOMETER AT 120˚C AS A FUNCTION OF THE LOGARITHM OF THE SBR VOLUME FRACTION FOR SBR_R1_UC BLENDS. COMPARISON WITH THE ESTIMATED VALUES FROM DILUTION LAW. DASHED LINES REPRESENT LINEAR FITS

In any case, it could be interesting to estimate the modulus that the polymer rich phase would have at ambient temperature. As a first and rough assumption, we used the dilution law with an exponent 2.25 and the modulus of the SBR_UC at the $Tan\ \delta_{min}$ - actually equal to the modulus at the onset of plateau modulus just after the main relaxation. Then we estimate the modulus of the matrix in which the inclusion of the resin rich phase play the role of fillers. From the ratio of the modulus of the R1 blends by this calculated modulus, and the theoretical modulus ratio estimated using Christensen-Lo (C-L) model (explained in chapter 2), one can then estimate the volume fraction of the resin rich phase. Results for both methods are reported in Table 5. 2. It predicts a very significant

volume fraction of resin rich phase in the SBR_R1_25_UC (20%vol.), and a huge amount of resin rich phase in the SBR_R1_45_UC (38%vol.), both higher than the values deduced from the Fox law (which may be partly explained by the fact that it assumes that the resin rich phase is made of 100% resin).

TABLE 5. 2 ESTIMATE OF THE VOLUME FRACTION OF THE RESIN RICH PAHSE IN THE SBR_UC BLENDS, FROM THE CHRISTENSEN AND LO MODEL, AND FROM THE FOX LAW APPLIED ON T_α.

Sample	Modulus M1[1], of the polymer rich phase (MPa)	Modulus, M2[2] of the blend (MPa) (E'_{DMA} at $Tan\ \delta_{min}$)	Reinforcement factor (M1/M2)	Resin rich phase vol% (in total blend) from C-L model)	Resin rich phase vol% (in total blend) from Fox law[3]
SBR_UC	3.14	3.14	-	-	-
SBR_R1_25_UC	1.70	4.3	0.40	20	9
SBR_R1_45_UC	0.85	6.4	0.13	37	29

[1] modulus of the polymer rich phase estimated from the modulus of SBR_UC at the plateau modulus onset of the SBR_UC and from the dilution law

[2] modulus of the blend at the onset of the plateau modulus (when the resin rich phase is rigid)

[3] see the supporting information for the details of the calculation

5.3 Influence of resin R1 on the curing reaction

Like in chapter 3 and 4 for SBR and R2 & R3 resin blends, DSC analysis also shows the presence of crystallized stearic acid in the SBR_R1_PC blends: in Figure 5. 7, a melting peak around 30-40˚C is observed on the DSC curves. The peak is also visible in the curves of the second heating ramp, but its shape is different due to a different thermal history as seen in the supporting information section of this chapter (Figure S5. 1). Like for the resin R2 and R3 blends, the temperature at the peak maximum decreases with the resin content, and the peak area decreases more rapidly than the acid stearic content in the formulation, which is likely due to a perturbation of the nucleation and growth of the crystallites by the resin molecules.

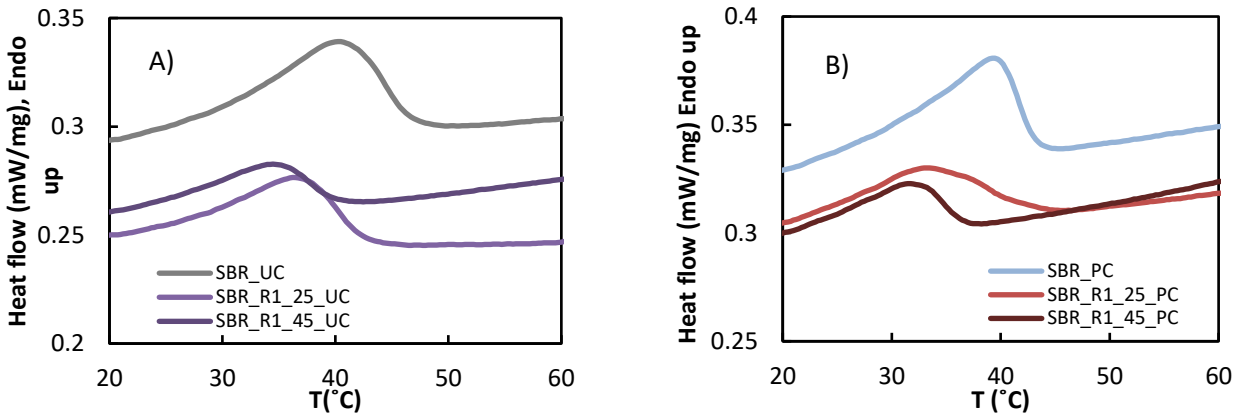

FIGURE 5. 7 DSC HEAT FLOW CURVES (2ND HEATING) VERSUS TEMPERATURE (T) OF: A) SBR_R1_UC BLENDS, AND B) SBR_R1_PC BLENDS.

As explained in chapter 3 for in SBR_SC, no peak around 40°C is observed for SBR_R1_SC blends as most of the stearic acid has reacted with ZnO to form a zinc stearate complex. In return, a melting peak around 100-110˚C related to this complex in SBR_R1_SC blends is shown in Figure 5. 8. The difference in the peak positions with the resin content, and its larger decrease than the one of the stearic acid content is also likely due to the perturbation of the crystallite nucleation and growth by the resin presence. This is confirmed by the DSC curves of the resin extracted materials (see supporting information, Figure S5. 2).

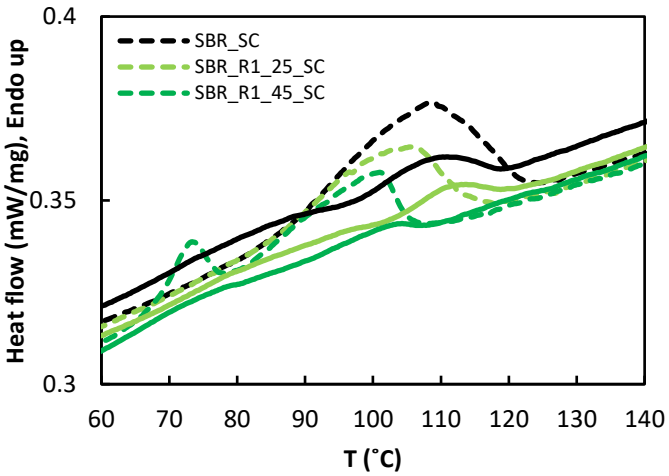

FIGURE 5. 8 DSC HEAT FLOW CURVES (DASHED LINES-1ST HEATING AND SOLID LINES-2ND HEATING) OF SBR_R1_SC BLENDS AT HIGHER TEMPERATURES.

The presence of zinc stearate complex in the crystallites form, like seen in the SBR_SC, is also confirmed by TEM observations in SBR_R1_SC blends as shown in Figure 5. 9.

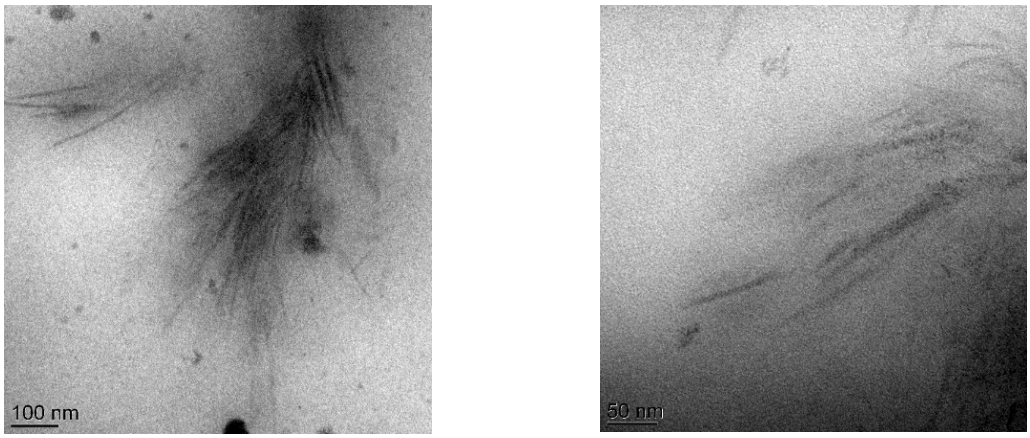

FIGURE 5. 9 TEM IMAGE OF MICROTOMED SBR_R1_25_SC (LEFT) AND SBR_R1_45_SC (RIGHT) HIGHLIGHTING ZINC STEARATE COMPLEX CRYSTALLITES.

The amount of soluble fraction for SBR_R1_SC blends, deduced from swelling experiment in cyclohexane (cf. chapter 2), is reported in Figure 5. 10 and compared to the resin fraction initially added to these blends. It is roughly equal. This indicates that most of the resin R1 can be extracted from the material, and confirm, like the previous experiments, that the chemical reactions involved during crosslinking involve little (not none of) the resin R1.

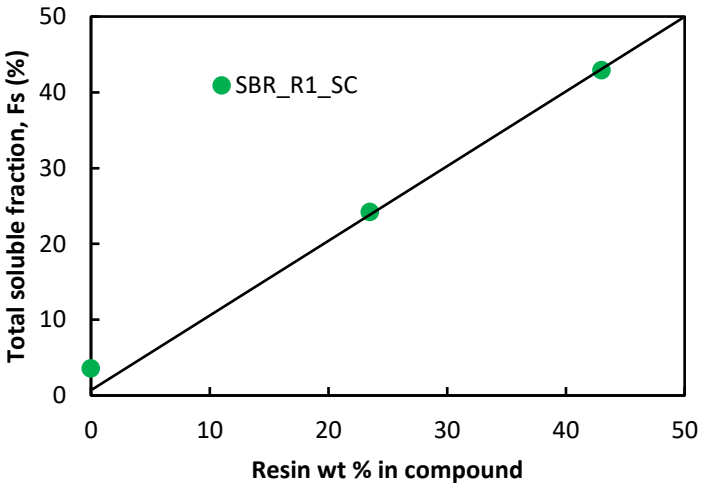

FIGURE 5. 10 TOTAL SOLUBLE FRACTION (IN CYCLOHEXANE) VERSUS RESIN FRACTION IN THE TOTAL COMPOUND IN SBR_R1_SC BLENDS.

Figure 5. 11 presents the loss factor, $Tan\ \delta$, as a function of the temperature obtained from DMA analysis for the uncrosslinked, peroxide cured and sulfur cured R1 blends. As previously discussed in chapter 3 (for pure SBR) and chapter 4 (for R2 and R3 blends), sulfur curing leads to a T_α shift, visible on the curves, that we ascribed to the restriction of the polymer mobility by the crosslinks and/or to the chemical modifications of the polymer chains. This shift is also confirmed by the DSC analysis (Figure 5. 12). Such shift is not observed with peroxide curing (for which the low

chemical crosslinks amount it creates makes difficult any definitive conclusion on this absence of shift).

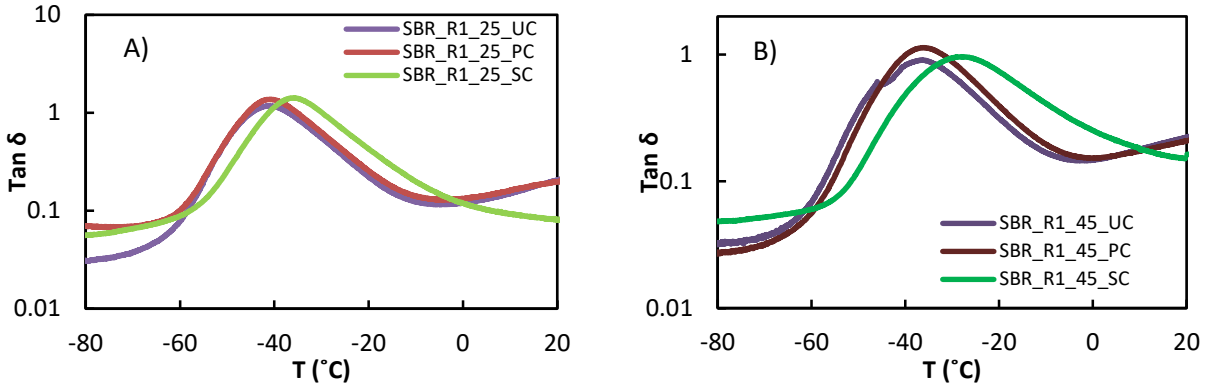

FIGURE 5. 11 DMA LOSS FACTOR (Tan δ) VERSUS TEMPERATURE (T) OF A) SBR_R1_25 AND B) SBR_R1_45 BLENDS.

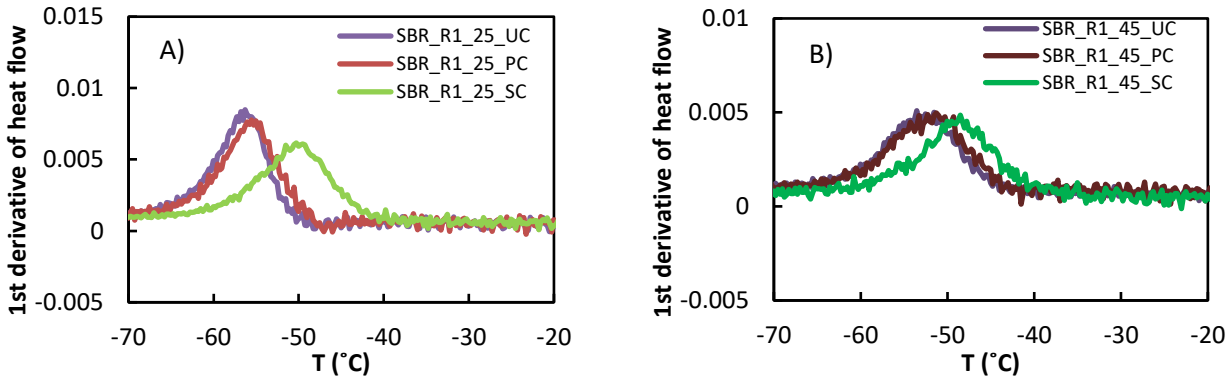

FIGURE 5. 12 DSC 1ST DERIVATIVE OF HEAT FLOW (2ND HEATING) VERSUS TEMPERATURE (T) OF A) SBR_R1_25 AND B) SBR_R1_45 BLENDS.

All the previous results suggest that the resin R1 does not seem to strongly impact the chemical reactions of crosslinking. DSC and DMA analysis have been performed on sulfur crosslinked SBR and R1 blends from which the resin have been extracted after swelling. As shown on Figure 5. **13**, these materials show the same T_g and T_α, confirming our analysis.

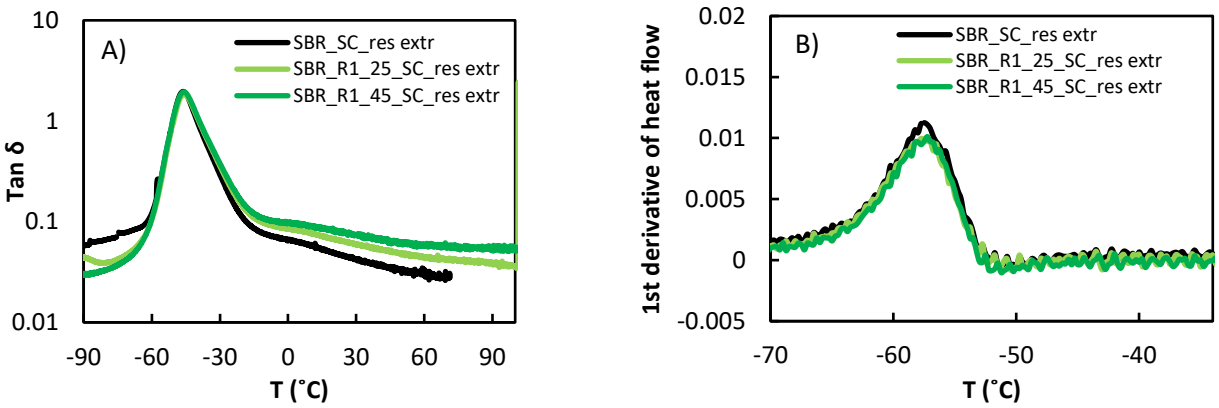

FIGURE 5. 13 **A) DMA LOSS FACTOR (Tan δ) AND B) DSC 1ST DERIVATIVE OF HEAT FLOW (2ND HEATING) VERSUS TEMPERATURE (T) OF SBR_R1_SC_RES EXTR SAMPLES. PROPERTIES OF THE CURED BLENDS**

5.3.1 Glass transition

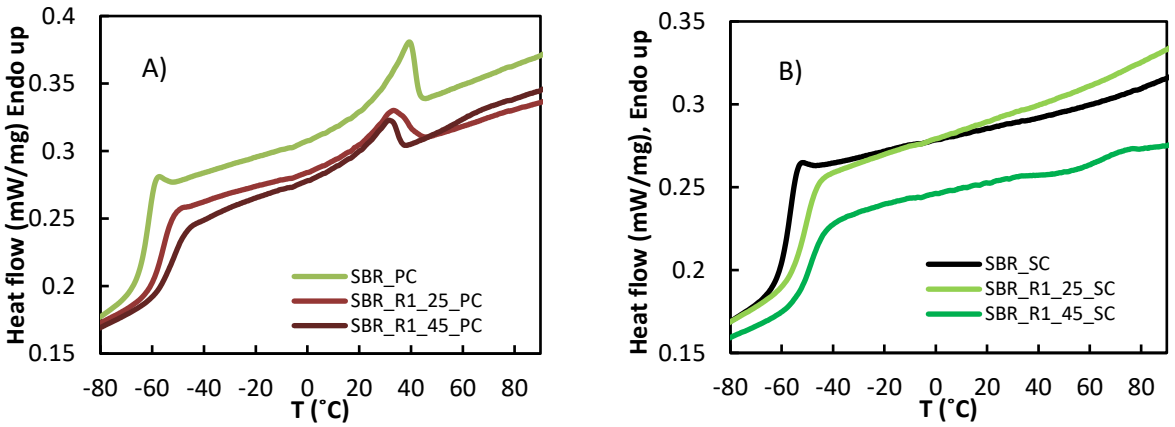

FIGURE 5. 14 DSC HEAT FLOW CURVES (2ND HEATING) VERSUS TEMPERATURE, T, OF A) SBR_R1_PC, AND B) SBR_R1_SC BLENDS.

Figure 5. 14 present the DSC curves of the PC and SC SBR_R1 blends. The T_g shift is the consequence of the resin R1 presence (already discussed in section 5.2) and of the influence (for SC, shift of 5°C) or not (for PC, no shift) of the crosslinking reactions. The phase separation still exists after crosslinking and does not seem much impacted by this reaction, as evidenced by the still strong disagreement between the T_g deduced from the Fox law equation and the experimental ones, especially with 45wt.% resin (cf. Figure 5. 15). In addition, another transition is still observed around 60˚C in both SBR_R1_45 blends, that can again be ascribed to the glass transition of the resin rich separated phase.

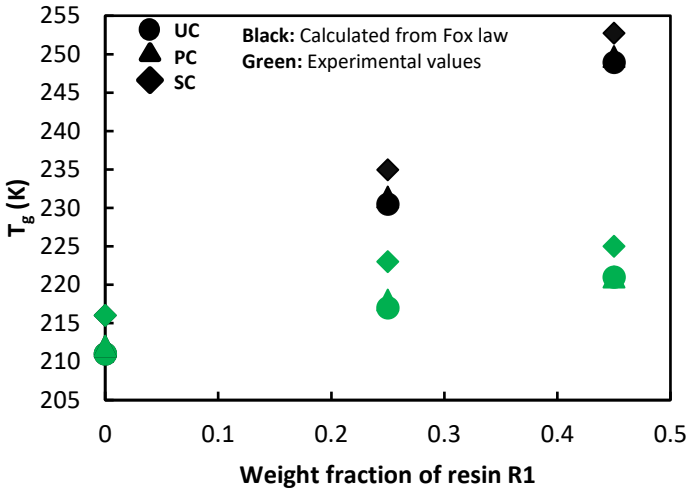

FIGURE 5. 15 EXPERIMENTAL T_g FROM DSC AND CALCULATED FROM FOX LAW VERSUS TOTAL RESIN AMOUNT IN THE UC, PC, AND SC SBR_R1_BLENDS.

5.3.2 Viscoelastic behaviour

As expected, the DMA curves of the SBR_R1_PC and SBR_R1_SC blends (cf Figure 5. 16 and Figure 5. 17) show a broadening of the temperature domain of the alpha relaxation, an increase of the modulus in the rubbery plateau regime for the highest resin content (ascribed to the presence of the glassy resin rich phase) and a modulus drop when the resin rich phase becomes soft. Note that one can also observe a supplementary $Tan\ \delta$ peak at around 110°C, and a corresponding small modulus drop for the materials with 45wt.% resin (sulfur and peroxide crosslinked). Further investigation would be necessary to understand its origin. It may come from the melting of a crystallized phase inside the resin rich phase, as suggested by some AFM and TEM images, as discussed in the next section dedicated to the microstructural characterization. This would be consistent with the melting peak observed on the DSC curve of the SBR_R1_45_SC (see Figure S5. 3 in supporting information section).

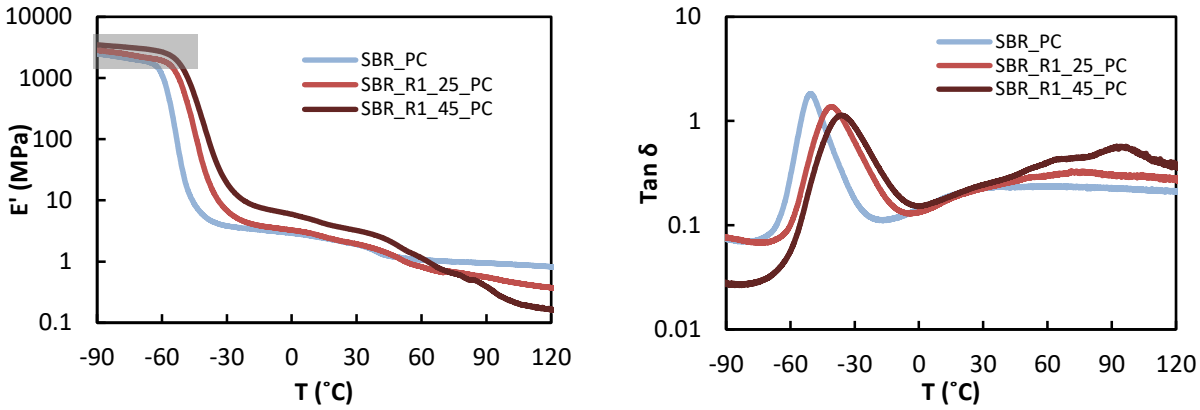

FIGURE 5. 16 STORAGE MODULUS (E') AND LOSS FACTOR (Tan δ) VERSUS TEMPERATURE (T) OF SBR_R1_PC BLENDS.

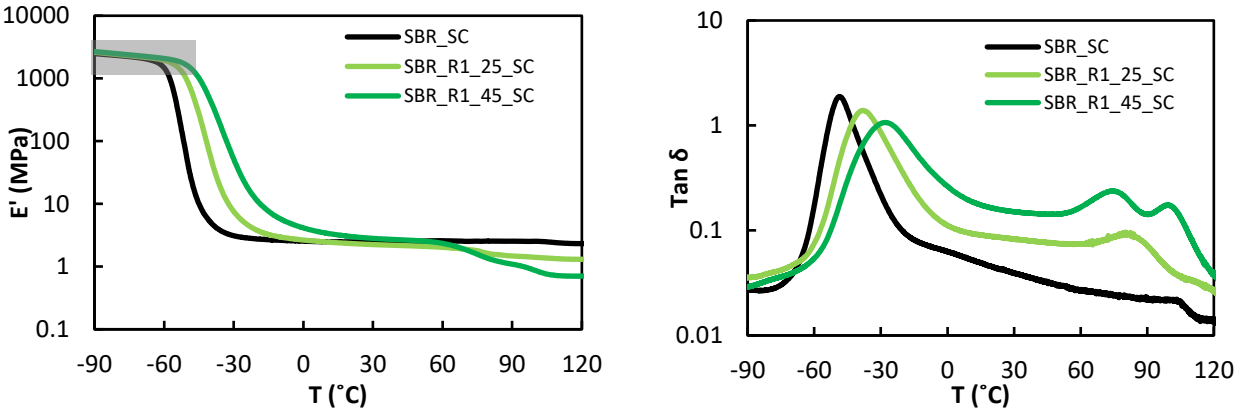

FIGURE 5. 17 STORAGE MODULUS (E') AND LOSS FACTOR (Tan δ) VERSUS TEMPERATURE (T) OF SBR_R1_SC BLENDS.

Like for the uncrosslinked blends we also compared the experimental T_α of the crosslinked blends to predictions of the Fox law (cf. Figure 5. 18). Conversely to what we observed for resin R2 and R3, applying the Fox law to T_α does not enable better prediction than when it is applied to the T_g. These comparisons could suggest that the crosslinking reactions do not change the T_g and T_α of the SBR rich phase more than it changes those of the SBR without resin, i.e. that it does not influence the phase separation. We will see later that this is not so simple.

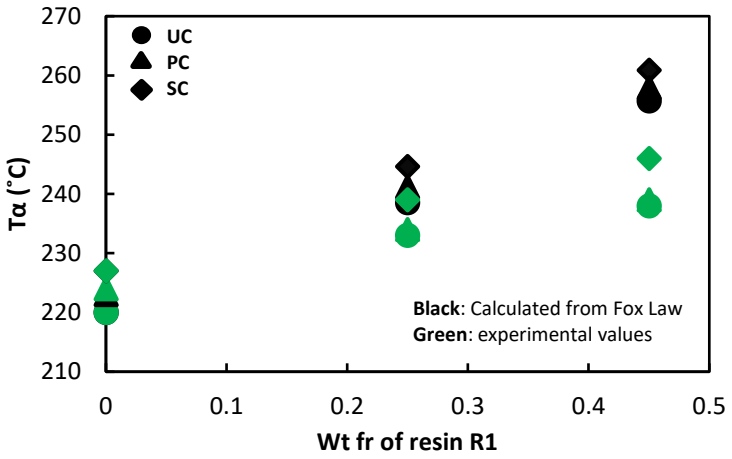

FIGURE 5. 18 T_α OF R1_SBR BLENDS CALCULATED FROM FOX LAW OR MEASURED FROM DMA, VERSUS RESIN R1 WEIGHT FRACTION.

5.3.3 About the modulus above T_α

The modulus of the R1 blends results from the mechanical response of the SBR matrix swollen by part of the miscible resin and reinforced (when it is glassy) by a resin rich phase. Let's first focus on the modulus of the SBR rich phase in the sulfur crosslinked blend. Trapped entanglements and chemical crosslinks concentration is small in the materials, as shown in Figure 5.19A where the elastically active chains concentration (EAC) deduced from swelling measurement is reported. This concentration decreases when the resin content increases, in a very similar way to what we observed with the resin R2, i.e. more rapidly than with the resin R3. Thus, the resin R1 may perturb, actually inhibit, some chemical crosslinking reactions during curing.

The disappearance of any relaxation on the plateau modulus of the resin extracted samples, shown in Figure 5.19B, confirm the reinforcing role of a glassy resin rich phase in the non extracted sample. The modulus evolution of the resin extracted sample, with the initial resin content is also consistent with NMR measurements (cf. Figure 5.19C, the NMR data treatments of SBR_R1_SC_res extr blends are presented in Figure S5. 5, Figure S5. 6, and Figure S5. 7 in supporting information section of this chapter). Moreover, the very low values of the EAC density deduced from swelling experiment compared to the values of the plateau modulus of the SC resin extracted blend indicates that a large part of this modulus results mainly from the elastically active chains created by untrapped entanglements which are formed after resin extraction, when the samples are dried.

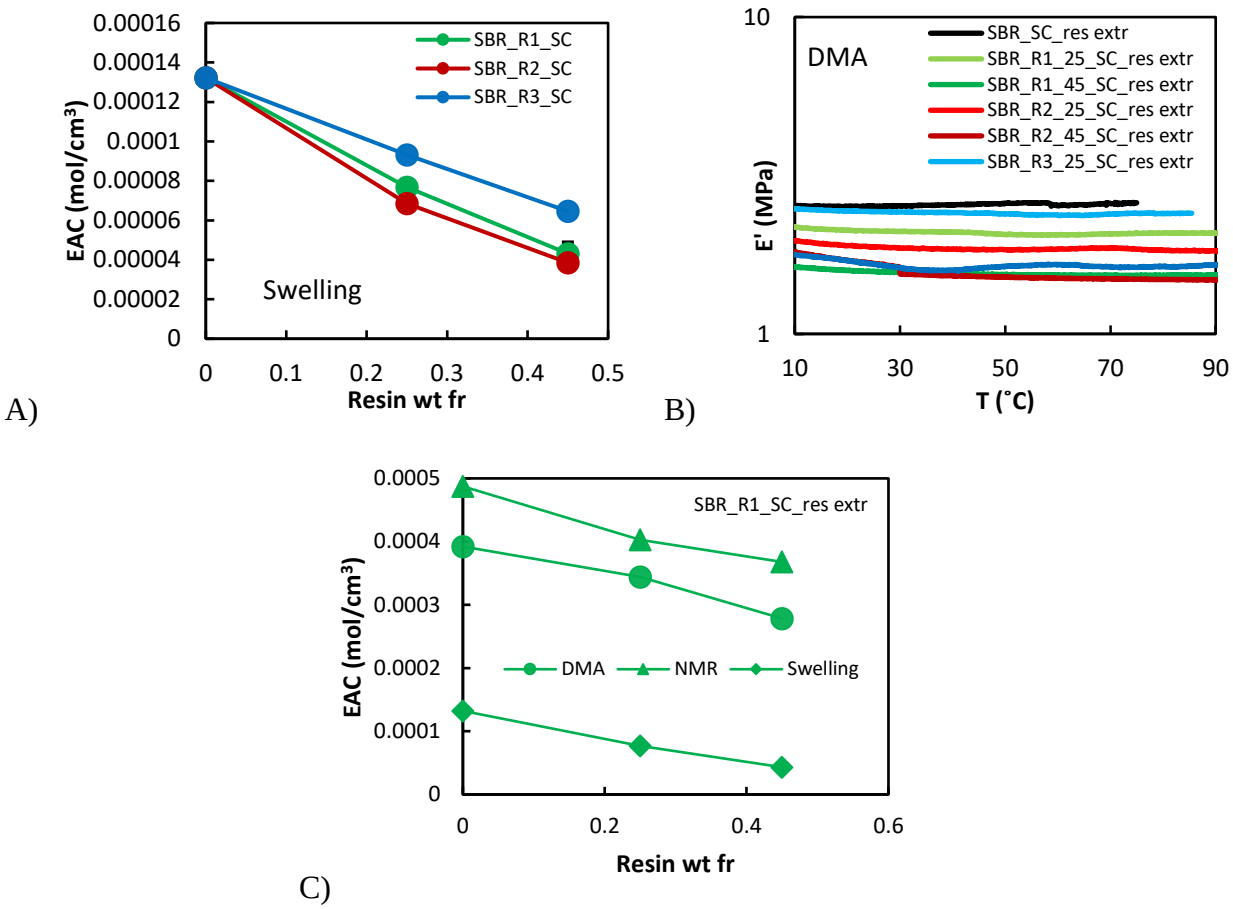

FIGURE 5.19: A) ELASTICALLY ACTIVE CHAINS DENSITY (EAC) DEDUCED FROM SWELLING MEASUREMENTS FOR THE BLENDS WITH DIFFERENT RESIN AS A FUNCITON OF THE RESIN WT%, B) DMA STORAGE MODULUS, E', VERSUS TEMPERATURE, T, OF SBR_R1_SC_RES EXTR BLENDS C) ELASTICALLY ACTIVE CHAINS DENSITY DEDUCED FROM SWELLING, MODULUS VALUES AND NMR, VERSUS RESIN WT% FOR THE SBR-R1_SC_RES EXTR SAMPLES.

The evolution of the plateau modulus is very different in the non-extracted sample. The DMA curves comparing the UC, SC and PC SBR_R1 blends are plotted on Figure 5. 20. The moduli in the rubbery plateau measured just after the main relaxation for the minimum Tan δ value, are reported in Figure 5. 21. It shows that the more the R1 blend is crosslinked, the lower the maximum value of the modulus after the glass transition (even though, of course, crosslinking increases the modulus at higher temperature, in the flow domain). The nominal stress strain curves at ambient temperature confirm this result (cf. Figure 5. 22). This suggests that crosslinking inhibits the phase separation and thus, reduces the amount of rigid phase at ambient.

This modification of the phase separation could lead to a modification of the composition of the polymer rich phase and of the resin rich phase. We have previously seen that the T_g modification by the crosslinking process is similar with and without the resin R1 presence. This may indicate that the composition of the polymer rich phase is not changed, which therefore implies that given

the increase of the amount of this phase, the fraction of the resin in the resin rich phase increases, and therefore its glass transition temperature. This is quite consistent with the comparison between the DMA curves of the UC, PC and SC SBR_R1 blends (Figure 5.20).

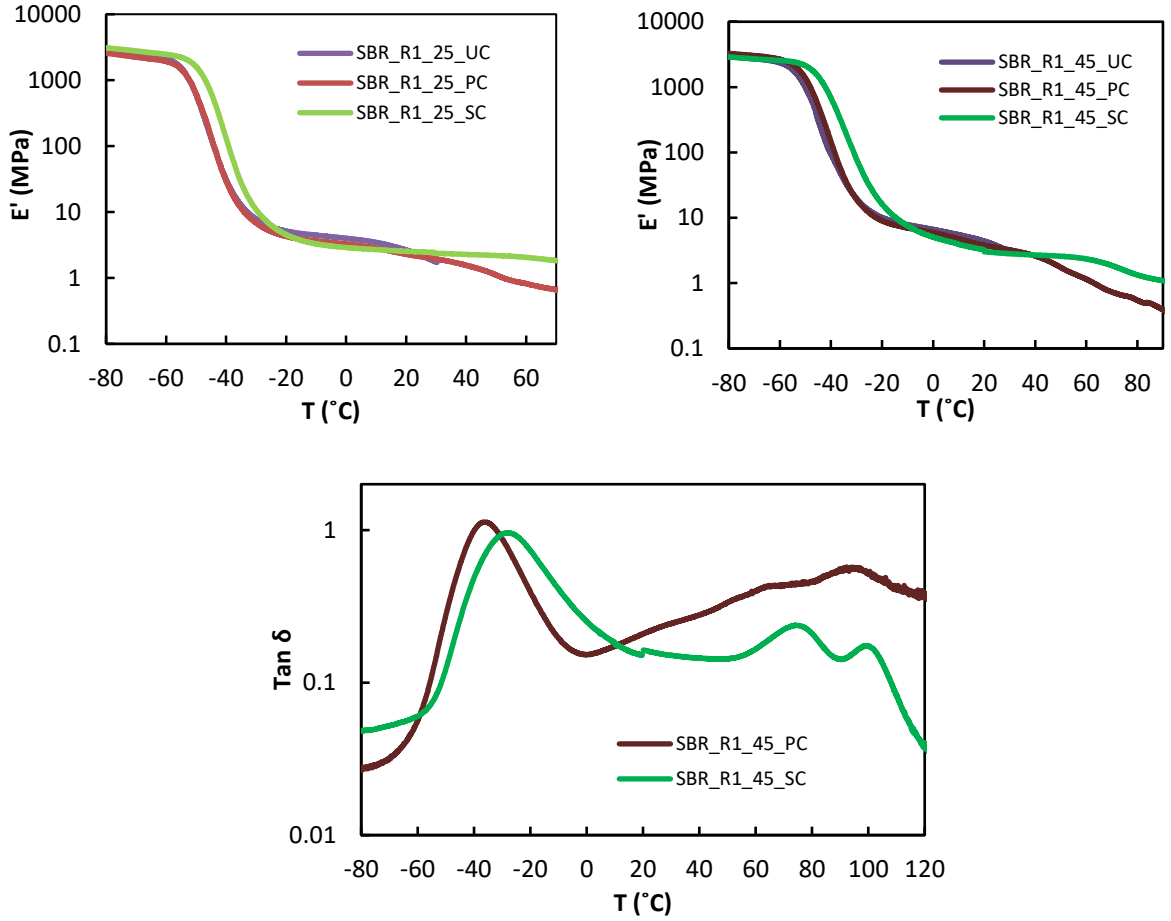

FIGURE 5. 20 STORAGE MODULUS (E') VERSUS TEMPERATURE (T) OF SBR_R1_25 AND SBR_R1_45 BLENDS WITH UC, PC, AND SC SYSTEMS.

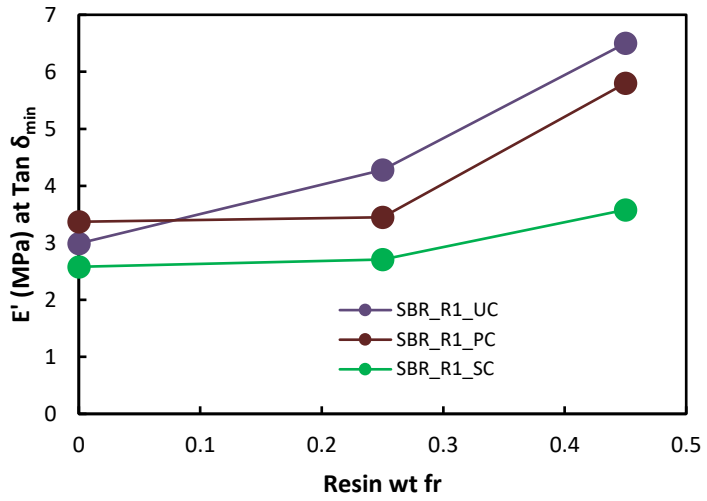

FIGURE 5. 21 STORAGE MODULI OF R1 BLENDS MEASURED FROM DMA JUST AFTER THE MAIN RELAXATION AT $Tan\ _{\delta\ min}$ VERSUS RESIN R1 WEIGHT FRACTION.

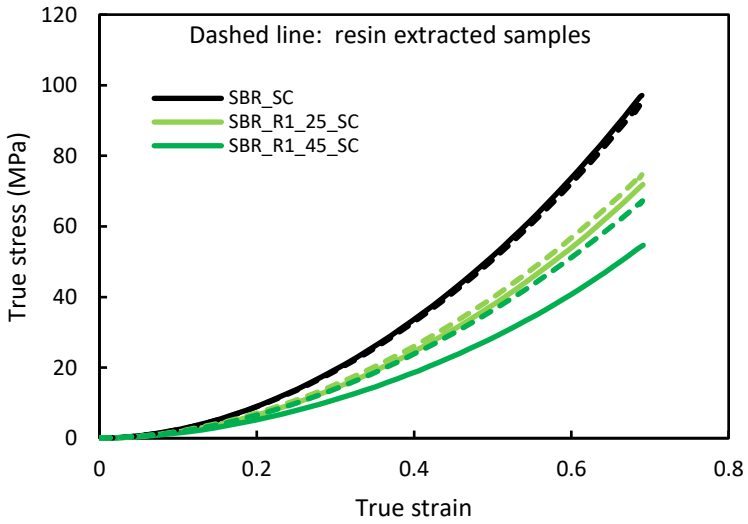

FIGURE 5. 22 TRUE STRESS VERSUS TRUE STRAIN OF SBR_R1_SC SAMPLES.

The ratio of the DMA modulus at the onset of the plateau modulus, just after the main relaxation (in the case of SC blend, $Tan\ \delta_{min}$ cannot be determined after the main relaxation) i.e. when the resin rich phase is completely rigid, by the one at 120°C (when all the rigid phase has softened), is then used to estimate the volume fraction of the phase separated resin rich domains. We use for that the theoretical modulus ratio estimated using Christensen-Lo (C-L) model (explained in chapter 2). The deduced estimated volume fractions of the rigid phase in the SBR_R1_SC blends are given in the Table 5. 3. They are 6% lower in SBR_R1_SC compared to SBR_R1_UC (see Table 5. 2). Thus, SC crosslinking seems to reduce significantly, by around 30% the phase separation that occurs in the SBR_R1_UC blends. [3 4 5]

TABLE 5. 3 MODULUS RATIO AND IMMISCIBLE RESIN VOLUME FRACTION ESTIMATED FROM CHRISTENSEN-LO (C-L) MODEL IN THE SBR_R1_SC BLENDS.

Sample	Modulus, M2 (MPa) (E'_{DMA} at the onset of plateau modulus just after main relaxation)	Modulus, M3 (MPa) (E'_{DMA} at 120˚C)	Modulus ratio (M3/M2)	Resin rich phase in total blend, c, (vol%) (C-L model)
SBR_SC	2.50	2.32	0.93	-
SBR_R1_25_SC	2.75	1.41	0.51	14
SBR_R1_45_SC	3.30	0.70	0.21	30

5.4 Resin structuration in blends

5.4.1 Morphological analysis by imaging

5.4.1.1 Micron scale observations

Figure 5. 23 shows TEM and SEM images of SC R1 blends. They highlight the presence of micron size domains. Their size, which vary on the images in the domain 0.5-5 μm, and their number increases with the resin content. These results are supported by AFM images (see Figure 5. 24A). In addition, we have also observed resin extracted SB1_R1_45_SC sample by AFM (cf. Figure 5. 25Figure 5. 24B) and by SEM Figure 5. 25. Holes are clearly visible after resin extraction which confirms that the micron size domain are mainly (if not totally) made of the resin R1.

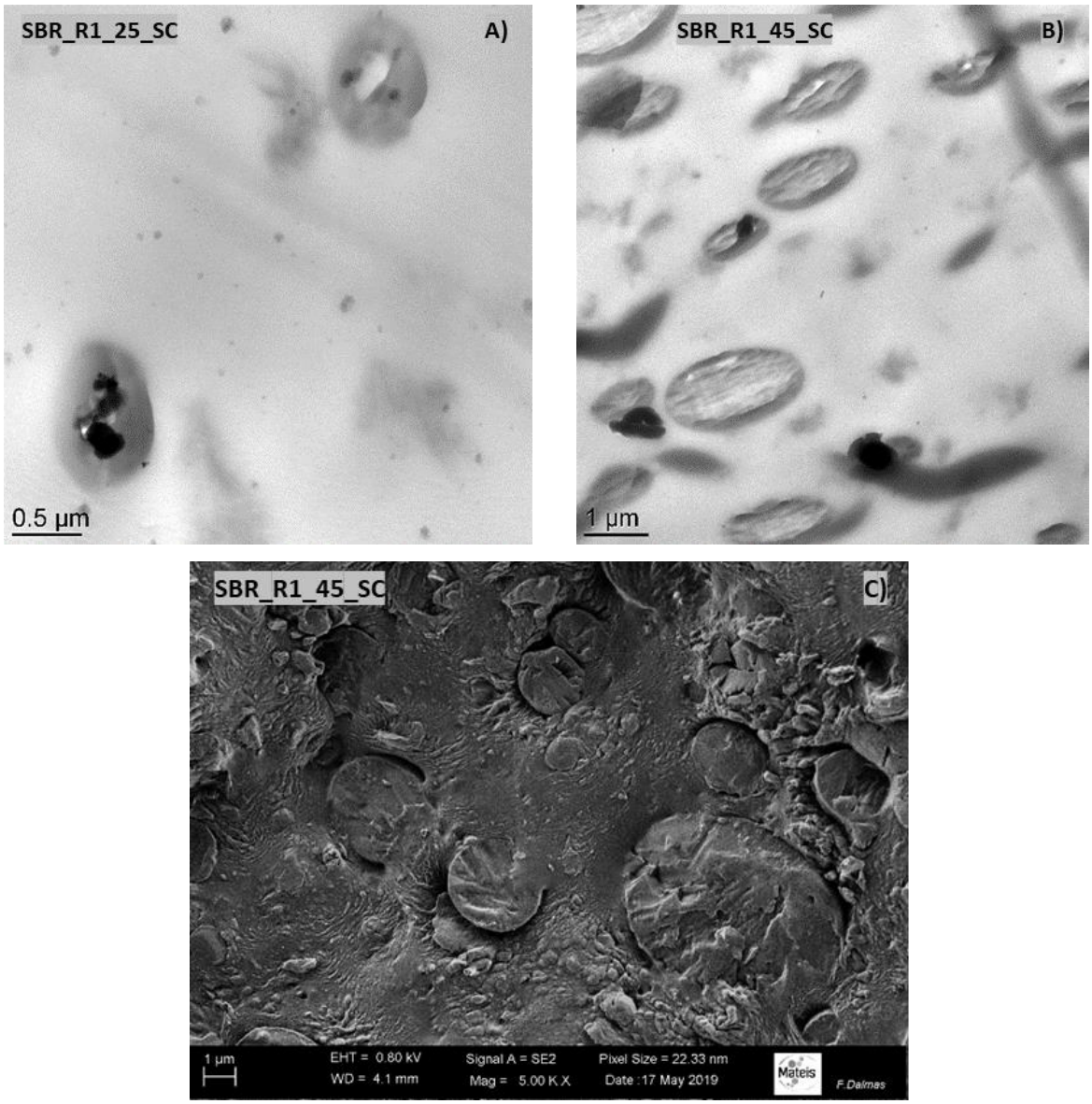

FIGURE 5. 23 A) TEM IMAGE OF SBR_R1_25_SC BLEND, B) TEM IMAGE OF SBR_R1_45_SC BLEND, AND C) SEM IMAGE OF CRYO-FRACTURED SBR_R1_45_SC BLEND.

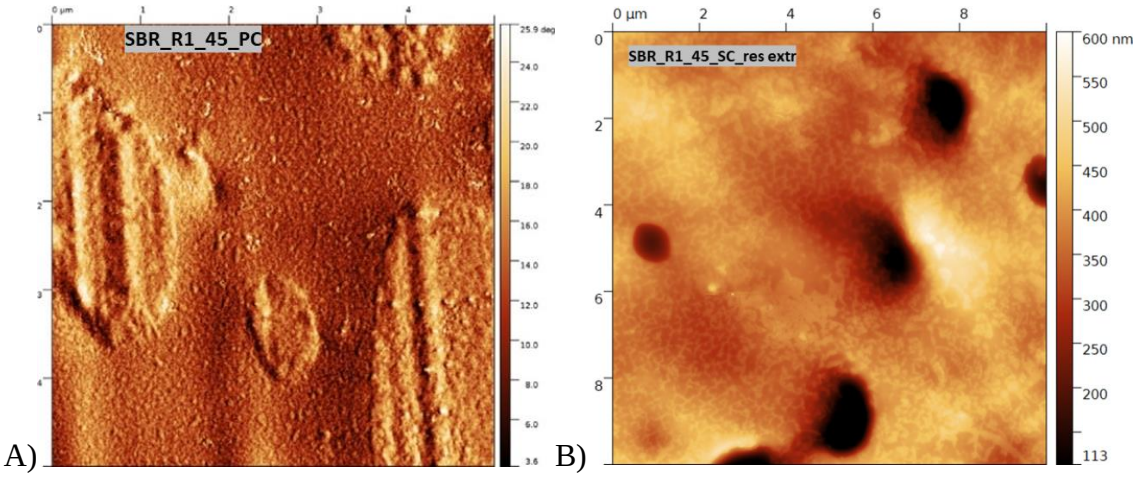

FIGURE 5. 24 A) AFM PHASE IMAGE OF THE SBR_R1_45_PC BLEND, B) AFM HEIGHT IMAGE OF A RESIN EXTRACTED SBR_R1_45_PC BLEND.

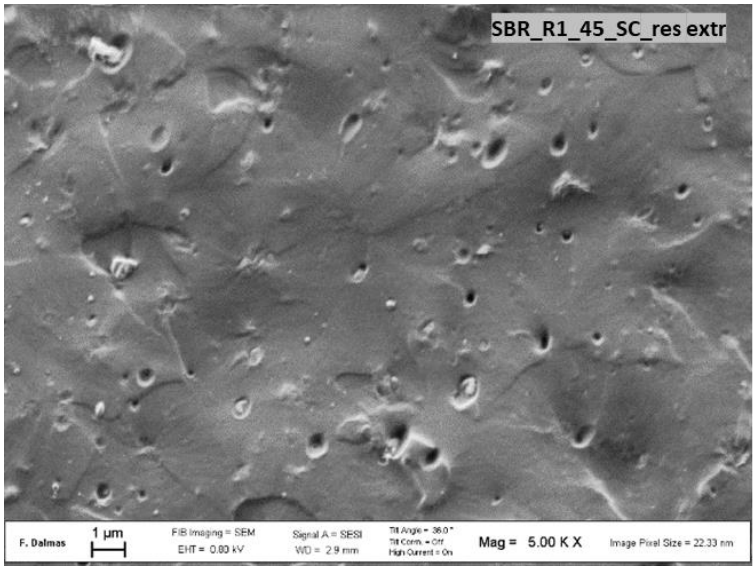

FIGURE 5. 25 SEM IMAGE OF A RESIN EXTRACTED SBR_R1_45_SC SAMPLE.

5.4.1.2 Nano-scale observations

We have also performed TEM imaging of the SBR_R1_45_SC sample at a lower scale, focusing on the microdomains. As seen in Figure 5. 26, nano-scale heterogeneities are visible inside the microdomains, which may be due to the crystallization of some peculiar molecules of the resin, as suggested by the previous DSC and DMA results.

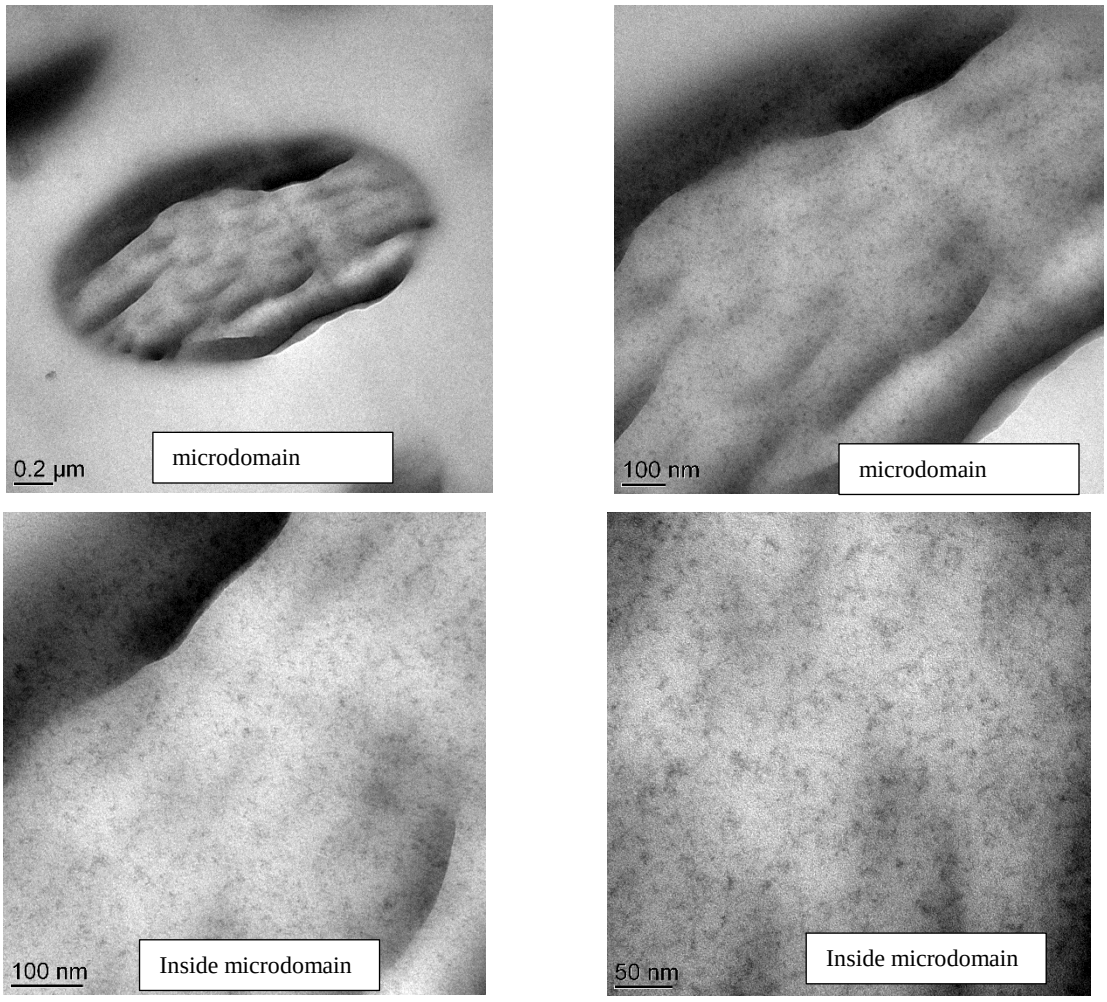

FIGURE 5. 26 TEM IMAGES OF SBR_R1_45_SC BLENDS

In addition, we observed at a lower scale by AFM, SBR_R1_25_SC and SBR_R1_45_SC blends, focusing on the phase outside the microdomains (cf. Figure 4. 27 and Figure 5. 28). The images, though quite different for the two resin contents (note that the two scales are different), shows that the materials are nanostructured but less homogeneously in SBR_R1_45_SC. The plot of an intensity profile over the lines drawn on the images enables to evidence a characteristic distance of the nanostructure. This one is roughly equal to 15 nm and 25 nm for respectively SBR_R1_25 and SBR_R1_45_SC. This distance is however less than the one found in SBR_SC (30 nm) or R2 and R3 SC blends (30-90 nm).

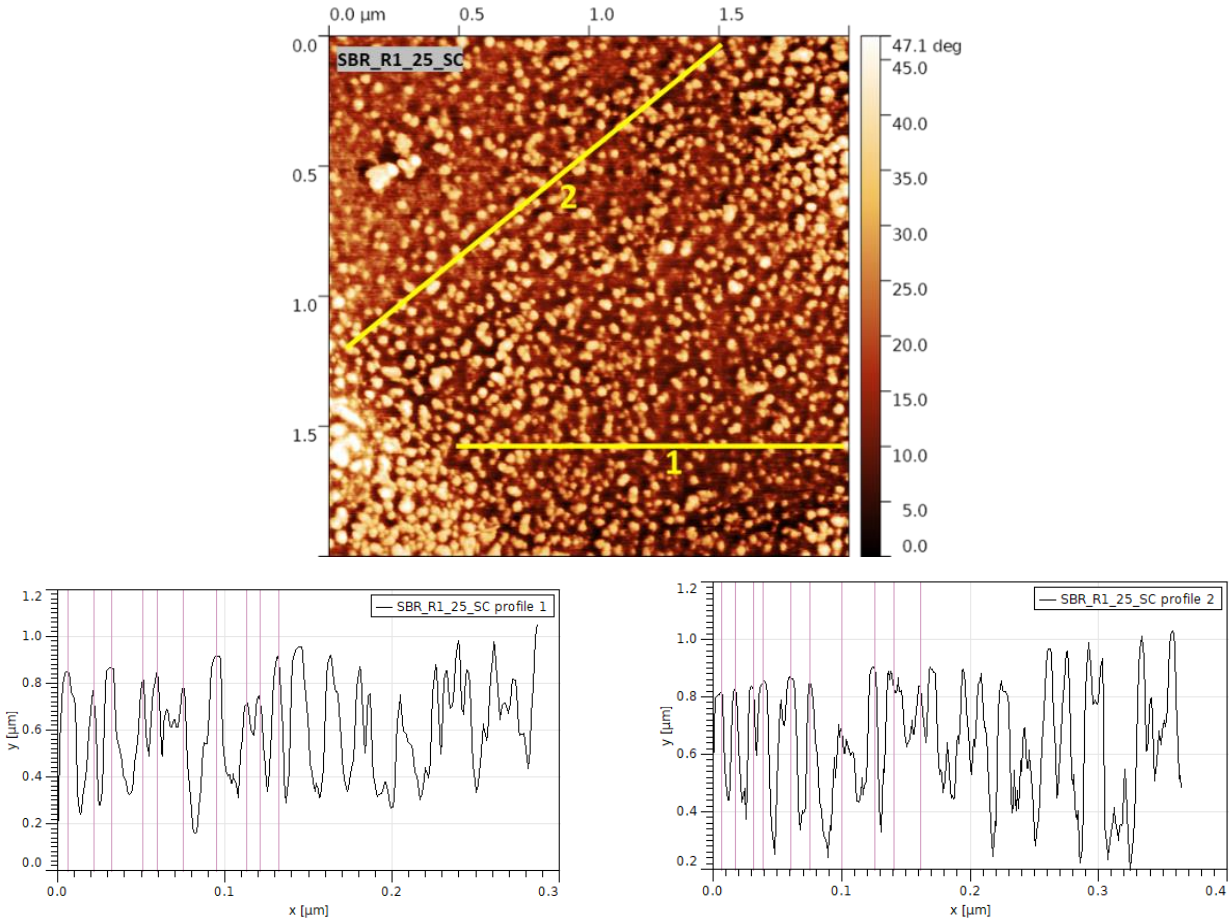

FIGURE 5. 27 AFM PHASE IMAGES AND INTENSITY PROFILE OVER THE YELLOW LINE FOR SBR_R1_25_SC BLEND.

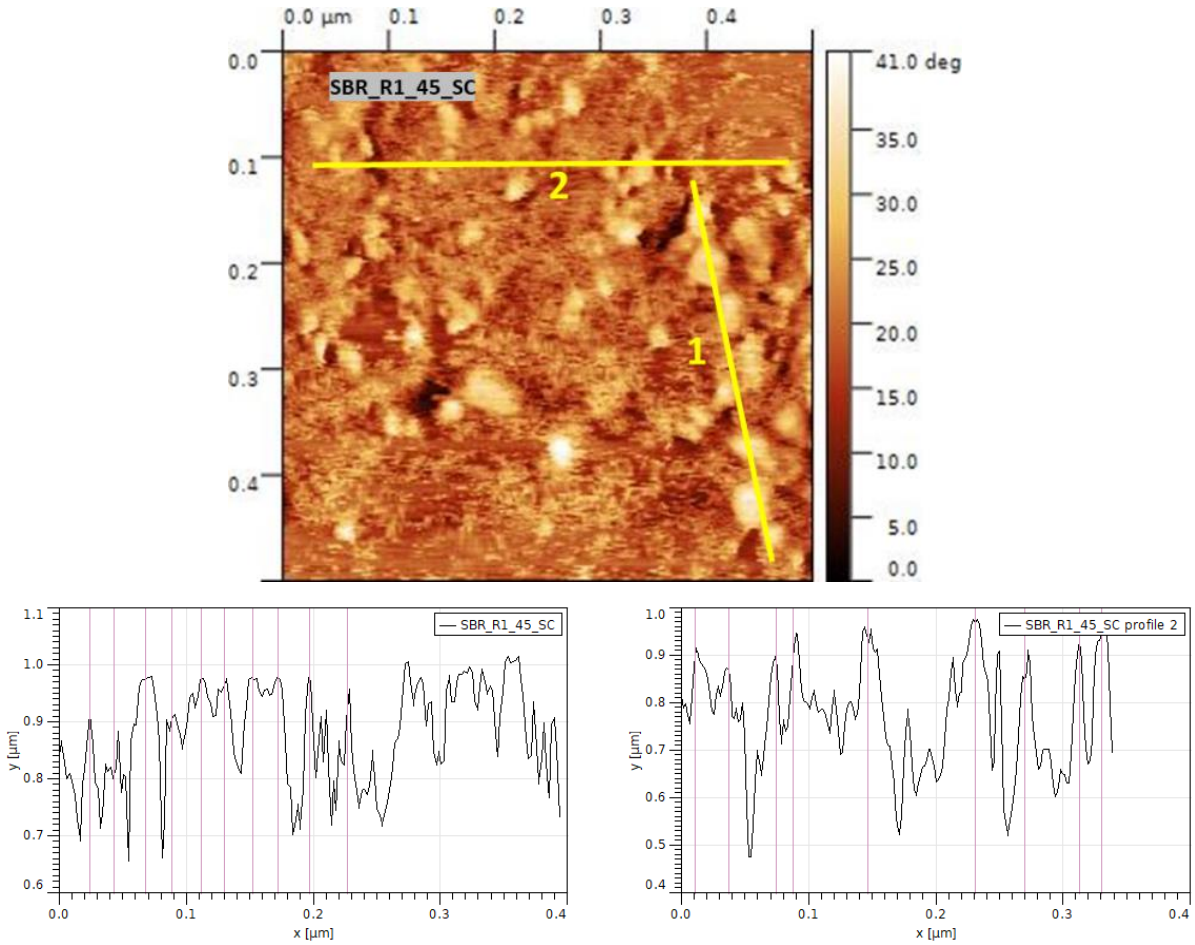

FIGURE 5. 28 AFM PHASE IMAGES AND INTENSITY PROFILE OVER THE YELLOW LINE FOR SBR_R1_45_SC BLEND.

Figure 5. 29 shows AFM phase image of SBR_R1_25_SC_res extr with the intensity profiles extracted along the yellow line drawn on the image. The correlation distance is found to be 22 nm, which is less than the one found for R2 and R3 resin extracted samples.

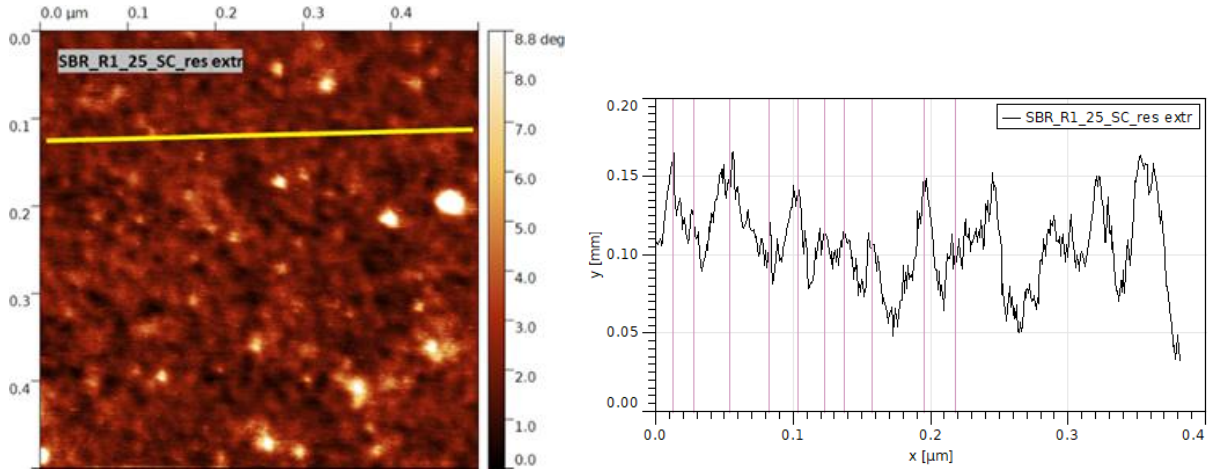

FIGURE 5. 29 AFM PHASE IMAGE AND INTENSITY PROFILE OVER THE YELLOW LINE FOR SBR_R1_25_SC_RES EXTR SAMPLE.

Figure 5. 30 and Figure 5. 31 show the AFM phase images of SBR_R1_25_PC and SBR_R1_45_PC respectively. Microdomains (see Figure 5. 31) and nanodomains seen in R1 SC blends are also visible in R1 PC blends. The correlation distance is found to be 25 nm and 30 nm for R1 25 and R1 45 PC samples respectively which is slightly higher than the values found for R1 SC blends.

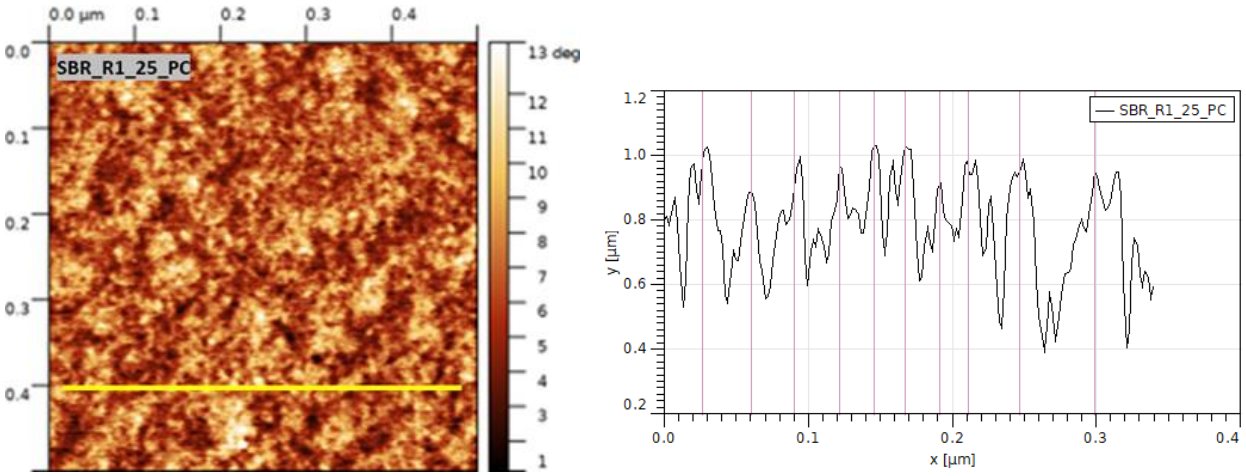

FIGURE 5. 30 AFM PHASE IMAGES AND INTENSITY PROFILE OVER THE YELLOW LINE FOR SBR_R1_25_PC BLEND.

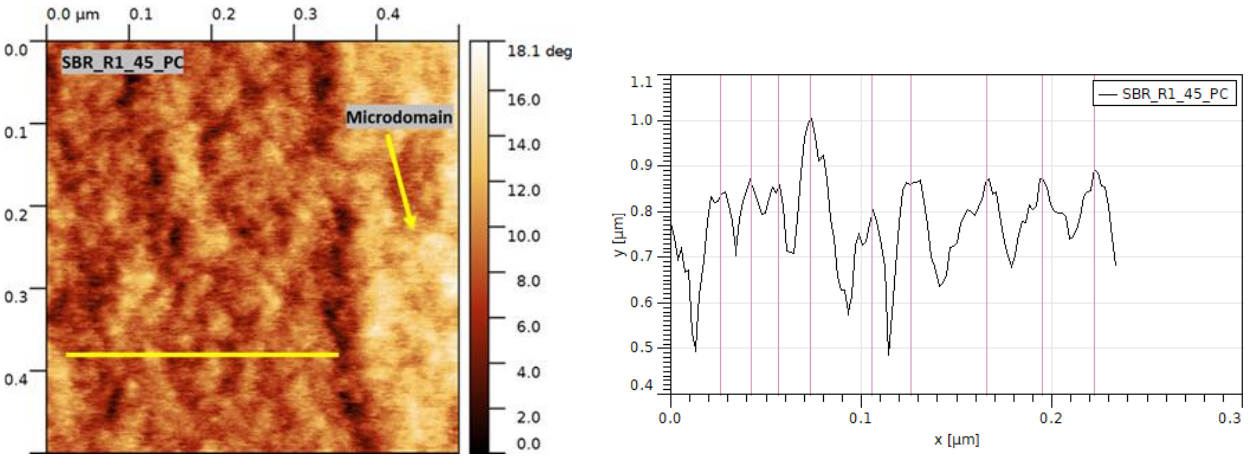

FIGURE 5. 31 AFM PHASE IMAGES AND INTENSITY PROFILES OVER THE YELLOW LINE FOR SBR_R1_25_PC BLEND.

Whether SBR_R1_PC blends phase separate differently than the SBR_R1_SC for the same amount of resin content, or not, the morphological analysis done on SC and PC R1 blends does not help to clarify it. For this reason, we also performed SAXS analysis of the UC and PC blends (it is not possible to do the experiments with sulfur crosslinking, since the ZnO particle scatter too much).

5.4.2 SAXS analysis

Uncrosslinked blends

Figure 5. 32 shows the SAXS profiles of the SBR_R1_UC blends. As expected, a sharp peak around q value of 1.6 nm^{-1}, attributed to the zinc stearate crystallites in chapter 4, is also present. However, in contrast with the R2 and R3 blends, there is no increase, with the resin content, of the intensity in the q range [0.2 to 6 nm^{-1}]. In the low q domain (q lower than 0.001 nm^{-1}), the $I(q)$ slope slightly decreases with the resin concentration down to a q^{-4} decrease of the intensity, which look like the signature of microdomains with a sharp interface, i.e. of microdomains similar to the ones seen in AFM in the SBR_R1_SC blend.

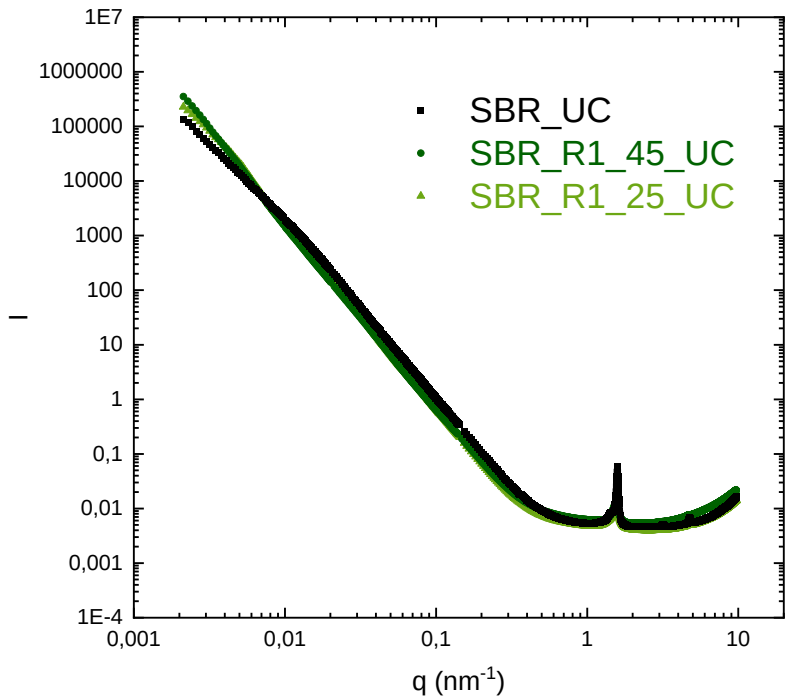

FIGURE 5. 32 SAXS PATTERNS OBTAINED ON THE SBR_UC AND SBR_R1_UC BLENDS.

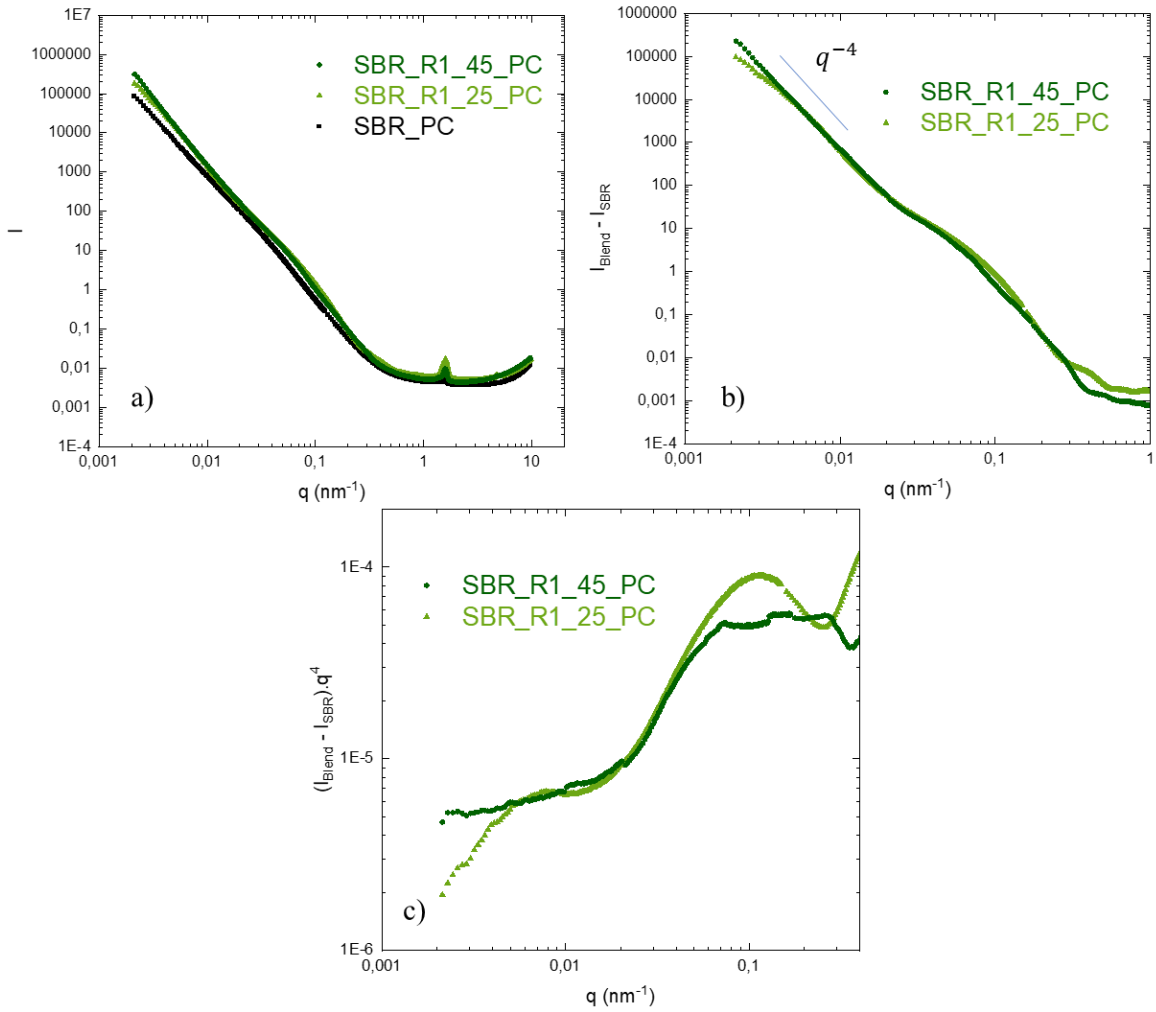

FIGURE 5. 33 SAXS PATTERNS OBTAINEDS ON SBR_PC AND SBR_R1_PC BLENDS : (A) $I = f(q)$, (B) CORRESPONDING INTENSITY PATTERN AFTER SUBSTRACTION OF THE SBR_PC SIGNAL, $I_{Blend} - I_{SBR} = f(q)$ AND (C) CORRESPONDING $(I_{Blend} - I_{SBR})q^4 = f(q)$ PLOT

The same decrease of the slope at low q is observed in the SBR_R1_PC blends (cf. Figure 5. 33). This is more highlighted in this q range by subtracting the pure SBR scattering signal to the blend ones, on the $(I_{Blend} - I_{SBR}) = f(q)$ plot on Figure 5. 33b. Here again, it confirms the presence of separated resin-rich microdomains with a sharp interface and whose size increases with resin content (as suggested by the slight shoulder observed at very low q with 25 wt% of resin, which should exist at lower q with 45wt% resin). In addition, one observes the appearance of a bump for q around 0.1 nm^{-1} in presence of resin. The $(I_{Blend} - I_{SBR})q^4 = f(q)$ highlights indeed a correlation peak arising around $q^* = 0.075\, nm^{-1}$ for both R1 blends, corresponding to a correlation distance of 84 nm. As previously suggested by AFM observations, it may correspond to resin-rich nanodomains. However, the q domain of their correlation distance is also close to the

one in which we observed a bump on the saxs curve of the SBR_PC sample. This means that these nanodomains are also related to heterogeneities of crosslinking created during the crosslinking process. One can propose the following scenario: when the material is PC cross-linked, the resin at the high temperature in the molten form, which is partly immiscible, is separated in small droplets and remains captured in the three-dimensional cross-linked network upon cooling. When even higher cross-links are introduced as in case of SBR_R1_SC blends, one can assume that more small droplets are stabilized into the three-dimensional network. This is supported by the AFM images, where correlation distance between nanoparticles in SBR_R1_25_SC blend was comparatively lower than in the SBR_R1_25_PC blend. This hypothesis however further needs to be investigated.

5.5 Effect of heating on nanostructuration

We also investigated the effect of heating on these nanostructuration in the SBR_R1_PC blends. We performed in-situ SAXS experiments on the sample during a heating ramp (10˚C/min) from room temperature to 110˚C followed by a cooling (10˚C/min) to room temperature with the isothermal time of 2 min at each temperature. The intensity (I) versus scattering vector (q) curves of SBR_R1_25_PC and SBR_R1_45_PC blends are shown in Figure 5. 34 and Figure 5. 35 respectively. The curves without any "+ sign" represent the first SAXS analysis at 25˚C. Then the curves with the single "+ sign" correspond to the sample heated up to 110˚C, rapidly cooled down to the ambient temperature and tested at 25˚C. The curves with the double "++ sign" correspond to the same sample tested at 25˚C, 1 month after its thermal treatment.

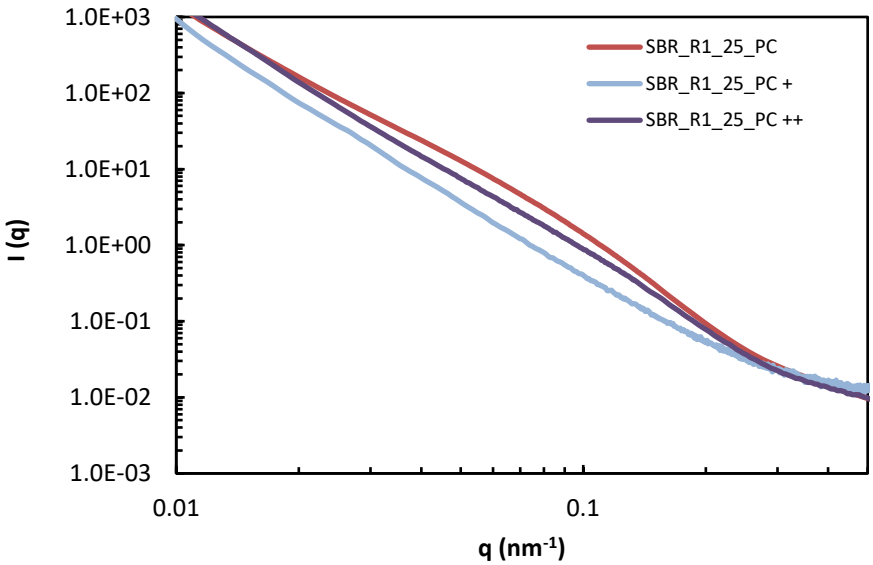

FIGURE 5. 34 SAXS PATTERNS OBTAINED ON SBR_R1_25_PC BLEND AT DIFFERENT TEMPERATURES AND TIMES (SEE THE TEXT FOR EXPLANATION OF THE DIFFERENT CURVES).

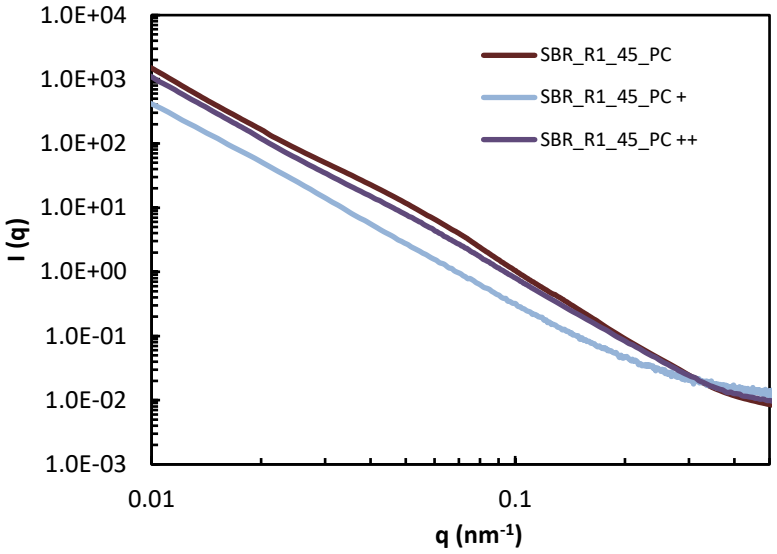

FIGURE 5. 35 PATTERNS OBTAINED ONSBR_R1_45_PC BLEND AT DIFFERENT TEMPERATURES AND TIMES (SEE THE TEXT FOR EXPLANATION OF THE DIFFERENT CURVES).

During the heating ramp, for temperature above 50°C, we observed on the SAXS curve of the resin blend a disappearance of the bump seen in Figure 5. 33 around $q = 0.1\ nm^{-1}$. This bump does not immediately reappear when the temperature returns to 25˚C in both SBR_R1_25_PC and SBR_R1_45_PC blends, as shown by the SBR_R1_25_PC+ and SBR_R1_45_PC+ curves. It does reappear however with a slow kinetics: even after one month, the SBR_R1_25_PC++ and SBR_R1_45_PC++ stay slightly below those of the sample prior its thermal treatment. We have also performed a DMA analysis of the samples just after it has been submitted to the same thermal treatment (inside the DMA apparatus with a temperature ramp of 2˚C/min from 25˚C to -80˚C), and 3 days after the treatment. The curves are presented in Figure 5. 36 and Figure 5. 37.

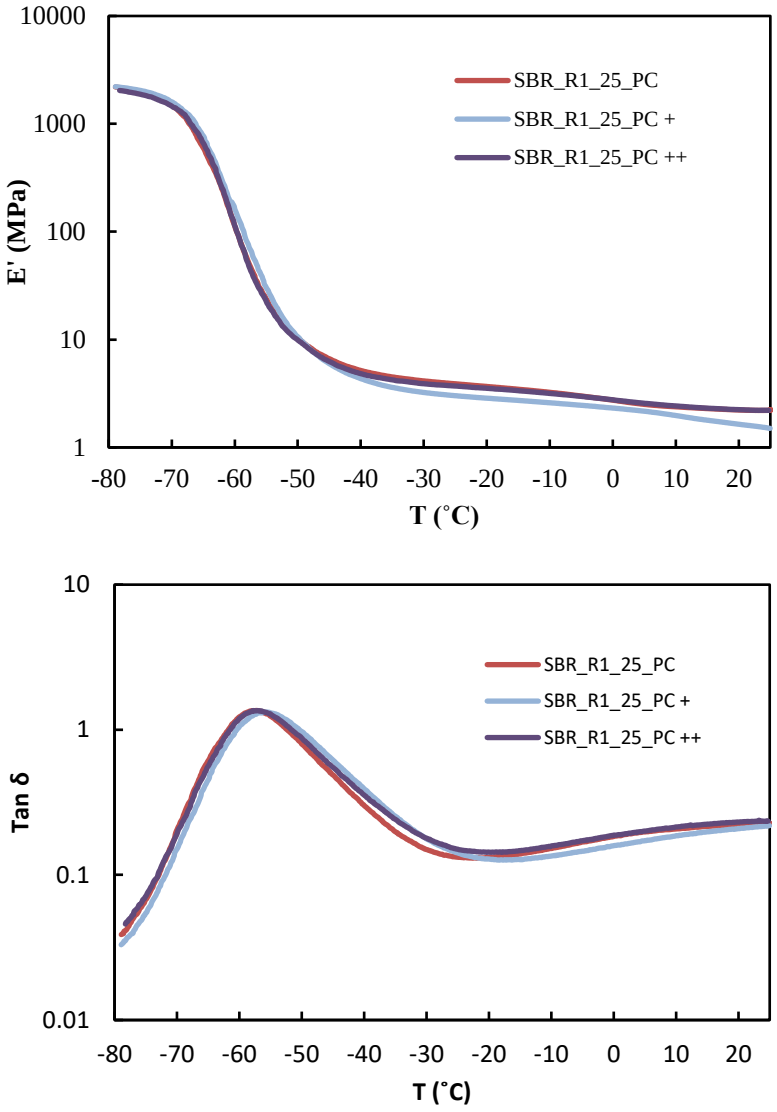

FIGURE 5. 36 DMA STORAGE MODULUS AND LOSS FACTOR VERSUS TEMPERATURE CURVES OF SBR_R1_25_PC BLEND WITH DIFFERENT THERMAL HISTORIES.

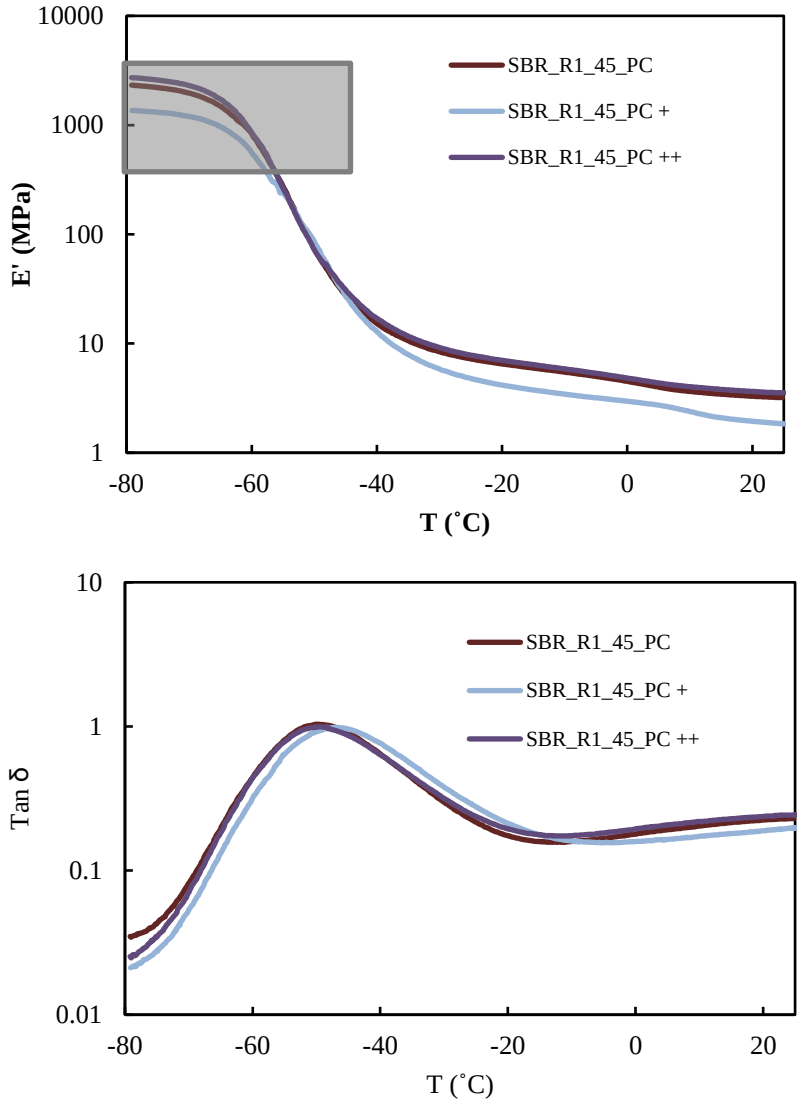

FIGURE 5. 37 DMA STORAGE MODULUS AND LOSS FACTOR VERSUS TEMPERATURE CURVES OF SBR_R1_45_PC BLEND WITH DIFFERENT THERMAL HISTORIES.

The differences are very suddle, but one can distinguish a decrease of the modulus (around 0.8MPa for 25% and 2.8MPa for 45%) when the measurement is performed just after the sample thermal treatment. And we see an almost complete recovery of the modulus value 3 days after. In addition, the shape of the α relaxation is modified: a small shift of 2˚C is observed which disappears after 3 days. These experiments, with the SAXS ones, suggest that the multiscale phase separation in the material depends on the temperature, and is a kinetic process. Heating the sample makes disappear the phase separation at the nanoscale. The disappearance of the small Payne effect observed for SBR_R1_45_SC at 90˚C is also consistent with this argument (cf. Figure S5. 8 in supporting information section of this chapter). The temporary better miscibility of the resin therefore leads to a slight increase of T_α.

5.6 Conclusions

A shift of the glass transition (and of the associated main relaxation temperature) to higher temperature is observed with the increase of the R1 resin content. The fact that this shift is far from being predicted by the Fox law (even using T_α) highlights the existence of a non-miscible resin quantity, in both uncrosslinked and crosslinked blends.

Like the resins R2 and R3, most of the resin R1 does not participate to the curing reaction and can be extracted from the blends. Swelling experiments show that the crosslink density of the R1 blend is similar to the one of R2 blends when the crosslinking is performed in presence of the resin.

DMA and DSC experiments show a transition around 60°C, i.e. around the resin glass transition, revealing the existence of resin rich domains. Morphological analysis highlighted a complex and multiscale microstructure. Microdomains resin rich are created in all blends, wether they are crosslinked or not. Their number and their size increase with the resin content. By assuming a separated phase rigid at ambient temperature, we have estimated its volume fraction using the Christensen and Lo approach. It is 14 vol.% and 30 vol% of the sulfur cured blends containing in overall 25 wt.% and 45 wt% of resin, respectively. This is around 30% less than in the corresponding uncrosslinked blend, indicating that the crosslinking process limits the phase separation.

In addition, resin-rich nanodomains have been evidenced in both SBR_R1_SC and SBR_R1_PC blends by AFM, and for the SBR_R1_PC blends also by SAXS. It is not possible to separate their contribution from the one of the microdomains to the reinforcement when they are in the glassy state. Moreover, SAXS experiments as a function of the temperature suggest that they disappear when the materials are heated above 60°C. This disappearance is reversible with a slow kinetics.

5.7 Supporting information

Calculation of the volume fraction of resin rich phase in blends using the Fox law

The Fox law applied to the T_α of the polymer rich phase writes:

$$\frac{1}{T_\alpha} = \frac{w_{SBR}^{in\ SBR\ rich\ phase}}{T_{\alpha\ SBR}} + \frac{w_{resin}^{in\ SBR\ rich\ phase}}{T_{\alpha\ Resin}}$$

Where $w_{SBR}^{in\ SBR\ rich\ phase}$ and $w_{resin}^{in\ SBR\ rich\ phase}$ are the weight fractions of the resin and SBR respectively *in this phase*. Therefore,

$$w_{resin}^{in\ SBR\ rich\ phase} = \frac{\frac{1}{T_\alpha} - \frac{1}{T_{\alpha\ SBR}}}{\frac{1}{T_{\alpha\ Resin}} - \frac{1}{T_{\alpha\ SBR}}}$$

Moreover

$$w_{Resin} = w_{SBR\ rich\ phase} w_{resin}^{in\ SBR\ rich\ phase} + w_{Resin\ rich\ phase} w_{resin}^{in\ resin\ rich\ phase}$$

Where $w_{SBR\ rich\ phase}$ and $w_{Resin\ rich\ phase}$ are the weight fraction of the SBR rich phase and of the resin rich phase *in the blend* (their summation is equal to 1), and w_{Resin} the resin weight fraction *in the blend*. Assuming that the resin rich phase contains 100% resin, $w_{resin}^{in\ resin\ rich\ phase} = 1$, and all the SBR is in the SBR rich phase

$$w_{Resin} = (1 - w_{resin\ rich\ phase}) w_{resin}^{in\ SBR\ rich\ phase} + w_{Resin\ rich\ phase}$$

We deduce that the weight fraction of the resin rich phase in the blend is:

$$w_{Resin\ rich\ phase} = \frac{w_{Resin} - w_{resin}^{in\ SBR\ rich\ phase}}{1 - w_{resin}^{in\ SBR\ rich\ phase}}$$

The vol% of resin rich phase in the blend (assumed to be made of 100% resin) is deduced from

$$\phi_{Resin\ rich\ phase} = \frac{\frac{W_{Resin\ rich\ phase}}{\rho_{resin}}}{\frac{W_{Resin}}{\rho_{resin}} + \frac{W_{SBR}}{\rho_{SBR}}} = \frac{\frac{W_{Resin\ rich\ phase} \cdot \rho_{resin}}{\rho_{resin}(W_{Resin} + W_{SBR})}}{\frac{W_{Resin} \cdot \rho_{resin}}{\rho_{resin}(W_{Resin} + W_{SBR})} + \frac{W_{SBR} \cdot \rho_{resin}}{\rho_{SBR}(W_{Resin} + W_{SBR})}}$$

$$= \frac{w_{Resin\ rich\ phase}}{w_{Resin} + \frac{w_{SBR} \cdot \rho_{resin}}{\rho_{SBR}}}$$

Where W is for the mass

The results are reported in Table 5. 2.

DSC curves of UC, PC and SC R1 blends

The melting peak corresponding to the melting stearic acid is seen in 1st heating-cooling-2nd heating cycles of SBR_R1_UC and SBR_R1_PC blends (Figure S5. 1). The difference in the two heating cycles is likely due to the difference in the thermal history.

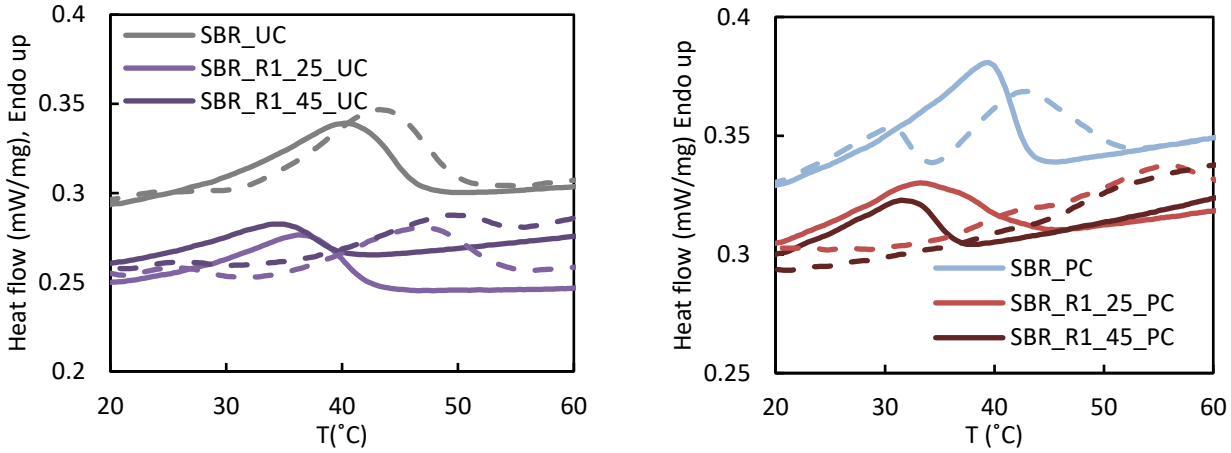

FIGURE S5. 1 DSC HEAT FLOW CURVES (DASHED LINE – 1ST HEATING AND SOLID LINE – 2ND HEATING) VERSUS TEMPERATURE (T) OF SBR_R1_UC SAMPLES AND SBR_R1_PC BLENDS.

The peaks related to zinc stearate complex is still observed on its DSC curve (Figure S5. 2) in resin extracted samples (indicating therefore that it is not soluble in cyclohexane). The peaks are very similar to the one observed for the SBR_SC material, confirming the fact that the resin delay the crystallites nucleation and growth.

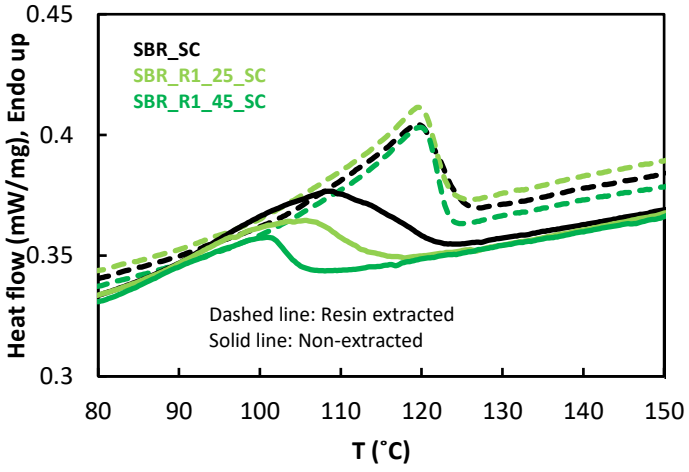

FIGURE S5. 2 DSC HEAT FLOW CURVES (1ST HEATING) OF SBR_R1_SC (SOLID LINES) AND SBR_R1_SC_RES EXTR (DASHED LINES) SAMPLES AT HIGHER TEMPERATURES.

Analysis of crystallization inside micro-domains

A peak at around 75˚C is observed on the curve of the SBR_R1_45_SC blend. It is not present on the curve of the SBR_R1_25_SC blend, as shown in Figure S5. 3A. The disappearance of this peak is not immediately reversible, as shown by its absence on the curves obtained through a 2nd heating cycle performed just after the first one and a rapid cooling down to the ambient temperature. This peak again reappears at around 68˚C when the measurement is performed 15 days or 1 month after the first heating ramp, as shown on Figure S5. 3B. The temperature at which it occurs corresponds to the temperature where the modulus decreases in DMA. It actually looks like a signature of the ageing during the glass transition of the resin rich phase.

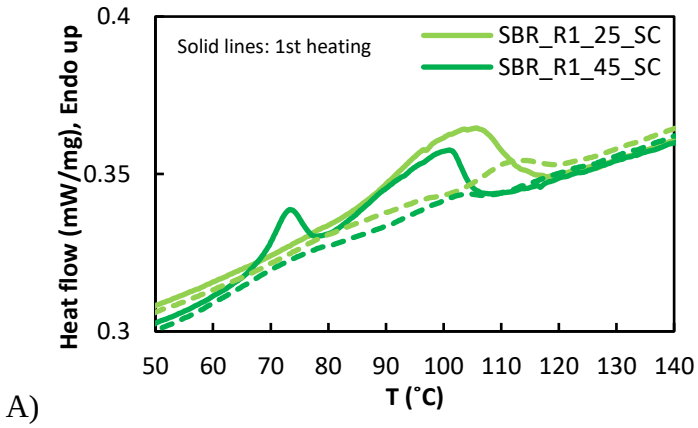

A)

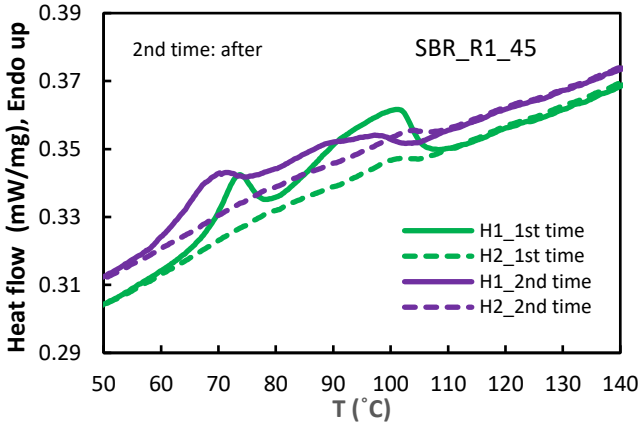

B)

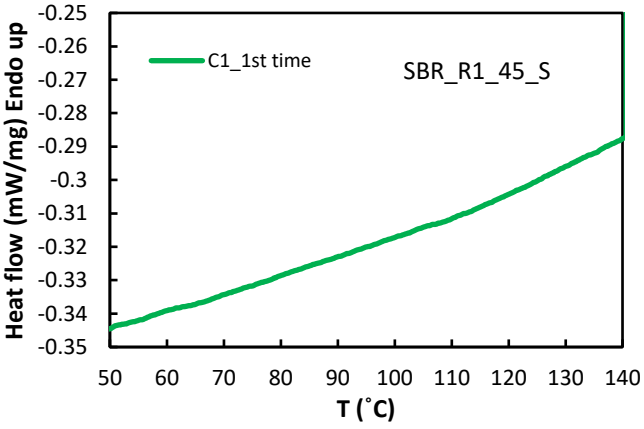

C)

FIGURE S5. 3 DSC CURVES IN THE [50°C TO 140°C] DOMAIN FOR A) SBR_R1_SC BLENDS DURING THE HEATING RAMPS AND B) SBR_R1_45_SC DURING THE HEATING RAMPS AFTER 15 DAYS AND C) SBR_R1_45_SC COOLING RAMP DURING THE FIRST MEASUREMENT.

DMA curves for SBR_R1_45_SC shows two peaks whereas only one is visible on the DMA curve of the SBR_R1_25_SC (Figure S5. 4A). The two peaks are similar when measurements are performed during a cooling or a heating ramp, which question the fact that it is due to melting.

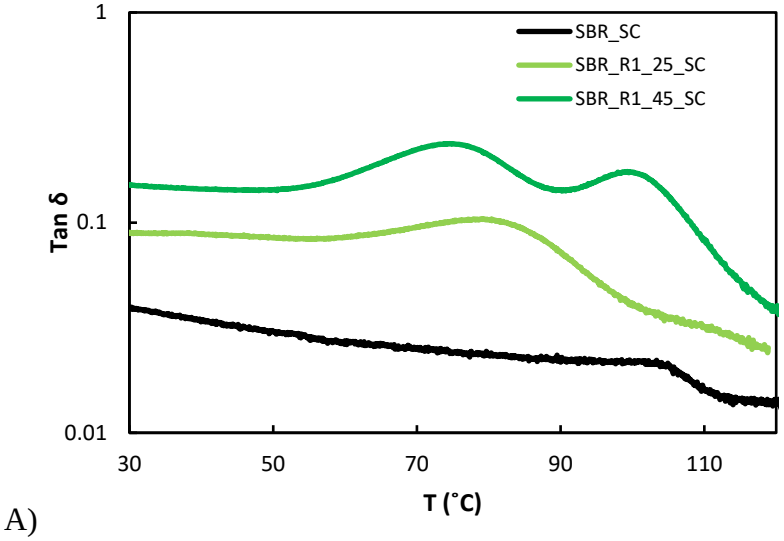

A)

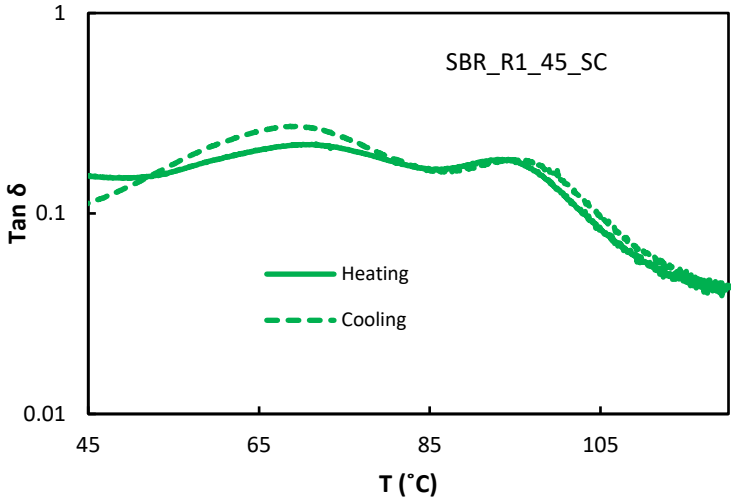

B)

FIGURE S5. 4 LOSS FACTOR VERSUS TEMPERATURE CURVES OF A) SBR_R1_SC BLENDS AND B) SBR_R1_45_SC DURING HEATING COOLING CYCLE.

Treated NMR data of SBR_UC and SBR_SC

The Figure S5. 5, Figure S5. 6, and Figure S5. 7 correspond to the NMR data treatment of SBR_R1_SC_res extr samples as described in chapter 2 and the cross-link density is estimated from this treated data.

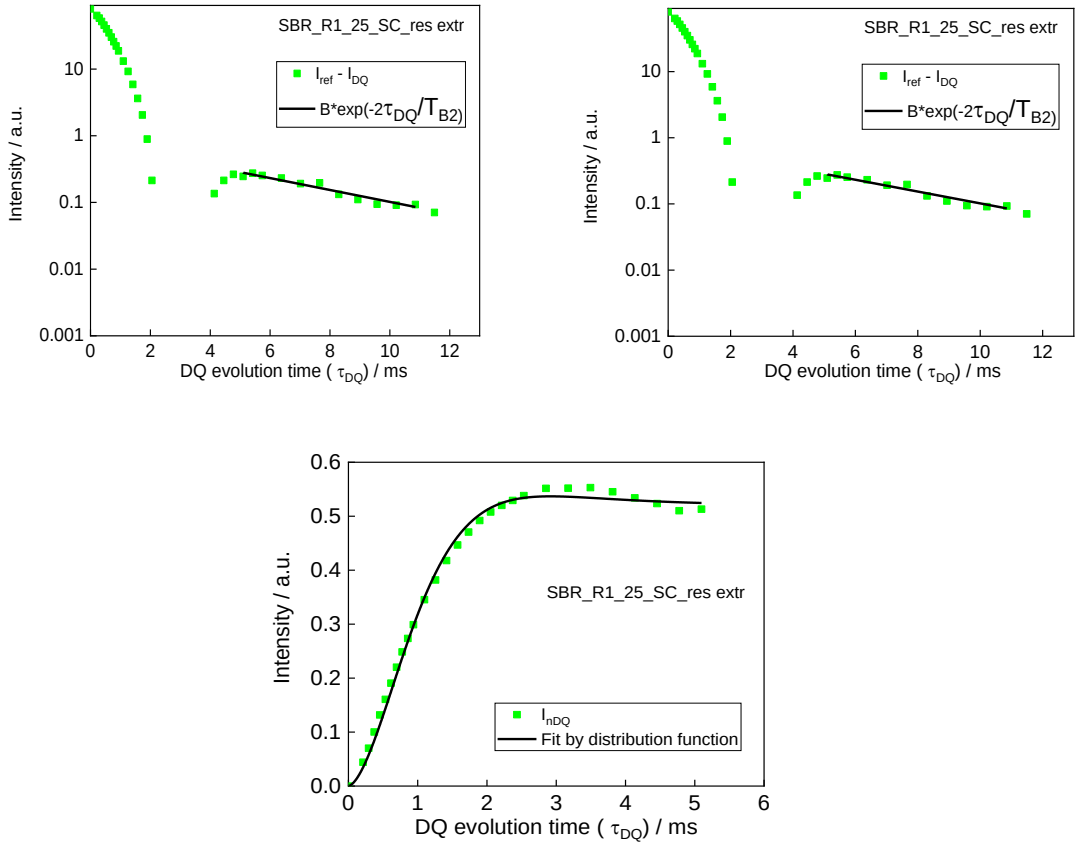

FIGURE S5. 5 A) RAW BUILD-UP (I_{DQ}) AND REFERENCE DECAY (I_{ref}) CURVES, B) THE DIFFERENCE OF I_{ref} - I_{DQ}, AND C) THE SUBSTRACTED AND NORMALIZED BUILD-UP (I_{nDQ}) AS A FUNCTION OF DOUBLE QUANTUM EVOLUTION TIME (τ_{DQ}) OF SBR_R1_25_SC_RES EXTR.

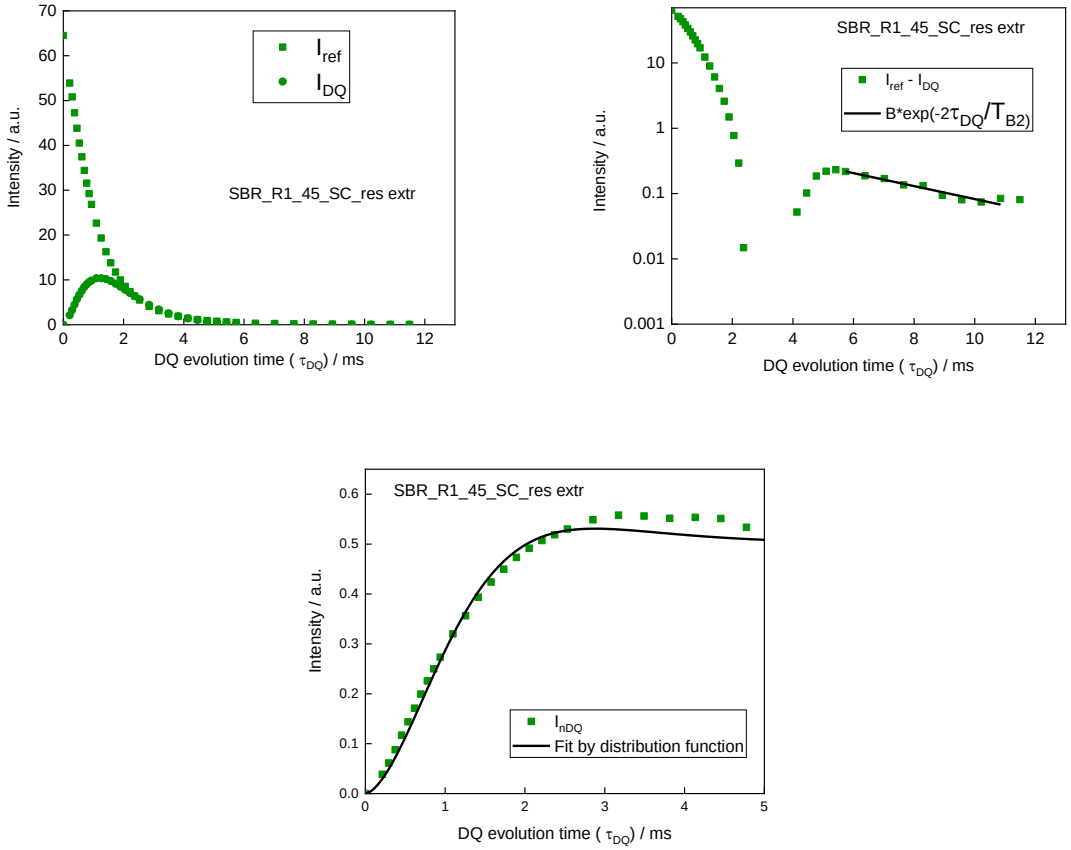

FIGURE S5. 6 A) RAW BUILD-UP (I_{DQ}) AND REFERENCE DECAY (I_{ref}) CURVES, B) THE DIFFERENCE OF I_{ref} - I_{DQ}, AND C) THE SUBSTRACTED AND NORMALIZED BUILD-UP (I_{nDQ}) AS A FUNCTION OF DOUBLE QUANTUM EVOLUTION TIME (τ_{DQ}) OF SBR_R1_45_SC_RES EXTR.

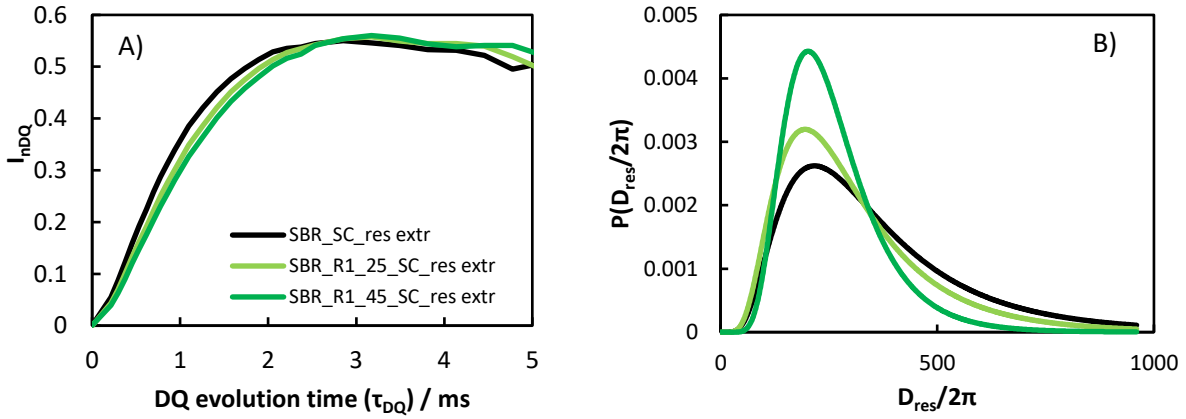

FIGURE S5. 7 A) NORMALIZED BUILD-UP (I_{nDQ}) VERSUS DQ EVOLUTION TIME (τ_{DQ}) AND B) THE CORRESPONDING DISTRIBUTIONS OF SBR_R1_SC_RES EXTR SAMPLES.

Payne effect in SBR_R1_SC blends

Small Payne effect at 30˚C in SBR_R1 _45_SC blend can be ascribed to the presence of microdomains and this Payne effect disappear at 90˚C because of softening of the microdomains (Figure S5. 8).

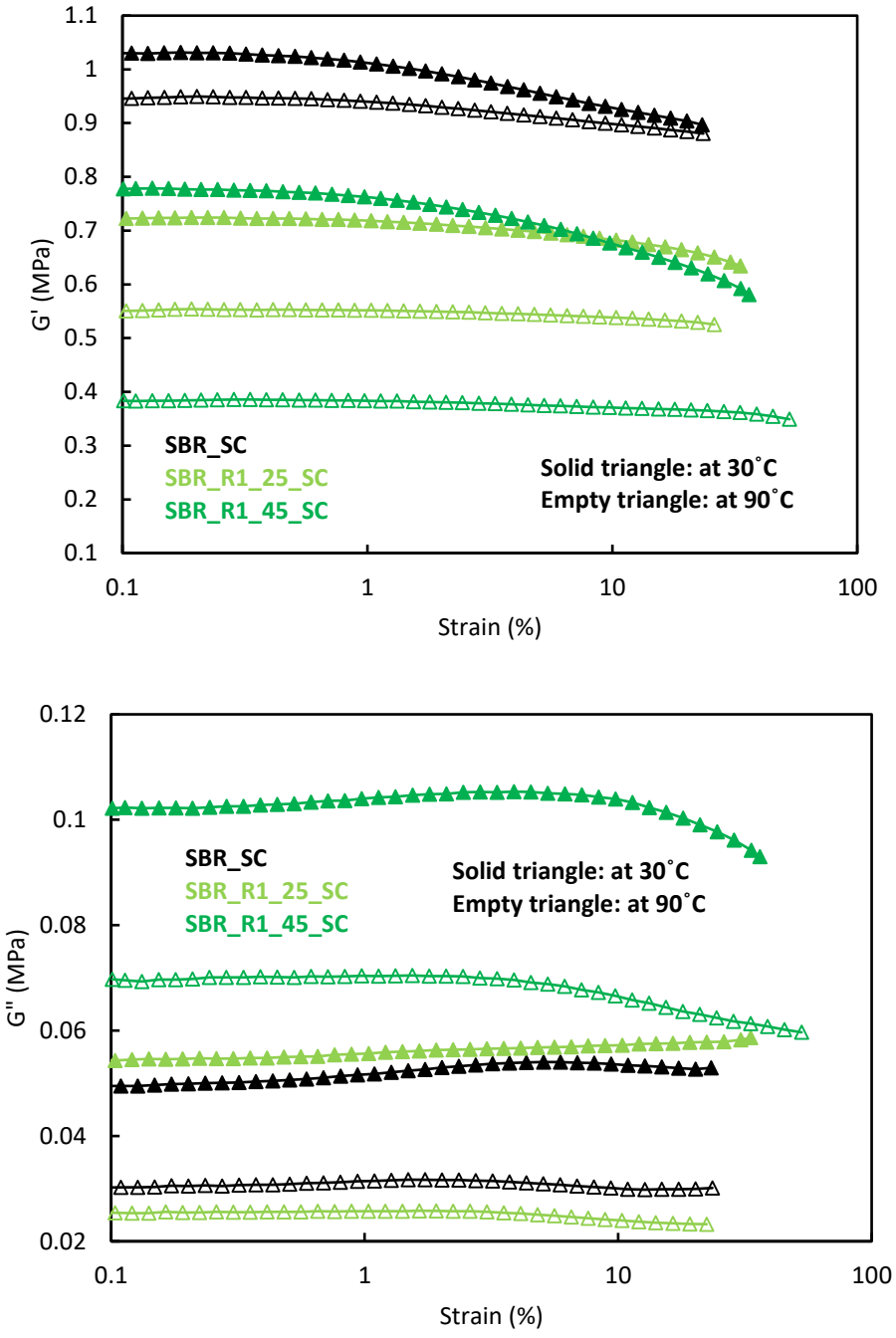

FIGURE S5. 8 SHEAR STORAGE MODULUS AND LOSS MODULUS VERSUS SHEARSTRAIN AMPLITUDE OF SBR_R1_SC BLENDS AT 30˚C AND 90˚C.

5.8 References

(1) Class, J. B.; Chu, S. G. The Viscoelastic Properties of Rubber–Resin Blends. I. The Effect of Resin Structure. *Journal of applied polymer science* **1985**, *30* (2), 805–814.

(2) Class, J. B.; Chu, S. G. The Viscoelastic Properties of Rubber–Resin Blends. II. The Effect of Resin Molecular Weight. *Journal of applied polymer science* **1985**, *30* (2), 815–824.

(3) Donatelli, A. A.; Sperling, L. H.; Thomas, D. A. Interpenetrating Polymer Networks Based on SBR/PS. 1. Control of Morphology by Level of Cross-Linking. *Macromolecules* **1976**, *9* (4), 671–675.

(4) Donatelli, A. A.; Sperling, L. H.; Thomas, D. A. Interpenetrating Polymer Networks Based on SBR/PS. 2. Influence of Synthetic Detail and Morphology on Mechanical Behavior. *Macromolecules* **1976**, *9* (4), 676–680.

(5) Allen, G.; Bowden, M. J.; Blundell, D. J.; Jeffs, G. M.; Vyvoda, J.; White, T. Composites Formed by Interstitial Polymerization of Vinyl Monomers in Polyurethane Elastomers: 2. Morphology and Relaxation Processes in Methyl Methacrylate Based Composites. *Polymer* **1973**, *14* (12), 604–616. https://doi.org/10.1016/0032-3861(73)90034-7.

General Conclusion

The main objective of this PhD thesis was to bring new insights about the complex structure-property relationship in crosslinked Styrene Butadiene Rubber blended with three different resins that originate from petroleum industry. The three studied resins, namely R1, R2 and R3, differ by their molecular weight, their chemical composition, and therefore their T_g. Their glass transition temperatures are higher than ambient temperature, with the order $T_{g\,R3} > T_{g\,R1} > T_{g\,R2}$, irrespective of their molecular weights order of $M_{w\,R1} > M_{w\,R2} > M_{w\,R3}$. Their thermodynamic miscibility with SBR has been investigated using the Hansen solubility parameter approach. However, this approach is insufficient to dissociate the consequence of their introduction in the SBR, as shown by the studies of the blends.

Before, studying them, specific attention has been paid to the Styrene Butadiene matrix in uncured and cured conditions with two different crosslinking systems i.e. sulfur and peroxide. First, and as expected, vulcanization leads to a slight shift towards higher temperature of the glass transition, compared to uncured material, and these results were attributed to the classical notion of decrease in the chain mobility due to crosslinks, as well as the possibility of chain modifications. We also evidenced the presence of stearic acid crystallites in SBR_UC and SBR_PC which do not exist anymore in SBR_SC, since stearic acid has been completely consumed during the crosslinking process. In the absence, or with low number of crosslinks (like in SBR_PC), it was possible to observe a mechanical relaxation at around 40°C, due to either specific chain length distribution and/or the presence of dangling chains. This relaxation is suppressed by the vulcanization process. At higher temperature (around 100°C), another mechanical relaxation can be detected and may be due to some phase separation of the styrene comonomer. In addition, a non-uniform spatial distribution of the crosslinks was evidenced by AFM and confirmed by SAXS analysis. The apparent correlation distance of this nanostructuration decreases with the crosslink density. Thus, even without the presence of resin, heterogeneities exist in the different studied materials, at different scales, which makes therefore more difficult the understanding of the nanostructuration and mechanical behavior of the same system in which resin is introduced.

We then studied the blends of resin R1, R2 and R3 with SBR, uncrosslinked and crosslinked with peroxide or sulfur curatives.

On the one hand, the phenomena observed for SBR alone with respect to the crosslinking process are still visible in the blends:

- The sulfur cross-linking of resin blends also shifted the T_α by around 5˚C, compared to the UC blends (the shift however was slightly less notable for resin R3 blends for which we could not find a reasonable explanation)
- The relaxation around 40˚C is still present in UC and PC blends, similar to SBR alone, and absent in SC blends. In other word all the polymer chains of the SC crosslinked blends are part of the elastomer network.

On the other hand, the presence of resin has different consequences on the characteristics of the blends:

- **Glass transition temperature**: as expected, the resin presence shifts the glass transition temperature and the associated α-transition temperature towards higher temperature and this shift is higher for higher resin content blends. Single T_g and associated T_α were observed for both R2 and R3 SBR blends and can be predicted by the Couchman-Karasz and Fox laws respectively. Moreover, significant broadening of the glass transition domain is observed and is ascribed to the presence of concentration fluctuations. Conversely, for R1 resin, the glass transition temperature of the blends (and associated main relaxation temperature) is far from the prediction, for both uncrosslinked and crosslinked materials. With the existence of an additional glass transition and relaxation, this highlights the existence of a separated phase with a glass transition close the resin one.

  Dilution effect: in uncured state, above their main relaxation temperature, the resins presence decreases the modulus of the UC materials due to a dilution effect. At 120°C, applying a classical dilution law leads to an exponent of 2.73, 2.57 and 2.38, and for R1, R3 and R2 respectively (R1 has therefore the highest dilution effect at high temperature). Thus, there is no correlation between the dilution effect and the molecular weight of these resins. Note that in the temperature domain where one usually applies the dilution law (i.e. in the "rubbery domain"), the exponents deduced are far from the expected ones, indicating that applying the model is questionable. It also indicates that the three resins behave differently. In particular, the rubbery modulus decreases less rapidly with the R2 resin than with the R3 resin. This could be ascribed to the larger (though not high) molecular weight

of the former. Another possible explanation may be the existence of a weak phase separation in the R2 blend, that would need further investigation.

- **Crosslinking impact**: in spite of the fact that the quasi-totality of the resins (R1, R2 and R3) can be extracted from the crosslinked blends, resins may interfere in the crosslinking process: indeed, R1 and R2 resins leads to a lower global crosslink density (deduced from swelling in cyclohexane) than the resin R3. One cannot completely exclude that in R2 this is also due to the existence of phase separation in the blends - different depending on the resin type - during the crosslinking step, although our rheometry data suggests that there is no such phase separation above 100°C.

- **Morphology**: this phase separation has not either been confirmed in SBR_R2_UC blends at ambient temperature by morphological characterization. Nevertheless, a complex morphology is observed for these materials, like for the R3 blends, with correlation distance in the range of tens of nm. This morphology is an indication of crosslinks/entanglements heterogeneities. Conversely to R2 and R3 blends, a clear micro-scale phase separation has been observed for R1 blends, strengthening the conclusions of DSC and DMA analysis. The number and size of the microdomains of resin rich phase increase with the resin content. In addition, in both SBR_R1_SC and SBR_R1_PC blends, resin-rich nanodomains are also evidenced. In situ SAXS experiments revealed the disappearance of these nanodomains when the materials are heated above the glass transition temperature of the resin rich phase. Interestingly, this disappearance is reversible with a slow kinetics.

To sum up, for the studied materials, different mechanisms/phenomena can contribute to the level of modulus measured in the range 20 to 60°C.

In particular, in the case of R1 resin, the rubbery modulus of the uncrosslinked blend increases with the resin content due to the presence of a separated resin rich phase in the glassy state. The reinforcement brought by this rigid phase is therefore more important than the dilution effect brought by the resin molecules remaining in the polymer rich phase. Nevertheless, this rubbery modulus is decreased by the crosslinking step, indicating that the crosslinks limit the phase separation. The Christensen and Lo model enables to estimate that the volume fraction of the

enriched resin phase, is around 20 and 37 vol% in the uncrosslinked SBR_R1_25 and SBR_R1_45 blends respectively, but decrease by more than 20% when these blends are crosslinked. As a consequence, in these materials, the reinforcement originating from the phase separation is actually not sufficient to compensate the dilution effect and the resulting rubbery modulus is close to the one of the crosslinked SBR.

Thus, mastering the rubbery plateau modulus by playing with industrial resins as the ones studied in this work is still a challenge.

Perspectives

Although this study provided interesting results and an improved understanding of the structure-properties relationships in complex resin elastomer blend systems, they also brought other perspectives for further works.

We evidenced that the study of the solubility parameters for SBR and the three resins at ambient temperature in solution conditions- suggesting good miscibility of all three resins with SBR – is not sufficient to predict the behavior of the blends. In particular this approach does not enable to a priori distinguish the resin R1 from the other two resins. This is not so surprising since the temperature should also be taken into account. Moreover, we are far from the solution conditions when studying the blends. In other words, a careful study of the evolution of the interaction parameter with the temperature, and the calculation of a phase diagram would have been helpful, especially to better understand the role of the crosslinking step on the phase separation process.

It could also be interesting to first study analogous but more controlled resin/SBR blends: the studied resin were industrial byproducts, containing molecules with different chemistries. This undoubtedly makes more difficult the data interpretation since it is always possible that phase separation occurs between the different molecules of the resin, an aspect that we chose to avoid. It can be circumvented by working with resins whose chemistry is well controlled. Moreover, the styrene butadiene matrix also showed a complex behavior and a complex morphology which pleads for the use of more model polymer.

The morphogical analysis of the different blends was particularly challenging. From the image observations and SAXS analysis, we made the assumption that the crosslinking step makes disappear some nanodomains in the R1 blend. This needs to be confirmed…and explained. Moreover, decorrelating the contribution of these nanodomains to the modulus, compared to the

one of the microdomains from more sophisticated model might be interesting to confirm our interpretations.

SAXS data were only performed on PC blends, in which the chemical crosslinking density was far from the one in the SC sample. For this reason, the analogy of these samples with the SC blends is not straightforward. Studying more crosslinked PC blends would have probably clarified some questions. Moreover, it was impossible to obtain correct imaging of AFM analysis of the uncrosslinked blends. These observations are missing and may be obtained through a better and longer optimization of the technique parameters.

At longer term, the work presented in this study was applied to simplified elastomer blend systems, instead of more complex elastomer compounds consisting of several other components used in the tire industry. Therefore, in the future work, it would be interesting to understand the structuration and its influence on dynamic mechanical properties in more “realistic” systems, by incorporating fillers such as silica which are known to improve the mechanical performance of rubber compounds. Additionally, part of SBR, in practice, is often substituted by other elastomers such as NR and BR, for economic and property improvement reasons, therefore it would be interesting to understand the structuration in ternary blends of SBR/BR or in NR/Resins.

FOLIO ADMINISTRATIF

THESE DE L'INSA LYON, MEMBRE DE L'UNIVERSITE DE LYON

NOM : KUMAR
(avec précision du nom de jeune fille, le cas échéant)

DATE de SOUTENANCE : 12 Décembre 2022

Prénoms : Robins

TITRE : Multi-scale structuration and dynamic mechanical response of multi-phasic elastomer systems

NATURE : Doctorat

Numéro d'ordre : 2022ISAL0111

Ecole doctorale : Materiaux de Lyon

Spécialité : Materiaux

RESUME : In this study, new types of elastomer systems - seen as an alternative for conventional nanocomposites widely used in tire industry- were prepared and investigated thoroughly. They are made of an SBR (Styrene-Butadiene Rubber) matrix, blended with one resin among three resins with low molecular weight resins, with a higher Tg than the polymer, and different miscibilities. Such materials raise different questions: How does the resin incorporation influence the elastomer network structure? Depending on the miscibility and the resin content, what is the resulting morphology? How does the morphology evolve with the temperature, the processing conditions and the crosslinking protocol? And of course, how this morphology impacts the macroscopic mechanical properties?
Two of the studied resins showed good miscibility, with the absence of phase separation, and no strong influence on the chemical crosslinking reactions of the polymer. Their impact on the viscoelastic behavior is the consequence (i) of a modification of the polymer glass transition, which is broadened due to the presence of resin concentration fluctuations, and shifted towards higher temperature, and (ii) of the dilution of the polymer during its crosslinking, which results in a decrease of the modulus above the glass transition temperature. The third resin has a lower miscibility. In addition to a modification of the glass transition and to a dilution effect, it leads to a phase separation, and therefore the existence of a resin rich phase. This phase is rigid at ambient temperature and reinforces the polymer rich phase, i.e the elastomer matrix. Interestingly, this phase separation slightly depends on the temperature, with a kinetics which may provide a new way to pilot the viscoelastic response of the material.
MOTS-CLÉS : Elastomer, Polymer/resin blends, phase separation, dynamic mechanical analysis

Laboratoire (s) de recherche : MATEIS, equipe PVMH, INSA Lyon

Directeur de thèse: Laurent CHAZEAU

Président de jury : Isabelle ROYOUD

Composition du jury : Valerie GAUCHER, Emilie PLANES, Catherine GAUTHIER, Laurent CHAZEAU, Florent DALMAS, Nicolas MALICKI